PhD Thesis

Experimental investigations of the fluid dynamics of vitreoretinal surgery

By

Irene Nepita

UNIVERSITÀ DEGLI STUDI
DI GENOVA

Department of Civil, Chemical and Environmental Engineering

Advisors:

Profs. Rodolfo Repetto, Alessandro Stocchino

Co-advisor:

Dr. Libero Liggieri

June 2021

Irene Nepita
PhD in Civil, Chemical and Environmental Engineering
Curriculum of Fluid Dynamics and Environmental Engineering, XXXIII cycle
Department of Civil, Chemical and Environmental Engineering
University of Genoa
email: irene.nepita@edu.unige.it

PhD supervisors:
Prof. Rodolfo Repetto
Prof. Alessandro Stocchino
Dr. Libero Liggieri

Reviewers:
Prof. Federica Boschetti (Polytechnic of Milan, Italy)
Prof. Giorgio Querzoli (University of Cagliari, Italy)

Exam committee:
Prof. Marco Clolombini (University of Genoa, Italy)
Prof. Stefania Espa (Sapienza University of Rome, Italy)
Prof. Francesca M. Susin (University of Padua, Italy)

Date of the Defense: June 8th, 2021

Credit for the cover: Erin Hayes. Large collection of eyes in glass - UCSF Library UC Regents, Danz Collection of Artificial Eyes Depicting Diseases and Defects, UCSF Archives & Special Collections.

- Per aspera ad astra -

Summary

Vitrectomy is a surgical procedure by which the vitreous humour is removed from the vitreous chamber of the eye and is replaced with a tamponade fluid. Vitrectomy is performed by means of a system consisting of several components, including the vitreous cutter, which aspirates the vitreous body, a viscoelastic fluid that occupies the vitreous chamber of the eye. The vitreous cutter port geometry may have great influence in vitrectomy surgery from the fluidics and safety standpoints. For this reason, there has been an increase interest from ophthalmic companies in optimising the fluidics within the vitreous chamber during surgical maneuvers, in order to avoid retinal tractions and intraocular pressure (IOP) variations.

Once removed, the vitreous is often replaced with Silicone Oils (SOs), which, however, inevitably tend to emulsify in the aqueous solution present in the eye, limiting the chances of using SOs as long term vitreous substitutes. Many months are indeed often required for complete healing of retinal damages. Moreover, formation of emulsions triggers local inflammatory processes, which can cause further complications.

This thesis is an experimental work related to the physics of ocular surgical procedures and it consists of two main parts. The first part concerns the fluid mechanics of the vitrectomy procedure. In particular, experiments with different approaches have been performed on the fluidics of various vitrectomy systems, with the objective of identifying ideal working conditions that minimise the risks of retinal damages, while keeping the surgical procedure efficient.

The second part is related to the characterisation of the interfacial rheology between SOs and aqueous solutions containing endogenous proteins released by the ocular tissue as a response to an inflammatory state. Aim of this part is to investigate to what extent biomolecules present in the aqueous solution can modify the rheological properties of the interface between the two fluids and, in turn, facilitate the formation of an emulsion. This work is carried out in collaboration with Dr. Libero Liggieri at CNR-ICMATE.

Each part consists of several chapters, which address various projects within these two topics and are briefly summarised below.

Part I. Performance assessment of vitrectomy devices

An important issue associated with vitrectomy is the risk of generation of retinal tractions by the vitreous cutter. It has been demonstrated that an intermittent flow generates fluid accelerations, with consequent pressure variations within the vitreous chamber, which may result in pulsatile tractions on the retina, with significant risk of iatrogenic retinal damage. Rossi et al. (2014b) proposed a conceptual diagram according to which, for a safe and efficient vitrectomy, optimisation of fluidics can be achieved by maximising the flow rate and minimising the acceleration around the cutter port.

Another important aspect of the surgical procedure is prevention of large IOP changes within the eye. In particular, ocular hypertension or ocular hypotony can have very important clinical consequences. In order to maintain a normal IOP value, the balance between the aspiration and the irrigation pressures during vitrectomy plays a very important role. In chapter 1 we reviewed the literature concerning fluid dynamics of vitreoretinal surgery.

In chapter 2 we evaluated the performance of vitreous cutters in vitro in terms of flow rate, using vitreous phantoms with different rheological properties (artificial vitreous, AV). On each fluid solution we performed rheological tests in order to obtain a good control of the properties of the working fluid and thus guarantee reproducibility of the experiments. This allowed us to compare the efficiency of the instruments in a highly controlled environment and to assess how their behavior is affected by fluid properties.

Our results showed that all cutters are higly sensitive to fluid rheology and this is particularly true for double blade cutters, which, however, always produce larger flow rates compared to single blade ones. These findings imply that large flow rate fluctuations should be expected when a vitreous cutter is operated in a medium with heterogeneous mechanical properties (Nepita et al., 2021).

In chapters 3 and 4 we show two experimental studies aimed at assessing the performance of two vitrectomy systems, characterised by different technologies (guillotine and ultrasound probes), tested both with balanced salt solution (BSS) and AVs. The following types of experiments have been performed in a cubic testing chamber.

- *Flow rate measurements*: mean flow rate has been measured using a digital image tracking process for all cutters, changing the operational parameters within a wide range (cutting frequency, aspiration pressure, etc.). Results for guillotine cutters show that for viscoelastic fluids the averaged flow rate only slightly decreases as the cutting frequency increases. The ultrasound cutters produce larger flows regardless the stroke (the amplitude of the ultrasound vibrations of the needle).

- *Flow fields measurements*: two dimensional PIV experiments have been performed with the goal of characterising the flow fields generated by all cutters. For each set of parameters, a sequence of images has been acquired on two different planes: “frontal view” and “lateral view”. Moreover, for a specific solution, two areas of interest have been used for the acquisition: a “large field” of view, aimed at describing the entire circulation induced by the cutters at the scale of the experimental box, and a “small field” of view, i.e. a zoom around the cutter tip, to describe more accurately flow structures around the cutter port. The flow induced by ultrasound cutters is strongly three dimensional and time dependent. Flow structures are generated at different spatial scales, from large scales similar to the experimental domain to smaller scales close to the cutter port (Stocchino et al., 2020).

- *Temperature measurements*: a specific task was dedicated to measure temperature variations induced by ultrasound cutters as a function of the stroke, maintaining the vacuum pressure equal to zero. The two dimensional variation of the temperature field has been monitored with an infrared thermal camera. The acquired thermal images were used to obtain the temperature variations in time at a particular spot, or to generate two dimensional temperature maps. The temperature slightly grows but this effect is likely to be clinically irrelevant, since infusion of a different fluid will mitigate it. Moreover, the cutter head reaches maximum values close to body temperature, meaning that it will not transmit much heat to the needle and eventually to the vitreous during surgery (Stocchino et al., 2020).

- *Pressure measurements*: for this specific type of experiments a model of the human vitreous chamber at real scale and with a realistic geometry has been employed. The eye model has been designed considering both infusion and aspirations lines, thus mimicking the real surgical procedure. The main goal of this part of the research activity is to perform pressure measurements at two different positions of the vitreous chamber (anterior and posterior): for this purpose two high precision pressure transducers (Viatran model 422) have been used.

Results show that dynamic variations of the pressure due to the motion of the cutter blade are always small compared to the average pressure in the eye. Pressure fluctuations related to fluid motion are felt more intensely by the pressure sensor placed on the back of the vitreous chamber, opposite with respect to the irrigation line. This is probably due to the generation of a jet that impinges the chamber wall opposite to its position. When the aspiration phase begins the pressure in the eye model drops, which is related to hydraulic head (pressure) losses along the pipelines of the system. This pressure drop is typically reduced (sometimes very efficiently) when the vitrectomy system can actively compensate pressure variations. Results suggest that maximum irrigation pressure that can be used for compensating pressure losses during aspiration should be selected depending on several parameters such as the minimum irrigation pressure and the aspiration pressure, in order to optimise the desired compensation.

PART II. STUDY OF SILICONE OIL EMULSIFICATION IN RELATION TO VITRECTOMY

The tendency of SOs to emulsify in water is influenced by the chemico-physical properties of the fluids and interface and by external factors, such as temperature and mechanical energy provided to the system. Exposition of the SO to endogenous molecules (proteins, lipids, etc.) in the vitreous chamber, the presence of which is favored by the post-surgical inflammatory state of ocular tissues, is also considered to be important for the generation of an emulsion. The mechanisms at the basis of the effects of these molecules on the emulsification process depend on their capability to adsorb at the water-oil interface, modifying the mechanical interfacial properties, such as the interfacial tension (IT) and the dilational viscoelasticity (DV), i.e interfacial rheological response to surface variations.

In chapters 5 and 6 we give an overview of the possible mechanisms for SO emulsion formation and stabilisation, with a particular focus on biomolecules adsorption processes at the SO-aqueous interface.

In chapter 7 we propose an experimental study aimed at achieving a chemico-physical characterisation of the interfacial properties between SOs and aqueous solutions and at investigating the effect of surfactant biomolecules, such as albumin and γ-globulins, possibly responsible for emulsion formation. In particular, measurements of IT on pendant drops of the protein aqueous solution in the SO have been performed. These measurements have been carried out by a Drop Shape Tensiometer (PAT1-Sinterface, Berlin). This technique allows one to quantify the DV by measuring the IT response to small sinusoidal perturbations of frequency imposed on the interfacial area.

Results show that adsorption of these proteins at the interface reduces the IT to values compatible with the generation of an emulsion and provides values of the DV compatible with a good stability of the resulting emulsions (Nepita et al., 2020). This study allowed us to understand the effect of individual, key blood proteins on the mechanical properties of the interface. In order to evaluate the overall effect of the presence of these proteins, we conducted a second series of experiments adopting whole human serum blood (WHSB) samples obtained from donors. The

results obtained with the serum dissolved in the solution showed that, already in concentrations of 1-2 orders of magnitude smaller than that of single proteins, the IT significantly decreases, up to values compatible with the formation of an emulsion, indicating therefore possible synergistic effects with other components of the serum, in addition to the proteins previously studied. Moreover, the DV modulus increases up to rather high values, compatible with the stabilisation of the emulsions against the coalescence.

Drugs used as intraoperative tools in vitrectomy can also act as surfactants. An example is the intraocular injection of an anti-inflammatory steroid, composed of micro crystal particles. To assess whether the drug has a surfactant role at the interface, we conducted a first series of experiments to quantify the IT and the DV properties. We performed the measurements on the aqueous phase of the dispersion (supernatant), which separates after the sedimentation of crystals. The experiments with the supernatant neither show a significant decrease of IT that can be associated with the formation of an emulsion, nor lead to significant DV values. However, it is known that dispersions of partially hydrophobic solid particles can give rise to particularly stable emulsions, known as Pickering emulsions (Binks, 2002).

In order to verify the capability of biomolecules to form emulsions stable over the timescale of months, comparative emulsification tests have been performed and shown in chapter 8. Emulsions were produced using to the Double Syringe method (Gaillard et al., 2017). Although this emulsification method may be very different from what occurs in practice, it is significant for investigating the stability of the emulsion formed and is, therefore, used as a simple screening test. For all samples containing blood proteins or the steroid drug, the presence of an emulsion layer was detected, the thickness of which decreases with increasing dilution, and which was stable over long times. On the contrary, the sample containing the Dulbecco buffer alone was already separated a few minutes after the emulsion formation. Thus, we can conclude that blood proteins are able to form and stabilise emulsions. Moreover, the steroid drug is able to stabilise Pickering-type emulsions.

Eye movements are the main source of mechanical energy applied to the interface between SO and aqueous solution inside the eye. A set of measurements in a realistic domain have been performed. A qualitative and a quantitative analysis of the risults are reported in chapter 9 and 10, respectively. In particular we have used a Plexiglass model of a vitreous chamber with realistic geometry. The experimental setup is equipped with an optical diagnostics for monitoring the emulsion, a mechanical system controlled by a computer to simulate eye saccadic movements and thermalised at 35°C. Once filled with SO and aqueous solution, the model is mounted on a support connected to a computer-controlled motor. In this study, harmonic rotations were considered. The temporal evolution of the emulsion has been studied through acquisition of images with a digital camera. In the case of emulsions characterised by very small droplets, a microscope (Leica Microsystems, Switzerland) has been used to determine their distribution and size. The main result obtained from these experiments consists in the formation and persistence of emulsions even when a low concentration of albumin has been dissolved in the aqueous solution (1% of the physiological concentration in blood). Moreover, the majority of the drops had a very small diameter: in the range of $0 - 10$ μm. Droplets with these characteristic dimensions are considered more dangerous from the clinical point of view, since they are able to favor the onset of ocular complications.

TABLE OF CONTENTS

PREFACE

The vitreous chamber is the largest cavity of the eye. It is delimited anteriorly by the lens and posteriorly by the retina. It is filled by the vitreous humor (or vitreous body), which is a transparent gel like material. From the mechanical point of view, the vitreous has viscoelastic properties that have been measured by several authors ex vivo (e.g. Lee et al., 1992, 1994; Nickerson et al., 2008; Swindle et al., 2008). The vitreous has important roles in the physiology of the eye. In particular, it fills the vitreous cavity and maintains the contact between the retina and the retinal pigment epithelium (RPE). It also acts as a barrier for transport of molecules and heat from the anterior to the posterior segments of the eye. It finally has the obvious role of transmitting the light entering the eye from the pupil to the retina, where light signals are transformed into electrical signals transmitted through the optic nerve to the brain (Sebag, 1989).

The vitreous humor gel structure typically degrades with advancing age. In particular, the vitreous undergoes the processes of liquefaction (synchysis) and collapse (syneresis). The former is associated with the formation of liquid lacunae in the vitreous body, typically located in the center and posterior regions of the vitreous cavity. Syneresis is, on the other hand, related to loss of liquid from the vitreous gel to the space forming between vitreous and retina.

A detachment of the retina from the RPE is called retina detachment. Retinal detachment is often associated with degenerative processes of the vitreous humor, in particular with the so-

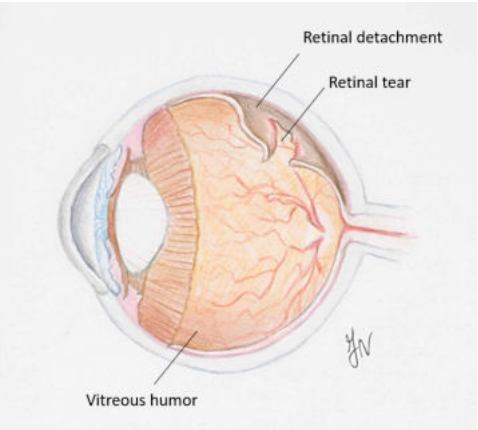

Figure 0.1: Retinal detachment with retinal tear.

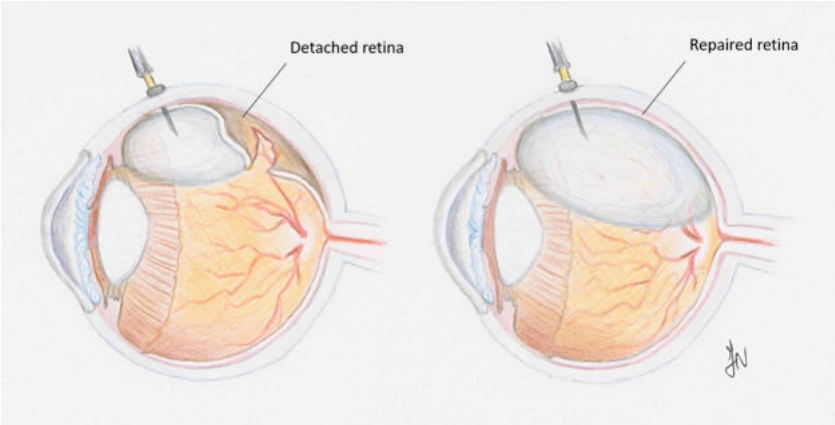

Figure 0.2: Repair of a retinal detachment with vitrectomy procedure.

called posterior vitreous detachment (PVD): the gel vitreous detaches, from the retina typically in the back of the eye, and the space left free is filled with aqueous (Tozer et al., 2014). This is a normal part of aging and can be harmless. Sometimes, however, PVD can produce large tractions of the retina and tear the retina (figure 0.1); this happens when the vitreous gel is tightly attached to the retina (Di Michele et al., 2020).

In this condition fluid may pass through a retinal tear, lifting the retina in the back of the eye. Retinal detachment is a very serious problem that may cause blindness, if not treated surgically. Risk factors for developing a retinal detachment are: an eye or head injury, nearsightedness (myopia), and diabetes.

Unfortunately, most cases of retinal detachment cannot be prevented. Many people have symptoms of a PVD, before they have symptoms of retinal detachment. When the vitreous gel shrinks and separates from the retina, it causes floaters and flashes, i.e. spots, specks, and lines that float and appear at the edges of the visual field. The first sign of detachment may be a shadow across part of the vision that does not go away. In other cases patients experience sudden loss of peripheral vision that gets worst over time.

Vitrectomy is the second most frequent surgical ophthalmic intervention after cataract and it consists in the replacement of the vitreous body with transparent vitreous substitutes. It is performed to treat several pathological or traumatic vitreoretinal conditions, such as retinal detachments, haemorrhages, inflammations and infections and presence in the eye of foreign bodies. During vitrectomy, an aqueous solution is infused into the vitreous chamber. Once surgery is complete, if the retina is not teared the aqueous solution is normally left indefinitely in the eye. On the other hand, if there are breaks in the retina from which fluid could move into the subretinal space and induce a detachment, saline solution, gas bubbles or SOs may be injected into the vitreous cavity, which have the role of filling the vitreous chamber and tamponating the sensory layer of the retina in contact with RPE (figure 0.2).

The goals of vitrectomy for retinal detachment are: to remove viteous opacities, due, for instance, to a vitreous hemorrhage, to eliminate vitreoretinal tractions, to identify and treat all retinal breaks, induce retinal re-attachment, to facilitate placement of a large intraocular tamponade and to avoid complications associated with scleral buckling surgery.

The usual sequence of events during this surgical procedure includes: removal of the vitreous gel and preretinal membranes, identification of retinal breaks, internal drainage of subretinal fluid (via retinal breaks or a retinotomy), laser therapy to all breaks and areas of significant vitreoretinal degeneration, and placement of an internal tamponade fluid (Sebag, 2014). Usually, various instruments are adoptded to assist the surgery such as: a light source to illuminate the eye, forceps to peel membranses and scar tissue, drainage needles to remove fluid form the vitreous chamber and an endolaser to seal around retinal tears or treat abnormal blood vessels in the eye.

There are number of risks associated with vitrectomy, such as: infection and increase in IOP. Post vitrectomy surgery may give rise to corneal edema with possible loss in transparency, bleeding inside the eye, cataract formation in patients above the age of 50.

Another important risk associated with vitrectomy is the generation of retinal tractions by the vitreous cutter. It has been demonstrated that an intermittent flow generates fluid accelerations, with consequent pressure variations within the vitreous chamber, which may result in pulsatile tractions on the retina, and significant risk of iatrogenic retinal damage.

An ideal substitute for an efficient vitrectomy procedure, should have all the qualities of the human vitreous, including transparency, buffer capacity and biocompatibility with the surrounding ocular tissues. Moreover, its density and refractive index (a characteristic that describes how the light propagates through a medium), should be close to those of the natural vitreous. It should be storable and sterilisable, chemically and biologically inert, and non-toxic, in order not to trigger undesirable biological responses. It should preferably have lasting viscoelastic properties, to avoid drainage through retinal breaks and to tamponade the retina in contact with the RPE. Moreover, it must allow transport of necessary metabolites and proteins inside the vitreous. However, none of the currently available vitreous substitutes possesses all these qualities: both short-acting and long-acting vitreous substitutes, which are used in vitroretinal surgery, have significant shortcomings, mostly related to lack of biocompatibility and inadequate behaviour. In particular gases and perfluocarbon liquids play an important role in short intraoperative procedures, while SOs are used as longer-term retinal tamponades.

SOs is in the group of inert hydrophobic liquid polymers and is constitued of repeated units of siloxane and the most commonly used consists of polydimethylsiloxane (siloxane with two attached methyl side chains), also known as PDMS. In 1980s, SO was successfully established in its role as a long-term internal tamponade agent and its use and potential risks have been further defined by the Silicone Oil Study (Lean et al., 1989; Azen et al., 1991). To date, SO remains an indispensable tool in retinal surgery, especially in complicated retinal pathologies

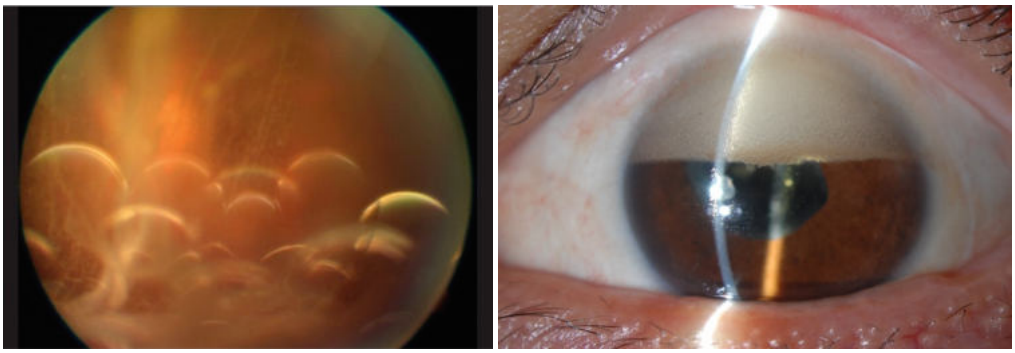

(a) (b)

Figure 0.3: SO emulsions observed after vitrectomy: (a) within the vitreus chamber, (b) in the anterior segment of the eye. Credit for the pictures: Yoshihiro Yonekawa, MD - Wills Eye Hospital / Mid Atlantic Retina.

requiring a longterm vitreous substitute for internal tamponade. Most PDMS have density equal 0.97 g/cm^3; hence they float on water and they are called lighter-than-water SO polymers. For heavier SOs, density varies between 1.02 and 1.06 g/cm^3. One of the advantages of using SOs is related to its high interfacial surface energy with the aqueous interface, which ensures closure of retinal breaks and reduces subretinal leakage. Moreover the lower density of SOs as compared to aqueous solutions causes it to float upon residual fluid and thus helps retinal reattachment in case of superior breaks. The use of SOs is also associated with some complications. Their hydrophobic nature leads to a poor contact with the retina, which inhibits the total filling of the vitreous cavity. The persistence of SO over long periods (6 months) leads to sight threatening complications such as cataract, glaucoma and keratopathy and these complications therefore necessitate its removal (Soman and Banerjee, 2003). If a SO is left for a long period in the vitreous chamber, it invariably tends to emulsify (see figure 0.3(a)). The occurance of an emulsion leads to a series of possible serious complications. This, in particular, when the oil droplets are small enough to pass from the vitreous to the anterior chamber, as shown in figure 0.3(b). In this case, the oil droplets may get trapped in the trabecular meshwork and block aqueous drainage, thus leading to an increase of the IOP.

In vitrectomy, a SO capable of being emulsion resistant would be extremely helpful to treat patients requiring a long term tamponating effect or with a high proliferation stimulus. This is because a lower tendency to emulsify would reduce the incidence of inflammatory processes after surgery. This, in turn, would imply a faster and steadier recovery of the patient, together with a lower risk of serious, sight threatening, complications. Moreover, since SO emulsion may cause an increase of the intraocular pressure and a higher risk of developing glaucoma, emulsion resistant SOs would lead to a significant decrease in the occurrence of such complications and in the related need for additional, more invasive, surgical treatments. In order to define

a strategy for limiting or controlling the emulsion of oils used as tamponade fluids during vitrectomy for the treatment of retinal detachment, it is therefore essential to fully characterise the interfacial properties between oil and aqueous humor, in particular in the presence of blood proteins produced by inflammatory processes in the eye, that might act as surfactants.

In this thesis we address two areas of fluid mechanics related to vitreoretinal surgery, which are discussed in two separate parts. In the first part we study the fluid mechanics which characterises the maneuvers of the surgical procedure. In the second part, we discuss the problem related to SO emulsification after vitrectomy. The thesis is concluded with a discussion of the main findings and their relevance along with possible future directions and extensions of the work.

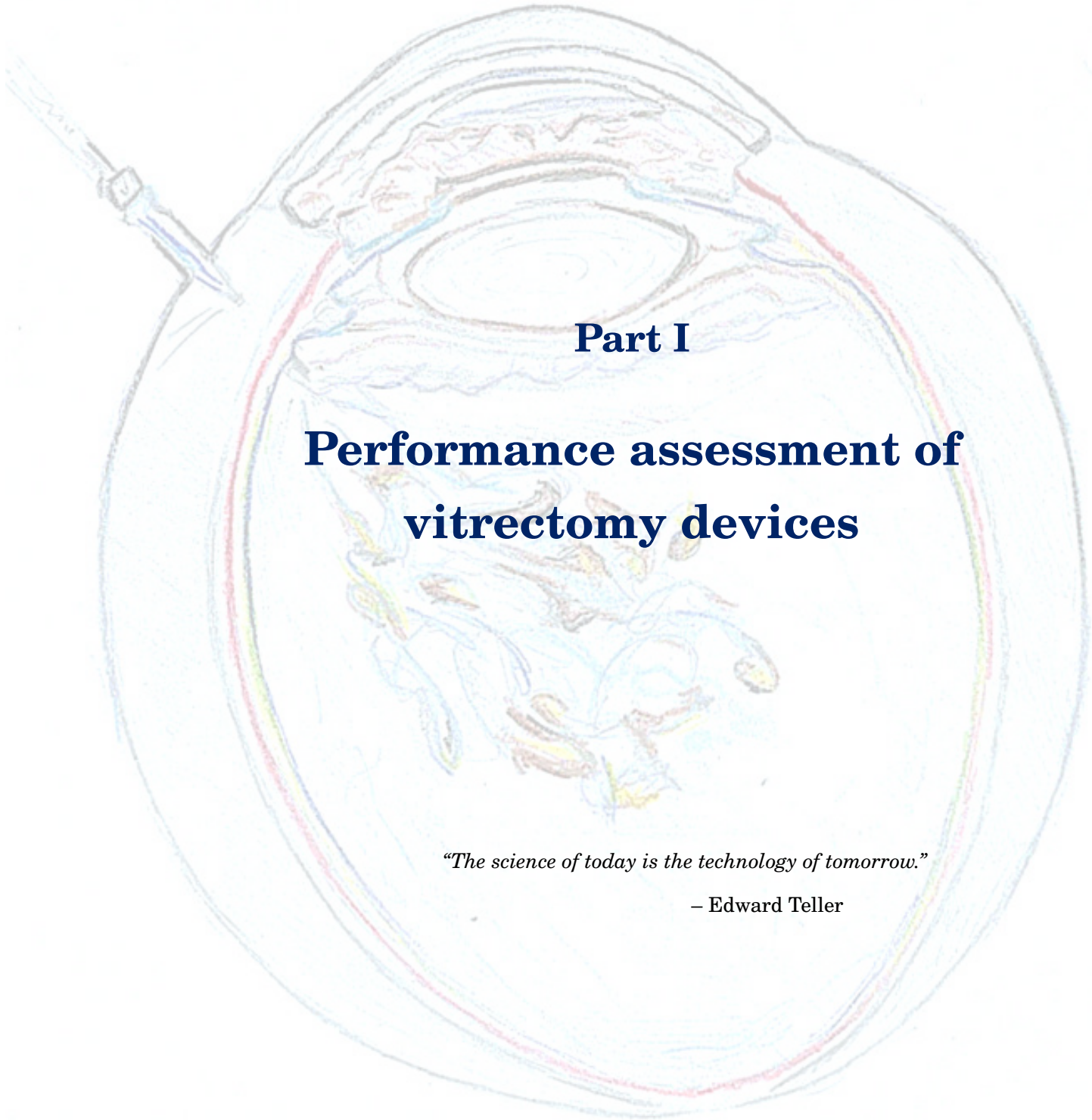

Part I

Performance assessment of vitrectomy devices

"The science of today is the technology of tomorrow."

– Edward Teller

CHAPTER 1

FLUID DYNAMICS OF VITREORETINAL SURGERY

This chapter is partly based on the publications by Nepita et al. (2021) and Stocchino et al. (2020), which Irene Nepita co-authored.

1.1 THE ROLE OF RHEOLOGICAL PROPERTIES OF THE VITREOUS BODY

The wide use of pars plana vitrectomy and the attempt to optimise the surgical procedure have led to a growing interest in the assessment of the performance of vitrectomy systems. The crucial demand for an effective and safe procedure is the maintenance of a stable and substantial flow rate, avoiding strong fluid accelerations and pressure fluctuations, which might result in retinal tractions that can possibly produce retinal damages (Rossi et al., 2014a). The influence of cutter size and design on flow conditions has been extensively studied, with particular reference to the role of cutting edges (single blade, SB, or double blade, DB, configuration), cut rate and duty cycle (Magalhaes Jr et al., 2008; Rossi et al., 2014a; Abulon, 2015; Abulon and Buboltz, 2016; Romano et al., 2018; Rossi et al., 2014e,b; Zehetner et al., 2018).

In recent years great attention has been devoted to emergencing technologies and, especially, to the use of small size cutters, i.e. 25 and 27-G (Osawa and Oshima, 2014; Rizzo et al., 2015; De Oliveira et al., 2016). In particular, the smallest cutter size has proven to be a valuable clinical solution in several treatments, although the aspiration flow rate has been reported to decrease with respect to larger cutters (Watanabe et al., 2016; Romano et al., 2017).

The human vitreous is a heterogeneous, non-Newtonian material, exhibiting a complex viscoelastic behavior. The rheology of the vitreous body has been studied using several different techniques, including bulk measurements (Bettelheim and Wang, 1976; Tokita et al., 1983), magnetic microrheology (Lee et al., 1992, 1994), in vivo visual tracking (Zimmerman, 1980), acoustic (Walton et al., 2002) and MRI-based (Piccirelli et al., 2012) techniques. Most experiments have

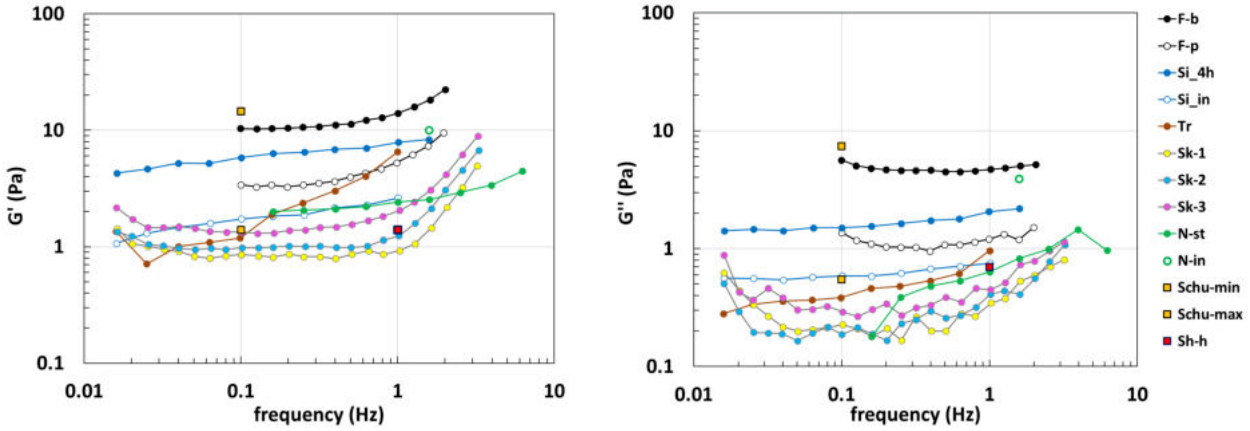

(a) (b)

Figure 1.1: Storage (a) and loss (b) moduli as a function of the testing frequency. F-b: Filas et al. (2014) bovine vitreous; F-p: Filas et al. (2014) porcine vitreous; S-i: da Silva et al. (2017) initial values, rabbit vitreous; Si-4h: da Silva et al. (2017) 4 hours after dissection, rabbit vitreous; Tr: Tram and Swindle-Reilly (2018) human vitreous; Sk-i: Sharif-Kashani et al. (2011) (i = 1; 2; 3 denotes different eyes), porcine vitreous; N-st: Nickerson et al. (2008) steady state values, porcine vitreous; N-in: Nickerson et al. (2008) initial values, porcine vitreous; Schu-min and Schu-max: Schulz et al. (2019) minimum and maximun values of 3365 years old vitreous patients; Sh-h: Shafaie et al. (2018) human vitreous.

been conducted on animal vitreous, typically bovine and porcine specimens. In spite of the significant quantitative differences in the mechanical properties estimated with different methods, all authors characterise the vitreous as a viscoelastic material. In figure 1.1 we report experimental data from experiments performed by many authors on real vitreous humour of various animal species.

The rheological properties of the medium have a significant impact on cutters performance (Abulon and Buboltz, 2016). Previous studies reported that the flow rate produced by vitrectomy cutters is larger in balanced salt solution (BSS) than in viscoelastic fluids, such as egg albumen (Rossi et al., 2014a,e,b; Zehetner et al., 2018), porcine vitreous (Abulon and Buboltz, 2016; Abulon, 2015) and artificial vitreous (AV) (Romano et al., 2018). Moreover, significant changes in flow field, flow fluctuations, acceleration and kinetic energy have been described, comparing the flows induced by different vitrectomy probes in BSS and egg albumen (Rossi et al., 2014a,e,b) or AV (Romano et al., 2018).

Thorough assessment of the performance of vitrectomy systems operating in different media is of great clinical relevance since, during vitrectomy, probes encounter media of different viscosity and elasticity, owing to the inhomogeneous consistency of vitreous humor (Rossi et al., 2014a). It is also well known that changes in vitreous macromolecular organisation, due to aging and various vitreoretinal diseases, result in significant spatial variations of the vitreous rheological properties (Pokki et al., 2015). Indeed, progressive vitreous liquefaction, leading to the

gradual formation of liquid pockets (lacunae) (Sebag, 1987), and changes in the distribution of collagen fibrils that collapse, forming bundles (Los et al., 2003), produce significant changes in the viscoelastic properties of the vitreous with age and within the vitreous chamber (Lee et al., 1992, 1994). In addition, the variability of material properties within the vitreous chamber can be higher than normal in some specific pathological conditions, typically treated by pars plana vitrectomy, such as vitreous hemorrhage or presence of lens residuals in the vitreous cavity. Finally, we note that, during surgery, the removed vitreous is continuously replaced by BSS, with a progressive increase of BSS-to-vitreous ratio (Abulon and Buboltz, 2016) and, consequently, a change in time of the overall properties of the medium within the vitreous chamber. For all the above reasons, a vitrectomy probe less influenced by changes of the medium mechanical properties will ensure a more stable flow rate and a more efficient vitrectomy.

1.2 THE INFLUENCE OF VITREOUS CUTTER TECHNOLOGY

It is well established that, in order to perform safe and effective surgery, it is important to minimise fluid accelerations while keeping sufficiently large values of the flow rate (Romano et al., 2018; Rossi et al., 2014a). This is because fluid acceleration and the consequent flow intermittency generate pressure variations, vitreoretinal tractions, and, potentially, iatrogenic breaks and/or removal of healthy tissue (Charles, 2014; Steel and Charles, 2011; Rossi et al., 2014c). Traditional guillotine vitrectomy probes (GVPs) have been optimised through progressive reductions in size and increases in cut rate (De Oliveira et al., 2016). Recently, hypersonic vitrectomy systems have been introduced in which a handpiece, the hypersonic vitrectomy probe (HVP), produces high-frequency longitudinal vibrations with the aim of inducing vitreous liquefaction close to the tip (Pastor-Idoate et al., 2017; Stanga et al., 2017). The potential advantages of HVPs are related to probe design and mechanism of action. With regard to the former, in a GVP the inner needle moves inside the outer one, determining the cyclic port opening and closing, whereas in the HVP there is a single needle and the port is always open. As a consequence, HVPs have a larger inner diameter than GVPs of the same nominal size. According to Poiseuilles law, the volumetric flux increases with the fourth power of the radius (the resistance to flow is proportional to the inverse of the fourth power of the radius). Thus, when using HVPs, one should expect significantly lower flow resistances, thus allowing the user to set the infusion pressure to lower values in order to keep the same flow rate (Thompson, 2011). Moreover, HVPs have no limitations associated with the duty cycle, as the port is always open (Abulon, 2015). Regarding the mechanism of action, the HVP is an ultrasonically, not pneumatically, driven probe, and rather than cutting the vitreous it is intended to cause its liquefaction. GVPs generate flow fluctuations that are inherently associated with the cutting process (Romano et al., 2018; Rossi et al., 2014c,e). Because there is no cutting with HVPs, fewer fluctuations are expected to occur. The cut rate of GVPs has been progressively increased with the aim of reducing the viscosity of the aspirated fluid (Charles, 2004; Sharif-Kashani et al., 2013); however, the maximum cut rate is

mechanically limited by the duty cycle and speed of the GVP blade (Diniz et al., 2013; Ribeiro et al., 2013; Abulon and Buboltz, 2016). Moreover, the fragmented vitreous has complicated viscoelastic properties, and recent data have demonstrated that increasing the cut rate does not effectively reduce its viscosity (Rossi et al., 2016). As mentioned above, HVPs are designed to produce vitreous liquefaction close to the tip (Stanga et al., 2017). Based on these findings, HVPs offer several benefits in terms of fluidics. Recently, Stanga et al. (2017) and Rizzo et al. (2020) reported high flow rates of water, BSS, and vitreous using various HVPs and an ultrasound-based vitrector prototype, respectively. On the other hand, it has been hypothesised that the use of HVPs might be associated with significant heat production, which can lead to temperature increases in the vitreous chamber, potentially causing thermal damage to the surrounding tissues (Sippel and Pineda, 2002).

1.3 The role of the intraocular pressure (IOP)

Among of all surgical factors, maintaining a constant intraocular pressure (IOP) is essential during vitrectomy. Several studies have evaluated IOP fluctuations during this surgical technique, reporting significant pressure variations, both in animal and human eyes (Rossi et al., 2014d; Dal Vecchio et al., 2017). In particular, IOP achieved values up to 40 mmHg in an animal model (Moorhead and Armeniades, 1986), and pressure oscillations ranging from 0 to 120 mmHg have been measured in human eyes (Moorhead et al., 2005; Okamoto et al., 2010). Such IOP fluctuations may lead to serious intraoperative and postoperative complications, such as choroidal detachment, vitreous hemorrhage, expulsive choroidal hemorrhage, retinal and optic nerve ischemia (Findl et al., 1997; Manschot, 1946; Brubaker, 1984; Gass and Parrish, 1982; Parrish et al., 1982; Tabandeh et al., 1999; Speaker et al., 1991).

Speaker et al. (1991) demonstrated that expulsive choroidal hemorrhage, which is one of the most common complications of vitrectomy, is significantly related to sudden IOP drops. This phenomenon is likely to occur when the vitreous cutter is activated and aspiration starts. Acute elevations of IOP are known to lead to juxtapapillary retinal and optic nerve head blood flow decrease in healthy patients. Thus, IOP changes during vitrectomy may be particularly harmful in eyes affected by proliferative diabetic retinopathy and retinal vein occlusion with compromised blood flow (Michelson et al., 1996; Minami et al., 2007).

An important aspect of vitrectomy is, therefore, to prevent excessive IOP changes and, understanding the cause and the intensity of IOP variations during surgery will help improving the safety of the surgical procedure. For this reason, there has been an increasing interest by ophthalmic companies in improving the design of vitrectomy systems and in optimising their use. In particular, several new vitrectomy devices are equipped with compensating systems, aimed at actively counteracting IOP changes during surgery. However, direct IOP measurements during vitrectomy are not performed in the usual surgical procedure (Rossi et al., 2017), which makes it difficult to achieve effective pressure compensation. In this respect, several studies have been

conducted with the aim to evaluate IOP changes during experimental vitrectomy and to estimate the efficacy of pressure compensation systems (Sugiura et al., 2013; Falabella et al., 2016; Kim and Choi, 2012; Kim et al., 2015; Abulon and Buboltz, 2015). In these works experiments were performed with Alcon vitrectomy systems (Alcon Ltd, Fort Worth, TX) and using either a pressurised model filled with BSS, or fresh porcine eyes. Moreover, a few reports have assessed IOP changes through other techniques: Rossi et al. (2019) proposed a physically based algorithm for the prediction of infusion pressure drop, whereas Okamoto et al. (2010) developed a method for measuring central retinal artery pressure during vitrectomy.

CHAPTER 2

EXPERIMENTAL ASSESSMENT OF THE PERFORMANCE OF VITREOUS CUTTERS WITH DIFFERENT VISCOELASTIC FLUID

This chapter is based on publication by Nepita et al. (2021).

In this chapter we discuss experimental results aimed at investigating how variations in the rheological properties of artificial vitreous solutions influence the performance of vitreous cutters of different gauges. In particular, we investigated how the performance of single blade (SB) and double blade (DB) vitreous cutters of different size (23, 25 and 27-G) depends on the rheological properties of a viscoelastic vitreous substitute, in controlled laboratory tests. Several reports on the response of small size instruments employed in different surgical procedures, have been published. However, in those cases knowledge of the actual mechanical properties of the removed vitreous is not available (Watanabe et al., 2016; Romano et al., 2017). Performance tests in a controlled environment, on the contrary, can be seen as a more suitable approach to compare the performances of different instruments.

2.1 MATERIALS AND METHODS

2.1.1 EXPERIMENTAL SETUP

We studied the suction flow rate obtained with different vitreous cutters connected to the EVA vitrectomy system (DORC International, Zuidland, The Netherlands), equipped with the VTi control system. All the experiments have been performed in "Core vitrectomy" modality, which operates in vacuum control, i.e. imposing the aspiration pressure. We tested different vitrectomy probes (23, 25 and 27-G in both SB and DB geometries) on AV solutions with different rheological properties.

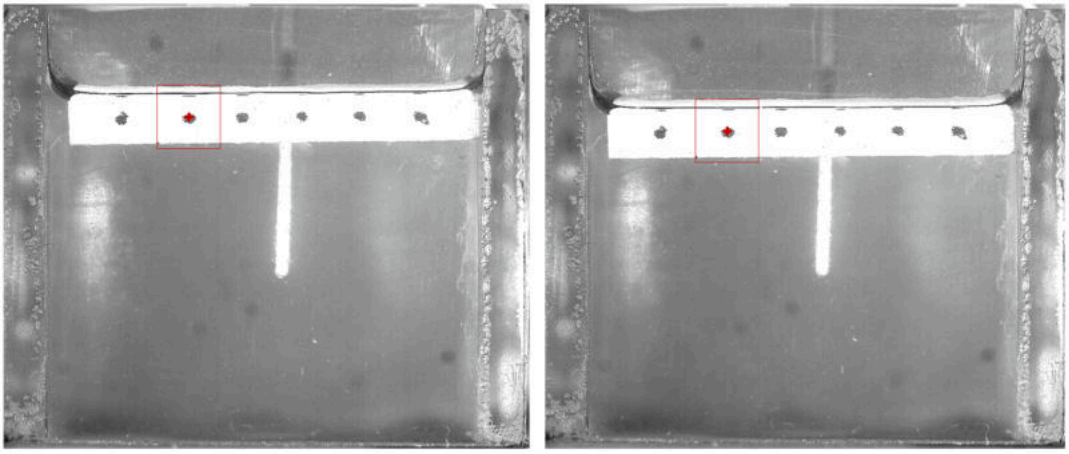

Figure 2.1: Images of the floating plastic panel at two successive times. The red cross indicates the material point tracked by the algorithm.

The experimental setup consisted of a cubical chamber ($3\times3\times3$ cm^3), with transparent Perspex walls, open on the top side, which was filled with the working fluid. Fluid was pumped out of the measuring chamber through an aspiration line and we did not use an infusion line, thus the amount of fluid in the chamber progressively decreased during the experiment. For the purpose of the present study, the geometry of the experimental chamber has little influence.

Flow rate has been measured adopting the following image-based technique. We recorded sequences of images of the lateral wall of the measurement chamber through a high speed digital camera (IDT Xstream Xs3). As the vitreous cutter pumped fluid out of the chamber, as the level of the free surface progressively dropped and we tracked its vertical position, $z(t)$, in time. We then determined the magnitude of the free surface velocity as $U = |dz/dt|$. Finally, the flow rate Q was obtained as $Q = U \cdot A$, where A is the horizontal cross section of the measuring chamber.

In order to make the level of the fluid clearly recognizable in the images, a floating, thin, white plastic panel was placed on the free surface of the fluid. The size of the panel was slightly smaller than that of the chamber section, so that it could freely move vertically as the fluid level varied, with minimal friction on the walls. The vitreous cutter was kept in the desired position by a vertical holder and entered the chamber thorough a hole in the plastic panel. Moreover, black dots were marked on the lateral side of the panel, which were used in the automatic tracking procedure (see figure 2.1).

Automatic tracking was performed, analysing the digital images with the software Motion Studio, IDT Inc. Images of the tracking procedure are shown in figure 2.1, in which two pictures relative to different times are reported. The algorithm is based on the cross correlation of a user-defined area around a target point, indicated with the red square in the pictures, between successive frames. We set the camera acquisition rate to 10 frames per second and the total recording time was between 10 and 20 seconds, depending on flow conditions. Calibration was

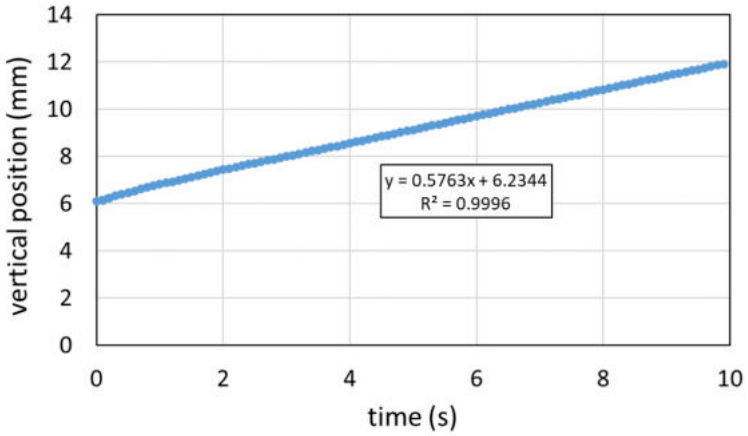

Figure 2.2: Vertical position of the Forex panel, z, as a function of time t, during an experiment. The signal is analysed with a linear regression.

done by acquiring a sheet of graph paper in the plane of interest. Based on the optical arrangement used, a single image pixel corresponded to a physical dimension equal to 0.035 mm. Since the tracking algorithm worked with a subpixel accuracy, about 0.1 pixel, this implies that the single position was known with a $\pm$ 0.0035 mm error.

When the cutter is operated keeping constant the controlling parameters, the suction flow rate is expected to be constant, which implies that in our experiments the vertical position of the free surface $z(t)$ varied linearly with time to a very good degree of approximation. Thus, we extracted the vertical surface speed by performing a linear regression of the signal $z(t)$. In all cases, the coefficient of determination, R^2, took values raging between 0.998 and 1. An example has been reported in figure 2.2. We do not know the total uncertainty associated with each of the measurements of the free surface level; however, assuming that a linear function is a good model for representing our data and following the procedure proposed reported by Press et al. (1992), we could estimate the standard deviation of the angular coefficient of the fitting line. This is a measure of the error on the flow rate divided by the cross-sectional area of our measuring box. The results of this analysis are discussed in section 2.2.3. In addition, for some specific sets of parameters we repeated the flow measurement 20 times and found that the standard deviation of the series of repetitions was $\approx$ 2% of the average value, which is a good indication of the repeatability of the experiments with our experimental setup.

In table 2.1, we summarise all experiments conducted in the present study, for a total number of 555 tests.

2.1.2 WORKING FLUIDS

In the present study we performed experiments on AV solutions. The AV consisted of a solution of Agar powder (Fluka, 05040-100G) and hyaluronic acid sodium salt (Sigma Aldrich, 53747-

cutter	**pressure** (mmHg)	**cut rate** (cpm)	**# of experiments**	**# of tested solutions**
23SB	300-600	2000-8000	97	11
23DB	300-600	2000-8000	97	11
25SB	300-600	2000-8000	97	11
25DB	300-600	2000-8000	97	11
27SB	300-600	2000-8000	79	9
27DB	300-600	2000-8000	88	10

Table 2.1: List of all experiments with corresponding controlling parameters.

10G), mixed in deionised water, and was based on the recipe proposed by Kummer et al. (2007). Starting from the recipe proposed by the Authors, we modified the concentrations of the constituents between 0.3 and 2 mg/ml, in order to change the rheological properties of the resulting fluid within a reasonable range. Each solution was prepared in the same working conditions and required a preparation time of about 24 hours.

The fluid obtained with the above procedure is viscoelastic. We note that hyaluronic acid is a natural component of the real vitreous, which, together with collagen, contributes to the biomechanical properties of the vitreous (Sebag, 1989). On the contrary, Agar is not present in the vitreous but it represents a good surrogate for collagen fibrils in terms of elastic properties. Moreover, Agar is a natural polysaccharide widely used for biomedical applications (Caló and Khutoryanskiy, 2015; Yadav et al., 2015). Overall we tested 10 different viscoelastic solutions (S1-S3, S3B, S4-S9) and BSS, in order to simulate the completely liquefied vitreous condition.

2.1.3 RHEOLOGICAL TESTS

On each fluid solution, we performed rheological tests, which informed us about the properties of the working fluids and also guarantees repeatability of the experiments.

Rheological tests on the AV were performed with the rotational viscometer Physica Anton Paar MCR 301. The instrument is equipped with a synchronous motor, with a high-resolution optical encoder and an air bearing system, to allow a torque resolution of 1 nN$\cdot$m, in a range between 0.1 μN$\cdot$m and 200 mN$\cdot$m. The rheometer can work both in constant rotation and oscillatory mode (frequency range, f, between 10^{-5} and 10^{2} Hz), with an angular deflection resolution of 0.01 μrad. For each solution we performed oscillatory tests in a range of frequencies from 1 to 10 Hz, with a shear strain of 0.1. Experiments were all within the linear viscoelastic region, as we determined via amplitude sweep tests. The oscillatory tests provide the two quantities G' and G''. The former is named storage modulus and is a measure of fluid elasticity while the latter, the loss modulus, quantifies the material viscosity. For mathematical convenience such quantities are typically arranged to form the complex modulus $G^* = G' + iG''$, with $i = \sqrt{-1}$ (Tanner, 2000). Both G' and G'' are function of the testing frequency. It is also convenient to introduce

the absolute value of the complex modulus, as a synthetic measure of the viscoelasticity of the fluid, defined as $|G^*| = \sqrt{G'^2 + G''^2}$.

We also tested all samples in continuous rotational configuration, which allowed us to determine the stress versus shear rate curve (τ vs $\dot{\gamma}$), in the range $0.1 \leq \dot{\gamma} \leq 1000$ 1/s. From this curve it is possible to derive the apparent viscosity η, defined as the ratio between shear stress $\tau(\dot{\gamma})$ and shear rate $\dot{\gamma}$.

In all experiments we adopted a double-gap configuration of the rheometer and measurements were taken at 20 ± 0.2°C, which is the temperature at which flow rate was also measured. For both oscillatory (i.e. frequency sweeps) and rotational tests (i.e. steady state flow sweeps) experiments were performed twice with the same procedure and environmental conditions, in order to ensure repeatability. The confidence interval estimated by Rheoplus Software resulted lower than 2%.

2.2 Results

2.2.1 Rheological measurements

In figure 2.3(a) we show the storage modulus G' for all the AV solutions, as a function of the testing frequency f, in the range 0.1–10 Hz. In panel (b) of the same figure we report the corresponding values of the loss modulus, G''. Both G' and G'' range from low values up to approximately 5 Pa and grow with the frequency.

Comparison with the experimental data relative to real vitreous humor of various animal species (Nickerson et al., 2008; Swindle et al., 2008; Sharif-Kashani et al., 2011; da Silva et al., 2017) reveals that, in our solutions, the complex modulus takes values in the appropriate range and, similarly as in the animal measurements, it grows with the frequency. We note that in most of our solutions G' assumes values slightly smaller than those measured experimentally for the real vitreous humor. This choice was suggested by the observation that, typically, vitreous cutters are used on patients of advanced age who, to some extent, have experienced vitreous liquefaction.

In figure 2.3(c) we show the results of steady state rheological tests in terms of values of the apparent viscosity η, as a function of the shear rate $\dot{\gamma}$, for all solutions. In all cases the viscosity drops for increasing values of $\dot{\gamma}$, which indicates that all solutions have shear thinning properties. This is in agreement with the measurements performed by da Silva et al. (2017) on rabbit vitreous humor.

2.2.2 Flow rate measurements

In this section, we discuss flow rate measurements taken with all cutters and using 10 different AV and BSS.

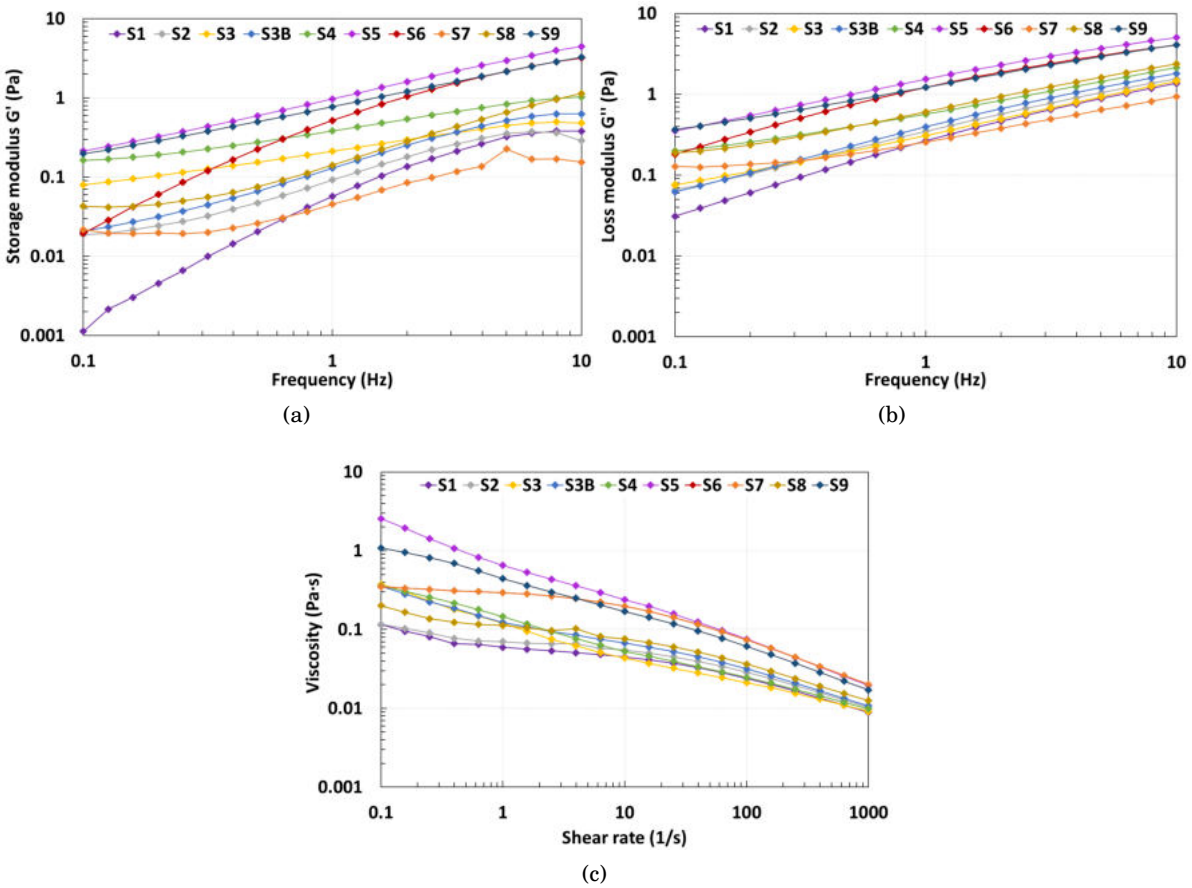

Figure 2.3: Rheological properties of the AV solutions at 20°C. Oscillatory tests: (a) storage modulus G' and (b) loss modulus G'' as a function of the testing frequency f. Steady state tests: (c) apparent viscosity η as a function of the shear rate $\dot{\gamma}$ for all solutions.

In figure 2.4 we plot the flow rate as a function of the pumping pressure, for a cutting frequency of 5000 cpm. Each panel reports measurements obtained for a single cutter and the different curves correspond to the tested solutions, as indicated in the plot legends. The figure clearly shows the importance of fluid rheology on the flow rate. In all cases the flow rates with AVs are significantly smaller than with BSS (black curve). Changes of the flow rate with fluid rheology are stronger for DB cutters (plots on the right column) at low aspiration pressure. However, the flow rates are larger with DB than SB, for all solutions. As expected, in all cases the flow rate increases with the pumping pressure.

Figure 2.5 is analogous to figure 2.4, but in this case the pumping pressure is kept fixed at 600 mmHg and the cutting frequency is varied between 2000 and 8000 cpm. The figure shows that the flow rate is typically slightly higher at small cutting frequencies and becomes almost frequency independent above $\approx$ 4000 cpm. This result confirms the findings of a previous study

(Romano et al., 2018).

The influence of the mechanical properties of the medium on the flow rate Q is illustrated in figures 2.6 and 2.7. In the first figure, panel (a), we plot Q for all tested solutions at a given cutting frequency (5000 cpm) and pressure (600 mmHg). With red solid dots connected by dashed lines (right vertical axis of the figure) we show the absolute value of the complex modulus $|G^*|$ of each solution at a fixed frequency equal to 7.94 Hz. We note that a different choice of the frequency at which the modulus $|G^*|$ is evaluated would not have altered these results qualitatively. In figures 2.6 the solutions are arranged on the x-axis in such a way that $|G^*|$ monotonically grows from left to right. Note that between the two figures there is a switch in the horizontal axis between S5 and S6. Each curve in the plot corresponds to a different cutter. As a general behavior, it appears that, as the modulus of the fluid grows, the flow rate decreases very significantly. This result is clearly visible also in figure 2.6(b) where the left vertical axis represents the difference between the flow rate Q for each solution and the corresponding value in BSS, Q_{BSS}, normalised with Q_{BSS}, $(Q - Q_{\mathrm{BSS}})/Q_{\mathrm{BSS}}$. For all cutters probes the normalised flow rate reduction is ≈ 0.6 for most solutions and up to ≈ 0.9 for the solutions characterised by a large modulus.

Figure 2.7(a,b) is analogous to the previous one, but the red dots (right axis) now refer to the value of the apparent viscosity at $\dot{\gamma}$ =1000 1/s. In this case the various solutions are ordered along the x-axis so that the viscosity grows monotonically from left to right. The flow rate decreases significantly with increasing fluid viscosity and this behavior is common to all cutter probes. It is worth noting that the smaller size cutter, 27-G SB and DB, were not able to produce a measurable aspiration flow rate for the solutions S5 and S6. In particular the SB cutter seems to not aspirate for both solutions S5 and S6, whereas the DB cutter still works for solution S5 and not for solution S6. In the following section, we comment further on this aspect.

2.2.3 Results of the error analysis

As described in section 2.1.1, the flow rate measurement error was estimated as the standard deviation of the angular coefficient of the line fitting the position of the free surface in time, multiplied by the cross-sectional area of the measuring box. In order to represent synthetically the output of the performed error analysis, we plot the relative error on the flow rate for each cutter and each working fluid using a *box-and-whisker* plot, see figure 2.8. Note that in the abscissa, the solutions have been ordered in analogy with figure 2.7, also adding the BSS data sets. The *box-and-whisker* plot is a graph used to synthetically show several characteristics of the distribution of a dataset, whether a distribution is skewed and whether there are potential unusual observations (outliers) in the data set. In this case, we consider the relative error of the measurements performed with a prescribed cutter with a particular working fluid as a single dataset. The box plot for each dataset will provide seven values that, from the lowest, can be listed as: minimum outliers defined as values less than 2/3 of the first quartile; minimum

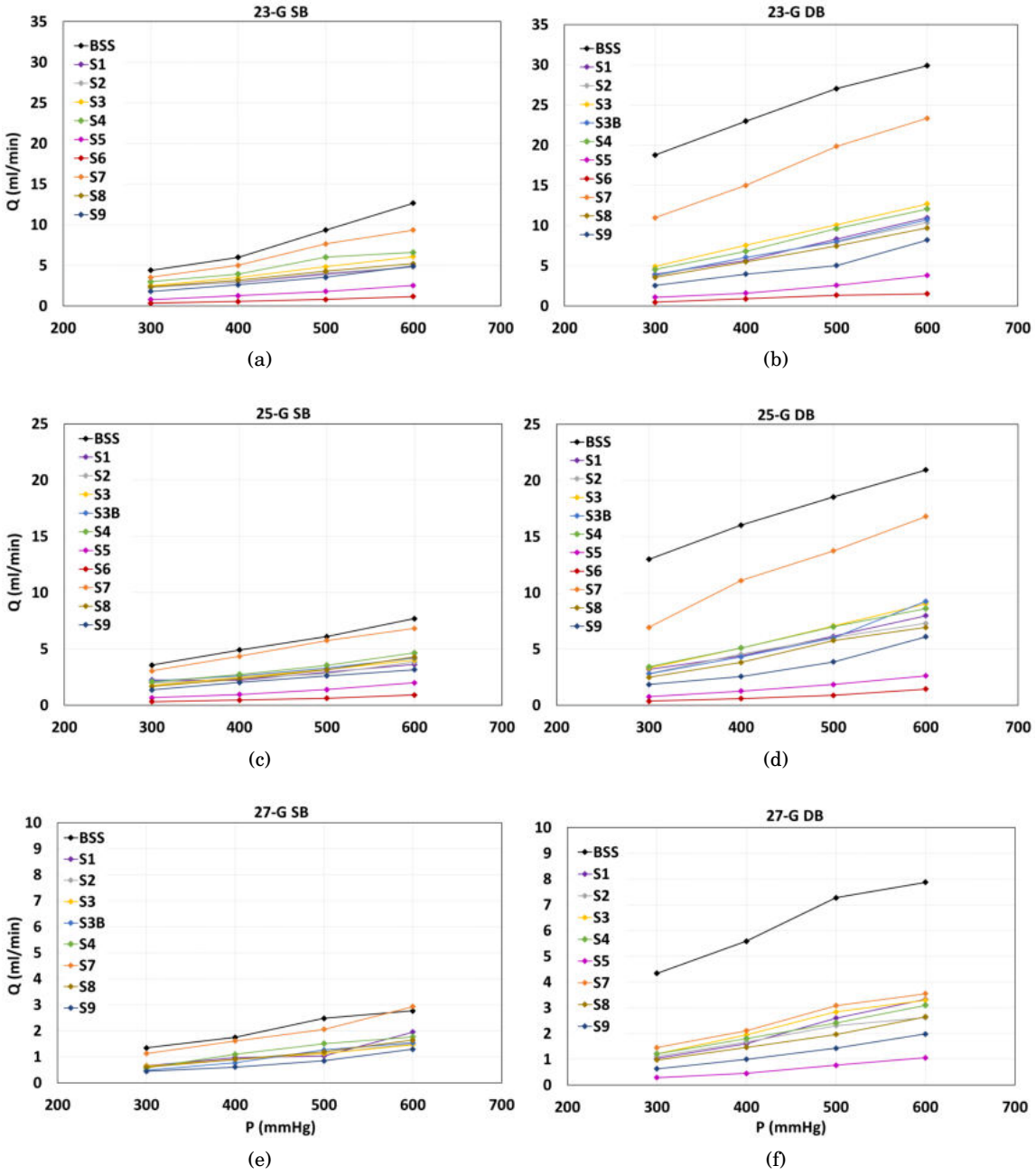

Figure 2.4: Flow rate as a function of the pumping pressure for all solutions. (a) 23-G SB; (b) 23-G DB; (c) 25-G SB; (d) 25-G DB; (e) 27-G SB; (f) 27-G DB. Cutting frequency: 5000 cpm.

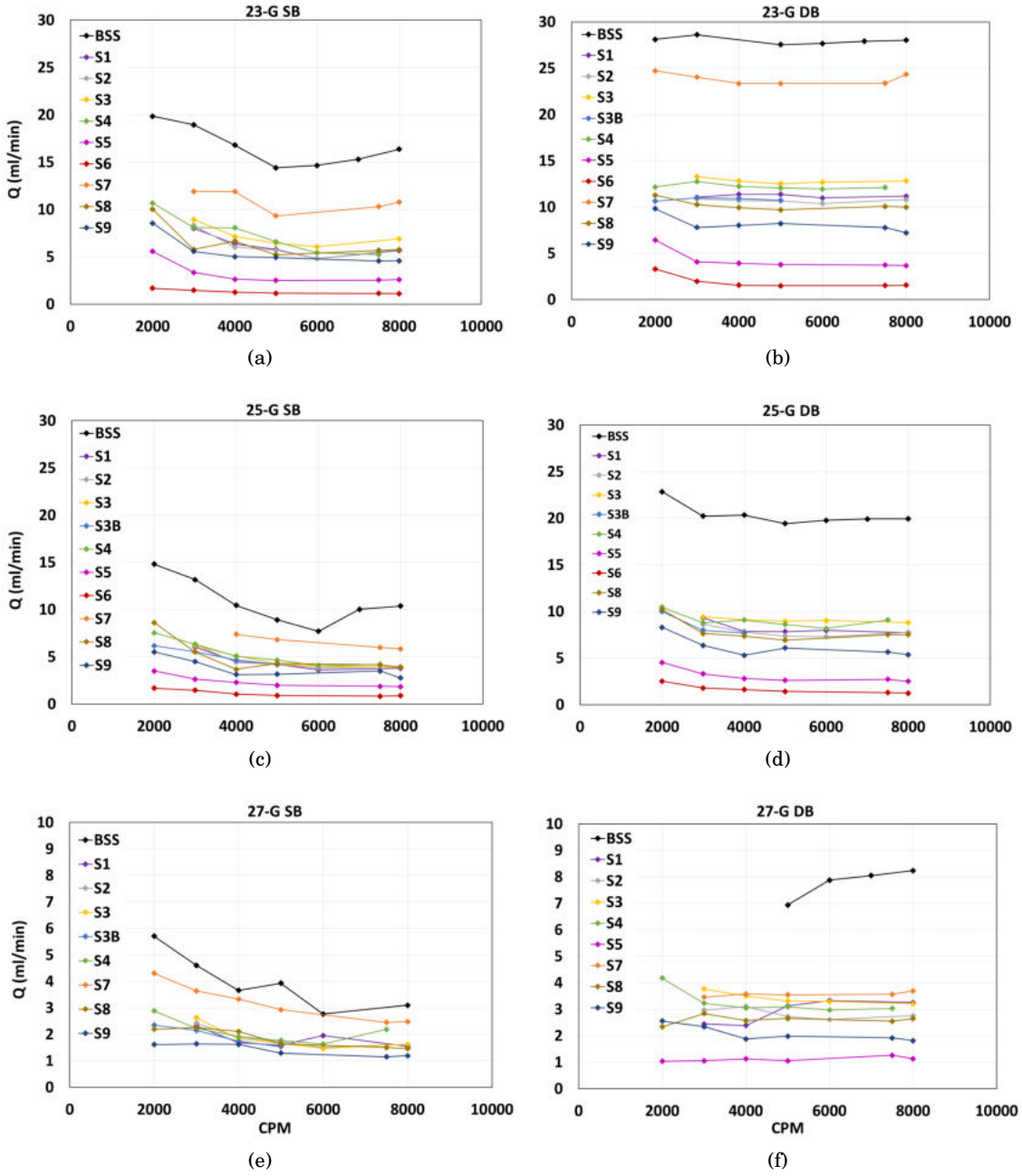

Figure 2.5: Flow rate as a function of the cutting frequency for all solutions. (a) 23-G SB; (b) 23-G DB; (c) 25-G SB; (d) 25-G DB; (e) 27-G SB; (f) 27-G DB. Pumping pressure: 600 mmHg.

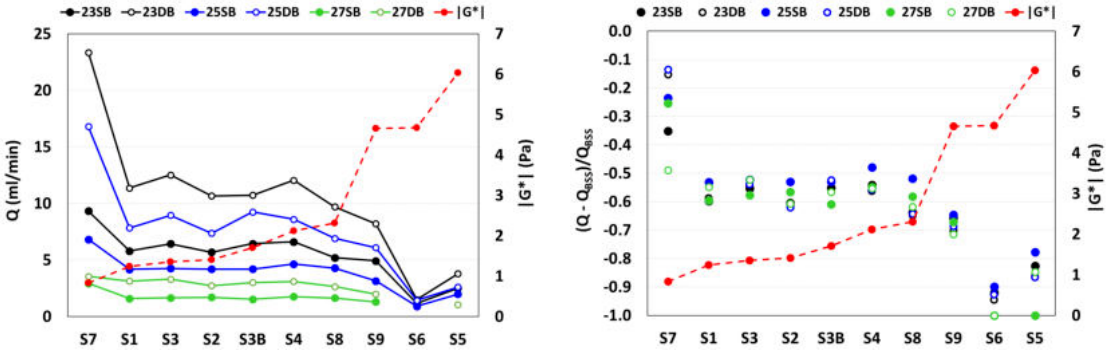

(a) (b)

Figure 2.6: (a) Flow rate Q pumped by the different cutters for all tested solutions. (b) normalised difference between the flow rate Q for each solution and the corresponding value in BSS, $(Q - Q_{\mathrm{BSS}})/Q_{\mathrm{BSS}}$. In both panels in the right vertical axis we show the absolute value of the complex modulus, $|G^*|$, of each solution at 7.94 Hz. Cutting frequency: 5000 cpm; pressure: 600 mmHg.

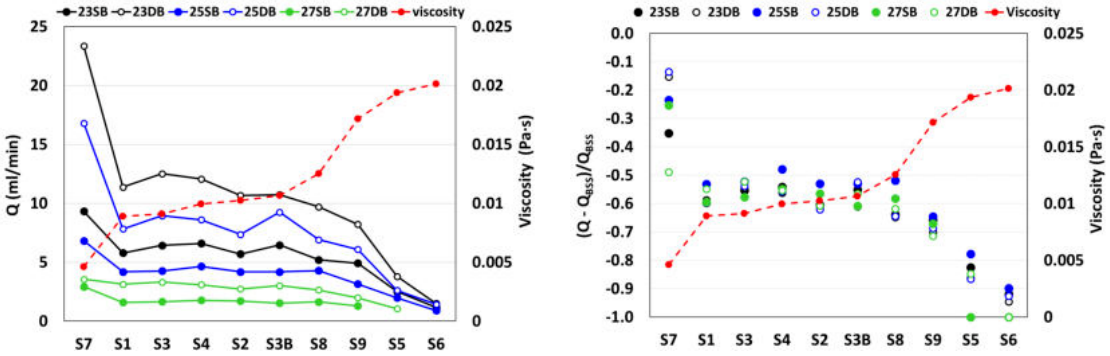

(a) (b)

Figure 2.7: (a) Flow rate Q pumped by the different cutters for all tested solutions. (b) normalised difference between the flow rate Q for each solution and the corresponding value in BSS, $(Q - Q_{\mathrm{BSS}})/Q_{\mathrm{BSS}}$. In both panels in the right vertical axis we show fluid viscosity at $\dot{\gamma} = 1000\ \mathrm{s}^{-1}$. Cutting frequency: 5000 cpm; pressure: 600 mmHg.

observed value excluding outliers; first quartile (Q1) corresponding to the 25th percentile; the median or second quartile (Q2); the mean value; third quartile (Q3) corresponding to the 75th percentile; maximum observed value excluding outliers; maximum outliers defined as values greater than 2/3 of the third quartile.

As a general comment on the present data, it is worth noting how the median values of the error (the second quartile Q_2) are in most of the cases below the 0.3% of relative error and the distributions are narrow, i.e. the interval between Q_1 and Q_3 (first and third quartiles) is small, thus, ensuring that the measurement results are accurate and reliable. In fact, also the third quartile is less than 0.5%. Only one or two outliers are detected in some data sets, with the highest values of the relative error around 2.5%.

The relative error distributions of all data sets tend to be wider as the solutions become more visco-elastic (with very few exceptions, e.g. the 25G-DB and 27G-DB cutters for the solution S7) and this behavior is more evident for the small cutter sizes.

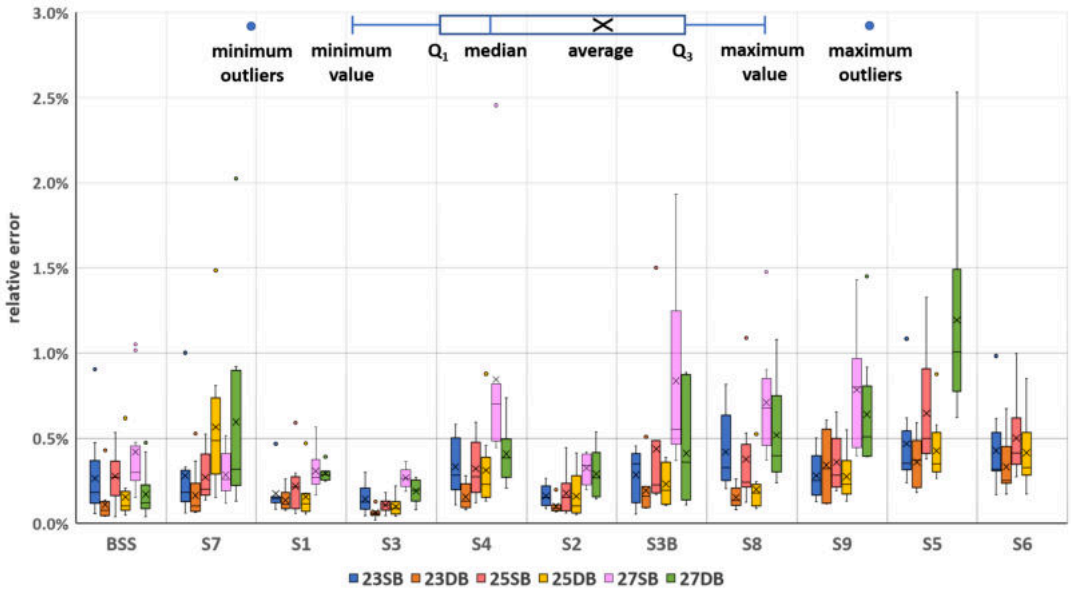

Figure 2.8: *box-and-whisker* plot of the relative error of the flow measurement for each cutter and all working fluids.

2.2.4 DIMENSIONAL ANALYSIS

The experiments showed in this chapter and the corresponding results depend on many parameters. For this reason, a dimensional analysis could provide a useful insight into the physical problem.

In the present case we are interested in the aspiration flow rate Q and we can write the

following functional relationship:

$$Q = f(\Delta p, \omega, d, L, \rho, \nu, \Theta),$$

where we use the following notation:

Δp is the pressure drop, $[p] = \mathrm{ML}^{-1}\mathrm{T}^{-2}$;
ω cutting frequency, $[\omega] = \mathrm{T}^{-1}$;
d cutter diameter, $[d] = \mathrm{L}$;
L needle length, $[L] = \mathrm{L}$;
ρ fluid density, $[\rho] = \mathrm{ML}^{-3}$;
ν fluid viscosity, $[\nu] = \mathrm{L}^2\mathrm{T}^{-1}$;
Θ fluid relaxation time, $[\Theta] = \mathrm{TT}^{-1}$.

The hydraulic circuit is quite complicated and not all of its parts are known to us in detail. Therefore, we have made some simplifying assumptions. In particular, we have taken the pressure drop Δp to be equal to the aspiration pressure. This implies that we neglect the pressure within the eye model, which is justified by the observation that it is always much smaller than the aspiration pressure imposed. We also assume that most of the pressure drop occurs within the needle; thus, we use for d the inner diameter of the needle and for L its length. We also entirely neglect localised pressure drops due, for instance, to variations of the cross-sectional area of the tubes. A more detailed description of pressure losses in vitrectomy probes, which accounts both for distributed and localised pressure drops is provided in Rossi et al. (2019).

Using Buckingham's Π theorem, with d, ρ and ν chosen as dimensionally independent variables, we obtain

$$Re = \tilde{f}\left(\frac{\Delta p}{\rho U^2}, W, De, \frac{d}{L}\right). \tag{2.1}$$

The Reynolds number (Re) is effectively a dimensionless flow rate. In the above expression $De = \Theta\omega$ represents the Deborah number and $W = \sqrt{\omega d^2/\nu}$ the Womersley number. De is the ratio between the fluid relaxation time and a characteristic time scale of the flow and W is a dimensionless frequency parameter.

In order to compute De, since the working fluids were very viscous, we estimated Θ of each by extrapolating the rheological data and identifying the frequency value at which the two complex moduli curves crossed (Ferry, 1980; Macosko, 1994). Moreover, in order to take into account the different rheological properties of the media, we adopted a definition of the Reynolds number as proposed by Metzner and Reed (1955) which reads:

$$\tilde{Re} = \frac{d^n U^{2-n} \rho}{\gamma}, \tag{2.2}$$

with $\gamma = K8^{n-1}$. In the above expressions, n and K define the degree of non-Newtonian behavior of the fluid and its consistency (the larger the value of K the more viscous the fluid), respectively.

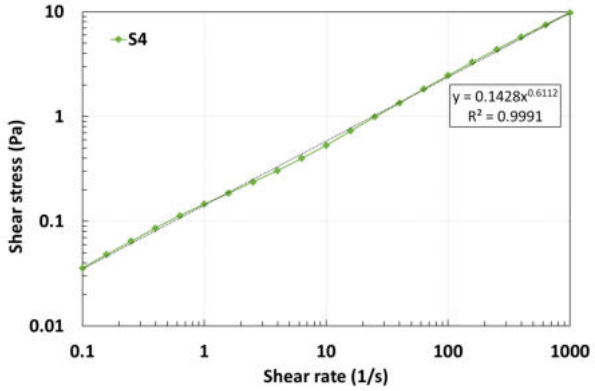

Figure 2.9: Shear stress vs shear reate rheological data for the solution S4 analysed with a power law fitting.

For pseudoplastic fluids, the functional relationship between shear stress and shear rate is the Ostwald equation

$$\tau = K\dot{\gamma}^n; \tag{2.3}$$

for Newtonian fluids, n is equal to 1, $K = \mu$ (the dynamic viscosity of the fluid) and $\tilde{Re}$ reduces to the familiar $d\rho U/\mu$. Since each AV in the present work belongs to the class of pseudoplastic fluids, the parameters K and n have been obtained by fitting the $\tau - \dot{\gamma}$ experimental points, as shown in figure 2.9.

Following the stadard procedure in fluid mechanics it is convenient to rewrite (2.1) as follows

$$Re = \tilde{f}\left(\lambda, W, De, \frac{d}{L}\right), \tag{2.4}$$

where we have introduced the friction factor λ defined as $\lambda = 2\Delta p d/\rho U^2 L$. It is known that, in the case of a laminar flow of a Newtonian fluid the relationship between Re and λ is $\lambda = 64/Re$.

In figure 2.10 we plot our results on the (Re, λ) plane. The experimental data approximately collapse on the straight line $64/Re$ on a log-log plane, both using AVs and BSS as working fluids. However, it is possible to notice that some black experimental points related to BSS (which correspond to results obtained with the DB cutters), are slightly isolated from the linear trend of the data.

In figure 2.11 we plot Re as a function of W, for BSS and AVs adopted as working fluids. Results show that using BSS (figure 2.11(a)) the dimensionless flow rate is approximately independent of W (the dashed line represents the trend line of the data), whereas the values of Re obtained with AVs appear to have a slight dependence on W (panel b of the same figure). Finally, we found that dimensionless flow rates are not significantly dependent on Deborah number (not shown).

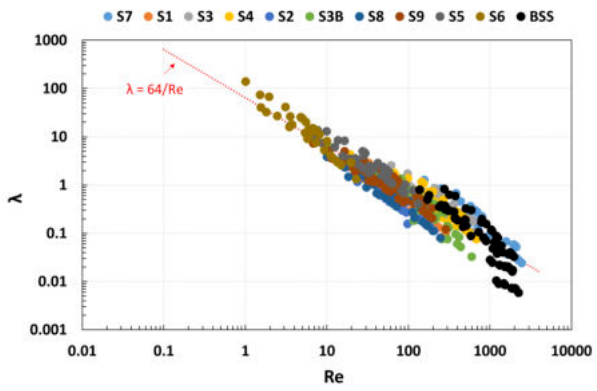

Figure 2.10: Experimental points on the plane (Re,λ) obtained using AVs and BSS.

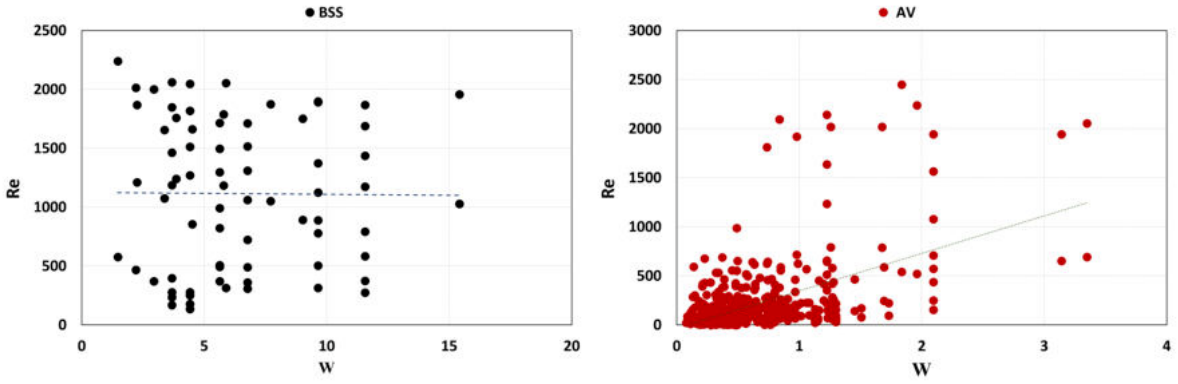

(a) (b)

Figure 2.11: Experimental points on the plane (W,Re) using BSS (a) and viscoelastic fluids (b).

2.3 Discussion

A comprehensive understanding of the factors that influence flow intensity and stability is fundamental to optimise the performance of vitrectomy systems. Among these factors, the medium viscoelastic properties have a well-recognised impact on cutter fluidics (Hubschman et al., 2008). Several viscoelastic materials have been used as surrogates for the human vitreous to simulate vitreous surgical removal, such as egg albumen (Rossi et al., 2014a,e,b; Zehetner et al., 2018), porcine vitreous (Abulon and Buboltz, 2016; Abulon, 2015) and artificial vitreous (AV) (Romano et al., 2018; Stocchino et al., 2020). However, investigating the performance of vitreous cutters operating in a single viscoelastic fluid does not adequately reproduce the surgical scenario, since the vitreous is inhomogeneous and its rheological properties change substantially with location within the vitreous chamber, with age, disease and progression of vitrectomy (Pokki et al., 2015; Lee et al., 1992, 1994; Charles, 2014).

Aim of this study was to achieve a reliable assessment of the performance of single blade (SB) and double blade (DB) cutters of various calibers (23, 25 and 27-G), working with viscoelastic fluids characterised by different rheological properties, thereby evaluating the effectiveness of vitrectomy systems operating in different media under controlled and repeatable laboratory conditions. We tested all cutters available for the EVA vitrectomy system (DORC International, Zuidland, The Netherlands) in terms of flow rate, changing both aspiration pressure and cutting frequency within a wide range of values.

We employed BSS and 10 different AVs, which had different viscoelastic properties and were obtained as solutions of Agar powder and hyaluronic acid, mixed in deionised water. The use of AVs has several advantages compared with egg albumen and porcine vitreous, since the medium rheology can be tested. Moreover, the fact that the composition is known ensures repeatability of the experiments and the rheological properties can be tuned according to the experimental purposes. In particular, in this study we tested different concentrations of the constituents in order to change both the elastic and viscous properties of the mixtures. Solutions were prepared changing Agar and hyaluronic acid concentrations, in order to span a wide but realistic range of rheological parameters of the fluid, so as to mimic various possible conditions that might be encountered during surgery, from a completely liquefied to a normal vitreous, as reported by previous authors (Sharif-Kashani et al., 2011; da Silva et al., 2017; Shafaie et al., 2018). The testing chamber was an open cubical domain. For each solution we tested the vitreous cutters both fixing the pressure and varying the cutting frequency and the other way round. As expected, for all cutters and all fluids, the flow rate increases significantly with the pumping pressure. This increase is almost linear for all tested fluids, which is not an obvious finding in the case of the viscoelastic fluids adopted in the present work.

For a given pumping pressure, the flow rate is generally slightly higher at small cutting frequencies and becomes frequency independent as the frequency increases. In the case of the 50/50 duty cycle, Abulon (2015) found a slight flow rate increase with the cutting rate. However, the Authors demonstrated that a biased open duty cycle is associated with a decrease in flow rate as the cut rate increases. Recent data, show that the hydraulic resistance of SB and DB systems does not change significantly with cutting frequency in the range between 1500 and 12000 cpm: a constant hydraulic resistance for a given aspiration pressure implies that the flow rate also does not significantly change with the cutting frequency (Rossi et al., 2016). Stanga et al. (2017) found that the flow rate is not significantly sensitive to the cut rate frequency. These last findings are in agreement with our results.

Regarding the differences between SB and DB geometries, relative changes of the flow rate with fluid rheology are stronger for DB cutters (see figure 2.5). However, the flow rate produced by DB cutters is slightly larger than that produced by SB cutters of the corresponding size, for all tested viscoelastic media. These results confirm and extend the findings of previous studies (Romano et al., 2018; Stocchino et al., 2020).

The flow rate depends significantly on fluid properties for all cutters. In a "real-life scenario", this implies that significant flow rate changes should be expected in the presence of spatial discontinuities of the mechanical properties of the vitreous, if the cutter is used in vacuum control mode. It is well established that an intermittent flow generates fluid accelerations and pressure variations within the vitreous chamber, which may result in pulsatile tractions on the retina, with higher risk of iatrogenic retinal damage (Charles, 2014). Thus, the present results suggest that care has to be taken when operating in a medium with properties characterised by large spatial variability.

We also observed that the 27-G cutters did not produce flow when tested in AVs with very large viscosity and elastic modulus. The present measurements with the 27-G apparently seem in contrast with previously published data. Several clinical studies analyse the outcomes of surgical procedures based on the use of 27-G cutters for treatment of idiopathic epiretinal membrane (ERM) (Mitsui et al., 2016), idiopathic macular hole (Oh and Oshima, 2014), proliferative diabetic retinopathy (PDR) with vitreous hemorrhage and tractional retinal detachment (Rizzo et al., 2015; Khan et al., 2016), rhegmatogenous retinal detachment (RRD) (Romano et al., 2017; Khan et al., 2016), vitreomacular traction syndrome (Rizzo et al., 2015) and dropped nucleus as a complication of cataract surgery (Watanabe et al., 2016). In all cases, the 27-G probe, proved to be a stable instrument which produced a relatively low but constant flow rate. However, all surgeons suggested to work at very high aspiration pressures and cutting frequency. Mitsui et al. (2016) reported that the smallest size cutters substantially increased the operation time, as also confirmed by a recent analysis (Ma et al., 2020). The 27-G SB and DB of different brands have been tested also in ex-vivo experiments with both BSS and porcine vitreous (CONSTELLATION Vision System, Alcon (Osawa and Oshima, 2014; Abulon, 2015) and EVA, DORC) (Osawa and Oshima, 2014). Note that, in these experimental studies the measured flow rate was well below 1-2 ml/min for a wide range of cutting frequencies and a pressure equal to 650 mmHg. However, the measured flow rates in laboratory tests or clinical trials, do not report the rheological properties of the vitreous, making a quantitative comparison with the present measurements impossible. The present experiments show that the flow generated by 27-G probes is quite low (on average, less than half of the flow generated by 25-G probes for the same solutions) and that above certain values of viscosity and elasticity flow rate with 27-G probes vanishes. Translated to the surgical practice, this findings may suggest that the use of this cutter size might not be the preferred option in case of very firm vitreous gels and dense vitreous hemorrhage and should be avoided in case of media much more rigid than the vitreous, such as nuclear lens remnants into vitreous cavity. It has also to be noted that rurgery time is one of the aspects to consider in the evaluation of the surgical performance of a probe and, thus, in the choice of the size. In this regard, our findings of lower flow with 27-G probes are supported by the evidence that they are associated to longer operative times (Ma et al., 2020). Note that all cited trials have been conducted with patients with average age around 61±10 years (Khan et al., 2016; Oshima et al.,

2010; Romano et al., 2017) and it is reasonable to assume that the mechanical characteristics of the vitreous were deteriorated, owing to age pathologic conditions, compared to an healthy vitreous.

2.4 Conclusions

This study demonstrates that the performance of all vitrectomy cutters is significantly influenced by the mechanical properties of the medium they operate in. We confirmed that, for all tested cutters, the flow rate increases almost linearly with the pumping pressure and depends only weakly on the cut rate, reaching a plateau above $\approx$ 4000 cpm. Comparing the DB with SB cutters, the flow rates produced by DB were larger in every tested condition, but DB cutters were slightly more sensitive to medium rheology. Finally, the use of vitreous substitutes for testing the performance of surgical devices is strongly suggested, owing to the good control on the mechanical properties which makes the experiments reproducible. This aspect guarantees the comparability between the results obtained on different vitrectomy systems.

CHAPTER 3

FLUID DYNAMIC ASSESSMENT OF HYPERSONIC AND GUILLOTINE VITRECTOMY PROBES

This chapter is based on the publication by Stocchino et al. (2020), which Irene Nepita co-authored.

In this chapter we present an experimental study aimed at reliably measuring the fluidics of 23-gauge (G) hypersonic vitrectomy probes (HVPs) in the two available port configurations and compare those findings with guillotine vitrectomy probes (GVPs) under various operating settings. All of the experiments were performed in both balance salt solution (BSS) and artificial vitreous (AV) in order to simulate both liquefied and healthy vitreous conditions. Finally, in order to assess whether the use of the HVP induce significant temperature increase in the vitreous chamber, we performed specific experiments monitoring the temperature over the time of operation of the HVPs.

3.1 METHODS

3.1.1 EXPERIMENTAL SETUP

Experiments were performed in the same cubic domain as described in the chapter 2. We carried out experiments with various vitrectomy probes connected to the Stellaris Elite system (Bausch + Lomb, St. Louis, MO, USA). In particular, we tested four GVPs: 23SB (23G, single blade), 25SB (25G, single blade), 25BB (25G, double blade), and 27BB (27G, double blade). We also tested the Vitesse (VIT) 23G HVP (Bausch + Lomb) in two existing configurations of the port: large (L), 225 μm, and tear-drop (TD), 255 μm, that differ for the shape of the port aperture (see figure 3.1). The vitrectomy handpieces were kept in vertical position by a specifically designed holder and entered the measuring chamber from the top.

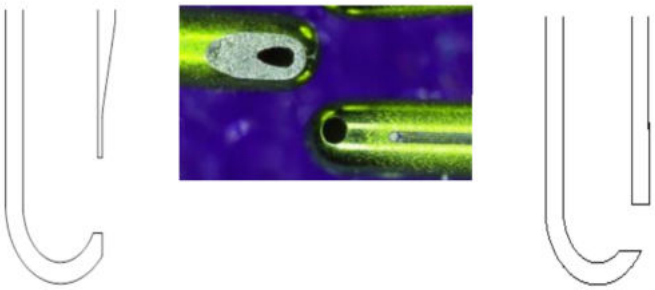

Figure 3.1: Geometric configurations of the ultrasound cutter ports. Left: VIT-TD; right: VIT-1L.

3.1.2 WORKING FLUIDS

We used three different working fluids: BSS and two AV solutions, which we labeled S1 and S2. As for the preparation of the solutions described in chapter 2, we adopted the recipe proposed by Kummer et al. (2007). However, because the transparency of the fluid is a strict requirement for the optical measurements of the flow, we did not add the agar powder. As a result, we obtained a solution of hyaluronic acid in deionised water.

We tested fluid samples with the Physica MCR 301 rotational rheometer both at a constant rotational velocity and through oscillatory tests in a range of frequency from 1 to 30 Hz. All measurements were taken at 20°C.

The results of rheological tests on the two AV solutions are shown in figure 3.2. The rheological properties, in terms of complex modulus (figure 3.2(A)), were reasonably close to those reported for porcine vitreous and in general with values in agreement with those obtained in chapter 2. The solutions had shear thinning properties, with an apparent viscosity that decreased significantly as the shear rate increased (figure 3.2(B)). Finally, solution S2 had a significantly higher complex modulus, in terms of both real and imaginary parts, at least at small frequencies.

3.1.3 PARTICLE IMAGE VELOCIMETRY (PIV) MEASUREMENTS

In figure 3.3 we report a picture of the experimental apparatus employed for particle Image Velocimetry (PIV) measurements, consisting in the components described below.

- Solid state laser: wave length of 532 nm (green light), continuous emission with variable power, up to 2 Watt.
- High speed digital camera: IDT Xstream Xs3 high frequency camera (maximum frequency in frames per second (fps) of $\approx$ 20K, CMOS resolution of 1280×1024 pixels).
- Acquisition and image analysis software: IDT proVsionXs.
- Optical system constitued by cylindrical lenses.

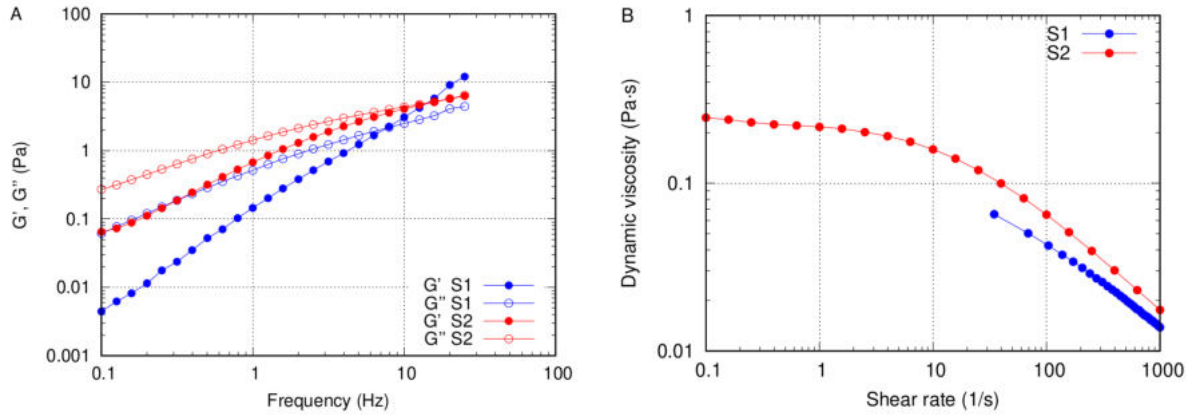

Figure 3.2: (A) Storage and loss moduli versus oscillation frequency (0.1-30 Hz); shear strain = 0.05%. (B) Apparent viscosity versus shear rate; temperature (T) = 20°C.

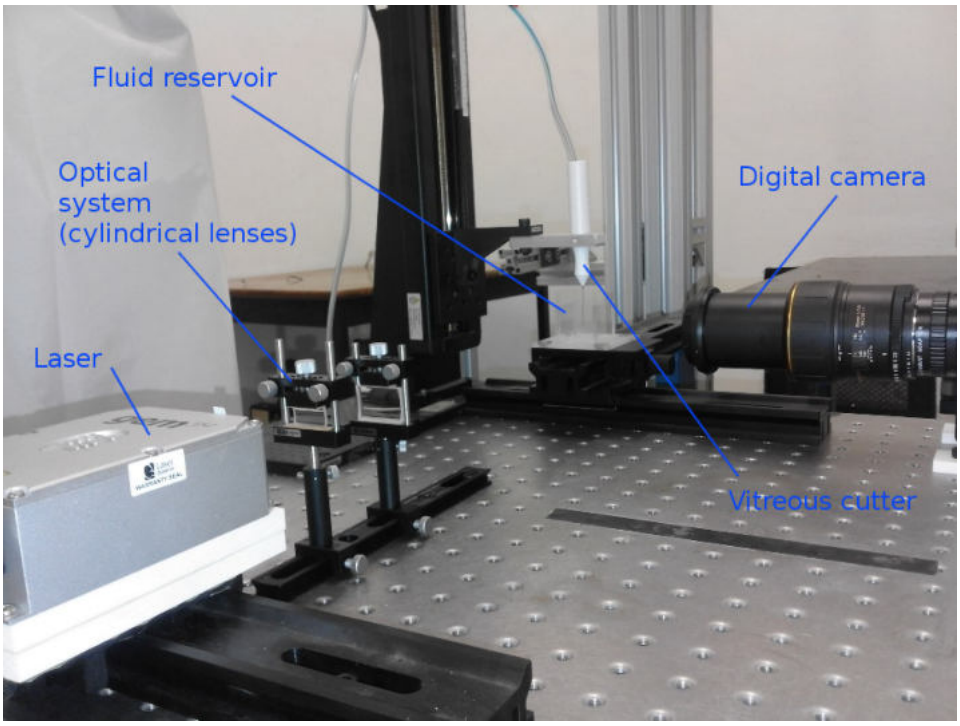

Figure 3.3: Picture of the experimental setup for the PIV measurements.

3.1.3.1 Description of the technique

Particle Image Velocimetry (PIV) is a purely optical technique used to measure flow fields in fluids. In the standard configuration, see figure 3.4, measurements are taken on a plane, on which it is assumed that the flow is almost two-dimensional (or axisymmetric). A plane of the

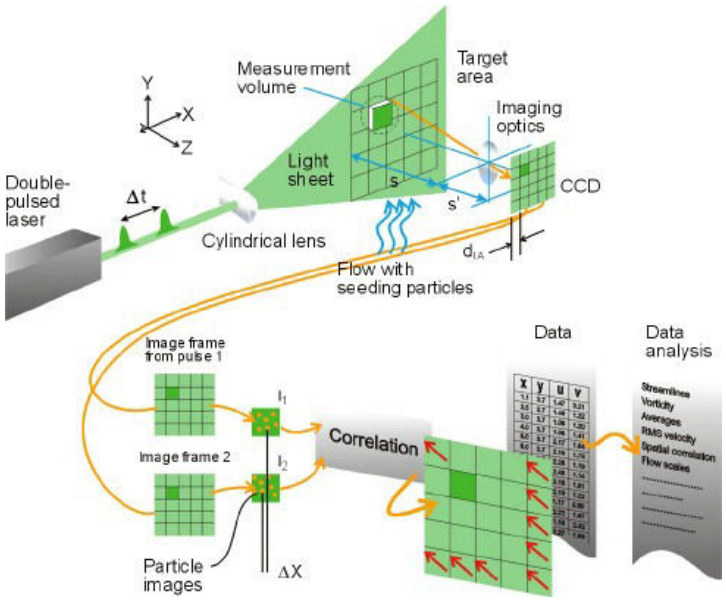

Figure 3.4: Typical two-dimensional PIV configuration.

flow is illuminated with a laser sheet and digital pictures of it are taken at a given temporal frequency.

The laser sheet thickness and width are controlled through an optical system, typically consisting of a sequence of cylindrical lenses (see figure 3.4). Tracing particles are dispersed in the fluid, which are small enough (and possibly neutrally buoyant) so that it can be assumed that their speed is a good measure of the local fluid velocity. Seeding particles are visible on the pictures as light spots. Using statistical techniques (cross-correlations) and comparing images taken at different times, it is possible to measure the average displacement of the particles. In particular, the images are subdivided into small regions, denoted as interrogation windows (IW), and correlation between corresponding IWs in two images taken at different times provides a displacement vector associated to the IW. Dividing the displacement vectors by the time interval between the pair of images one obtains a velocity field (with one velocity vector for each IW). In figure 3.4 the correlation analysis procedure is schematically illustrated.

The number of IWs depends on the image quality and on particle density. The spatial resolution of the velocity vector field depends on the number of IWs and the time resolution is dictated by the time frequency of the image acquisition. We note that in the case of a steady flow, one is free to correlate an image with any of the following ones in the time series. This gives the user a lot of freedom in the choice of the time step between the two images to correlate. On the other hand, in the case on an unsteady flow, in order for the unsteadiness to be properly resolved in the measurements, it is necessary to correlate images that are separated in time by an interval significantly shorter than the time scale of flow variations. This is a very demanding

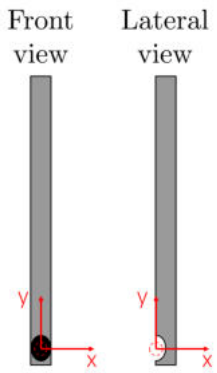

Figure 3.5: Sketch of the front and lateral views.

requirement in the case of the present application, because we deal with very fast oscillations superimposed to a slow flow. In our experiments, if we correlate two successive images (that on average are separated in time by 1/10 of the cutting cycle for the guillotine cutters) the average fluid displacement is going to be extremely small. In order to resolve it in a proper way, we need to work with small IWs and a large concentration of tracing particles. We note that the technique adopted for the present project is not capable of resolving the time scale of vibrations of the HPVs, which has a frequency of 28.5 kHz.

In particular we adopted the Adaptive Window technique proposed by Lourenço and Krothapalli (2000), working with an IW of size 24×24 pixels and a sampling frequency of 500 Hz. These working conditions have provided a quality of the images such that we can compute ≈ 2500 velocity vectors on the measurement plane. We performed measurements on two vertical planes containing the probe: one parallel to the port aperture (front view) and one across it (lateral view). In the front view the cutter port faces the camera, whereas in the lateral view it points to the left, as schematically shown in figure 3.5. The cutter itself is not visible, since we took measurements on a plane slightly displaced (in the z-direction) from the position of the needle, to avoid light reflections. Calibration was done by acquiring a sheet of graph paper in the plane of interest.

Moreover, in order to more accurately describe the flow structures, for solution S2 two areas of interest were used for the acquisitions: (i) a large field with size of about 30×22 mm, with the aim of describing possible large-scale circulations within the experimental box; and (ii) a small field, which was a zoomed area of about 11×13 mm around the cutter tip, in order to increase the resolution. All acceleration values discussed in the following are based on the measurements taken on the reduced area. We also verified that the percentage of the outliers for each velocity fields never exceeded 3% of the total number of velocity vectors, which is an indication of the reliability of the measurements.

3.1.3.2 Post-processing of the experimental data

From the PIV measurements we obtain the spatial velocity flow field at different times, $\mathbf{u}(\mathbf{x},t)$ or, in components with respect to a Cartesian coordinate system (x,y) on the measurements plane, $(u(x,y,t),v(x,y,t))$. From the velocity field many other quantities with relevant physical meaning can be derived.

In order to compare the behavior of vitrectomy probes employed in various conditions, we referred to synthetic quantities obtained by performing averages of the experimental measurements over time and space. For spatial averages, we adopted a circular averaging area, with a diameter of 6 mm, centered in correspondence with the port of the probe. This choice is obviously arbitrary. However, since we kept S constant in all cases, the results shown in the following are directly comparable to each other. Spatial averaging leads to time signals, which we analysed by constructing power spectra density (PSD) of the kinetic energy per unit mass in order to identify the dominant frequencies of the flow (Press et al., 1992). Time averaging, on the other hand, produces spatial maps that provide information about the mean flow characteristics. Finally, the result of averaging over time and space is a single quantity that is a synthetic measure of flow properties.

Local and instantaneous quantities

Acceleration

The acceleration field **a**(**x**,t) can be obtained from the velocity field as

$$\mathbf{a} = \frac{\partial \mathbf{u}}{\partial t} + (\mathbf{u}\cdot\nabla)\mathbf{u}. \tag{3.1}$$

Local derivative of the velocity with respect to time

$$\dot{\mathbf{u}} = \frac{\partial \mathbf{u}}{\partial t}. \tag{3.2}$$

This quantity represents the time derivative with respect to time of the velocity at a certain point in space. It does not coincide with the acceleration because a specific point in space is, in general, occupied by different particles at different times.

Kinetic energy per unit mass

The kinetic energy of the fluid per unit mass is defined as

$$E_c = \frac{1}{2}\mathbf{u}\cdot\mathbf{u}. \tag{3.3}$$

Averaged quantities

In many cases it is convenient to consider the average (or integral) of a physical quantity over space. In the present case integration can be made over a region, say S, of the plane of measurement. Therefore, quantities can be averaged over a surface.

Let us consider a generic quantity $f(\mathbf{x},t)$. We define its spatial average as

$$\overline{f}(t) = \frac{1}{S}\int_S f(\mathbf{x},t)dS. \tag{3.4}$$

Overlines will be used consistently in the following to identify spatially averaged quantities. We note that a spatially averaged quantity is function of time, but not of space.

Similarly, we can take a time average of a quantity $f(\mathbf{x},t)$ over a certain time interval T. Time averaged quantities will be denoted with a hat and the averaging operation is defined as

$$\hat{f}(\mathbf{x}) = \frac{1}{T}\int_T f(\mathbf{x},t)dt. \tag{3.5}$$

Note that $\hat{f}(\mathbf{x})$ is a function of space, but not of time.

Finally, we can take a space and time averages of a quantity $f(\mathbf{x},t)$

$$\hat{\overline{f}} = \frac{1}{T}\int_T \left(\frac{1}{S}\int_S f(\mathbf{x},t)dS\right)dt. \tag{3.6}$$

Obviously, the order of the two above integrals can be changed ($\hat{\overline{f}} = \overline{\hat{f}}$). Since the time and space dependency are eliminated by the averaging procedures, $\hat{\overline{f}}$ is a constant.

We focus in particular on two parameters: the time and space averaged magnitude of fluid acceleration $|a| = \hat{\overline{|\mathbf{a}|}}$ and the volumetric flux Q, which is directly measured using the technique explained in section 3.1.4.

3.1.4 Flow rate measurements

Flow rate measurements were taken tracking the free surface of the liquid in the measuring chamber over time through the automatic tracking procedure described in chapter 2 and the digital images were analysed with the same software (Motion Studio - integrated Design Tools, Pasadena, CA, USA).

3.1.5 Temperature measurements

One of the objectives of the present project is to measure whether the use of HVPs can induce significant increase of vitreous temperature.

To this end, we used an infrared thermal camera (FLIR Systems,Inc., Wilsonville, OR, USA). An infrared thermal camera images and measures the infrared radiation emitted by an object, which depends on temperature. On the basis of the radiation it is possible to obtain a measure of the object temperature. The output is a temperature map on the measuring plane. In order for the temperature measurement to be accurate and reliable, various corrections have to be applied. In particular, the radiation measured by the camera does not only depend on the object temperature, but also on its emissivity. Moreover, radiation originated from the surrounding environment is reflected onto the object. Radiation absorption by the atmosphere also affects the measurements. In order to compensate for the these effects the following parameters are used and must be supplied: emissivity of the object, reflected apparent temperature, distance between the object and the camera, relative humidity and air temperature. Along with the temperature map the camera provides the value of the temperature at a particular spot in the centre of the image. The precision of the thermal camera FLIR i7 is of 0.5°C, with image resolution of 120×120 pixels. The temperature measurements obtained by the FLIR camera have been preliminarily validated against air and BSS temperature measurements performed with a standard thermometer with a resolution of 0.1°C. At the beginning of the test, the fluid was at room temperature (around 21.5°C).

A typical experiment performed in the present activity consists in the following steps.

- The measuring chamber is filled with BSS at room temperature (as its thermal properties are very similar to those of AV).

- The HVP is operated at a fixed stroke and zero vacuum pressure. This means that no fluid is pumped out the measuring chamber during the test. However, fluid flow is generated by the movement of the needle (see section 3.2.2), which produces velocities large enough for thermal convection to be the strongest mechanism of heat transfer in the chamber, with diffusion being largely subdominant. In this sense we have been estimate the Péclet number as

  $$P_e = \frac{\rho c d v}{k}, \tag{3.7}$$

  where ρ is water density, c and k the specific heat capacity and the thermal conductivity of water respectively, d the length of the probe aperture ($\approx$ 0.6 mm) and v the mean velocity obtained from velocity results obtained in section 3.2.2. We found $P_e \approx \mathcal{O}(10^4)$.

- Starting from the beginning of the test one measurement is taken every minute for 5 minutes. The image is such that all the cross section of the testing chamber is visible.

- At the end of the test the head of the cutter is also imaged, which is the hottest part of the tool.

	Material	Thermal conductivity k	Surface area S	Thickness d
Lateral walls	Perspex	0.2085 $W \cdot m^{-1} \cdot K^{-1}$	3600 mm^2	3.5 mm
Top wall	Perspex	0.2085 $W \cdot m^{-1} \cdot K^{-1}$	900 mm^2	3 mm

Table 3.1: Thermal and geometrical properties of the walls of the measuring chamber.

We now estimate the amount of heat transferred by the cutter to the fluid. The heat Q necessary to produce a temperature variation ΔT in a body with mass m and specific heat capacity c, is given by

$$Q = mc\Delta T. \tag{3.8}$$

For water, c = 4186.8 J/kg. The mass of the fluid contained in our measuring chamber is m = 0.027 kg. This means that, in order to increase the temperature of the fluid in the chamber by 1 degree a heat of Q = 113 J is needed.

In reality, more heat is required if heat flux through the chamber walls occurs. We estimate this heat loss as follows. The power lost from the chamber to the external environment through a flat surface of area S, thickness d and thermal conductivity k, can be computed as

$$\mathscr{P} = kSd(T - T_0), \tag{3.9}$$

where T is the temperature inside the chamber (assumed uniform) and T_0 the external temperature. In equation 3.1.5, $\mathscr{P}$ is assumed positive if the heat leaves the domain. In our experiments we measure the time evolution of the temperature in the chamber $T(t)$. Thus, if the experiment has a duration t_{fin} (5 minutes in our case), we can calculate the total heat loss from the wall as

$$Q_{\text{loss}} = \int_0^{t_{\text{fin}}} \mathscr{P}(t)dt, \tag{3.10}$$

We can thus estimate the total amount of heat Q_{tot} transferred by the cutter to the fluid during the experiment as

$$Q_{\text{tot}} = Q + Q_{\text{loss}}. \tag{3.11}$$

The calculation of Q_{tot} has been done adopting the values reported in table 3.1 for the thermal and geometrical properties of the walls of the measuring chamber. We note that we did not account for heat loss from the bottom wall of the domain, since the chamber sits on a thick floor and a Perspex panel (top wall) was placed on the free surface of the experimental chamber in order to decrease thermal dispersion.

3.1.6 Description of the experiments

We performed different series of experiments varying the aspiration pressure and the cutting frequency (GVPs) or ultrasound stroke (HVPs). Both probes were tested with different working

Working fluid	Cutter	Pressure (mmHg)	Cuts per minute/Stroke	View	Field of view	Measurements
BSS	23SB	200-600	2000-7500	F	LF	Flow rate / PIV
	25SB	200-600	2000-7500	F	LF	Flow rate / PIV
	27BB	200-600	2000-7500	F	LF	Flow rate / Temp. / PIV
	VIT-TD	300-600	5-60	F	LF	Flow rate / Temp. / PIV
	VIT-L	300-600	5-60	F	LF	Flow rate / PIV
S1	23SB	200-600	2000-7500	F/L	LF	Flow rate / PIV
	VIT-TD	100-600	5-60	F/L	LF	Flow rate / PIV
	VIT-L	100-600	5-60	F/L	LF	Flow rate / PIV
S2	23SB	200-600	2000-7500	F/L	LF/SF	Flow rate / PIV
	25SB	200-600	2000-7500	F/L	LF/SF	Flow rate / PIV
	25BB	200-600	2000-7500	F/L	LF/SF	Flow rate / PIV
	27BB	200-600	2000-7500	F/L	LF/SF	Flow rate / PIV
	VIT-TD	100-600	5-60	F/L	LF/SF	Flow rate / PIV
	VIT-L	100-600	5-60	F/L	LF/SF	Flow rate / PIV

Table 3.2: List of the performed experiments. Acronyms: F = frontal, L = lateral, LF = large field, SF = small field.

fluids. Table 3.2 provides a summary of all of the experiments, divided into three separate series depending on the working fluid (BSS, S1, or S2). It is worth noting that in the case of BSS we acquired only one view, as previous works suggested that, in this case, the flow has axial symmetry (Romano et al., 2018; Rossi et al., 2014a). Some experiments were repeated in order to verify the repeatability of the measurements.

3.2 Results

3.2.1 Two-Dimensional flow fields

The velocity distributions in BSS for both GVPs and HPVs were axisymmetric with respect to the needle and decayed monotonically with distance r from the cutter port, which behaves like a sink. Examples of results with BSS are reported in figure 3.6, where we show front views of time-averaged maps of the kinetic energy per unit mass and velocity vectors, for both HVPs and GVPs vitreous probes. In particular in figure 3.6(A, B) and (C, D) we show the results obtained with HPVs and GVPs, respectively. In order to highlight the motion structure produced by each handpiece, the legend is different for each panel.

The flow fields in AV differed significantly from those in BSS. In all maps shown in the following the cutter is located along the axis $x = 0$ (for $y > 0$) and the port is centred at the point $x = (0;0)$ (lateral view).

Some examples obtained with GVPs in AV are shown in figure 3.7. The flow fields in AV were highly asymmetric, and, on a lateral plane, a confinement region developed, inside of which fluid

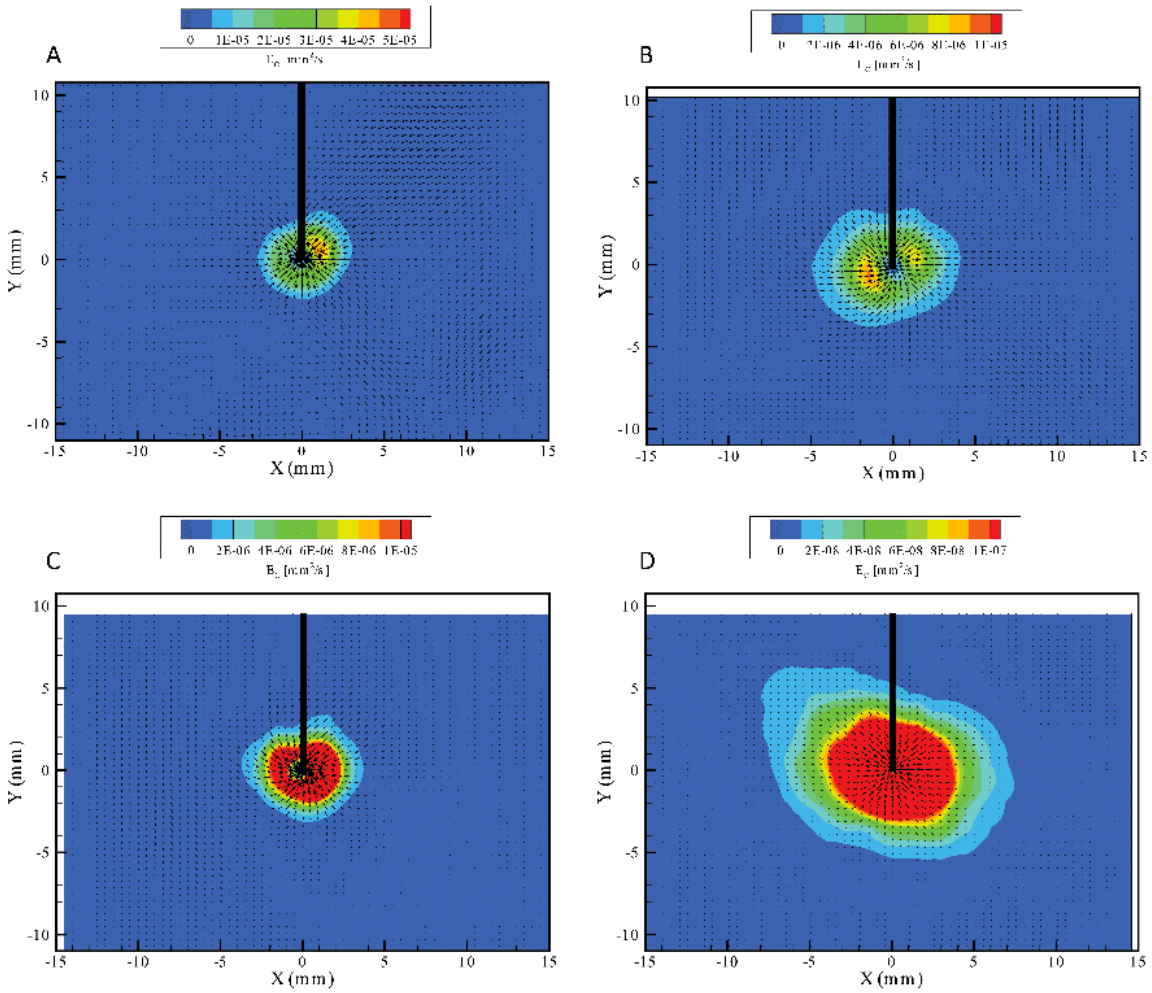

Figure 3.6: Time-averaged maps of the kinetic energy per unit mass and velocity vectors for the HVPs probes (A, B) and for GVPs (C, D). In particular: (A) VIT-TD, stroke = 30 μm, pressure set at600 mmHg; (B) VIT-L, stroke = 30 μm, pressure set at 600 mmHg; (C) 23SB, f = 5000 cpm, pressure set at 600 mmHg; (C) 25SB, f = 5000 cpm, pressure set at 600 mmHg. Front view. Large field. BSS as working fluid.

velocity was large and directed toward the port and outside of which was very small. This happened with all of the GVPs, regardless of the gauge and operating conditions. The confinement region had approximately a conical shape, and its axis formed an obtuse angle with the cutter axis, which decreased as the cutting frequency increased (figure 3.7). Similar results were found by Romano et al. (2018). We note that the instantaneous velocity fields were qualitatively similar to the time-averaged ones, as relatively small fluctuations in the time scale of the cutting cycle were superimposed onto the averaged flow.

Information about the time dependency of the flow can be inferred by inspecting the PSD

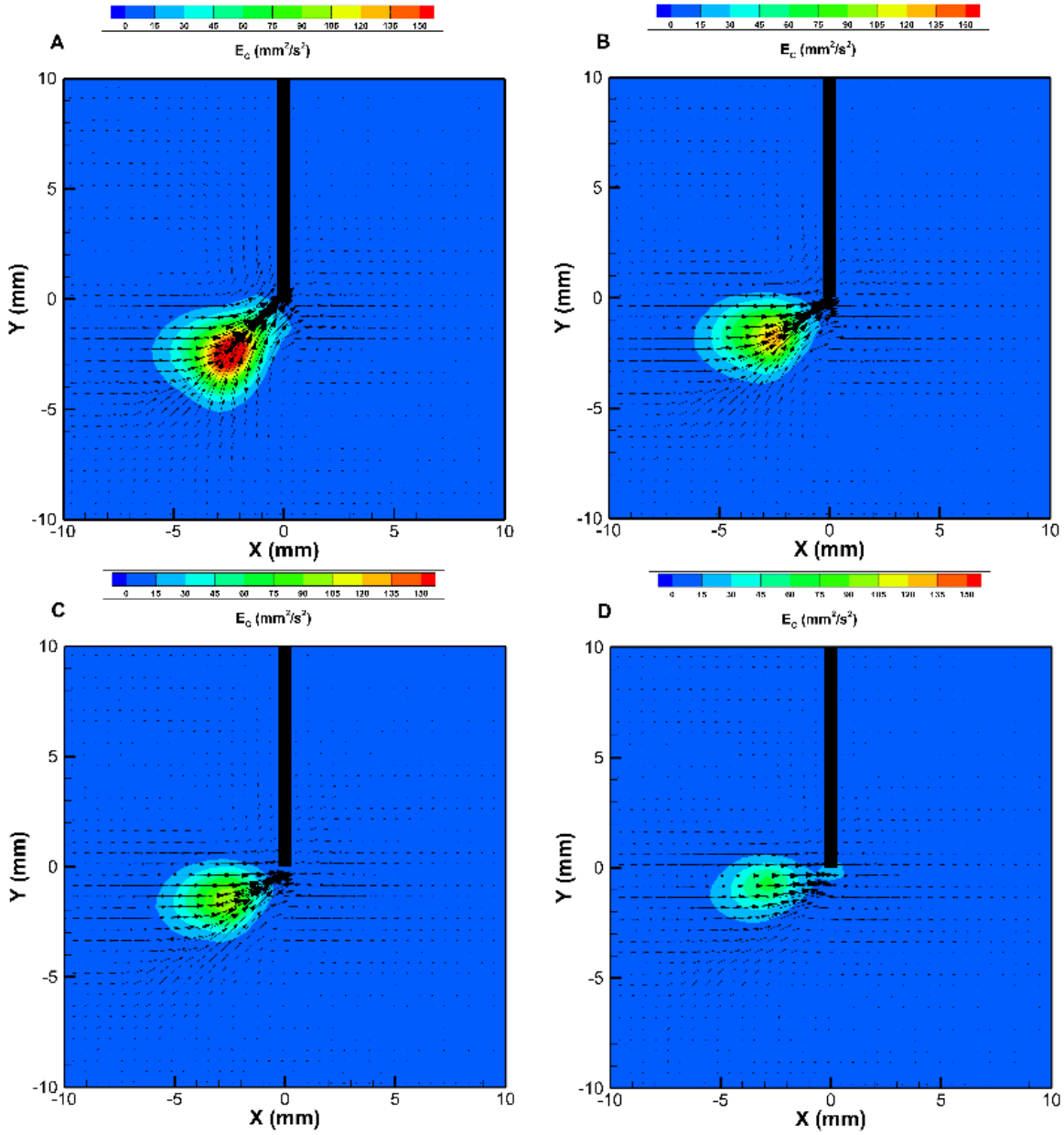

Figure 3.7: Time-averaged maps of the kinetic energy per unit mass and velocity vectors for the guillotine cutter. Lateral view with the cutter port on the negative side of the x-axis; 23G cutter with pressure set at 600 mmHg. The plots correspond to the various cutting frequencies (f): (A) f = 2000 cpm; (B) f = 4000 cpm; (C) f = 5000 cpm; (D) f = 7500 cpm. AV as working fluid. Large field.

reported in figure 3.9(A). Clear peaks were found corresponding to the cutting frequency, both its super- and subharmonics. For example, referring to the curve corresponding to a cutting frequency of 2000 cuts per minute (cpm), or 33.3 Hz, we found peaks at 16.7 Hz, 33.3 Hz, and

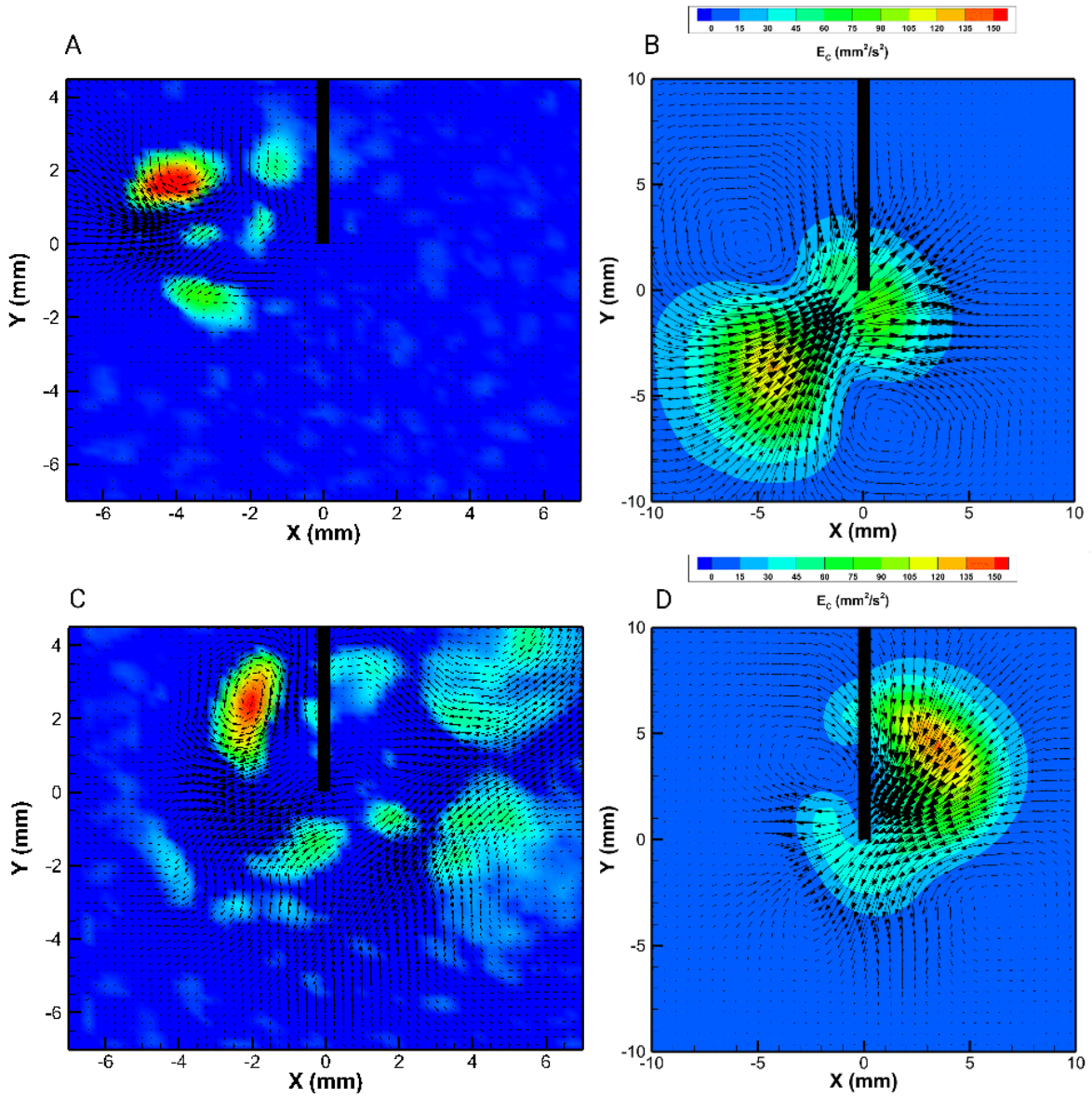

Figure 3.8: (A, C) Instantaneous and (B, D) time-averaged maps of the kinetic energy per unit mass and corresponding velocity vectors for the ultrasound VIT-L probe. The contour in panels A and C enlighten the position of vortical structures. Lateral view with the cutter port on the negative side of the x-axis; 23G cutter with pressure set at 600 mmHg. The plots correspond to various stroke values: (A, B) 10 μm; (C, D) 30 μm. AV as working fluid. (A, C) Small field, (B, D) Large field.

66.6 Hz. In this case, a peak also existed at 50 Hz, which is a frequency unrelated to the cutting and was probably a natural frequency of oscillation of the viscoelastic fluid in the measuring chamber (Romano et al., 2018; Meskauskas et al., 2011).

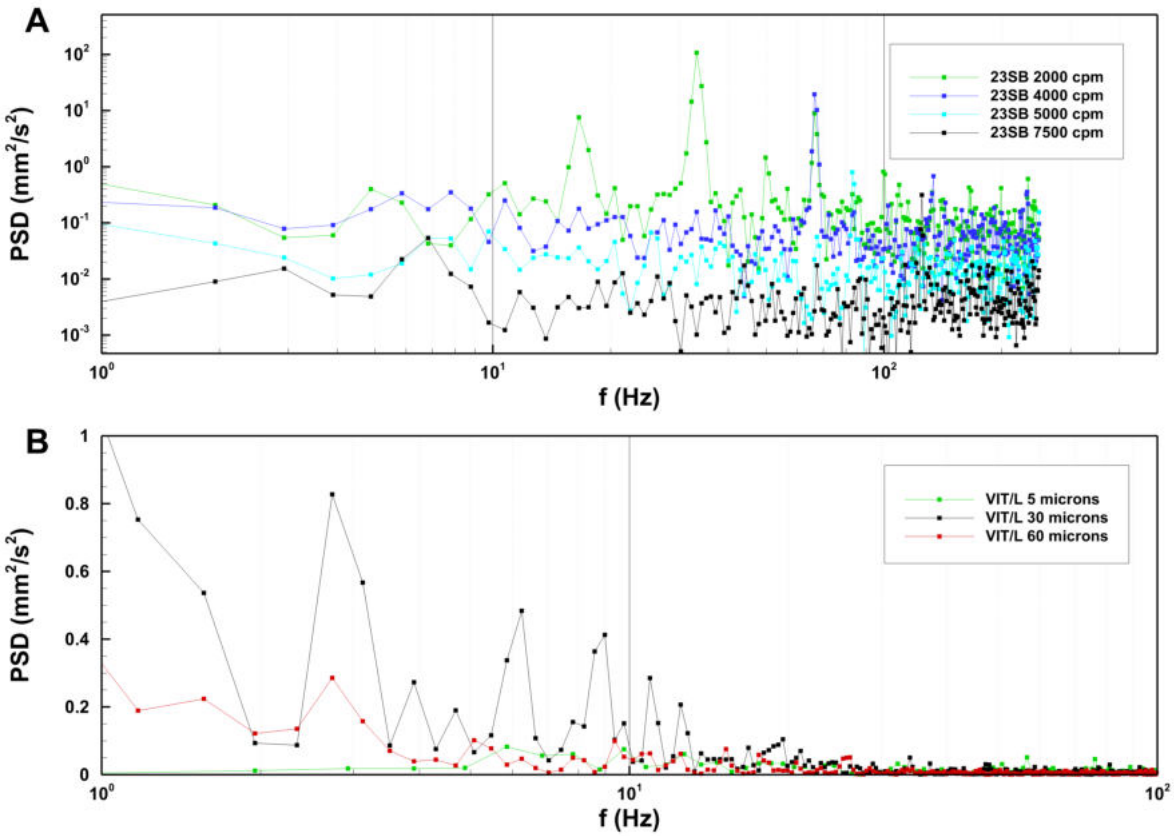

Figure 3.9: PDS of the kinetic energy per unit mass obtained for solution S1: (A) guillotine cutter 23SB; (B) ultrasound VIT-L probe. Note that the PDS obtained with S1 and S2 were qualitatively similar.

The flow field induced by HVPs was significantly different from that produced by GVPs, as shown in figure 3.8. The instantaneous flow maps (figures 3.7(A,C)) were highly irregular, and, even when the pumping pressure was kept constant in the experiments, the flow was unsteady. In order to help the visualisation of the time-dependent vortical structures, contour of a specific scalar quantity, known as swirling strength (i.e the imaginary part of complex eigenvalues for the velocity gradient tensor) which assumes high values in flow regions dominated by strong local rotations (Weiss, 1991; Okubo, 1970), is plotted together with the velocity vectors. The frequency of oscillations of the probe is far too high to be resolved by our measurements (28.5 kHz). However, the power spectrum shows that there are specific (typically small) frequencies associated with a large energy content. Changes in time had frequencies much smaller than for the HVP probes, as shown in the PSD reported in figure 3.9(B). These frequencies are likely to be dependent on the size of the domain adopted.

This behavior is likely due to the onset of flow instabilities, which is a typical occurrence in fluid mechanics. Of course, in the time-averaged flow fields the velocity was, on average, directed

toward the port (figures 3.7(B,D)); however, the spatial structure of the time-averaged flow field varied significantly with the stroke, as can be seen by comparing figures 3.7(B) and 3.7(D).

Polymeric solutions, exhibit significant elastic and shear-thinning phenomena (Bird and Curtiss, 1984) which are represented by non-linear terms in constitutive relations that describe the state of stress in flowing polymeric materials. The complex interaction of non-linear terms in the momentum and constitutive equations gives rise to unstable flows with a complex dynamical structure. Elastic instabilities in the flow of non-Newtonian fluids (Larson, 1992) can occur in various circumstances. In a seminal work, Groisman and Steinberg (2000) discuss the occurance of elastic instabilities in flows of elastic fluids. Turbulence is a common occurrence in fluid mechanics and typically associated with large values of the Reynolds number. Viscoelastic fuids have non-linear mechanical properties and therefore may behave differently from purely viscous fluids. The Authors observed experimentally that the flow of a fluid consisting of a high contentration solution of an elastic polymer becomes irregular even at low velocity and high viscosity. Such flows have characteristics similar to turbulent flows and this phenomenon is therefore referred to as "elastic turbulence". Elastic turbulence can arise even in the limit of $Re \longrightarrow 0$. The motion observed by the authors was characterised by significant stretching of the polymer molecules, which leads to an increase in the elastic stresses of up to two orders of magnitude.

The non-Newtonian nature of the flow may be quantified adopting the Deborah number (De), a dimensionless group defined as:

$$De = \Theta / t_{flow}, \tag{3.12}$$

where Θ is a characteristic relaxation time of the fluid (Bird et al., 1987). We estimated De both considering $t_{flow} = 1/f_{HVP}$ ($f_{HVP} = 28.5kHz$) and $t_{flow} \approx L/U$ (U is a typical velocity, L is a characteristic length scale). When t_{flow} is taken equal to L/U the above dimensionless parameter become $\Theta U/L$, which is named Weissemberg number (Wi) and is the parameter Groisman and Steinberg (2000) refer to in their work.

If we choose $t_{flow} = 1/f_{HVP}$ we obtained $De \approx 3000$, wheareas considering as characteristic time L/U we obtained values of $De \approx 2$. Although a critical value of De, which determines the onset of elastic instabilities, depends on the material tested and on the physical problem considered (Shiang et al., 2000; McKinley et al., 1993, 2007), many studies observed unstable flows already at De values of the order of 1 (Pakdel and McKinley, 1996; Kenney et al., 2013). Groisman and Steinberg (2000) found that elastic turbulance can occur at moderate values of Wi and vanishingly values of Re. Following the above observations, the irregularities of the flow that we observed in our experiments with AVs, can probably be attributed to the onset of flow instabilities leading to elastic turbulance. This speculation is corroborated by the fact that the flow in BSS was always regular and no turbulance was observed in that case, even if the viscosity of BSS is much more smaller than that of AVs and therefore the Re number is higher.

3.2.2 FLOW IN THE ABSENCE OF ASPIRATION

Another peculiar finding for HVPs was the generation of fluid flow even in the absence of vacuum pressure, which was, therefore, entirely due to the oscillations of the ultrasound probe without aspiration. The occurrence of steady flows produced from the action of an oscillatory non-conservative body force in a fluid is a well-known phenomenon in fluid mechanics and is referred to as steady streaming, which occurs in both viscous (Riley, 2001) and viscoelastic fluids (Repetto et al., 2014; Böhme, 1992). In our case, the phenomenon is generated in a quiescent viscoelastic fluid subjected to a periodical acoustic vibration field and the net mean flow originates from non-linear interactions. The subject of acoustic streaming has a history that is over a century long (Boluriaan and Morris, 2003). The phenomenon is the steady streaming flow that is generated due to acoustic or oscillatory motion of fluid. While acoustic oscillations are described by the linear approximation to the Navier-Stokes equations, the non-linear inertial term, generates a steady component which is quadratically small in the velocity.

In figure 3.10 we plot instantaneous snapshots of the flow field generated by the handpiece at zero pumping pressure and operating in an AV as working fluid (S1). The four panels correspond to four different values of imposed stroke and all measurements are performed in the large field and the velocities values averaged among the lateral view data. In all cases, the flow pattern consisted of a stream directed away from the probe tip, which is fed by the fluid coming from the side. Moreover, velocities achieved maximum values as larger as ≈ 6 mm/s.

In the last decade, a few theoretical and experimental works have been conducted to fundamentally investigate acoustic streaming emanating from sharp edge of solid bodies (i.e. tip of a needle) that are vibrating in fluids. Ovchinnikov et al. (2014) attributed the origin of this new type of streaming to the centrifugal force around the sharp vibrating structure. Moreover, they observed that this streaming pattern is independent of the direction the acoustic oscillation.

Even if with some different experimental conditions (e.g. the use of water as working fluid, a smaller testing chamber and a frequancy of oscilation of 2.5 kHz), also Zhang et al. (2019) evaluated the role of the amplitude of the vibration in the generation of acoustical streaming. In particular, Zhang et al. (2019) found that the relationship between the acoustic amplitude and the local vibration velocity is linear. Also Ovchinnikov et al. (2014) clearly showed that above certain amplitude the streaming velocity deviates from quadratic behavior.

This experimental phenomenon has been supported by results obtained by the model proposed by Repetto et al. (2008), showing that for corrections of amplitude, ϵ, of the order of ϵ^4 it would probably give a negative contribution to the steady streaming velocity. These findings are in agreement with our results reported in figure 3.11 in which we plot the avaraged velocities values shown in figure 3.10, U_m, over the total area (LF), as a function of the imposed stroke.

In order to evaluate if the presence of the walls could affect the velocities values, we also considered circumscribed areas around the tip of the needle and we obtained that the averaged velocities as a function of the stroke maintained the same behavior.

If such a phenomenon could potentially improve processes such as mixing and heat transfer, during vitreoretinal surgery the generation of motion in the absence of aspiration and with significant velocity values could be a highly undesirable effect.

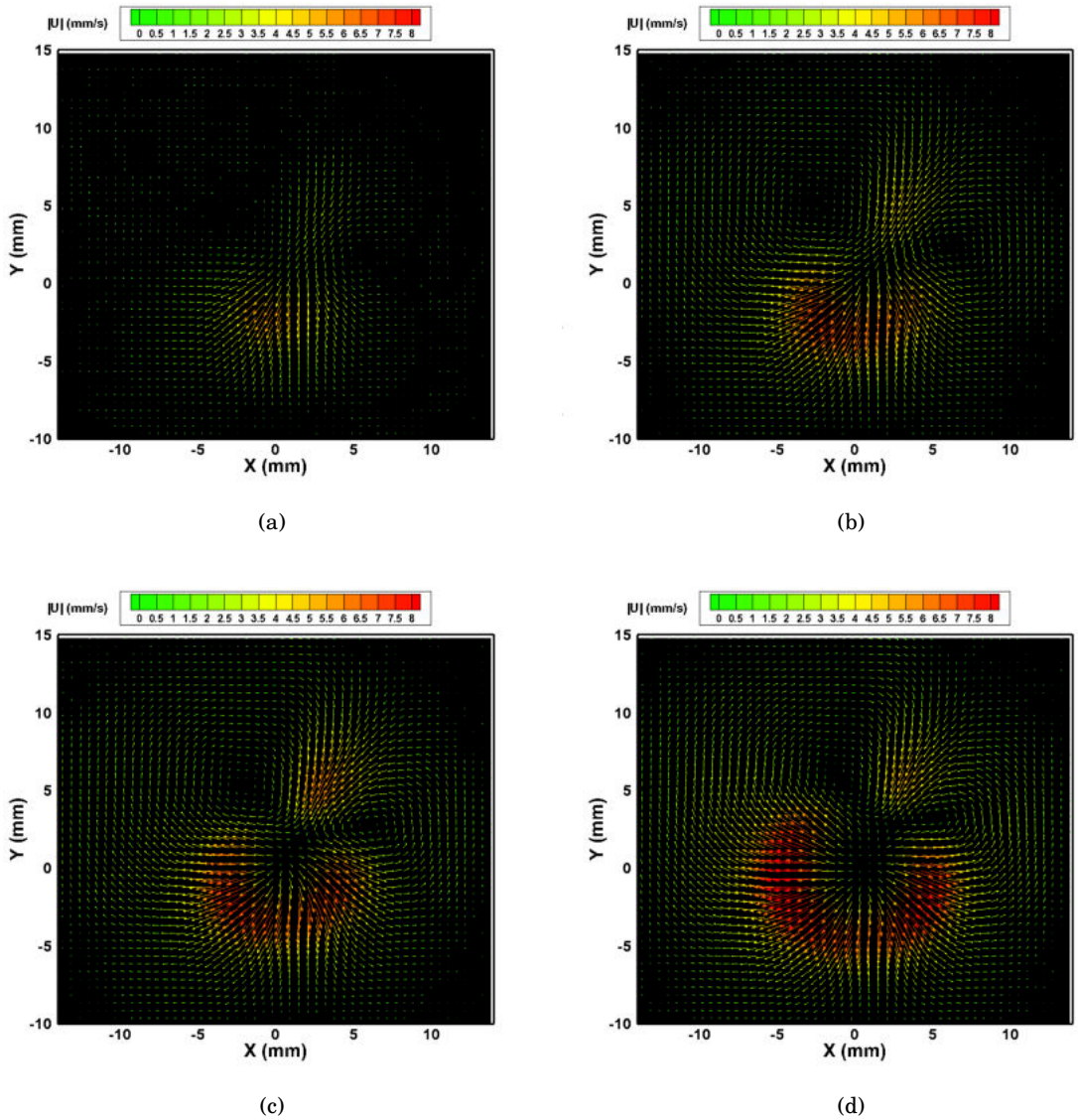

Figure 3.10: Velocity maps in the absence of pumping pressure for different strokes. Each panel corresponds to a different value of the stroke: (a) 20 μm, (b) 30 μm, (c) 40 μm, (d) 50 μm. LF, S1 as working fluid, VIT-L probe.

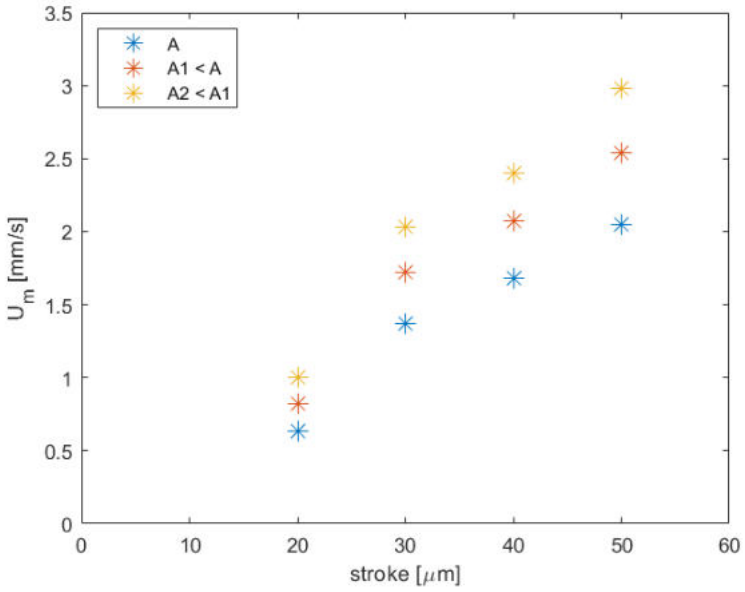

Figure 3.11: Avareged velocities values U_m over different considered areas as a function of stroke. A = 660 mm^2, $A1$ = 448 mm^2, $A2$ = 336 mm^2.

3.2.3 AVARAGED RESULTS

We focused on two quantities: time- and space-averaged magnitude of fluid acceleration and volumetric flux (or flow rate). The values of the averaged acceleration displayed in the following are based on the PIV measurements performed in the small field and are averaged among the lateral and front view data. Figure 3.12 shows the average acceleration as a function of the cutting frequency for GVPs (figure 3.12(A)), of the stroke for HVPs (figure 3.12(C)), and of the pumping pressure for all probes (figures 3.12(B,D)). For GVPs, the acceleration peaked at a cutting frequency of 4000 to 5000 cpm (figure 3.12(A)). For HPVs, the acceleration lightly grews with the stroke in BSS experiments. On the other hand, with the AV, it reached a maximum in a range of strokes between 20 and 40 μm (figure 3.12(C)). Finally, for all probes, the acceleration grew monotonically with the pumping pressure (figures 3.12(B, D)).

Figure 3.13 shows results obtained measuring the flow rate, Q, as a function of cutting frequency for GVPs (figure 3.13(A)) and stroke for HVPs (figure 3.13(C)). Moreover, in panels (B) and (D), we show the dependency of Q on pumping pressure for all probes. For GVPs, the flow rate was obviously higher the larger the needle; it decreased slightly with cutting frequency in the case of the 23SB, whereas it was almost constant for the other gauges (figure 3.13(A)). For HVPs, the flux was approximately independent of stroke in BSS and slightly decreased with it in AVs. The TD port was always characterised by larger fluxes than the L port. Moreover, for all of the probes, the flux increased as the pumping pressure grew (figures 3.13(B, D)).

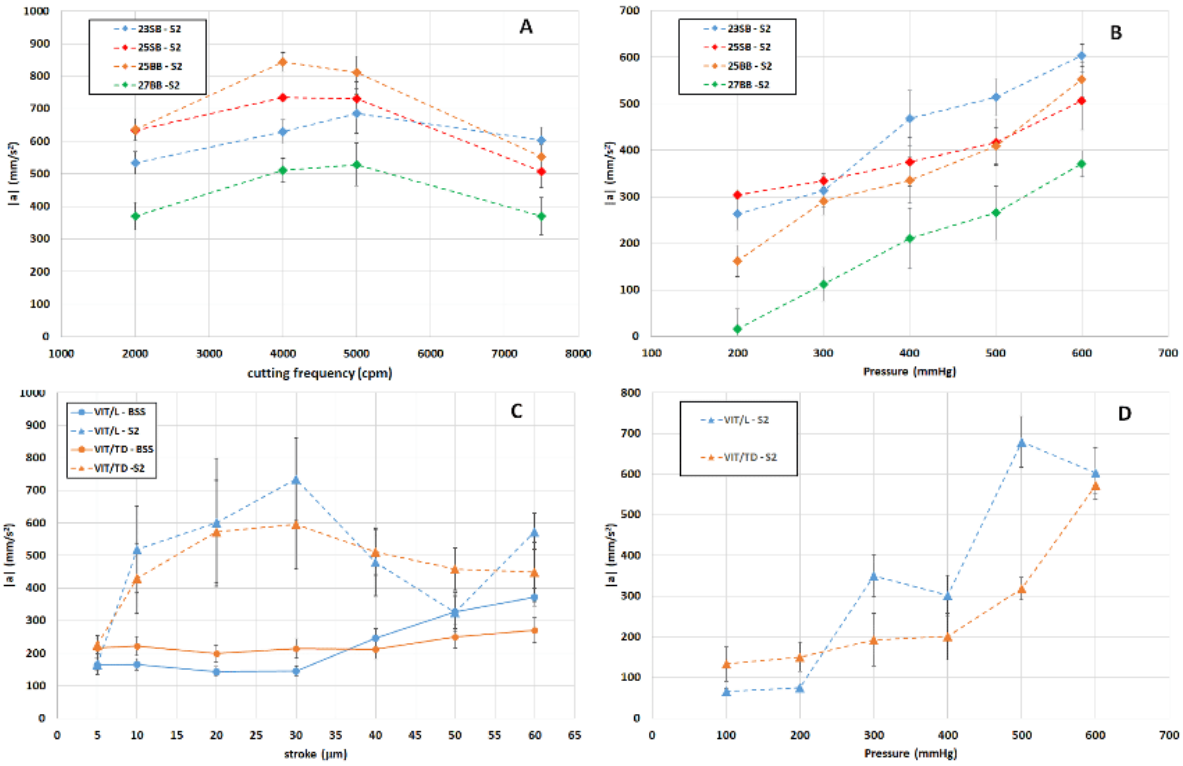

Figure 3.12: (A) Space and time averages of the magnitude of fluid acceleration as a function of cutting frequency for the guillotine cutter with solution S2, with fixed pressure set at 600 mmHg. (B) Space and time averages of the magnitude of fluid acceleration as a function of pumping pressure for the guillotine cutter, with a fixed cutting frequency equal to 7500 cpm. (C) Space and time averages of the magnitude of fluid acceleration as a function of stroke for the HVP, with vacuum pressure set at 600 mmHg. (D) Space and time averages of the magnitude of fluid acceleration as a function of pumping frequency for the HVP with solution S2, with a stroke of 20 μm.

3.2.4 Temperature measurements

Temperature measurements were taken during use of the HVPs. A sequence of temperature maps at different times is shown in figure 3.14. Because temperature gradients within the domain were quite small, the following text refers to the average temperature over the measuring plane.

Temperature evolutions in time are shown in figure 3.15, and we found similar results comparing VIT-L and VIT-TD. In particular, no significant temperature change was observed when the stroke was $\leq$ 30 μm, whereas temperature began to increase for higher strokes, reaching a maximum increase of about 2.5°C after 5 minutes with the VIT-TD operated at a stroke equal to 60 μm (figure 3.15). The temperature of the probe head, which we also monitored over time, never exceeded a temperature of 40°C (see figure 3.16(a)); this means that the head of the hand-

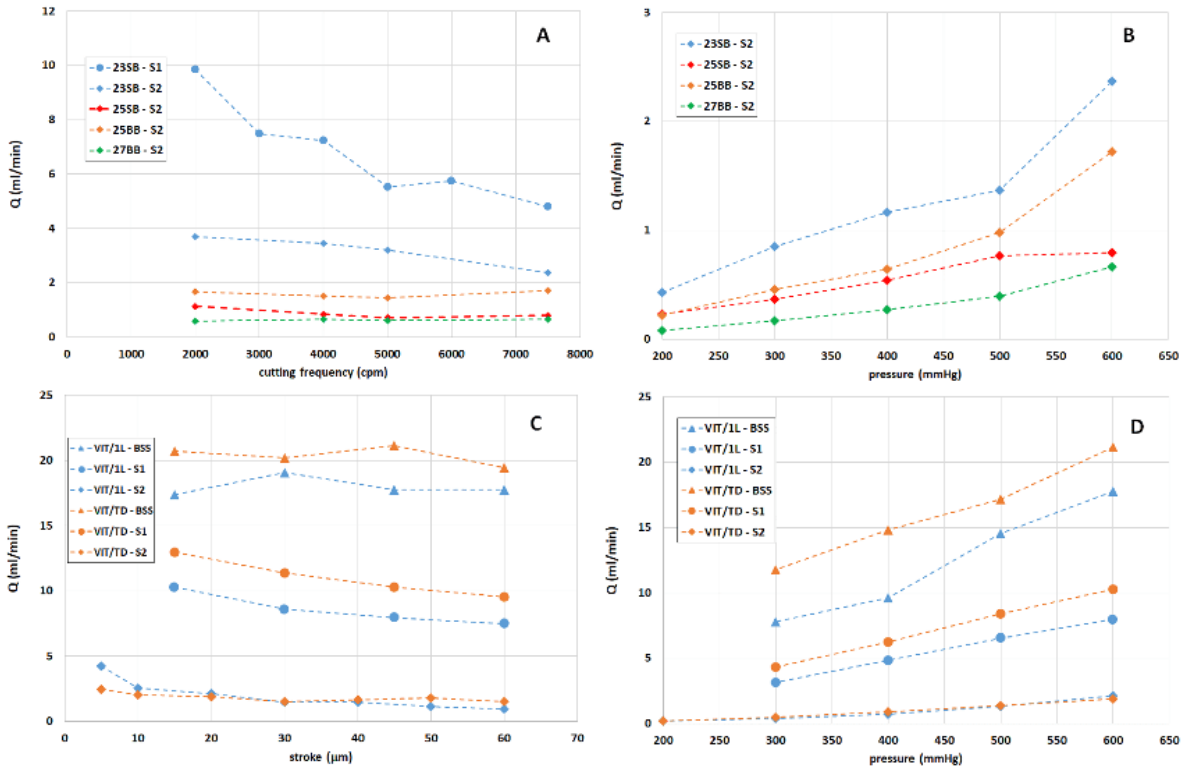

Figure 3.13: (A) Flow rate versus cutting rate for the guillotine cutter, with vacuum pressure set at 600 mmHg. (B) Flow rate versus pumping pressure for the guillotine cutter at a cutting frequency of 7500 cpm. (C) Flow rate versus stroke for the ultrasound probe with vacuum pressure set at 600 mmHg. (D) Flow rate versus pumping pressure for the ultrasound probe with a stroke of 20 μm.

piece is unlikely to transfer much heat to the vitreous during vitrectomy.

In figure 3.16(b) Q_{tot} is plotted versus the stroke for both probe configurations. In all cases we found that Q_{loss} is smaller than Q ($0.4 \leq |Q_{loss}/Q|$), meaning that the heat loss through the chamber walls is quite small compared to the heat production.

3.3 Discussion and conclusions

Ultrasound-based vitrectomy systems have been recently introduced as promising alternatives to the traditional guillotine-based cutters (GVPs) (Stanga et al., 2017, 2020). HVPs possibly have several advantages over GVPs (Stanga et al., 2017), such as the design of the probe that includes a single needle and a port that is always open, as well as the fact that vitreous liquefaction is likely to be induced, thus facilitating vitreous aspiration. These effects are thought to have a favorable influence in terms of steadiness of the flow, which is widely recognised as a crucial point for safe and effective surgery. So far, however, our knowledge about the effect of HVPs

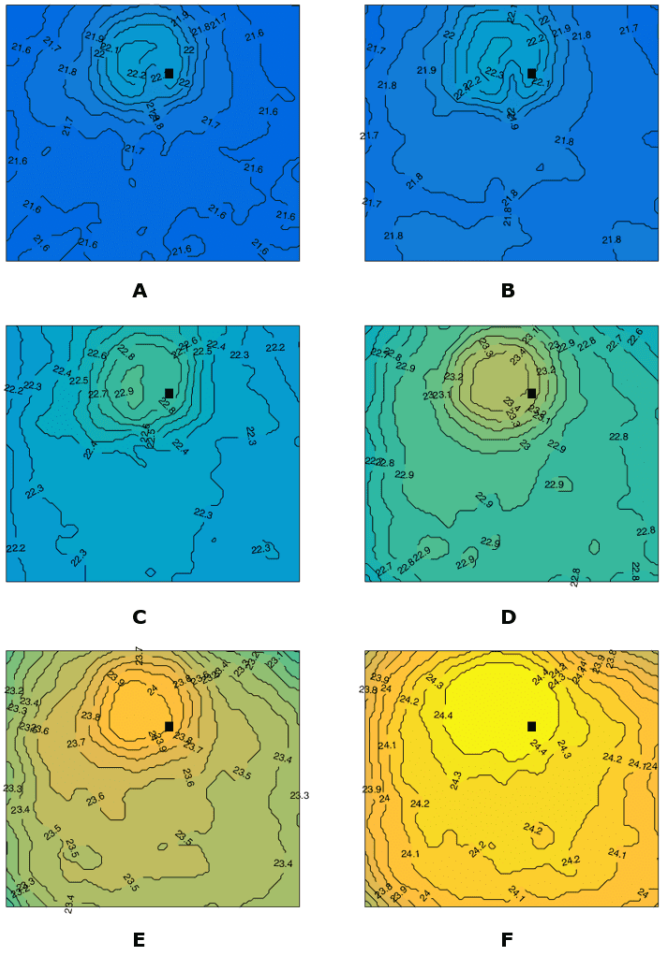

Figure 3.14: Temperature maps at different times t for the ultrasound VIT-L probe: (A) t = 0; (B) t = 1 minutes; (C) t = 2 minutes; (D) t = 3 minutes, (E) t = 4 minutes, (F) t = 5 minutes. Stroke set at 60 μm. The area depicted in the picture has a side of approximately 2 cm. The black square in the images indicates the approximate position of the probe tip. Temperature ranged from 21°C to 24.5°C.

on vitreous properties and characteristics of the flow generated in the vitreous chamber is very limited (Stanga et al., 2017).

In the present study, we investigated experimentally the fluidics of two HPVs (VIT-L and VIT-TD) and compared them with four GVPs (23SB, 25SB, 25BB, and 27BB). We performed the experiments in a cubical measuring chamber, using both BSS and AV as working fluids, in order to simulate both liquefied and healthy vitreous conditions.

The choice of an open cubical domain implies that pressure values generated in the fluid will differ from those in the eye, which is a pressurised organ. However, the intraocular pressure is small compared to the aspiration pressure imposed on the vitrectomy device, which means that the flow rate would not significantly change if a pressurised chamber was adopted. Moreover,

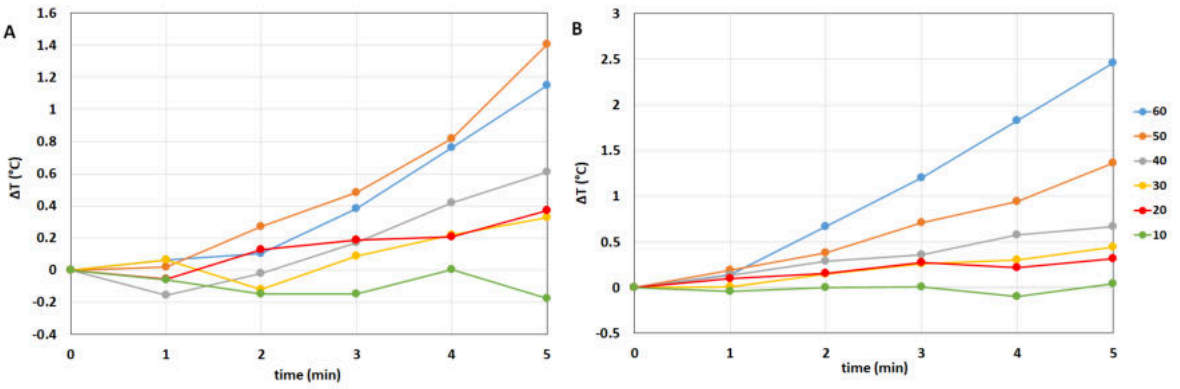

Figure 3.15: Temperature variation (ΔT) over time for different strokes: $\Delta T = T - T_0$, where T is the actual temperature and T_0 is the initial temperature. (A) VIT-L; (B) VIT-TD.

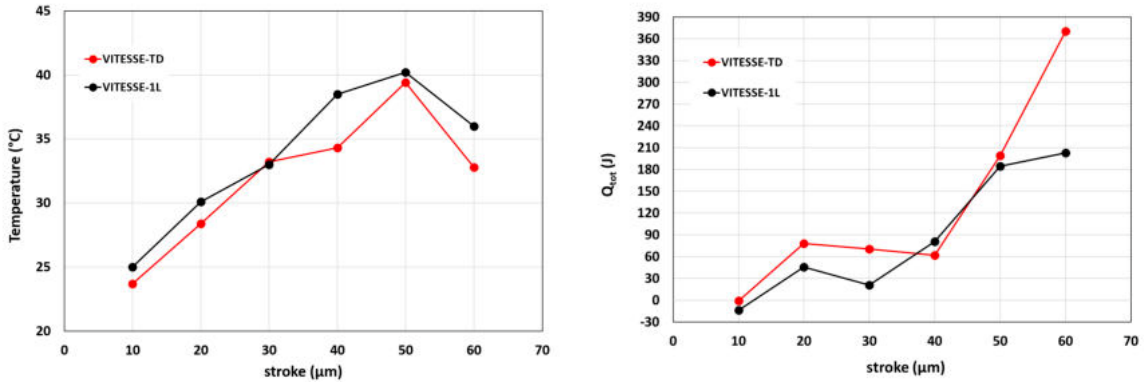

(a) (b)

Figure 3.16: (a) Total amount of heat Q_{tot} transferred by the cutter to the fluid during each experiment as a function of the stroke. Q_{tot} is computed according to equation 3.11. (b) Temperature of the cutter head after 5 minutes of use versus stroke.

pressure variations associated with fluid flow are correctly reproduced in our model, as fluid motion is produced by pressure gradients so there is gauge freedom in the pressure.

We also note that, during vitrectomy, fluid is pumped out of the vitreous chamber by the vitrectomy probe and is replaced with fluid entering from an infusion line; therefore, the overall circulation in the vitreous chamber is likely to differ from what we measured, as we do not account for infusion. However, we are mostly interested in fluid motion in the vicinity of the vitrectomy probe tip, which is not likely to be significantly affected by the overall circulation in the domain.

The use of an artificial rather than a real vitreous can obviously be seen as a limitation of the present approach, as measurements on a real vitreous would more closely mimic actual surgical

conditions. However, the use of AV also offers significant benefits, in that the experiments are reproducible and the rheological properties of the fluid can be accurately measured and controlled. This is not the case with real vitreous, as it is well known that the properties of the vitreous body can vary significantly among individuals, with both age and location in the vitreous cavity. Moreover, measuring fluid flow in the vitreous cavity is very challenging, and the approaches proposed so far do not allow one to obtain temporal or spatial resolutions even nearly comparable to those for in vitro experiments (Rossi et al., 2012). We, therefore, believe that our approach complements similar studies performed on real vitreous humor, which better reproduce surgical conditions but cannot provide a deep description of the fluid mechanics events occurring close to the tip of the vitrectomy probe and the results of which are difficult to generalise.

For tests in BSS, the flow field was invariably found to be axisymmetric. The situation was significantly more complicated in the case of AV. In particular, for all tested GVPs the flow in the AV developed a confinement region in front of the tip port (figure 3.7). This result is consistent with previous observations in both AV (Romano et al., 2018) and egg albumen (Rossi et al., 2014a,e). The possible generation of confinement regions in viscoelastic and anisotropic viscous fluids is a known phenomenon in fluid mechanics and has been investigated in various contexts, such as the flow through an abrupt narrowing (Keiller et al., 1992; Boger et al., 1992; Szabo et al., 1997) and into an orifice (Oliver, 1973), which, similarly to the flow produced by a vitrectomy probe, is accelerated. The physical argument is that as the fluid is accelerated towards the orifice any viscoelastic components are stretched at first and then align with the sink flow once they are (nearly) fully stretched. The stretched material behaves like a suspension of rigid rods with much greater extensional viscosity than shear viscosity. The anisotropy in viscosity induces a corresponding non-uniformity in flow which splits into a conical region (in which the fluid has been extended) and a recirculation region outside, as opposed to a conventional axisymmetric sink flow. The cone angle is then set by a balance between extensional stresses inside the conical region and shear stresses in a recirculating toroidal region outside (the wine-glass or champagne-glass model (Szabo et al., 1997).

From the surgical point of view, the generation of a confinement region characterised by large velocities and its extension and orientation are relevant whenever the cutter is used in the proximity of the retina, because, in that case, the orientation of the cutter port has a significant influence on the stresses on the retina. The flow generated by GVPs was also characterised by time fluctuations related to cutting frequency. In addition, in viscoelastic fluids, we also found one additional frequency with a high energy content that is likely to be related to a natural frequency of oscillation of the fluid in the domain (Romano et al., 2018; Rossi et al., 2014c; Meskauskas et al., 2011).

For HVPs, the flow was highly unsteady and irregular in space. Unsteadiness in flows generated by steady mechanisms (such as a steady pumping pressure) is very common in fluid mechanics and is due to the onset of instabilities. This typically happens when the Reynolds

number ($Re = U \cdot L/\nu$, where U is a typical velocity, L is a characteristic length scale, and ν is the kinematic viscosity of the fluid), a measure of the relative importance of inertial over viscous forces, is large enough. In the case of flows induced by vitreous cutters, Re is at most of order 10 (Re computed with L equal to the probe diameter and with the viscosity estimated at large shear rates), which is not likely to result in the onset of hydrodynamic instabilities. However, in viscoelastic fluids, elastic instabilities are also known to possibly arise, even in the limit $Re \longrightarrow 0$ (Pakdel and McKinley, 1996) and this might explain the phenomena observed in our tests. A deeper understanding of the mechanisms underlying our observations is complicated by a lack of knowledge regarding the effects that HVPs have locally on fluid properties.

We observed the generation of a steady flow (steady streaming), in the absence of an applied vacuum, that can be attributed to the periodic vibrations of the probe (Meskauskas et al., 2011).

Finally, we never detected the occurrence of cavitation, even at high ultrasound power (Rizzo et al., 2020). This is an important finding, as cavitation is highly undesirable in vitrectomy because it could disrupt the retinal tissue.

In order to characterise the efficiency of HVPs compared with GVPs, we focused on two synthetic quantities: flow rate and average fluid acceleration (Romano et al., 2018; Rossi et al., 2014a,c). With regard to GVPs, our results are consistent with previous studies (Romano et al., 2018; Rossi et al., 2014c; Stanga et al., 2017; Rossi et al., 2014e, 2016). On the other hand, only two studies considered the flow rate generated by ultrasound-based vitrectomy systems, and none of them measured fluid acceleration or any other physical quantity related to the fluidics of HVPs (Stanga et al., 2017; Rizzo et al., 2020). Thus, this is, to our knowledge, the first study to provide a comprehensive assessment of the fluidics of hypersonic vitrectomy systems.

We found that flow rate and acceleration had an approximately linear dependence on the pumping pressure and that flow rate was almost independent of the stroke for both BSS and AV. This last result is in agreement with the work by Stanga et al. (2017) and Rizzo et al. (2020) for BSS. On the other hand, on porcine vitreous, the authors found that the flow rate increased with increasing ultrasound power, although Rizzo et al. (2020) observed that this increase was small and not invariably present. This difference with respect to our findings is possibly related to the use of a different medium. Acceleration, on the other hand, changed significantly with stroke and peaked for stroke values ranging from 20 to 40 μm.

In a seminal paper in the field, Rossi et al. (2014b) proposed estimating the safety and efficiency of vitrectomy probes using a scatterplot in the plane $(Q, |a|)$ (i.e., flow rate and acceleration) for a given set of controlling parameters. The rationale behind this approach is that a vitrectomy system is efficient if it allows the surgeon to perform surgery in a short time (which implies large flow rates), and it is safe if it does not generate large stresses on the retina (which implies small fluid accelerations). Accordingly, we plotted the results of our experiments in the $(Q, |a|)$ diagram shown in figure 3.17. Overall, the results suggest that HVPs offered better performance than the GVPs; for a given flux, accelerations were (on average) smaller for HVPs than

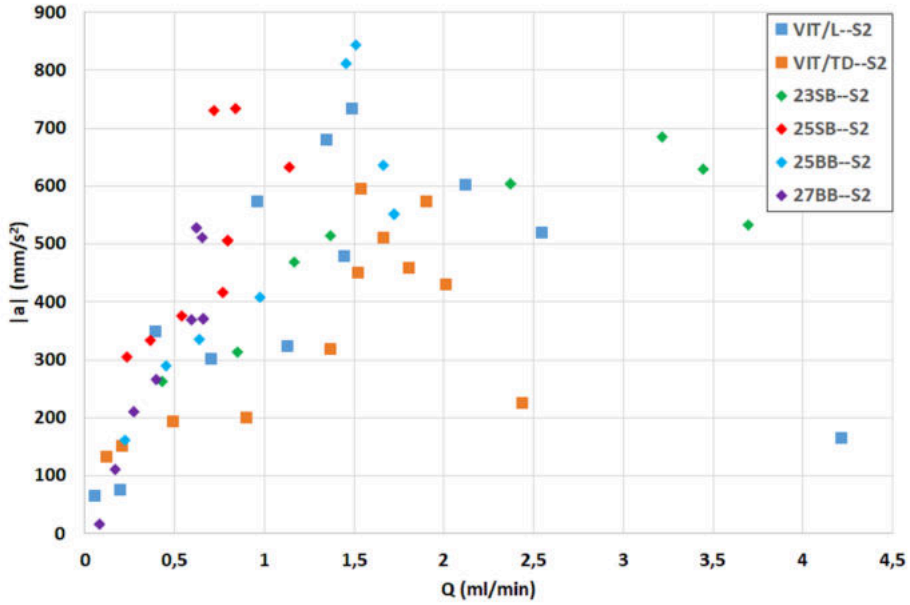

Figure 3.17: Diagram showing, for each experiment, flow rate versus time- and space-averaged magnitude of fluid acceleration.

for GVPs. Among the GVPs, the 25BB was found to perform better than the 25SB, as it produced higher flow rates with similar accelerations. This is consistent with previous studies comparing the fluidics of single-blade and double-blade cutters of the same size (Romano et al., 2018; Rossi et al., 2014c). Comparing the two HVPs we found that the VIT-TD offered better performance, as it produced larger flows regardless of the stroke. The superiority of the VIT-TD over the VIT-L has also been documented by Stanga et al. (2020).

With regard to the 27BB GVP, under our experimental setup and medium we observed that no flow rate was produced at all when the fluid was very viscous and elastic. This could be related to the extremely reduced internal lumen of the needle and obviously depends on the properties of the AV considered.

Finally, we measured temperature variations in the fluid during HVP operation, which is an important factor because high temperatures can damage ocular tissues (Sippel and Pineda, 2002). In our experiments, we found a maximum temperature increase of 2.5°C after 5 minutes of continuous use of the HVP at a stroke of 60 μm. During the experiment, the temperature of the head of the HVP also increased, to a maximum of approximately 40°C. We note that, in terms of temperature variations in the fluid, our experimental setup did not accurately reproduce what happens during surgery, as we did not have an infusion line and the vacuum pressure was set to zero for temperature measurements, implying that there was no fluid exchange in the measuring chamber. During vitrectomy surgery, on the other hand, vitreous is pumped out of the eye and is replaced by a fluid that typically has a significantly lower temperature. This would drastically

mitigate the tendency of the HVP to increase fluid temperature, which is already very small. For these reasons, we think that high temperatures in the vitreous chamber during vitrectomy with HVPs are not an issue.

In conclusion, we assessed the fluid dynamic performance of vitrectomy probes in BSS and AV using a cubical measuring chamber. This study confirmed that flow rate and acceleration grow with aspiration pressure for all vitrectomy probes. Flow rate exhibited a weak dependence on cutting frequency and stroke for GVPs and HVPs, respectively, whereas acceleration peaked at 4000 to 5000 cpm for GVPs and between 20 and 40 μm for HVPs. Overall, the HVPs performed better than the GVPs, producing lower acceleration for a given flow rate. However, the HVPs produced an irregular and time-dependent flow, probably due to the onset of flow instabilities. Temperature elevation during surgery is very unlikely to be an issue.

CHAPTER 4

DYNAMIC PRESSURE MEASUREMENTS IN A MODEL OF THE EYE

This chapter is based on the manuscript of Nepita et al., which is in preparation.

Purpose of the present chapter is to investigate and quantify dynamic pressure variations during vitrectomy maneuvers in a real scale model of the viteous chamber. We tested the efficency of the EVA phaco-vitrectomy system (D.O.R.C. Dutch Ophthalmic Research Center) in maintaining baseline pressure values during the various phases of the surgical procedure. In addition, flow rate experiments have been performed with the aim of assessing the performance of EVA High flow connection for infusion system.

4.1 MATERIAL AND METHODS

4.1.1 EXPERIMENTAL SETUP AND MEASURING TECHNIQUES

Experiments were carried out in a transparent physical model of the vitreous chamber at real scale and with a realistic geometry, based on typical human eye geometrical features, which we report in figure 4.1 (Commission, 1999; Atchison and Smith, 2000; Atchison et al., 2004, 2005; Nogueira et al., 2011). The model was made of Plexiglas and produced with a 3D CNC milling machine. It consists of two identical parts, each representing half of the vitreous chamber, see figure 4.2(a). The model is anchored to a rigid support and held in the “face up” position and connected to both infusion and aspirations lines, thus mimicking the real surgical procedure. Infusion and aspiration lines are approximately in correspondence of the limbus, as shown in figure 4.2(a), to replicate the location of the trocar incisions, performed during surgery. A specific connection for the infusion line was prepared, considering the geometry of both Standard (SF) and High Flow (HF) infusion systems. In SF configuration, the end of the infusion line tube is inserted into the trocar of the appropriate diameter. On the other hand, in HF configuration, the

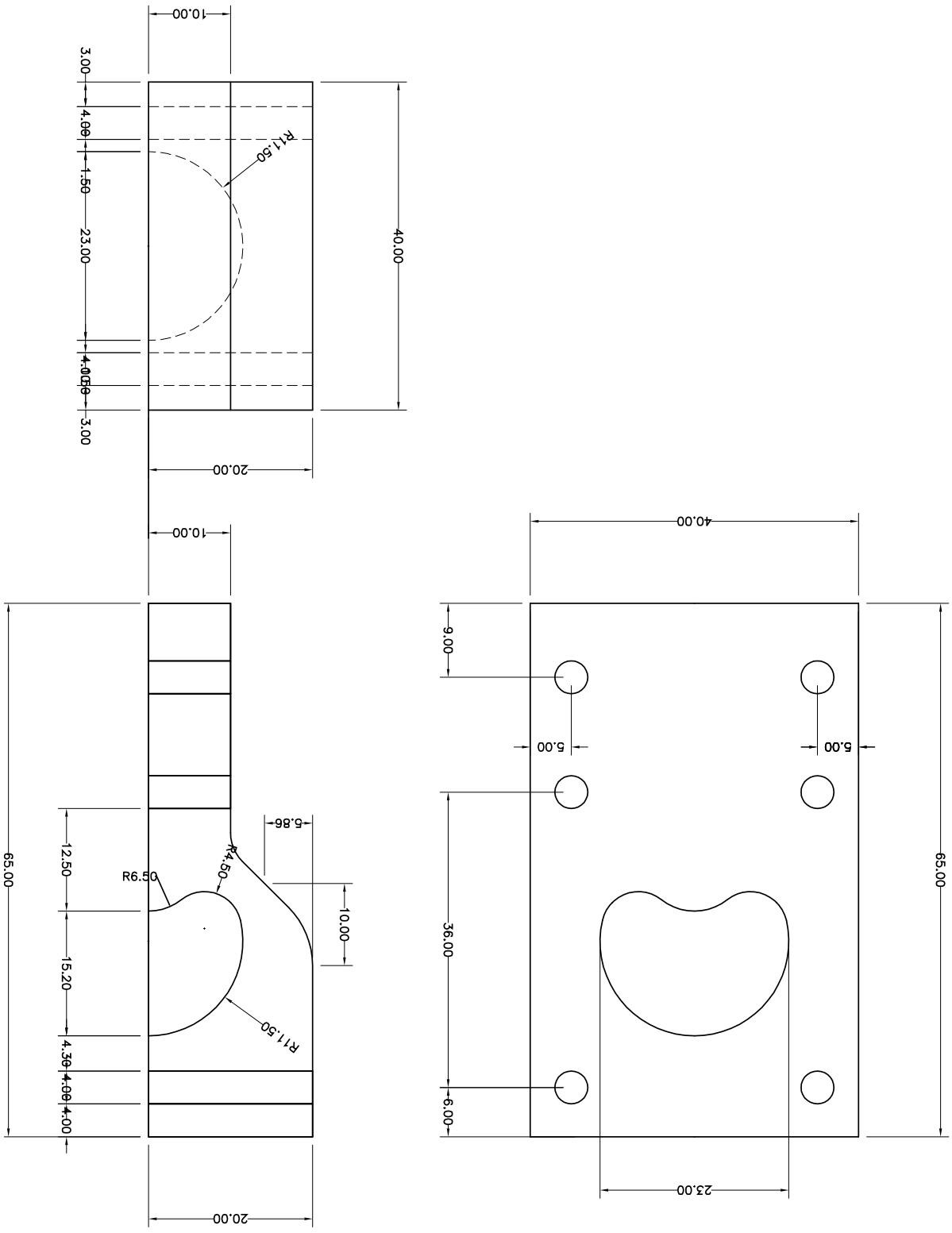

Figure 4.1: Technical drawing of the model of the vitreous chamber and measurements of its various parts.

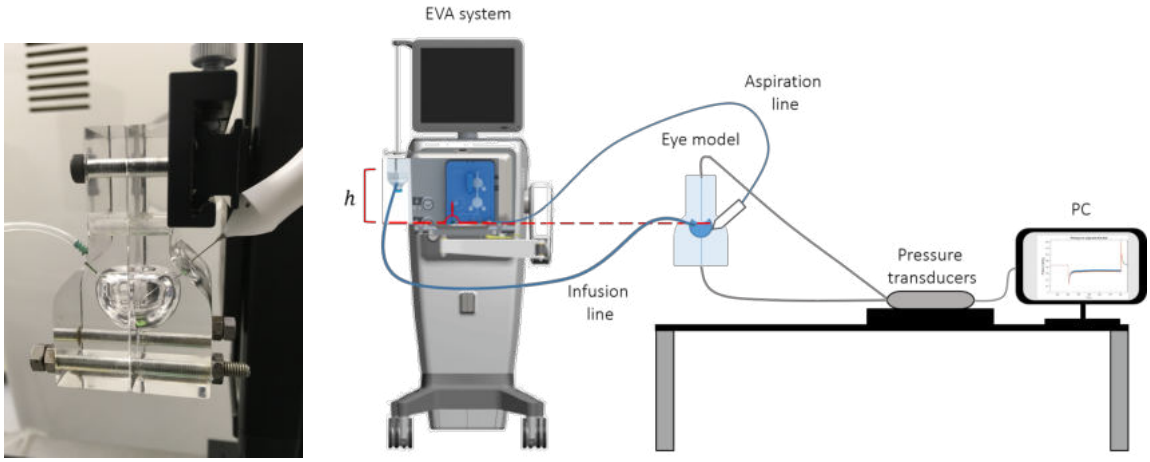

(a) (b)

Figure 4.2: (a) Picture of the assembled eye model connected with irrigation and aspiration lines; (b) sketch of the experimental apparatus.

infusion tube is connected to the external part of the trocar, so that pressure losses are reduced and the infusion rate increased. In addition to the infusion and aspiration lines, two pressure trasducers (Viatran model 422) are connected to the eye model, through two identical tubes. Pressure transducers can register pressures in a range of 155.15 mmHg, with an accuracy of 0.01 mmHg.

The pressure measuring point are located along the axis of symmetry of the vitreous chamber, one at the top (center of the lens) and one at the bottom side of the model (posterior pole), see figure 4.2(b). Pressure signals have been acquired using a DAQ system (National Instruments©) controlled by a Labview Graphical User Interface (GUI). The acquisition frequency was set for all experiments to 1.5 KHz, which is more than ten times the maximum cutting rate used during experiments. Prior to the measurements, transducers were calibrated with a graduated water column. In the present experimental set up, in static conditions the two pressure transducers register slightly different pressure values (≈ 2 mmHg), owing to the elevation difference between the two measuring points in the eye model. The EVA system controls the infusion pressure by imposing a prescribed pressure value in the air content of the infusion bottle. Thus, the sensors measure a static pressure, before the infusion starts, equal to $p_0 + \gamma h$, where p_0 is the pressure in the air phase of the bottle imposed by the device, γ is the specific weight of the fluid and h is the height between the free surface in the bottle and the connection of the infusion line in the cartridge (see figure 4.2(b)). Since p_0 is one of the parameters that the operator can choose, if we want to compare experiments run with the same value of p_0 the height of the water level in the bottle has to be considered. This contribution should also be taken into account during surgery, since it effectively increases the pressure in the eye with respect to the imposed infusion

pressure p_0.

A typical experiment consists of three phases: i) continuous irrigation is switched on and there is no aspiration by the vitreous cutter (infusion phase); ii) aspiration is activated and this causes a sudden pressure drop in the eye model. This second phase is characterised by irrigation and aspiration occurring at the same time (aspiration phase). iii) Aspiration is stopped, all fluxes vanish and the pressure returns to its original value (baseline pressure).

Pressure data have been post-processed as follows: first, the starting and end times of infusion and aspiration phases were identified; then, pressure averaged values (P_b and P_a, corresponding to the infusion and to aspiration phase, respectively) and corresponding standard deviations were computed. We also computed the avarage pressure jump, ΔP defined as $\Delta P = P_b - P_a$. A moving average was applied to the signals of each phase in order to remove overall trends and, thus, to compute the pressure residuals. Power spectra of the pressure residuals (for the aspiration phase) were computed, in order to identify the main frequencies of pressure oscillations.

For each experiment, we measured the flow rate using a remotely controlled precision digital scale (A&D compact scale, EK-1200G). The aspirated liquid was collected directly from the cartridge into a beaker positioned on the scale and its mass, $M(t)$, was recorded in time (t) with a sampling frequency of 5 Hz. The time derivative of the signal, dM/dt, provides an estimate of the mass flow rate Q_m, from which the volumetric flux Q can be obtained as $Q = Q_m/\rho$, with ρ being the fluid density. This calculation was done by performing a linear regression of fluid mass in time $M(t)$; the slope of the line represents Q_m. The coefficient of determination R^2 of the linear regression was found on average equal 0.9986 ± 0.001 over all the experiments, which means that the signals are linear to a very good degree of approximation.

We tested 23, 25 and 27 gauge High Speed TDC cutters, both in VGPC (Vented Global Pressure Control) and in AIC (Automatic Infusion Compensation) modes of the EVA vitrectomy system. The EVA system has been operated in "Core vitrectomy" modality, imposing a vacuum aspiration pressure. In VGPC mode, a fixed irrigation pressure is imposed (baseline pressure). On the other hand, in AIC mode a minimum and a maximum infusion pressures are set and EVA switches from one value to the other, with the aim of compensating pressure fluctuations during surgical maneuvers. In all experiments performed in AIC mode the maximum infusion pressure value was set equal to 55 mmHg. For the 23 and 25TDC cutters we tested both the SF and HF infusion systems. The different operating conditions imposed during all experiments are reported in table 4.1. We performed a total number of experiments equal to 68, using both Balanced Salt Solution (BSS) and an artificial vitreous (AV) substitute. Details of the AV preparation and the mechanical characterisation are provided in section 4.1.2. All experiments with AV have been performed with HF infusion connection.

Reproducibility of the experiments has been tested repeating one test 7 times, with a specific set of parameters imposed. The pressure relative error with respect to the average as a function of the various experimental repetitions, $(P_n - \overline{P})/\overline{P}$, with P_n pressure measured in the generic

Inf. System	TDC cutter	Asp. Pressure (mmHg)	Cut rate (cpm)	working Fluid	Inf. Pressure (mmHg)	Infusion type	# Exp
VGPC	23	400	6000	BSS	20-25-30-35-40	SF/HF	10
VGPC	25	600	6000	BSS	20-25-30-35-40	SF/HF	10
VGPC	27	600	6000	BSS	20-25-30-35-40	HF	5
VGPC	23	600	6000	AV	20-30-40	HF	6
VGPC	25	600	6000	AV	20-30-40	HF	6
AIC	23	400	6000	BSS	20-25-30-35-40	SF/HF	10
AIC	25	600	6000	BSS	20-25-30-35-40	SF/HF	10
AIC	27	600	6000	BSS	20-25-30-35-40	HF	5
AIC	23	400	6000	AV	20-30-40	HF	3
AIC	25	600	6000	AV	20-30-40	HF	3

Table 4.1: Experimental parameters.

n-th repetition, $n \in (0,N)$, and $\overline{P} = \sum_{n=1}^{N} P_n/N$, was found to be always less than $\pm 4\%$. Moreover, the standard deviation of the single measurement is $\approx 2.5\%$ of the average value, indicating a fairly good repeatability of measurements.

4.1.2 Aritifical vitreous preparation and rheological tests

For the experiments presented in this chapter, we obtained AV solution optimising the recipe proposed in the previous chapters. In particular, only Agar-agar polysaccharide diluted in pure water was used to prepare AV fluids.

Polymer powder was first added at a concentration of 0.1, 0.15 or 0.2% to deionised water and then completely solubilised by heating the samples with a microwave oven operating at 700 W. The solutions were heated up to 100°C for a few seconds, vigorously mixed and brought to boil again. The samples were finally allowed to slowly cool down at room temperature and then preserved at 4°C to avoid polymer degradation.

The viscoelastic behaviour of the prepared AV was assessed through the rotational rheometer already introduced in chapters 2 and 3. The temperature was set at 20.0 ± 0.2°C or at 37.0 ± 0.2°C. A normal force of 0 N was applied to the samples in order to ensure the measurement of the linear properties of agar gels (Mao et al., 2016). In previous chapters, steady-state viscosity measurements were exploited to explore the flow behaviour of artificial fluids with different properties. Here, owing to the gel-like nature of the prepared agar-based AV, we instead performed only oscillatory tests as a function of frequency. Amplitude sweep tests were carried out in the strain range 0.01 – 10%, at frequency ω = 1 Hz. Frequency sweep tests were then used to evaluate the viscoelastic response of the samples at a strain of 1% by varying the frequency between 0.1 and 10 Hz. We avaluated the storage ($G^{'}$) and loss ($G^{''}$) moduli, as well as the complex viscosity, $|\eta^*| = (G'^2 + G''^2)^{1/2}/\omega$.

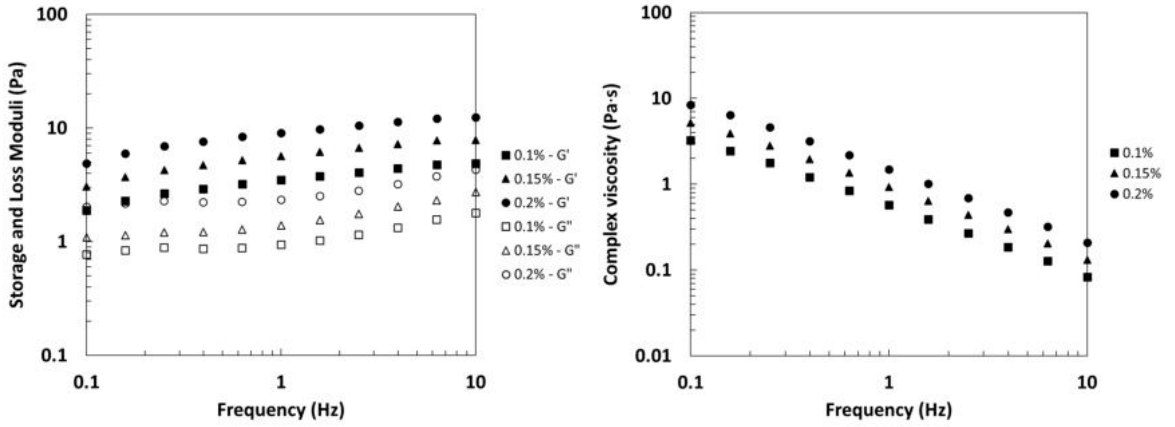

(a) (b)

Figure 4.3: Dependence of viscoelastic spectra upon the polymer concentration at T = 20°C at a strain of 1% and variable frequency: a) $G^{'}$ (black markers) and $G^{''}$ (white markers) moduli; b) complex viscosity, $|\eta^*|$.

4.2 Results

4.2.1 Rheological measurements

For all polymer concentrations, all tested AVs show a gel-like behaviour in the whole range of investigated frequency, with a larger value of the elastic modulus compared to the viscous one (see figure 4.3). Increasing the Agar-agar concentration leads to an increase in both viscoelastic moduli, as well as the complex viscosity of the prepared AVs. This is because a higher number of polymer chains leads to a "denser" polymer network, characterised by closer crosslinking points and entanglements (Urueña et al., 2015; Nesrinne and Djamel, 2017). Moreover, all samples show a decrease of $|\eta^*|$ as the frequency is increased, which is consistent with their gel-like behavior (figure 4.3(b)). Such finding is related to the fact that, as the frequency is risen, the gels are subjected to a progressively larger stress, able to break their microstructure (i.e., physical crosslinking points between the polymer chains), thereby facilitating their flowing.

Taking into account that the rheological characterisation in figure 4.3 was performed at T = 20°C in order to match the temperature of the investigated in vitro model, the sample with a polymer concentration of 0.15% was selected for the following experiments.

AVs should have values of the viscoelastic moduli similar to those of the human vitreous. Repetto and Dvoriashyna (2019) report a fairly detailed picture of the existing measurements of vitreous properties.

In particular, Tram and Swindle-Reilly (2018) presented the rheological characterisation of human as a function of the patient age and the post-mortem time of investigation, with $G^{'}$ and $G^{''}$ values of 6.5 Pa and 0.96 Pa, respectively, at a frequency of 1 Hz and T = 37°C (see figure 4.4). Shafaie et al. (2018) reported that the human vitreous is characterised by $G^{'}$ = 1.4 Pa and $G^{''}$

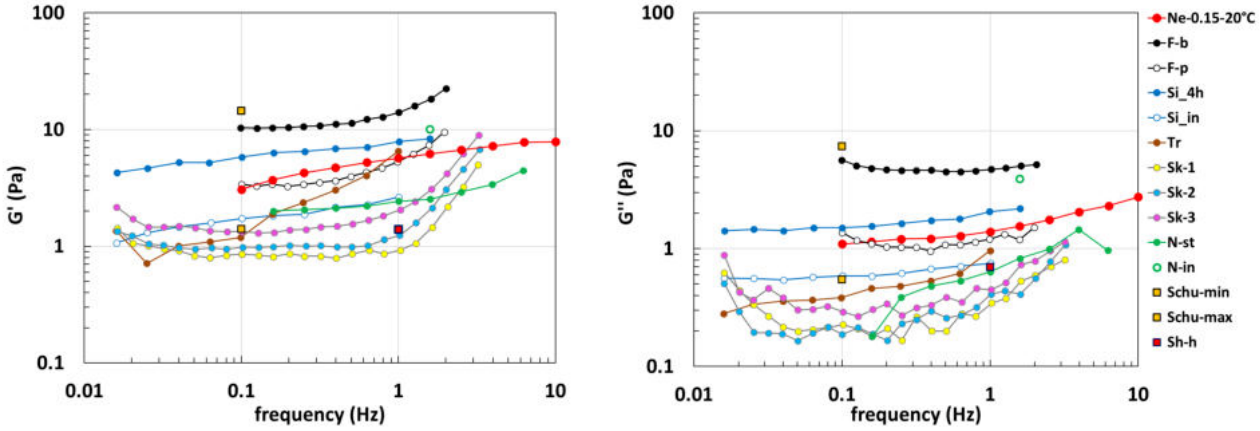

(a) (b)

Figure 4.4: Storage (a) and loss (b) moduli as a function of the testing frequency. Ne-0.15-20°C: results of the present analysis; F-b: Filas et al. (2014) bovine vitreous; F-p: Filas et al. (2014) porcine vitreous; S-i: da Silva et al. (2017) initial values, rabbit vitreous; Si-4h: da Silva et al. (2017) 4 hours after dissection, rabbit vitreous; Tr: Tram and Swindle-Reilly (2018) human vitreous; Sk-i: Sharif-Kashani et al. (2011) (i = 1; 2; 3 denotes different eyes), porcine vitreous; N-st: Nickerson et al. (2008) steady state values, porcine vitreous; N-in: Nickerson et al. (2008) initial values, porcine vitreous; Schu-min and Schu-max: Schulz et al. (2019) minimum and maximun values of 3365 years old vitreous patients; Sh-h: Shafaie et al. (2018) human vitreous.

Concentration (%)	$G^{'}$ (Pa)	$G^{''}$ (Pa)
0.1	3.5	0.9
0.15	5.7	1.4
0.2	9.1	2.3

Table 4.2: Measured values of $G^{'}$ and $G^{''}$ moduli at frequency equal to 1 Hz and T = 20°C.

= 0.7 Pa at a frequency of 1 Hz and a temperature of 37°C. Furthermore, Schulz et al. (2019) reported storage and loss moduli of 69 vitreous donors ranged from 1.4 to 14.5 Pa and from 0.55 to 7.39 Pa, respectively.

Moreover, several other studies were carried out by different research groups even on animal samples and similar results were obtained, as shown in figure 4.4 (da Silva et al., 2017; Nickerson et al., 2008; Filas et al., 2014; Sharif-Kashani et al., 2011).

To contextualise our results in the overall landscape of the measures reported in the literature, we propose the figure shown in chapter 1, adding rheological data obtained from the present analysis (figure 4.4, red curves). All the investigated AVs in the present work present viscoelastic properties appropriate to match the ones of human vitreous. Table 4.2 summarises the rheological properties (frequency equal to 1 Hz and T = 20°C) of the AVs tested in the present work.

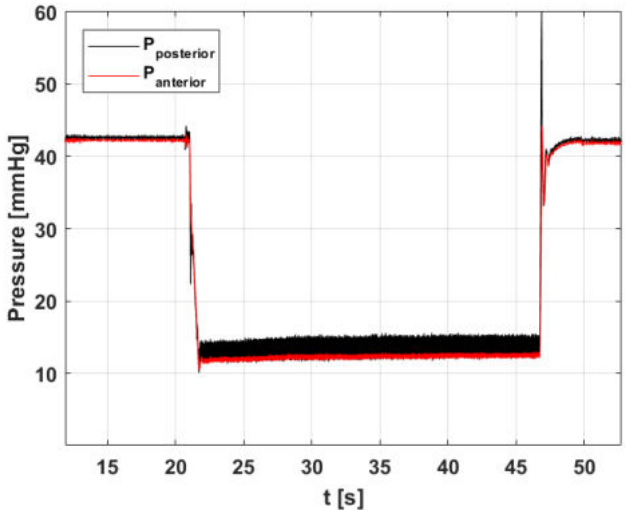

Figure 4.5: Example of pressure versus time signals, measured at two different positions of the eye model, using BSS in VGPC mode. Black curve: posterior position; red curve: anterior position.

4.2.2 Pressure measurements with BSS

In figure 4.5 we report an example of typical signals measured by the two pressure probes, which correspond to different positions in the vitreous chamber, anterior (red curve) and posterior (black curve), respectively. During the first phase of the experiment, continous irrigation was switched on and there was no aspiration by the vitreous cutter. In this phase, the system attained a constant pressure value that will be considered as the baseline value during the experiment. When the pedal is pressed, aspiration starts (approximately at t = 22 s in figure 4.5 and the pressure in the eye model drops, owing to hydraulic pressure losses along the system. Once the pedal is released and aspiration stops and the measured pressure returns to the baseline value. Typically, in experiments with BSS the pressure remains fairly constant during the aspiration phase (figure 4.5). Moreover, the amplitude of pressure fluctuations related to fluid motion is larger at the posterior position (black curve) of the vitreous chamber model than it is at its anterior one. This happens in all experiments and is probably due to the generation of a jet that impinges the chamber wall opposite to the sensor located in front of the irrigation line.

4.2.3 Pressure measurements with AV

When we performed measurements with AV the material contained in the vitreous chamber model progressively changed properties during the experiment, since AV mixed with the infused BSS. This is quite clearly shown in figure 4.6, where we report examples of the pressure measured in the eye model with both the 23 and 25TDC cutters versus time, using AV. The

pressure signals refer to the transducer connected to the upper part of the model (anterior position). In each panel the two curves refer to two different values of the infusion pressure. The figures show that, during the aspiration phase, in most experiments the pressure progressively decreases from a minimum value of 1 to a maximum of 12 mmHg. This is a consequence of the fact that BSS viscosity is smaller than that of AV and the more water enters the hydraulic circuit the smaller the pressure is expected to be in the eye model, owing to an overall decrease of hydraulic resistance. Leaving aside the differences highlighted above, the main characteristics of the experiments performed using BSS only and AV are the same, as described in section 4.2.2. In VGPC mode, see figure 4.6(a,c), as the aspiration phase begins, the pressure experiences a sudden drop, which is recovered when aspiration ceases. The pressures signlas obtained with the 23 and 25TDC cutters are qualitatively similar, however, the pressure jump is higher for the case of 25TDC probe and, in that case, the relative pressure might reach negative values.

Figure 4.6(b,d) shows pressure signals aquired when the AIC control system was turned on. This implies that the system attempts to compensate the pressure drop by increasing the infusion pressure. Results demonstrated that the pressure drop, is typically reduced and, in particular, for an irrigation pressure of 30 mmHg (orange curves) the pressure variation is totally compensated.

In all cases, we observed that stopping aspiration caused a pressure spike. This behaviour is likely do to the fact that we operated in a rigid domain and the only compliance is due to the pipes. This behavior is likely to be reduced in a real eye, which is significantly more deformable. During the spike the pressure achieved values of ≈ 50 mmHg, which are in line with what found in previous experiments performed in porcine eyes (Sugiura et al., 2013).

In figure 4.7 we report the average pressure jump (ΔP) versus the imposed irrigation pressure for experiments performed with both infusion systems (black curves VGPC, red curves AIC). Note that ΔP is positive when the pressure during aspiration is smaller than the baseline value (this is always the case in VGPC mode). In this graph the two cutters are distinguished by different symbols: the empty bullet marker for the 23TDC and the full bullet marker for the 25TDC cutter. These results show that, without compensation (VGPC mode), ΔP remains fairly constant with the imposed value of infusion pressure. When AIC mode is activated (red curves) the pressure drop is typically reduced, expecially with the 23TDC cutter. However, compensation has a detrimental effect at low infusion pressures as it produces a pressure increase in the measuring chamber during the aspiration phase resulting in a negative value of ΔP. This result suggests that this phenomenon could be reduced setting a smaller value of maximum infusion pressure.

In general, pressure drop values obtained with AV resulted smaller than those obtained with BSS with the same wotking parameters. In figure 4.8, we show the comparison of ΔP values obtained using both BSS (red curves) and AV (green curves), for experiments performed in AIC mode. Using BSS (red curves), the 25TDC cutter achieved values very similar to those ob-

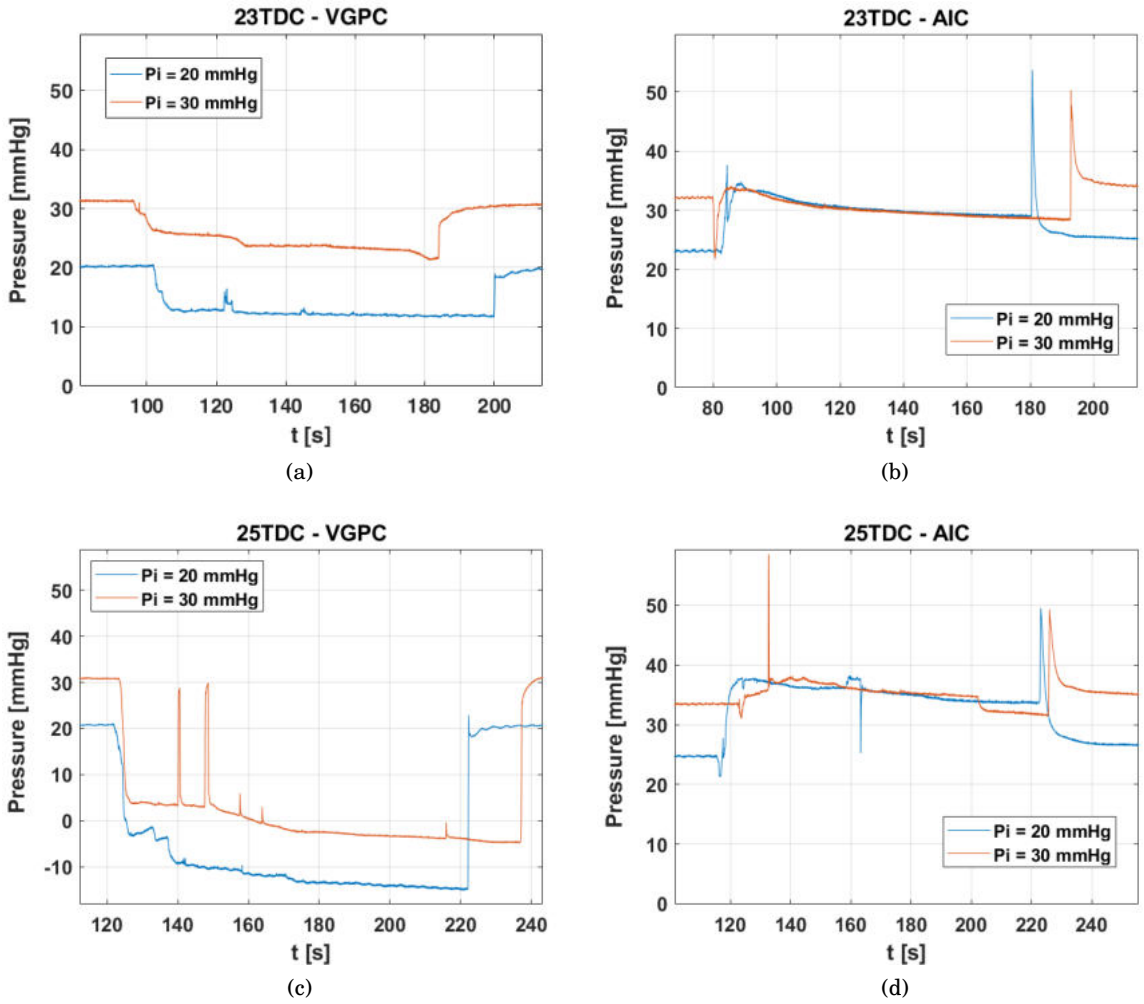

Figure 4.6: Pressure versus time as measured in experiments with AV: 23TDC cutter (a,b), 25TDC cutter (c,d); experiments in VGPC mode (a,c); experiments in AIC mode (b,d). In all panels the blue curves correspond to infusion pressure Pi = 20 mmHg, orange curves Pi = 30 mmHg. Signals refer to the transducer connected to the upper part of the model.

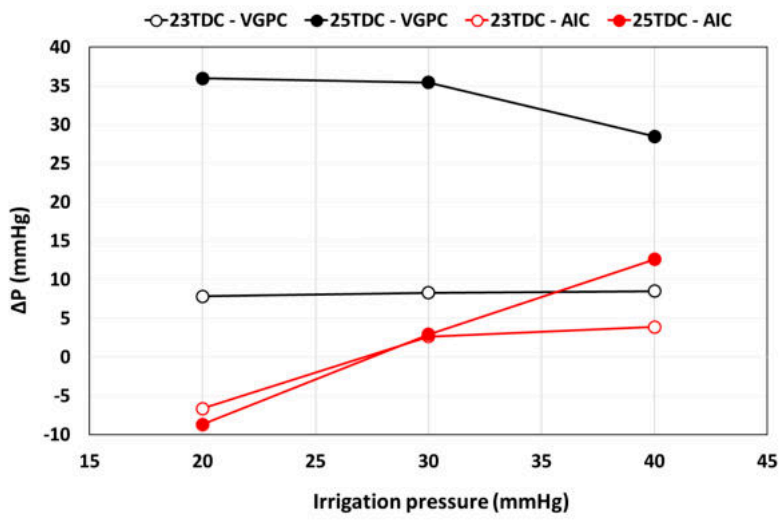

Figure 4.7: Pressures drop, ΔP, defined as the difference between the baseline and the time averaged aspiration pressures, as a function of the imposed irrigation pressure. Black curves: VGPC mode; red curves: AIC mode. Empty bullets refer to experiments with 23TDC cutter; full bullets refer to experiments with 25TDC cutter. All experiments have been performed with AV.

tained with AV for the usual infusion pressures set during vitrectomy (25-30 mmHg). In general, 23TDC probe in AV produced smaller values of ΔP. Finally, for an infusion pressure set to 20 mmHg, both cutter gauges compensated very efficiently pressure variations.

4.2.4 Pressure and flow results with HF and SF connections

Results of measurements regarding the differences between HF and SF connections for the infusion system are summarised in figure 4.9. For both 23 and 25TDC cutters and infusion systems, the HF connection resulted in much lower ΔP values than the corresponding value obtained with the SF one (see figure 4.9(a,b)). In addition, flow rate experiments (see figure 4.9(c,d)), demonstrated a greater aspiration flow efficiency when the HF is used, for both vitreous probes and infusion systems.

In order to obtain an overall evaluation of the HF infusion connection, we performed experiments in AIC mode, also using the 27TDC vitreous cutter. Results relative to pressure variations are shown in figure 4.10, in comparison with the larger vitreous cutters. The figure shows that, compensation with the 27TDC cutter (green curve) was less efficient than with 23 and 25TDC cutters (higher values of ΔP). We note however, that ΔP is positive and quite large for the 27TDC cutter; this implies that a smaller maximum infusion pressure value is required to obtain the desire compensation.

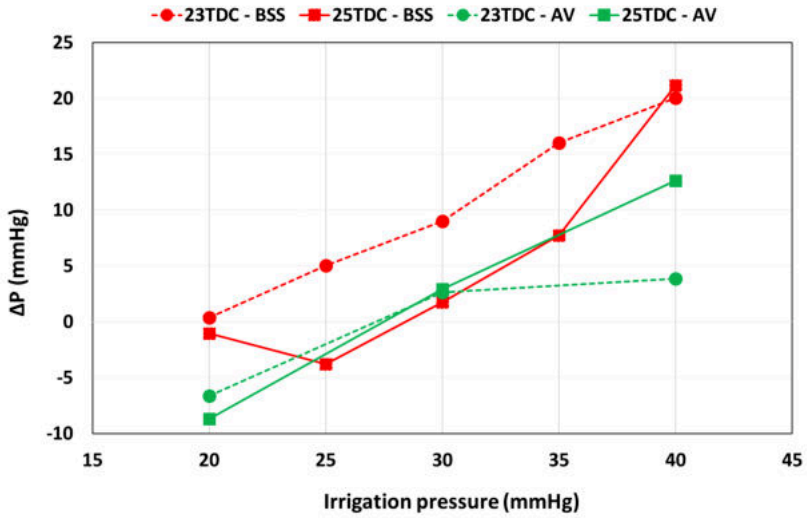

Figure 4.8: Pressures drop in AIC mode, ΔP, defined as the difference between the baseline and the time averaged aspiration pressures, as a function of the imposed irrigation pressure. Red curves: experiments with BSS; green curves experiments with AV. Circles: 23TDC cutter; squares: 25TDC cutter.

4.2.5 Power spectra of the pressure signals

Examples of the power spectra obtained during the aspiration phase of the experiments are reported in figures 4.11 and 4.12, for the 23 and 25 gauge cutters. The features of the power spectra that will be discussed in this section are common to all experiments and, therefore, there is no need for us to comment separately the results for each cutter size or mode of functioning of the EVA device (AIC or VGPC).

In each figure, panels (a),(c),(e) and (b),(d),(f) refer to the pressure probes located in the posterior and anterior positions, respectively, with different imposed irrigation pressures. Moreover, in each figure, lines with different colours correspond to BSS and AV working fluids, the other controlling parameters being kept fixed. The reported spectra refer to experiments in which the cutter was operated at 6000 cpm, corresponding to a frequency of 100 Hz.

As expected, in all cases a clear peak in the power spectrum was found in correspondence of the cutting frequency (100 Hz); smaller peaks were also present at superharmonic frequencies. This shows that the pressure sensors were capable of measuring pressure variations induced by the movement of the cutter blade. We note that in all experiments, pressure fluctuations induced by the cutter movement were very small compared to the value of the pressure itself (figure 4.5 is a good representation of what happens in all experiments in this respect).

The power spectra relative to the pressure probes located at the anterior and posterior positions of the eye model were similar to each other. A subtle but significant difference is the fact that superharmonic peaks were typically broader and higher for the bottom pressure probe (P1).

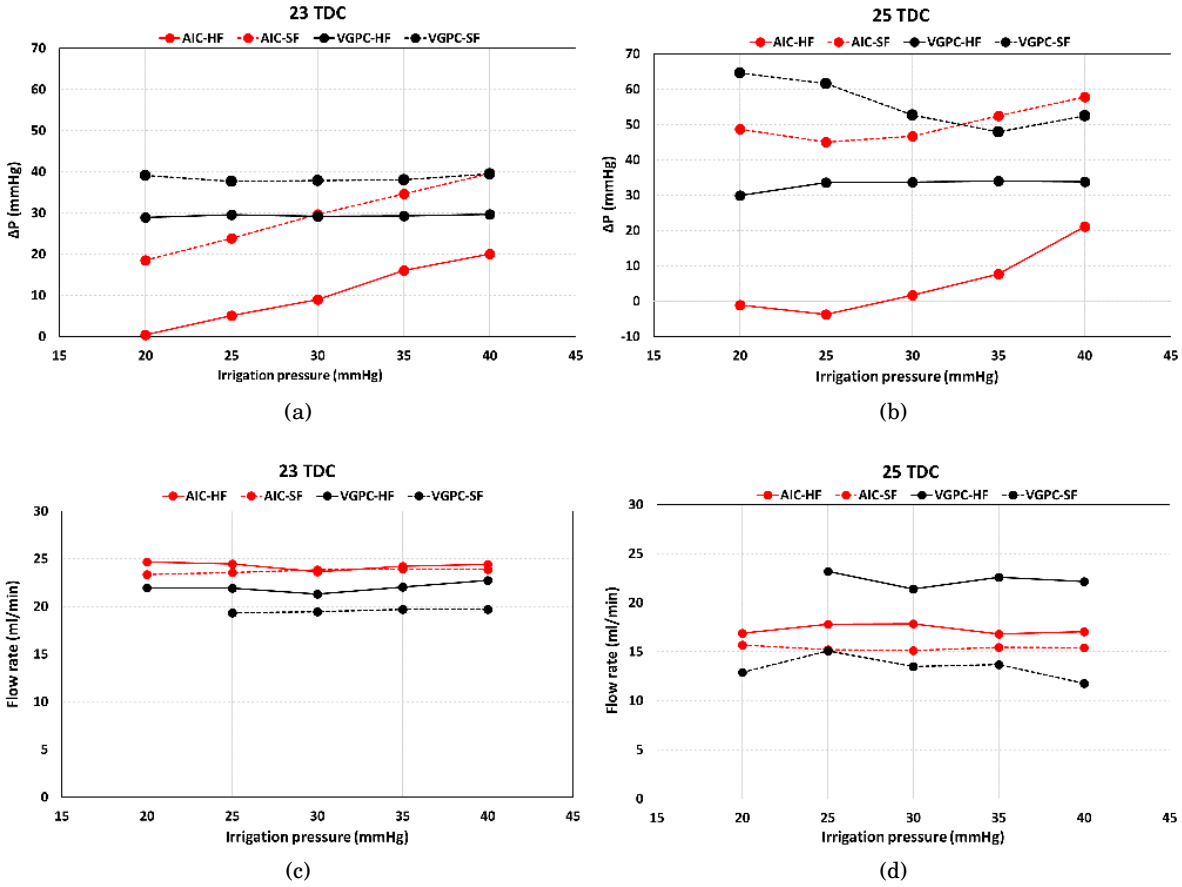

Figure 4.9: Top row: pressures drop, ΔP, defined as the difference between the baseline and the time averaged aspiration pressures, as a function of the imposed irrigation pressure (a) 23TDC cutter, (b) 25TDC cutter. Bottom row: flow rate as a function of the imposed irrigation pressure (c) 23TDC cutter, (d) 25TDC cutter. In all panels: black curves refer to VGPC mode, red curves to AIC mode, solid lines to experiments with HF, dashed lines to experiments with SF.

Moreover, only P1 detected an additional peak (typically at lower frequencies in the case of AV, at higher frequencies with BSS). These features have been found in all experiments and are probably due to the fact that the jet generated in correspondence of the infusion line impinges the chamber wall in its posterior part.

In general, power spectra relative to signals obtained using BSS showed higher values with respect to the signals obtained adopting AV as working fluid; however, this difference decreased with larger infusion pressures imposed (figures 4.11(e,f) and 4.12(e,f)).

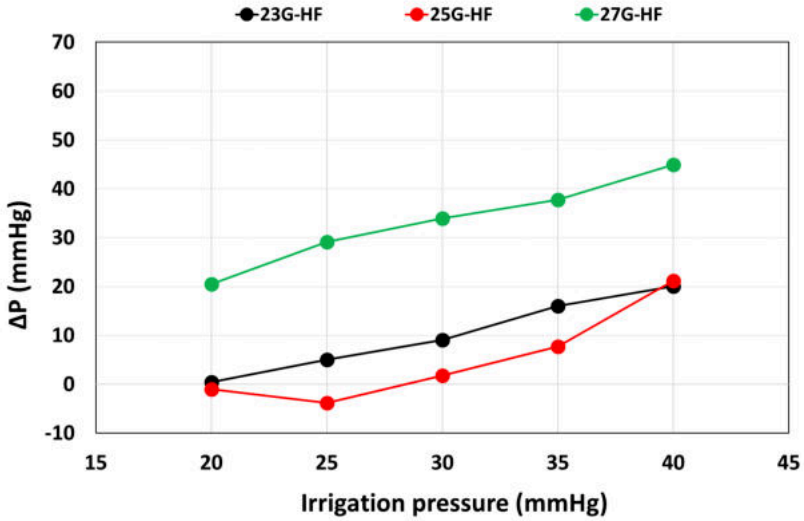

Figure 4.10: Pressures drop in AIC mode, ΔP, defined as the difference between the baseline and the time averaged aspiration pressures, as a function of the imposed irrigation pressure. Colours correspond to different cutter gauge. All experiments have been performed with BSS.

4.3 Discussion

In order to maintain a normal value of IOP during vitectomy, balance between the aspiration and irrigation pressures plays a very important role. Moreover, during surgery the cutter produces high frequency pressure fluctuations and understanding their magnitude and frequency is important for a safe and efficient surgical procedure (Rossi et al., 2014a).

Recent phaco-vitrectomy devices are equipped with pressure compensation systems that actively attempt to limit pressure variations in the eye during surgery. In this context, several experimental studies have been conducted in porcine eyes (Falabella et al., 2016; Kim and Choi, 2012), with the aim of evaluating the efficacy of compensating systems. Many experiments performed with recent vitrectomy devices demonstrated a reduction in pressure drop during surgical maneuvers, with specific imposed operating parameters (Sugiura et al., 2013; Abulon and Buboltz, 2015).

With this study we reproduced the vitrectomy procedure in vitro and evaluated the efficiency of the EVA phaco-vitrectomy system (D.O.R.C) in balancing IOP variations during aspiration. We conducted a series of experiments in a realistic model of the human vitreous chamber. In particular, we considered the presence of the lens in the front of the vitreous chamber, which has a significant influence on the motion of the fluid within the domain (Stocchino et al., 2007; Repetto et al., 2010). We performed pressure measurements at two different locations in the vitreous chamber model, in order to quantify dynamic pressure fluctuations within the domain.

A prerogative of the present study is to properly compare the behaviour of different cutters,

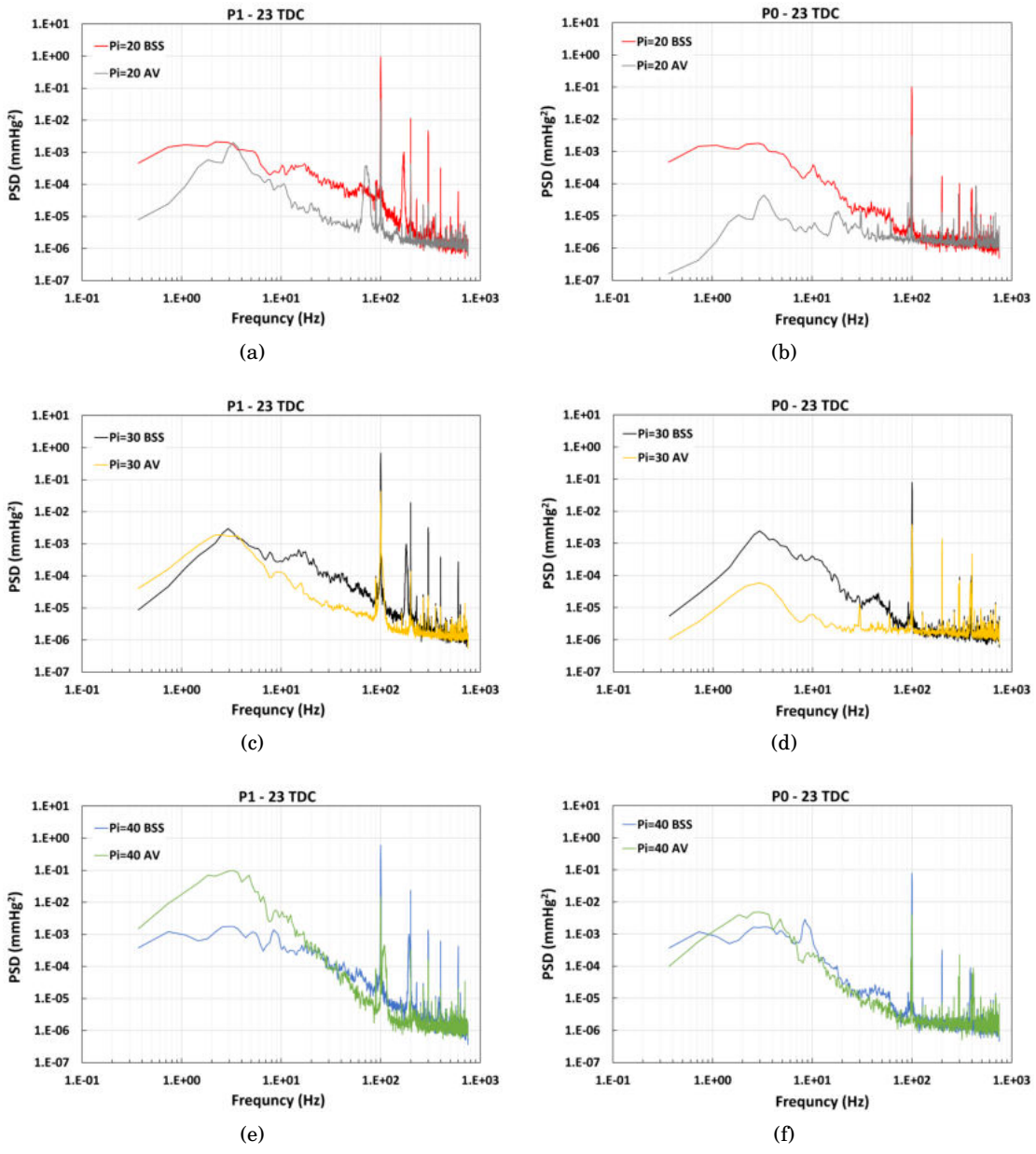

Figure 4.11: Power spectra of the pressure signals for the case of 23TDC cutter. (a),(c),(e) refers to pressure probe located at the anterior position, P1; (b),(d),(f) to pressure probe at the anterior posotion (P0). (a,b) correspond to experiments with an infusion pressure Pi = 20 mmHg, (c,d) Pi = 30 mmHg, (e,f) Pi = 40 mmHg. Each panel show signals obtained with BSS and AV. Cutting frequency: 6000 cpm, corresponding to 100 Hz. AIC mode, HF infusion system.

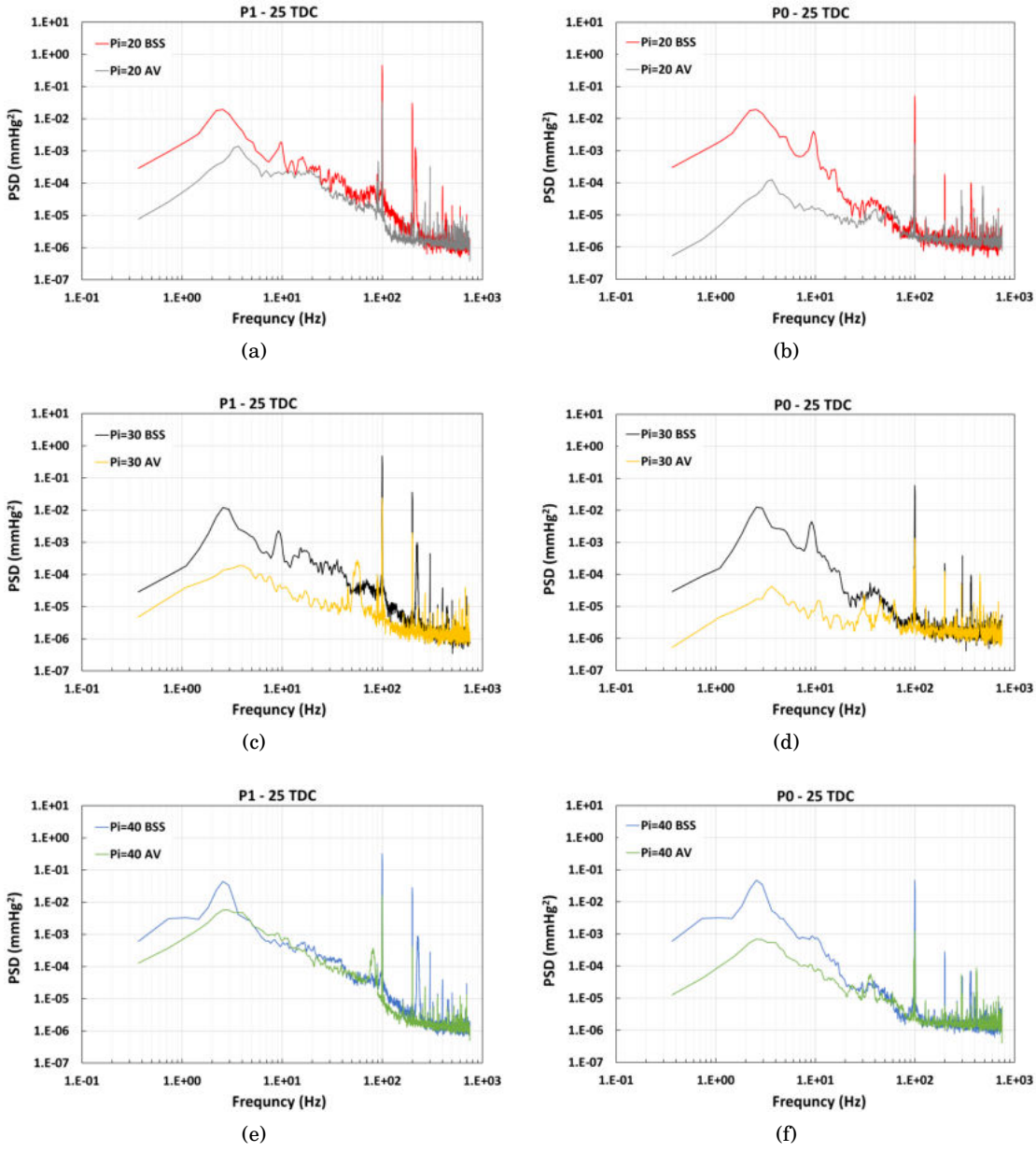

Figure 4.12: Power spectra of the pressure signals for the case of 25TDC cutter. (a),(c),(e) refers to pressure probe located at the anterior position, P1; (b),(d),(f) to pressure probe at the anterior posotion (P0). (a,b) correspond to experiments with an infusion pressure Pi = 20 mmHg, (c,d) Pi = 30 mmHg, (e,f) Pi = 40 mmHg. Each panel show signals obtained with BSS and AV. Cutting frequency: 6000 cpm, corresponding to 100 Hz. AIC mode, HF infusion system.

used in a variety of conditions, but always operating in the same controlled environment. For this reason, as in the previous chapters, we used an AV. In particular, we have prepared solutions of Agar-agar powder in BSS with a different approach from that proposed in the literature (Kummer et al., 2007). The resulting material has rheological properties very similar to those of the real vitreous.

When the aspiration phase begins, the pressure in the eye model experiences a drop, due to hydraulic head losses along the pipelines of the system. This pressure drop is typically reduced in AIC mode, i.e when EVA can actively compensate pressure variations. Results with AV demonstrated that 23TDC cutter is able to better compensate pressure variations during aspiration with respect to 25TDC cutter. However, with a minimum imposed irrigation pressure of 30 mmHg in AIC mode, the EVA system was capable to efficiently re-establish the baseline pressure with both cutter gauges. During aspiration in AV, the pressure in the eye model was found to progressively decrease due to changes in rheological properties induced by the fact that the infusion fluid was BSS and was thus different from the AV which initially filled the chamber.

Since vitrectomy is often conducted on elderly patients, whose vitreous is typically extensively liquefied (Sebag, 1987), we also performed a series of experiments with only BSS, with the aim to compare results obtained with fluids with different rheological properties. In this case, we found average pressure jump (ΔP) values larger than with those obtained with AV, especially using the 23TDC cutter or imposing high value of irrigation pressure. Moreover, in some cases compensation may lead to a significant pressure increase in the eye model, which is an undesirable effect. This is found, for example, when the largest cutters are used in AV with a low value of minimum infusion pressure imposed, resulting in negative values of ΔP. These results suggest that the maximum pressure imposed in AIC mode (i.e. the maximum irrigation pressure that can be used for compensating pressure looses during aspiration) should be selected depending on several parameters such as the minimum irrigation pressure, rheological properties and aspiration pressure, in order to optimise the desired compensation. In this respect, a direct assessment of pressure changes during vitreoretinal surgery would be useful (Rossi et al., 2014d).

Dynamic variations of the pressure due to the motion of the cutter blade have been measured and always found to be small compared with the avarage pressure in the eye model. However, inspection of the pressure signals, shows that the amplitude of pressure fluctuations is larger at the back pole than in the front region of the vitreous chamber model. This observation means that the posterior pressure probe is more affected by the flow than the anterior one, in agreement with previous studies (Dal Vecchio et al., 2017). Translated to the surgical practice, this last finding suggests to the surgeon to be aware that the pressure due to flow from the irrigation line, could favor a focal chorioretinal damage (Hirata et al., 2000).

In general, with both BSS and AV, when the 25TDC cutter is used, the pressure experiences large amplitude oscillations ($\approx$ 50 mmHg) on a time scale much shorter than that associated

with cutting, in agreement with what observed by Falabella et al. (2016) in porcine eyes.

Finally, we also carried out flow rate experiments during aspiration with BSS, with the aim to compare the performance of HF and SF connections for the irrigation line. Purpose of the HF configuration is to maximise the aspiration flow rate, as the infusion line is connected to the external part of the trocar, thus exploiting the entire section of the pipe. HF infusion system demonstrated to be more efficient in terms of flow rate with values up to 3 ml/min and 8 ml/min more than the SF configuration, in AIC and VGPC mode respectively. The achieved flow rate values with HF connection result to be almost double compared to what found in previous studies with a different vitrectomy device (Abulon and Buboltz, 2015). Moreover, when the HF configuration was used, smaller values of $|\Delta P|$ were found with respect to SF connection, for the same operating conditions.

4.4 Conclusions

Dynamic pressure variations during vitrectomy maneuvers in a real scale model of the vitreous chamber have been investigated and quantified. In order to ensure repeatability of the experiments, an AV has been adopted. The rheological characterisation of the AV showed viscoelastic properties comparable to those of the human vitreous. The pressure drop occurring as aspiration generates flow, is typically reduced in Automatic Infusion Compensation (AIC) mode. In particular, our results demonstrated that, with imposed minimum and maximum irrigation pressures of 30 and 55 mmHg respectively, pressure drop is totally compensated when both 23 and 25TDC cutters are used. The irrigation jet appears to have a greater impact on the pressure sensor placed on the back of the vitreous chamber (corresponding to the retina position); however, fluctuations due to the motion of the cutter blade remain small compared to the average pressure in the eye.

Results of the experiments performed with EVA High Flow (HF) connection for infusion system showed that the HF optimises the aspiration flow rate, resulting in much lower ΔP values than the corresponding value obtained with the Standard Flow one.

Part II

Study of silicone oil emulsification in relation to vitrectomy

"Nothing in life is to be feared, it is only to be understood."

– Marie Curie

CHAPTER 5

FACTORS INFLUENCING SO EMULSIFICATION AFTER VITRECTOMY

This chapter is based on the manuscript of Romano et al., accepted for publication, which Irene Nepita co-authored.

Emulsification of SO is the process by which small oil droplets are generated by the breakdown of the original SO drop, resulting to be dispersed in the aqueous phase. When, after vitrectomy, SO is injected in the eye, the filling of the vitreous chamber is never complete (a filling of 90% is considered satisfactory) and a pocket of aqueous phase is invariably present and forms an interface with the SO. The shape of such an interface, which determines the amount of retinal area that is effectively tamponated by the SO, depends on the contact angle at the triple line between SO, aqueous phase and the retinal wall, on the interfacial tension (IT), on fluid densities and on the degree of filling and the geometry of the vitreous chamber.

Eames et al. (2010) performed ex vivo experiments and theoretical calculations and produced curves of retinal coverage as a function of the SO volume, modeling the vitreous chamber as a sphere. Isakova et al. (2017) obtained similar curves numerically, for the case of realistic shapes of emmetropic and myopic eyes and showed that, for a given filling ratio, the percentage of tamponated retinal surface area is smaller in myopic eyes. The contact angle was measured by Fawcett et al. (1994) on ex vivo retinal samples in an aqueous environment of phosphate-buffered saline and the authors found a value of 18.2°. Similar values have obtained by Eames et al. (2010), who used an acrylic eye model, soaked with a 30% solution of bovine serum albumin (BSA) to simulate the wetting properties of retinal tissue. They found that the contact angle ranges from 16° to 20°, depending on the SO considered (Eames et al., 2010).

Once an interface between SO and aqueous solution forms in the vitreous chamber, the tendency of SO to emulsify is influenced by the chemico-physical properties of the interface and of the bulk, and by external factors, such as temperature and mechanical energy provided to

the system. Several clinical studies have investigated the conditions leading to the formation of an emulsion in the eye and it is generally believed that shear stresses at the tamponade fluid-aqueous interface generated during eye rotations, plays a crucial role on the generation of the interface instability (Chan et al., 2011, 2015). Fluid dynamics in the vitreous chamber produced by eye rotations has been studied by various authors, with numerical models (Abouali et al., 2012; Modarreszadeh and Abouali, 2014; Repetto, 2006; Repetto et al., 2010; Silva et al., 2020), experimental approaches (Bonfiglio et al., 2013; Repetto et al., 2005; Stocchino et al., 2007), and in vivo measurements (Piccirelli et al., 2012; Rossi et al., 2012) demonstrating that the flow field induced by eye rotations has a complicated three-dimensional structure. Motion in the presence of a partially liquefied vitreous has also been recently studied with numerical techniques (Bayat et al., 2019, 2020). The motion of SO partially filling a model of the vitreous chamber was investigated in a series of works by Chan and co-workers (Chan et al., 2014a,b). Isakova et al. (2014) used a theoretical approach to investigate the mechanisms relating shear flow generated by eye rotations with the breakdown of the SO aqueous interface.

The formation of SO emulsions in aqueous solutions has been extensively studied, using various different emulsification techniques, such as vortex, orifice homogenisers and sonication (Caramoy et al., 2010; Nakamura et al., 1990). These researches were primarily intended to assess the role of SO properties on its tendency to emulsify. Among bulk chemico-physical properties, viscosity has been shown to play a particularly significant role. Several studies demonstrated that increasing SO viscosity has a stabilizing effect on the interface with water, essentially because highly viscous oils are less capable of flowing in the vitreous chamber than low viscosity fluids (Chan et al., 2014b; Heidenkummer et al., 1992). However, if on one hand a large viscosity is associated with a lower tendency to develop an emulsion, on the other hand it makes it very difficult to inject and remove the oil from the eye. In that respect, some studies have been specifically aimed at identifying optimal viscosity ranges for SO to be used during vitrectomy (Crisp et al., 1987; de Juan Jr et al., 1985; Williams et al., 2011).

Encircling bands, used for retinal detachment repair, have also been observed to reduce the tendency of emulsification of the SO, again owing to the fact that the indentation produced by the band reduces the mobility of the fluids in the eye (Chan et al., 2014a; De Silva et al., 2005).

Recently Wang et al. (2020) published an interesting study, in which they tried to produce emulsions in a spherical model of the vitreous chamber subjected to a sequence of saccadic rotations. The authors used various SOs with different properties and saline solutions, with the addiction of surfactant molecules (such as albumin and Triton X-100). The eye model was set in motion for several minutes and the interface between the two liquids was monitored with a camera. Interestingly, the authors never observed the formation of a bulk emulsion, even when the IT was quite small, owing to the presence of surface active molecules. However, in some cases, they observed the formation of small droplets in correspondence of the moving triple line of contact between the interface and the solid wall (Wang et al. 2020). Thus, they concluded, that

droplet formation driven by a surface emulsification mechanism might be more relevant than bulk emulsification in the eye.

Francis et al. (2007) showed with laboratory experiments that also the energy from surgical handpieces could be sufficient to produce SO emulsification.

5.1 The effect of molecule adsorption on SO interfacial properties

Exposition of SO in the vitreous chamber to endogenous molecules (proteins, lipids, etc.), the presence of which is favored by the post-surgery inflammatory state of ocular tissues, has been shown to be relevant for SO emulsification. Bartov et al. (1992) demonstrated that various blood constituents, such as lymphocytes, plasma, red blood cells and hemoglobin, act as emulsifiers for SO when dissolved in aqueous solution. Heidenkummer et al. (1991) characterised various SOs with specific physicochemical properties in terms of their rate of emulsification. The authors added biomolecules to the system and, in particular, used 0.1% solutions of fibrinogen, fibrin, γ-globulins, acidic alpha-l-glycoprotein and serum dissolved in sterile, distilled water as well as in balanced salt solution (Heidenkummer et al., 1991). The group of low-viscosity SOs (1000 mPa·s) was the least stable. The authors found that the most effective emulsifiers were fibrinogen, fibrin and serum, followed by γ-globulins (Heidenkummer et al., 1991). Emulsions obtained by sonicating and centrifuging mixtures of SO and saline solutions containing various blood components were investigated by Savion et al. (1996), who found that red blood cell membranes, plasma lipoproteins and purified HDL-apolipoproteins favored SO emulsification. These observations clearly demonstrate the capability of several biomolecules to act as surfactants, adsorbing at the water-oil interface. In fact, a large number of studies exists, concerned with adsorption of proteins (e.g. albumin, lacto-globulins) at water-oil interfaces, relevant for food emulsions (Maldonado-Valderrama et al., 2008; Saito et al., 2006; Sarkar et al., 2009). Multiprotein adsorption studies have also been performed, providing new insight into the role of protein-protein interactions (Fang and Szleifer, 2003; Kubiak-Ossowska and Mulheran, 2011).

Owing to the importance of adsorption processes of endogenous molecules for the generation of emulsions, it is of great relevance to understand how such molecules modify the properties of the SO-aqueous interface, such as the interfacial tension (IT) and the dilational viscoelasticity (DV), i.e the dynamic response of the IT to perturbation of the interfacial area. In fact, these properties are primary concerned with emulsion formation and stability (Ravera et al., 2021). In the absence of surfactant molecules, the IT of the SO-water system at equilibrium are reported to range between 35 and 42 mN/m, depending on the specific SO composition. These values, however, are somehow irrelevant for the emulsification problem since, in realistic conditions, the IT is dramatically affected by the adsorption at the interface of the endogenous surfactants. These effects have been explicitly investigated only in a few studies. Nakamura et al. (1990) reported an IT value, measured at 37°C, of about 16 mN/m between SO (1000 mPa·s) and liquefied bovine vitreous, which is significantly lower compared with the IT between SO and water. In addition,

they found that the IT value of SO against intraocular fluids was less than half of that against distilled water and still lower after the oils were put in contact with retinal tissue specimens for 24 hours (≈ 12.6 mN/m) (Nakamura et al., 1990). DV is also crucial to understand the mechanisms leading to an emulsion and its stability once formed (Ivanov and Kralchevsky, 1997; Langevin, 2000; Liggieri and Miller, 2010).

Besides biomolecules, other types of molecules can adsorb and modify SO interfacial properties. Despite purification and ultrapurification processes, a variable content of low molecular weight components (LMWC) can be still detected in purified SOs and these compounds are known to act as surfactants (Januschowski et al., 2018). Moreover, comparing solutions of buffer, human serum albumin (HSA) and SOs of different composition, SOs with greater concentrations of LMW silicones have been associated with the increase of both protein denaturation/aggregation and SO-in water emulsions (Nayef et al., 2015). Dresp and Menz (2004) investigated the effect of detergent contamination on a ready-to-use standard set of vitrectomy instruments. Their conclusion was that, in case of reusable instruments, remnants of cleaning substances or of the sterilization process, can increase the risk of emulsification of SO, due to a significant decrease of the IT value.

5.2 THE ROLE OF EMULSION DROPLETS DIMENSION IN OCULAR COMPLICATIONS

SOs emulsification and inflammation appear to have a crucial role on complications affecting nearly all ocular structures. Complications can include corneal decompensation, band keratopathy, acute and chronic changes in IOP, lens opacities, epiretinal membrane, retinopathy, optic neuropathy and extraocular extension (Heidenkummer et al., 1991). A role of SO emulsification has been speculated in many of the pathogenetic mechanisms, such as sequestration of emulsified SO in the retina and optic nerve with consequent structural damage (Wickham et al., 2007), emulsified SO tissue infiltration causing neuronal cell loss (Newsom et al., 2004) or, alternatively, a mechanical vascular obstruction with consequent retinal hypoxia (Lou et al., 2015).

Emulsification and inflammation appear to have a crucial role also on IOP increase and glaucoma (Ichhpujani et al., 2009). Secondary glaucoma is a complication in which emulsified SO droplets, if sufficiently small, migrate into the anterior chamber of the eye inducing both inflammation and mechanical obstruction of the trabecular meshwork, thus compromising aqueous humor outflow (Ichhpujani et al., 2009). The reported incidence of secondary glaucoma due to SO ranges from 11% to 56% (Al-Jazzaf et al., 2005; de Corral et al., 1987; Honavar et al., 1999). Ocular hypertension secondary to SO tamponade varies from early, usually transient, postoperative IOP rise to long-term ocular hypertension, with intermediate or late onset, potentially impairing visual function (Ichhpujani et al., 2009; Wagenfeld et al., 2010).

It has been hypothesised that chemotaxis of inflammatory cells and foreign body inflammatory reaction can be triggered by SO microemulsion, phagocytosed by macrophages and retinal pigment epithelium cells (Semeraro et al., 2019). This inflammation, in turn, further stimulates

SO emulsification (Kociok et al., 2005), starting a vicious circle in which emulsification and intraocular inflammation stimulate each other (Semeraro et al., 2019). Moreover, it has been reported that SO droplets induce a granulomatous foreign-body reaction with the presence of epithelioid cells (de Queiroz Jr et al., 1992; Morescalchi et al., 2014; Wong et al., 2009). Persistent IOP elevation may be explained by small remaining emulsified oil droplets continuing to obstruct the trabecular meshwork or by persistent inflammation (Ichhpujani et al., 2009). The sustained elevated IOP can result in a glaucomatous optic neuropathy; moreover, a direct toxic effect of SO droplets migrated in the retrolaminar optic nerve has been suggested to contribute to the development of SO-related neuropathy (Romano et al., 2010).

Emulsified SO droplets migrated to the anterior chamber can play a role also in SO-related keratopathy, as the presumed mechanism of this complication is the direct contact between SO and the corneal endothelium (Miller et al., 2014). This occurs mainly in aphakic eyes and characterised by a decrease of endothelial cell density, retrocorneal membrane, attenuated endothelial cell borders, stromal hypercellularity and calcification and vascularisation of the superficial stroma (Foulks et al., 1991; Miller et al., 2014; Sternberg et al., 1985).

Emulsified SO can also cause retinopathy, which is becoming more evident with new imaging techniques. Until the introduction of Optical Coherence Tomography (OCT), there was no way to assess the presence of emulsified SO within the retina and optic nerve in vivo. Using OCT, it is possible to identify SO droplets within the retina after macular hole surgery with SO tamponade (Chung and Spaide, 2003). More recently, there have been additional studies of SO infiltration within the retina and optic nerve head using swept-source OCT and adaptive optics (Errera et al., 2013; Mrejen et al., 2014).

Studies using spectral-domain OCT (SD-OCT) have shown hyper-reflective spherical bodies underneath epiretinal membranes, within the retina and in the subretinal space (Errera et al., 2013; Odrobina and Laudańska-Olszewska, 2014). The proposed mechanisms include iatrogenic defects that may increase the ability of emulsified oil to penetrate retinal tissues or retinal breaks, in turn allowing migration into the subretinal space (Chung and Spaide, 2003). In a study of 24 eyes that underwent vitrectomy with SO for retinal detachment, SD-OCT performed 3 months after surgery showed emulsified oil in intraretinal cystoid spaces in five eyes (21%) and between the hyper-reflective line of SO and the optic disc in one eye (4%) (Odrobina and Laudańska-Olszewska, 2014). The long-term impact of emulsified SO in these locations is unknown.

CHAPTER 6

FUNDAMENTALS OF INTERFACIAL RHEOLOGY AND EMULSIONS

In its general meaning, interfacial rheology is the study of surface modification induced by mechanical forces, like shear or dilational stress. If we consider the presence of more fluids, their molecules can be mixed or separated from surfaces that refer to fluid interfaces. In order to account for the presence of interfaces, it is important to understand which physico-chemical phenomena have to be introduced in the continuum description of fluids.

6.1 INTERFACIAL TENSION AND YOUNG-LAPLACE EQUATION

Let us consider the interface between two immiscible fluids.

Microscopically, liquids are constituted of molecules interacting through forces (cohesion forces), mainly of electrical origin. A molecule inside the liquid is attracted to all the other molecules surrounding it so that, the net resulting force is vanishing. Moreover a molecule close to the interface suffers a normal force, so it is balanced by the resistance of the liquid to compression (figure 6.1), due to the existence of the interface and thus, to the unbalance of molecular forces acting on particles very close to the interface.

Surface molecules try to minimise the surface area of the liquid to bring them to a lower energy state, so they tend to collapse their surface area to achieve the lowest surface area possible, resulting a curve surface. This phenomenon occurs since the cohesive forces form a net tangential force on the surface, the interfacial tension (IT), which leads the surface of the liquid itself to assume the characteristics of an elastic membrane. The IT, γ, is positive (traction force on the surface) or negative (compression force on the surface); IT can also be theoretically predicted, referring to the transient interface between miscible liquids.

Because of the existence of the IT, there will be a tendency to curve the interface, as a consequence of which there must be a pressure difference across the interface with the highest

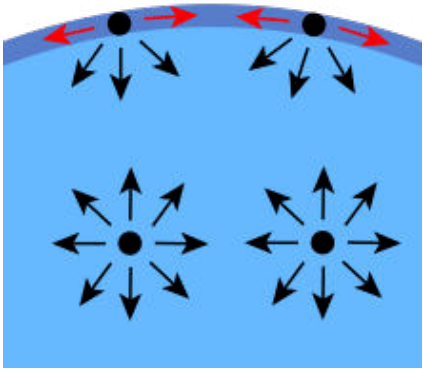

Figure 6.1: Sketch of the intermolecular forces acting at the surface and in the bulk phase.

pressure on the concave side. The expression relating this pressure difference to the curvature of the interface is referred to as the Young-Laplace equation

$$\Delta P = \gamma\left(\frac{1}{R_1}+\frac{1}{R_2}\right), \tag{6.1}$$

where R_1 and R_2 are the principal radii of curvature of the surface, and ΔP is the difference in fluid pressure across the curved interface.

This equation is applicable to arbitrarily shaped surfaces where the radii of curvature may change spatially. Moreover, this formula is consistent with the fact that in stable equilibrium the energy of the surface must be a minimum for a drop volume. Obviously for a plane interface, where the mean radius tends to infinity, the pressure difference will be zero.

6.1.1 THE THERMODYNAMIC DEFINITION OF THE IT

In a classical equivalent thermodynamic approach, the IT is directly proportional to the mechanical work needed to create a new interface.

Let us consider a generic surface with unitary perimeter, with an infinitesimal variation dx, in the perpendicular direction to the surface area A, produced by the force F per unith length: the work, W, performed by the system to accomplish this dilation is given by

$$\delta W = F dx = -\gamma dA. \tag{6.2}$$

This expression provides an alternative view of IT for pure liquids, such as the work required to vary the surface of a unitary area quantity. In this case, γ is a surface energy and dimensionally equivalent to the definition of a force per unit of length.

For now the IT has been related to a mechanical work, the thermodynamic connection is obtained using the first principle and the Gibbs free energy function (Gibbs, 1906):

$$dG = -SdT + VdP + \gamma dA, \tag{6.3}$$

where S, T, V and P are the entropy, temperature, volume and pressure of the system respectively. From this relation the IT can be defined as the variation of Gibbs free energy, G, related to the formation of new interface. At constant temperature and pressure, γ is in fact given by

$$\gamma = \left(\frac{dG}{dA}\right)_{T,P}. \tag{6.4}$$

The mechanical definition is more general than the thermodynamic one because the latter applies only to reversible changes of area, namely, to equilibrium conditions, whereas the mechanical interpretation in terms of equation 6.1 does not required thermodynamic equilibrium.

Providing kinetic energy to a biphasic system, the Gibbs free energy varies so that the dispersed phase, for example a macro-drop of oil, is broken into smaller droplets, thus favoring emulsification. Since the variation of free energy is a positive quantity, it can be said that emulsification is a non-spontaneous process. This also means that emulsions are thermodynamically unstable therefore, they tend to separate. Such separation can be however contrasted and slowed down by the presence of surfactant layers, that in fact inroduces new terms in the expression of the Gibbs free energy.

6.2 SURFACTANTS

Surfactants are substances that have the property of lowering the IT of a liquid, facilitating surface wettability or miscibility between different liquids, and thereby changing the amount of work required to create new interface. Generally, they are organic compounds with a polar head (hydroxyl, carboxyl, ionic groups) and non-polar tail which have affinity with non-polar solvents and contain hydrocarbon chains. Figure (6.2) shows the structure of some common surfactants composed by a hydrophilic “head" to which a hydrophobic “tail" is bound. This dual physicochemical nature, known as anphiphilicity, is responsible for the surfactant surface activity.

For these chemicals, the equilibrium configuration is reached after their spontaneous accumulation at the interface, where, in fact, they can maximise their interaction with the two liquid phases and therefore, minimise the Gibbs energy for the system. This results in a dramatic change of the value of the IT compared to that of pure liquid, by the formation of a monomolecular layer at the interface (figure 6.3). Commonly it is saied that surfactant molecules “adsorb" at the interface.

Surfactants are generally classified according to the polarity of their hydrophilic heads as follow:

- *non-ionic surfactants* (e.g. polyethenoxy and polyhydroxy surfactants);

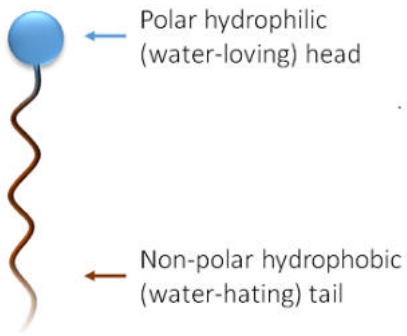

Figure 6.2: Surfactant molecule.

- *ionic surfactants*, which can be distinguished in anionic surfactants, contain anionic functional groups at their head (such as sulfonate, phosphate, sulfate and carboxylates) and cationic surfactants (e.g. fatty nitriles and amines), wich are comprised of a positively charged head;

- *zwitterionic* (amphoteric) surfactants have both cationic and anionic centers attached to the same molecule. Zwitterionic are often sensitive to pH and the anionic part can be variable and include sulfonates.

Surfactants are molecules which possess two fundamental properties:

- on the one hand they tend to be located preferentially at the interface between a polar and an apolar phase. The phenomenon according to which a molecule migrates from the bulk of a solution to place itself at the interface (with some specific orientation) is called adsorption.

- On the other hand surfactant molecules in solution, at relatively high concentrations, exhibit a tendency to self associate to produce aggregates called micelles, as well as other structures.

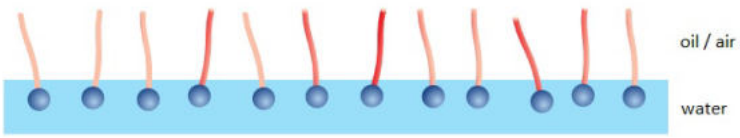

Figure 6.3: Surfactant adsorption at the fluid interface: the surfactant molecules form a monomolecular layer with the polar heads oriented to the aqueous solution.

In fact when numerous surfactants achieve a certain critical concentration level, called *micellar critical concentration* (cmc), they organised themselves in supramolecular aggregates. Typical micelles in aqueous solution form an aggregate with the hydrophilic head regions in contact with the surrounding solvent, with the hydrophobic tail regions in the micelle centre. This type of micelle is known as a normal micelle. Reverse micelles have the headgroups at the centre with the tails extending out.

Micelles can be spherical or have more complex shapes, such as ellipsoids, cylinders, and bilayers. The shape and size of a micelle is a function of the molecular geometry of its surfactant molecules and solution conditions such as surfactant concentration, temperature, pH, and ionic strength. The process of forming micelle is known as micellisation.

6.2.1 Adsorption phenomenon and equilibrium IT

A surfactant molecule attains a minimum energy configuration when it is located at the interface between the polar and non-polar phases. Surfactant molecules migrate (adsorb) spontaneously at the interface, determining an interfacial surfactant excess and resulting in a dramatic decrease of the value of the IT, as compared to that of the pure liquid (Heimann et al., 2008). The excess of surfactant molecules at the interface, usually expressed as the amount of surfactant molecules per unit interfacial area, A, is denoted as *Adsorption* (Defay et al., 1966) and defined as

$$\Gamma_i = \frac{n_i^\gamma}{A}, \tag{6.5}$$

where $n_i^\gamma = n_i - c_{i,1}V_1 - c_{i,2}V_2$ is the surface excess of surfactant molecules, n_i is the total number of moles of components i contained in the system, and the distinction with the numbers 1 and 2 denotes the the two fluid phases (with V their volume and c their surfactant concentration).

Gibbs'approach allows to treat the adsorption process as an equilibrium phenomenon, which means having no variation of free energy. Working with a soluble surfactant at constant temperature, which represents the case of interest for our study, the thermodynamic considerations allow one to obtain the Gibbs adsorption equation:

$$d\gamma = -\Gamma_i d\mu_i, \tag{6.6}$$

where $d\gamma$ is the change in IT of the solvent and $d\mu_i$, is the change in chemical potential of the components in the system. Equation (6.6) describes the connection between the surface excess of solute and the IT.

For adsorption from dilute solutions, considering a single surfactant specie, the surface concentration at the interface can be written, omitting some obvious mathematical passages, as follows:

$$\Gamma = -\frac{1}{RT}\left(\frac{\partial\gamma}{\partial ln c}\right)_T, \tag{6.7}$$

where R is the gas constant, T the absolute temperature and c the concentration of surfactant. Therefore, the surface concentrations Γ at the interface may be estimated from the slope of a γ-concentration plot at constant temperature, based on the Gibbs adsorption equation. The relation between γ and Γ is a material property desribed by the surface equation of state

$$\gamma = \gamma(\Gamma), \tag{6.8}$$

which coupled with equation 6.7 provides

$$\gamma = \gamma(c). \tag{6.9}$$

For surfactants soluble in one of the two phases, adsorption depends on surfactant concentration in the bulk and achieves specific values at equilibrium. The equilibrium state of a the interfacial layer in a surfactant solution is therefore described by the three variables, (Γ, γ, c). We can sumarise the relations between Γ, c and γ with the three plots shown in figure (6.4). These plots point out how adsorption increases with the bulk concentration and IT decreases with the adsorption.

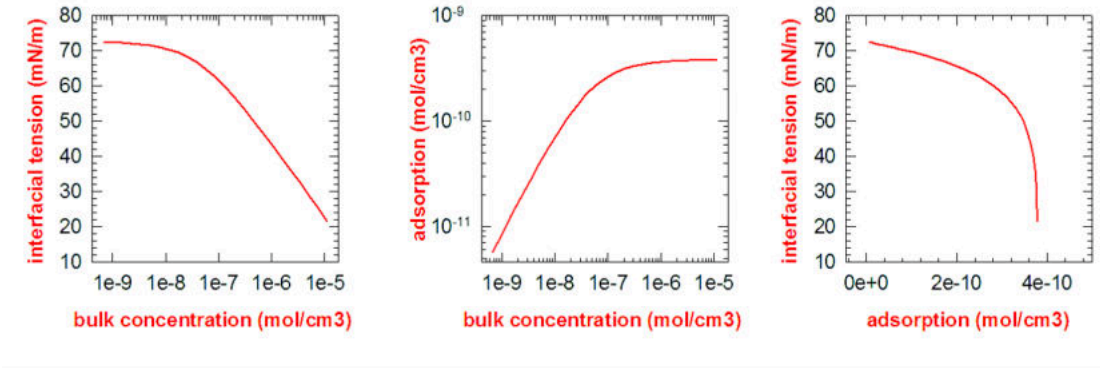

Figure 6.4: Correlations between adsorption, IT, surfactant concentration.

Usually, for single-component surfactants, the equilibrium IT decreases monotonically with increasing surfactant concentration. Moreover above the cmc of the surfactant, monomer activity is essentially constant and under these conditions adsorption also remains constant (Somasundaran and Zhang, 2006), which is manifested as a slope change in the γ-concentration curve as shown in figure (6.5). For concentrations below, but near the cmc, the slope of the curve is essentially constant, indicating that the surface concentration has reached a constant maximum value. In this range the interface achieves the maximum possible adsorption.

In a surfactant solution, the bulk concentration determines the adsorption value, which, in turn, sets the IT value. Owing to the very short characteristic times of the involved microscopic processes, under practical conditions, the equilibrium between IT and adsorption is instanta-

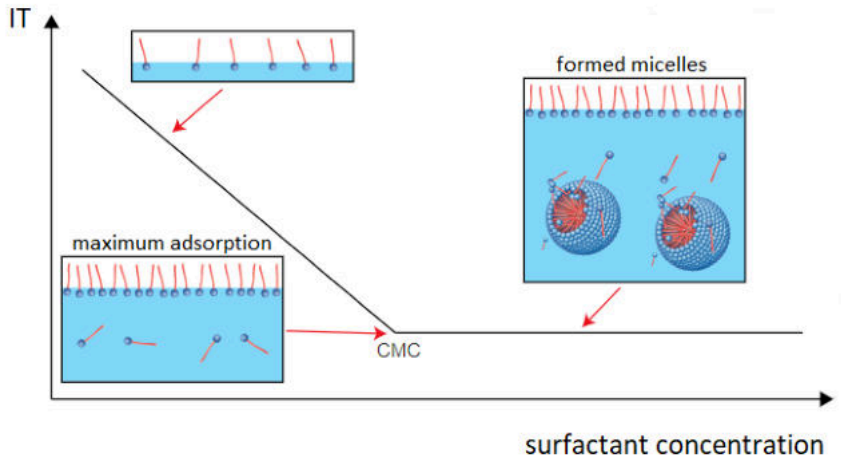

Figure 6.5: IT of a surfactant solution with increasing concentration, formation of micelles.

neously achieved. On the other hand, the equilibrium between bulk concentration and adsorption can be easily perturbed, as occurs, for example, if a new interface of a surfactant solution is suddenly formed, or an existing interface is expanded or contracted. In the former case, an interface with virtually no adsorbed surfactant is created, while in the latter, the already existing adsorbed surfactant is respectively diluted or concentrated. In all these cases equilibrium is restored by time-dependent processes, driven by diffusion of surfactant between the bulk and the interfacial layer and that can also include reorganisations of the surfactant molecules within the interfacial layer. For these interfaces IT is a dynamic quantity, which depends on time through surface composition and in turn on the history of the system.

6.2.2 Dynamic IT

The IT can be considered as a characteristic quantity of each fluid. Let us consider a surface area suddenly created. If one streatches this area at a sufficiently fast rate, the composition of the layer can become identical to that of the bulk. This condition is kept for a characteristic time until diffusion from the bulk to the surface occurs and tends to restore the equilibrium composition, which for solutions is usually quite different from that of bulk (Chen, 1995). If the solution contains surfactants, then it will have a *dynamic IT* which varies as the adsoprtion process progresses.

In particular, in the first phase of surface area formation there will not be an excess of surfactant molecules at the interface and part of the bulk liquid is forced to enter the surface layer: this surface area is defined as zero “age" and will be characterised by a *pure IT*, i.e. the interface is clear of surfactant molecules.

For a surfactant solution this is an out-of-equilibrium condition. Thus the surfactant molecules

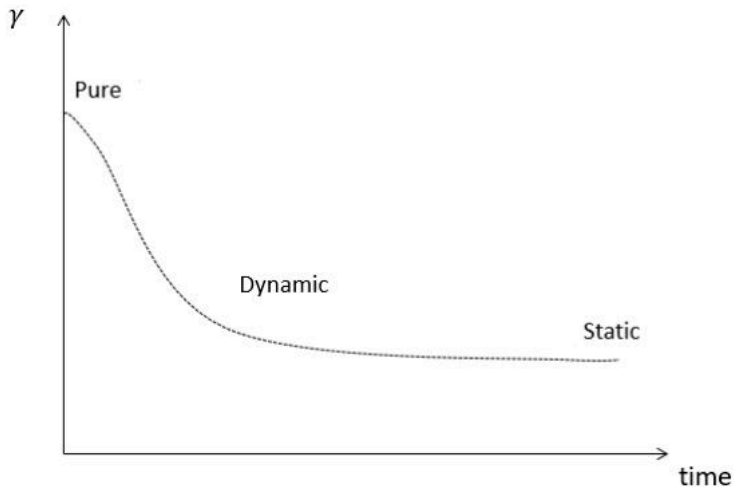

Figure 6.6: Typical evolution of γ of a solution during the ageing of the surface.

adjacent the interface start to adsorb, causing a reduction in the dynamic IT (figure 6.6). Thus immediately after the surface is produced, IT has the same value as the pure liquid, then the value decreases until the equilibrium value is restored. The time required for this depends on the diffusion rate and the adsorption rate of the surfactant.

The dynamic IT is a function of time and surface composition. In the simplest model for solutions of soluble surfactants, the dynamic adsorption behaviour is governed by a two-step process: the first one is an adsorption process and the second step is a bulk mass transfer process.

In the first step surfactants are adsorbed from the solution to the new interface and the concentration decreases in the subsurface: the boundary between the domain in which the diffusion of surfactant molecules in the bulk takes place and the region in which the exchange of surfactant molecules between the bulk and the interface occurs, which has a thickness of a few molecular diameters only (figure 6.7). The depletion of surfactant in the subsurface, triggers surfactant diffusion from the bulk. When diffusion is much slower than the interface-sublayer exchange, adsoprtion is diffusion-controlled. Viceversa, adsoprtion is the controlling step (Hartland, 2004).

However, in some cases, other kinetic processes can occur inside the adsorbed layer, depending on the nature of the surface-active species and of the liquid bulk phases. In fact, in order to understand the dynamic adsorption process at the surface, can be important to take into account molecular surface re-orientation and surface aggregation phenomena, which can occur in particular cases (Ravera et al., 2000).

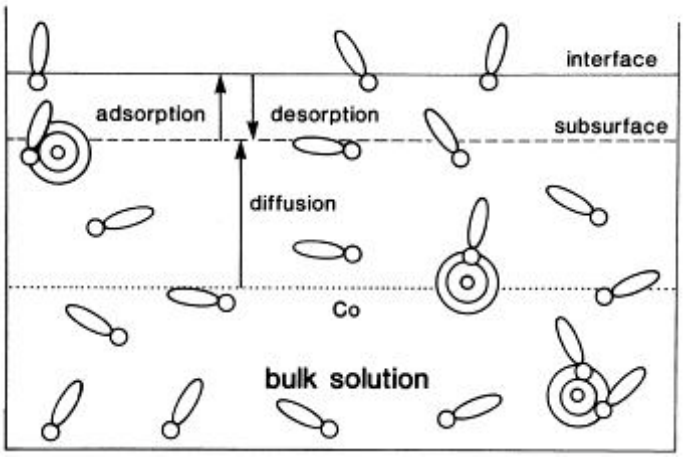

Figure 6.7: A schematic diagram of the dynamic adsorption mechanism.

6.3 DILATIONAL RHEOLOGY

Dilational rheology represents a powerful topic to investigate equilibrium and dynamic properties of interfacial layers containing surfactants.

In the presence of surfactants, IT is a dynamic quantity, which attains an equilibrium value only for interfaces at rest. In fact, in a surfactant solution a thermodynamic equilibrium is established between the concentration of surfactant molecules in the liquid volume and at the interface. When the interface interface area, A, changes in time with respect to an initial value A^0, a variation of the IT, γ, with respect to its initial equilibrium value (γ^0) occurs, which can be interpreted as a dilational stress. Such IT variation can be written as the sum of two terms

$$\Delta\gamma = \mathscr{E}\frac{\Delta A}{A^0} + \eta\frac{d}{dt}\left(\frac{\Delta A}{A^0}\right), \tag{6.10}$$

with $\Delta\gamma = \gamma(t) - \gamma^0$ and $\Delta A = A(t) - A^0$. The coefficients $\mathscr{E}$ and η, are termed dilational surface elasticity and viscosity, respectively.

For the purposes of the present study, it is useful to analyse the response of IT to sinusoidal oscillations of the interfacial area, A, with frequency f and amplitude $\tilde{A}$, around a reference value A^0

$$A - A^0 = \Delta A = \tilde{A}\sin(2\pi f t). \tag{6.11}$$

For small amplitude perturbations, the IT response is linear, thus, the value of γ also oscillates harmonically in time with frequency f, so that

$$\gamma - \gamma^0 = \Delta\gamma = \tilde{\gamma}\sin(2\pi f t + \phi), \tag{6.12}$$

where γ is the actual value of the IT and γ^0 is its equilibrium reference value. The amplitude of IT variations, $\tilde{\gamma}$, and the phase shift, ϕ, between the interfacial area and the IT response, are related to the equilibrium and kinetic characteristics of the adsorption process.

In the case of small amplitude harmonic perturbations of the surface, equation 6.10 can be recasted introducing the complex modulus e which defined complex DV:

$$E = \mathscr{E} + i2\pi f\eta = \frac{\Delta\gamma}{\Delta A/A^0} = \frac{\tilde{\gamma}}{\tilde{A}/A^0}e^{i\phi}. \tag{6.13}$$

E is a frequency dependent complex quantity, where the real part, $E' = \mathscr{E}$, is the dilational elasticity and the imaginary part, $E'' = 2\pi f\eta$, is directly linked to the dilational viscosity (Ravera et al., 2009).

In the case of low forcing frequencies, namely for slow disturbances of the interfacial area, the system has time to adapt. As a result, the variation in IT is almost equal to zero and therefore also the dilational viscoelasticity modulus E. On the contrary, in the case of large forcing frequencies, perturbations of the surface area are very fast and surfactant molecules do not have time to transfer to/from the interface, thus neither adsorption nor desorption occur. Therefore, during the area oscillation, the same number of molecules will be spread on the surface alternatively increasing or decreasing the adsorption and, accordingly, the IT. Under this condition the value of E' attains the largest possible value for the specific chemical system, while the dilational viscosity vanishes.

DV plays an important role in the stabilisation of emulsions against phase separation.

6.4 EMULSIONS PROPERTIES

An emulsion is a stable suspension of droplets of a certain size within a second, immiscible liquid. More complex emulsions are multiple emulsions (Matsumoto et al., 1976), in which the dispersed drops are themselves emulsions. Two immiscible, pure liquids cannot form an emulsion. For a suspension of one liquid in another to be stable enough to be classified as an emulsion, a third component must be present to stabilise the system. The third component is called the emulsifying agent. The most effective emulsifying agents are usually mixtures of two or more substances.

The present work focuses on ordinary emulsions, or *macroemulsions*, which can be of two types, based on the nature of the dispersed phase: oil-in-water (O/W) and water-in-oil (W/O). The oil is, in this case, the discontinuous (inner) phase; the aqueous phase is the continuous (outer) phase. The W/O type is a dispersion of water or an aqueous solution (W) in a water-immiscible liquid (O). The type of emulsion formed by the water and the oil depends primarily on the nature of the emulsifying agent and, to some extent, on the process used in preparing the emulsion and the relative proportions of oil and water present. In general, O/W emulsions are produced by emulsifying agents that are more soluble in the water than in the oil phase, whereas W/O emulsions are produced by emulsifying agents that are more soluble in the oil than in the water

phase. This is known as the Bancroft rule (Bancroft, 1913). One type is usually inherently more stable than the other for a particular emulsifying agent at a given concentration under a given set of conditions. In the formation of macroemulsions, one of the two immiscible liquids is broken up into droplets that are dispersed in the second liquid. Since the IT between two immiscible pure liquids is always greater than zero, this dispersion of the inner liquid, which produces a big increase in the area of the interface between them, results in a correspondingly large increase in the interfacial free energy of the system. The emulsion produced is consequently highly unstable thermodynamically relative to the two bulk phases separated by a minimum area interface. It is for this reason that two immiscible liquids, when pure, cannot form an emulsion. The function of the emulsifying agent is to stabilise this basically unstable system for a sufficient time so that it can perform some function. Thus the emulsifying agent acts by adsorption at the liquid-liquid interface as an oriented interfacial film. This oriented film performs two functions: it reduces the IT between the two liquids and consequently the thermodynamic instability of the system resulting from the increase in the interfacial area between the two phases; it decreases the rate of coalescence of the dispersed liquid droplets by forming mechanical, steric, and/or electrical barriers around them. Steric and electrical barriers inhibit the close approach of one drop to another. The mechanical barrier increases the resistance of the dispersed droplets to mechanical shock and prevents them from coalescing when they do collide. In the formation of macroemulsions, the reduction of IT reduces the amount of mechanical work required to break the inner phase into dispersed drops.

6.4.1 EMULSIFICATION

Emulsion formation, is in principle related to the adsorption kinetics of surfactant molecules. Indeed, when droplets are formed by whathever method, a large surface area is created, free of surfactant. After some time, the surfactant molecules adsorb from the bulk solution, the air/water or O/W interfaces retarding the de-emulsification mechanisms. When the emulsion is formed, the interfaces are stretched rapidly and ruptured in different flow conditions according to the method used. At large, the mechanical energy supplied to the system, together with the amount of surfactant, determines the droplets size. Different types of flow lead to different rupture mechanisms. For instance, in an extensional flow, one drop can be strongly elongated and then ruptured into several smaller droplets after a Rayleigh type of instability. This process leads to more monodisperse droplets than with the simpler rupture of a drop in a shear flow. Surface rheology also plays an important role: the energy used during the emulsification process is smaller if the surface elasticity is small. However, if the elasticity is decreased, coalescence is favored and a compromise needs to be found. Obviously, a third requirement for efficient emulsification is to achieve good foam and emulsion stability. Otherwise, the emulsion can partially destabilise during the process, and larger droplets will be obtained. In the case of emulsions, one obtains less monodisperse populations of droplets when partial coalescence occurs during

the emulsification process.

6.4.2 EMULSION DESTABILISATION

After formation, an emulsion can separate again in the liquids forming it, under the effect of four major processes: coalescence, creaming (or sedimentation), flocculation and Ostwald ripening.

Coalescence

Coalescence is the process in which two or more emulsion drops fuse together to form a single larger drop, and is irreversible. For coalescence to occur, the forces between the drop surfaces must be such that the film of continuous phase separating them can become sufficiently thin that film rupture becomes a likely possibility. The film thinning stage depends on the hydrodynamics of film flow and on the forces acting across the film, whilst film rupture depends on fluctuations in film thickness and on the mechanical properties of the film.

For two large emulsion drops approaching each other, when the distance between them is less than 1 μm, their interfaces interact and begin to deform (Ivanov, 1980). In the final stage, a plane-parallel thin film is formed. The rate of thinning of this film and its stability against rupture are among the main factors determining the overall stability of the emulsion. In the present study, the mechanism involved in the stabilisation of a macroemulsion is due to the so-called Marangoni effect. If we consider two approaching droplets, as shown in figure 6.8, in the

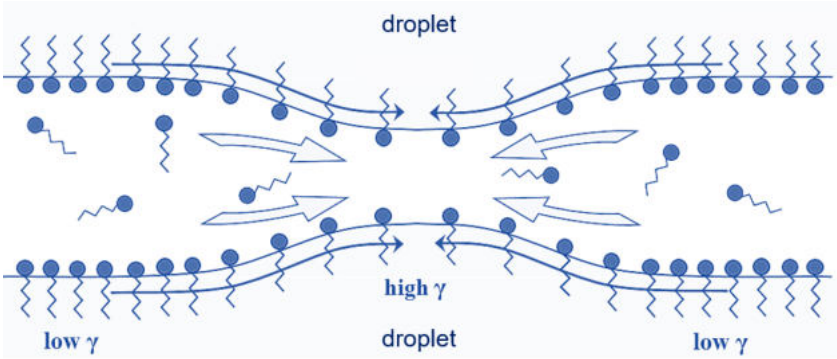

Figure 6.8: Inhibition of coalescence by Marangoni flow.

early stage of such a process, their interface flattens in the contact area. Since the drop volume does not change, such a deformation causes an increase of the drop surface area, resulting in a dilution of the surfactant adsorbed at the interface. In turn, this causes a local increase of the IT. The thinning of the film dilutes the adsorbed layer setting an IT gradient, then monolayer material tends to flow from region of high to region of low surfactant concentration. This motion of the interfacial monolayer material creates a drag on the liquid adjacent to in the bulk phases,

known as capillary Marangoni flow, proportional to the IT gradient bringing liquid into the film. The dilational elasticity plays a major role in determining the dynamics of the film between coalescing droplets. In fact, the more the value of IT rises with respect to an increase in A (i.e, the higher the value of E), then the greater is the restoring force. At the same time, after the dilution of the adsorbed layer, the concentration of surfactant at the interface is no longer at equilibrium with the one in the solution. This triggers adsorption of new surfactant molecules from the solution, which contrasts the increase of IT. These intricate dynamic processes (interface deformation versus surfactant transport) determine the capability of a surfactant to act as an efficient emulsion stabiliser, by resisting the rupture of the thin liquid film between approaching droplets. As a result, these processes tend to oppose the droplet deformation and, therefore, counteracts coalescence. The above concepts are schematically summarised in figure 6.9, where we show the effect of surfactant induced changes of IT and E on the occurrence and stability of emulsions.

The rate at which the droplets of a macroemulsion coalesce to form larger droplets and eventually break the emulsion has been found to depend on a number of factors summarised below.

Physical nature of the interfacial film

The droplets of dispersed liquid in an emulsion are in constant motion, and therefore there are frequent collisions between them. If, upon collision, the interfacial film surrounding the two colliding droplets in a macroemulsion ruptures, the two droplets will coalesce to form a larger one, since this results in a decrease in the free energy of the system. If this process continues, the dispersed phase will separate from the emulsion. The mechanical strength of the interfacial film is therefore one of the prime factors determining emulsion stability. For maximum mechanical stability, the interfacial film resulting from the adsorbed surfactants should be condensed, with strong lateral intermolecular forces, and should exhibit high elasticity. Solid particles and soft colloidal microstructures can also stabilise emulsions. For example, by accumulating at the interface, liquid crystals surround the droplets with a high-viscosity region that resists the coalescence of individual droplets and also acts as a steric barrier preventing the dispersed drops from approaching each other closely enough for van der Waals forces of attraction to operate (Friberg et al., 1976).

Existence of an electrical or steric barrier to coalescence

The presence of a charge on the dispersed droplets constitutes an electrical barrier to the close approach of two droplets to each other. This is believed to be a significant factor only in O/W emulsions. In O/W emulsions, the source of the charge on the dispersed droplets is the

adsorbed layer of surfactant with its hydrophilic group and oriented toward the water phase. In emulsions stabilised by ionic surfactants, the sign of the charge on the dispersed droplets is always that of the amphipathic ion. In emulsions stabilised by nonionic surfactants, the charge on the dispersed phase may arise either from adsorption of ions from the aqueous phase or from frictional contact between droplets and the aqueous phase. In the latter case, the phase with the higher dielectric constant is charged positively. In W/O emulsions, there is very little charge, if any, on the dispersed drops, and experimental data indicate no correlation between stability and any charge present.

Viscosity of the continuous phase

An increase in the dynamic viscosity μ of the continuous phase reduces the diffusion coefficient D of the droplets, since, for spherical droplets,

$$D = \frac{kT}{6\pi\mu r}, \tag{6.14}$$

where k is the Boltzmann constant, T the absolute temperature, r is the radius of the droplets. As the diffusion constant is reduced, the frequency of collision of the droplets and their rate of coalescence is reduced. The viscosity of the external phase is increased as the number of suspended droplets increases, and this is one of the reasons that many emulsions are more stable in concentrated form than when diluted.

Size distribution of droplets

A factor influencing the rate of coalescence of the droplets is the size distribution. The smaller the range of sizes, the more stable the emulsion. Since larger droplets have less interfacial surface per unit volume than smaller droplets, in macroemulsions they are thermodynamically more stable than the smaller droplets and tend to grow at the expense of the smaller ones. If this process continues, the emulsion eventually breaks. An emulsion with a fairly uniform size distribution is therefore more stable than one with the same average droplets size having a wider distribution of sizes.

Phase volume ratio

As the volume of the dispersed phase in a macroemulsion increases, the interfacial film expands further and further to surround the droplets of dispersed material, and the basic instability of the system increases. As the volume of the dispersed phase increases beyond that of the continuous phase, the type of emulsion (O/W) or (W/O) becomes basically more and more unstable relative to the other type of emulsion, since the area of the interface that is now enclosing

the dispersed phase is larger than that which would be needed to enclose the continuous phase. The increase of the volume of the disperse can result in the emulsion phase inversion, that is a catastrophic process resulting in the formation of a W/O emulsion from a O/W one (or viceversa).

Temperature

A change in temperature causes changes in the IT between the two phases, in the nature and viscosity of the interfacial film, in the relative solubility of the emulsifying agent in the two phases, in the vapour pressures and viscosities of the liquid phases, and in the thermal agitation of the dispersed drops. Therefore, temperature changes usually cause considerable changes in the stability of emulsionsemulsion. When, undser the effect of temperature, the predominant solubility of the surfactant changes from one phase to the other, the emulsion phase inversion may occur.

Creaming

In an O/W emulsion, creaming is the movement of oil drops under gravity or in a centrifuge to form a concentrated layer at the top of the sample, without a change in drop size distribution, caused by the difference of density between the liquid phases. Initially, a concentration gradient of drops develops in the vertical direction, often followed by the appearance of a distinct boundary between an upper cream layer and a lower depleted emulsion layer. In a W/O emulsion, the equivalent phenomenon is called sedimentation. If flocculation (see next paragraph) does not occur, creaming is reversible in that gentle agitation can re-establish the original uniform distribution of drops. In very dilute emulsions, the creaming speed v_s of an isolated, spherical drop of radius r moving through a fluid medium of density ρ_0 and viscosity μ_0 is given by Stokes' Law

$$v_s = \frac{2r^2(\rho - \rho_0)g}{9\mu_0}, \tag{6.15}$$

where g is the acceleration due to gravity and ρ is the density of the dispersed phase.

In a concentrated, polydisperse emulsion, a region of increasing concentration with height appears for the largest drops. These drops accumulate fastest at the top of emulsion and occupy a greater proportion of the volume fraction in the upper regions. The smallest drops move downwards from the top of the emulsion and increase in concentration at a lower level. All drops except the largest have a region of decreasing concentration with increasing height, caused by the slowing down of the descend of the cream interface with time (Pinfield et al., 1994).

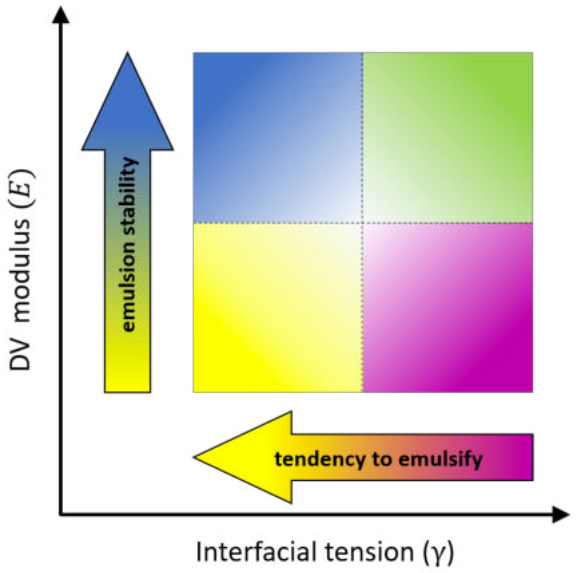

Figure 6.9: Schematic diagram illustrating the interplay between IT and E in determining the formation and stability of emulsions.

Flocculation

Flocculation is the process in which emulsion drops aggregate, without rupture of the stabilising layer at the interface, if the pair interaction free energy becomes appreciably negative at a certain separation. It may be weak (reversible) or strong (not easly reversible) depending on the strength of the interdrop forces. Flocculation usually leads to enhanced creaming because higher mass object are formed (therefore, less prone to diffusive interactions). Exceptions occur in concentrated emulsions where the formation of a gel-like network structure can have a stabilising influence. Flocculation is enhanced by polydispersity since the differential creaming speeds of small and large drops cause them to come into close proximity (and hence possibly aggregate) more often than would occur in a monodisperse system. The rate of flocculation can be estimated from the product of a frequency factor (how often drops encounter each other) and a probability factor (how long they stay in contact). The former can be calculated for the case of Brownian motion or under shear flow, whilst the latter depends on the interaction energy, i.e. the free energy required to bring drops from infinity to a specified distance apart. In calculating the interaction energy as a function of interdrop distance, three terms are normally considered: van der Waals attraction (depends on the drop diameter), electrostatic repulsion (depends mainly on the surface potential of the drops, drop diameter and the ionic strength of the continuous phase) and steric repulsion due to protruding, flexible chains (depends on the surface density and length of these chains).

Droplet coelescence can be statistically favored within the flocs due to the close conatct between droplets.

Ostwald Ripening

Ostwald ripening is the result of the solubility differences of oil contained within drops of differing sizes. According to the Kelvin equation (Thomson, 1872), the solubility of a substance in the form of spherical drops increases with decreasing size. As a consequence of its increased solubility, material contained within the smaller drops tends to dissolve and diffuse through the aqueous phase, recondensing onto the larger drops. This results in an overall increase in the size of the emulsion drops and an accompanying decrease in the interfacial area. This provides the driving force for the growth of the drops. Theoretically, the process of Ostwald ripening should bring to the complete separation of the disperse phase into a single drop, but this does not occur in practice owing to a considerable decrease in the rate of the process as the average size of the drops increases. The process of the Ostwald ripening can be described by the LSW theory (Lifshitz, Slezov and Wagner theory (Lifshitz and Slyozov, 1961)). This theory assumes that the droplets of the dispersed phase are spherical and separated from each other by distances which are much larger than the drop sizes, and that the mass transport of oil is limited by the molecular diffusion in the continuous phase.

6.5 PROTEINS

In this section we focus our attention on proteins, which in many cases are natural surface active substances. Investigations of proteins adsorption process are of importance for understanding of the stability of emulsions, which is of great interest for the purpose of this work.

Properties of protein adsorption layers differ in a number of aspects from those characteristic to monolayers of usual surfactant. In fact, proteins have specific structures that are related to their functionality, but they readily lose their native conformation through interacting with their surroundings. This phenomenon is known as protein *unfolding* or *denaturation*, which may take place also within the surface layer. The structure and kinetics of protein unfolding depend on the driving force of this phenomenon. The conformation of protein molecules adsorbed at interfaces is determined by a balance of various forces (van der Waals attraction, electrostatic interaction, etc.) among which changes in conformational entropy which is associated with adsorption.

Since the purpose of the present study is to evaluate how some human blood proteins may be involved in the emulsification phenomenon within the vitreous chamber of the eye, it is important to understand how the main globular proteins (albumin, γ-globulins) present in human blood behave at the interface.

6.5.1 PROTEINS OF THE BLOOD SERUM

Blood serum is simply plasma without fibrinogen, factor VIII, factor V and prothrombin. It is obtained by letting the blood coagulate and then centrifuging it. Separating serum proteins by electrophoresis is a valuable diagnostic tool as well as a way to monitor clinical progress. Human blood serum contains about 7% protein, two-thirds of which consists of albumin fraction; the other third is in the globulin fraction. Electrophoresis of serum reveals a large albumin peak and three smaller globulin peaks, the α-, β-, and γ-globulins (Daniel and Felix, 2017).

Human serum albumin (HSA) is synthesised in the liver, is soluble in water, precipitated by acid, and coagulated by heat. The main functions of albumin are to transport a wide variety of ligands, to maintain plasma oncotic pressure, and to serve as a source for endogenous amino acids. Moreover, it transports certain hormones (thyroid, estrogen, cortisol) when their specific binding globulins are saturated, unconjugated bilirubin and other organic anions, and many drugs (penicillin, warfarin, etc.). HSA has a crystal structure complexed with fatty acid reveals an asymmetric distribution of binding sites (Curry et al., 1998).

The γ-globulins are the most heterogeneous globulins and participate in immune system. Although most have a molecular weight of approximately 150000, that of some, called macroglobulins, is as high as 800000. The structure is characterised by a symmetrical T-shaped or Y-shaped molecule made up of two heavy chains and two light chains of amino acids. Binding the chains together at various sites are sulfur bonds.

6.5.2 PROTEIN ADSORPTION PROCESS

The protein has a higher affinity to hydrophobic substrates than hydrophilic substrates (Anand et al., 2010; Kim and Somorjai, 2003). Further, hydrophobic surfaces usually induce protein unfolding (Dickinson, 1999). Proteins generally adsorb at the air-water interfaces as anphiphilic molecules and they dramatically reduce the IT. Adsorption consists of the following four steps: bulk diffusion, adsorption, protein unfolding, and lateral diffusion and proteinprotein rearrangements (Tripp et al., 1995).

The conformation of a protein at an interface affects the IT, and the kinetics of protein unfolding can be determined from the relationship between the dynamic IT and the adsorbed amount. Bovine serum albumin (BSA), which is very similar to HSA, is a soft, highly foamable protein and the dynamic IT is similar to that of aqueous solutions of simple detergents. The adsorption rate is initially very rapid, but it decreases slightly with decreasing protein concentration (Chakarova and Carlsson, 2004), see section 6.2.2.

Recent studies have revealed that protein conformation changes during the adsorption process due to the protein-protein interaction increasing with increasing interface coverage. External conditions also affect the protein conformation.

Wierenga et al. (2006) demonstrate that unfolding will only occur if the adsorption kinetics is similar or slower than the unfolding kinetics.

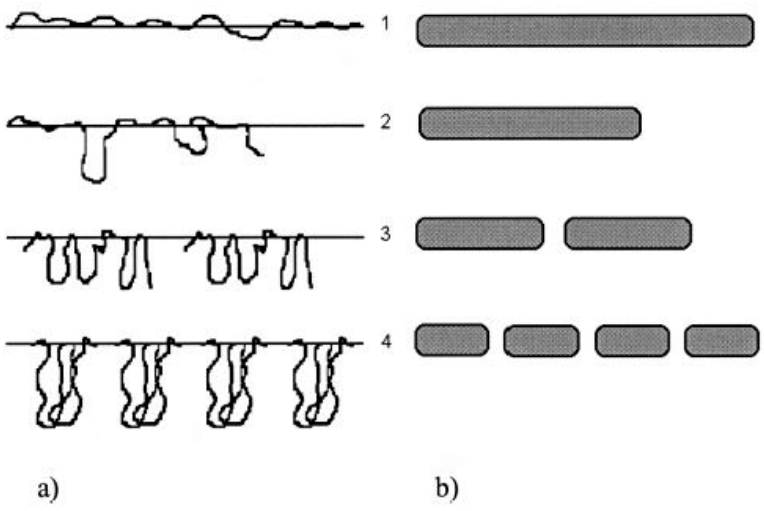

Figure 6.10: Conceptual model of protein adsorption: (a) schematic diagrams showing conformational changes of adsorbed protein molecules; (b) molar area occupied by one adsorbed molecule; the IT decreases in the order 1-4 which corresponds to increasing surface coverage (Miller et al., 2000).

A lower protein concentration reduces the adsorption rate and hence induces a larger conformational change of adsorbed protein molecules (Miller et al., 2000) and consequently, the molar area occupied by one adsorbed protein molecule increases due to unfolding because the adsorbed protein molecule tends to cover the water surface to reduce the surface energy (figure 6.10). This means that the adsorption layer thickness increases with increasing protein concentration. Thus, with increasing surface coverage, namley stronger competition between the adsorbed protein molecules, their molar area becomes smaller until finally a minimum area is reached, as shown in figure 6.10.

Mixtures of proteins and surfactants are also of practical relevance. For example, blood serum is a mixture of HSA with a number of compounds, including low-molecular surface-active molecules. This implies the scientific and practical importance of studies on the adsorption behavior and its dynamics of mixed protein-surfactant systems. In particular, if the effect of low molecular non-ionic surfactants (alcohols, acids and oxyethylated ether), on the adsorption dynamics of a protein depends on their concentration and surface activity and on the solution conditions, no definite predictions can be made concerning the effect of ionic surfactants on the adsorption dynamics (Turro et al., 1995).

Because the phenomena that occur at the interface when proteins are present are complicated, we can only give only some general conclusions which result from the evolution of protein molecules in different states in an adsorption layer.

Processes of unfolding and rearrangement with increasing saturation of the adsorption layer

may be explained by the influence of the protein concentration on the adjusting time of adsorption equilibrium. These processes may cause some strong effects on the surface rheology too.

Moreover, multiprotein adsorption studies have been perfomed, providing new insight into the role of protein-protein interactions in the adsorption process and also highlighting a competitive aspect among the molecules (Fang and Szleifer, 2003; Kubiak-Ossowska and Mulheran, 2011).

6.5.3 Adsorption of proteins at liquid-liquid interface

Most meaningful in the context of this work is the study of the interfacial properties of immiscible liquids containing endogenous molecules. Experimental studies of proteins at oil/water interfaces are however scarce.

The IT between aqueous solutions cointaining 0.002 g/L of HSA and decane has been obtained by Möbius and Miller (1998) in the temperature range from 20°C to 60°C. The γ-time curve obtained through the experiment performed at 35°C, in order to simulate physiological conditions, shows that for the small HSA concentration adopted the equilibrium IT value is 19.47 mN/m.

Benjamins et al. (1996) used the Dynamic Drop tensiometer at a triacylglycerol oil/water interface (i.e., sunflower oil) using two concentrations of BSA (5 mg/L and 10 mg/L). These experiments have been also performed with β-casein and β-lactoglobulin. As at air/water surface behavior at high frequency is found to be purely elastic for all proteins at not too high surface coverage.

The effect of different proteins on interfacial properties has been studied on water-oil systems for food applications (Saito et al., 2006; Sarkar et al., 2009). In these studies the selected endogenous molecules were albumin and β-lactoglobulin. The interfacial properties of SOs used in vitrectomy are, on the other hand, poorly investigated.

CHAPTER 7

THE ROLE OF ENDOGENOUS PROTEINS AND STEROID DRUGS IN THE PROCESS OF SO EMULSIFICATION

This chapter is based on the publication by Nepita et al. (2020).

In order to study whether endogenous molecules can modify the interfacial properties enough to make them compatible with the generation of an emulsion, we performed experiments aimed at investigating the capability of biomolecules to act as surfactants, adsorbing at the water–SO interface, and to quantify their role on the equilibrium IT and the DV.

Steroid drugs (SDs) aimed at treating inflammatory conditions in vitrectomised eyes can also act as surfactants and modify the properties of the interface between SO and aqueous phase. An anti-inflammatory SD adopted for these purposes is commonly injected before the vitrectomy procedure begins. This kind of product is an aqueous dispersion of solid crystals of triamcinolone, which have the tendency to sediment in a time of the order of a minute. Specific studies would be required to assess their effect on the rheological properties of the interface between aqueous solution and SO.

7.1 WORKING FLUIDS

The SO used in the experiments is Siluron 1000cs (Fluoron GmbH, Germany), which is composed of ultrapure polydimethylsiloxane and is of common use in ophthalmic surgery.

We first characterised the interfacial properties between SO and ultrapure water, characterised by resistivity larger than 18 MOhm and produced by a MilliRO plus Milli-Q (Millipore, Burlington, MA, USA) reverse osmosis system. These measurements are used as a benchmark reference for comparison with existing results in the literature and also to verify the effect of adding endogenous molecules.

We then studied the effect of endogenous proteins on the interfacial properties between an aqueous solution and SO. Two proteins were selected for the experimental activity: bovine serum albumin (Sigma, A2153-50G) and γ-globulins from bovine blood (Sigma G7516-10G). For the present study albumin and γ-globulins have been chosen as they are present in high concentration in blood serum (Daniel and Felix, 2017; Alberghina et al., 2011). Solutions of these molecules were prepared in a Dulbecco phosphate buffered saline (DPBS, Sigma D8662), simulating the in-vivo protein environment. Protein concentrations ranged between 0% (pure buffer) and 100% of the corresponding physiological protein concentration in blood serum. In particular, we considered as physiological concentration 50 g/L in the case of albumin and 25 g/L for γ-globulins (**?**Patton and Thibodeau, 2018). Using bovine proteins allowed us to easily obtain them in suitable amounts. These proteins have been shown to be excellent models of human ones, as far as the study of interfacial properties are concerned (Kazakov et al., 2000; Makievski et al., 1998; Tripp et al., 1995).

We also tested the interfacial properties between SO and aqueous solutions of whole human blood serum (WHBS). The serum was obtained from blood collected from healthy subjects, who gave their consensus to the use of the samples for research purposes. Blood was collected in test tubes free from anticoagulants and serum was separated by centrifugation at 3000 rpm at the temperature of 4°C and then stored at -40°C. Before use, serum samples were unfrosen at a temperature of 4°C and then diluted with buffer to the desired concentrations. These solutions were then brought to 35°C, immediately before performing the measurements.

We also evaluated the influence of an anti-inflammatory steroid, on the chemico-physical properties of the interface between SO and aqueous phase. The intraocular use of this drug during vitrectomy is aimed at treating many different inflammatory conditions. To assess whether a SD has a surfactant role at the interface, we conducted a first series of experiments to quantify the IT and the DV properties through the Drop Profile Analysis. Since the SD is an aqueous dispersion of solid crystals of triamcinolone, which has the tendency to sediment in a time of the order of a minute, it was not possible to carry out measurements of IT and DV on the whole product, as the dispersion was not sufficiently stable over the time scales relevant for the adsorption phenomena. Therefore, we performed the measurements on the aqueous phase of the dispersion (supernatant), which separates after the sedimentation of crystals.

The same experiment was conducted by adopting the supernatant as a solution with the addition of albumin at a concentration of 10% with respect to the physiological concentration in blood, in order to evaluate if the residual particles of the SD in suspension may have any interaction with the serum proteins, modifying their possible surfactant properties.

In order to avoid contamination from surface active molecules, all glass and plastic wares and pieces of equipment brought in contact with the fluids were first carefully cleaned with standards procedures adopted in surface science laboratories. Between different cycles of measurements, the absence of contamination was checked by measuring the IT of pure water, veri-

fying that it assumed a value close to 72.5 mN/m, stable over several minutes.

7.2 MEASUREMENTS OF THE IT AND DV

In all experiments, the IT was measured using a dynamic tensiometer (PAT1-Sinterface Technology, Berlin), based on the the Drop Shape method (DST). The method relies on the acquisition, through a digital camera and on an algorithm ensuring a resolution of 2 μm, of a pendant drop profile. The shape of the drop under the action of gravity depends on the IT and on the density difference between the two fluids.

It results in fact from the equilibrium between hydrostatic and capillary pressure in each point $p(x,z)$, according to the Young-Laplace equation:

$$P^0 + \Delta\rho\, gz = \gamma\left(\frac{1}{R_1} + \frac{1}{R_2}\right), \tag{7.1}$$

where P^0 is a constant, R_1 and R_2 are the surface radii of curvature, $\Delta\rho$ is the density difference between the two fluids, g the gravity, z a vertical coordinate and γ the IT. This relation for the axis-symmetric profile of a drop (Bashforth and Adams, 1883) can be redrawn as follow:

$$2 + \frac{\beta z}{b} = \frac{1}{\frac{R^*}{b}} + \frac{\sin\phi}{\frac{x}{b}}, \tag{7.2}$$

where b is the curvature radius at the drop apex, R^* the curvature radius of the meridian section at the point p. Moreover ϕ is the angle between the normal to the surface at the same point and the vertical axes (figure 7.1). β is the so-called shape factor: a dimensionless parameter defined as

$$\beta = \frac{\Delta\rho g b^2}{\gamma}, \tag{7.3}$$

where $\Delta\rho$ is the density difference between the internal and the external phases, g is the gravity acceleration taken with positive sign if directed accordingly to the $z-$axis, gives an estimation of the level of drop deformation due to gravity effect.

Once the densities of the two fluids are known, the IT can be obtained by a best fitting procedure of the theoretical drop profile (Bashforth and Adams, 1883) to the acquired one (figure 7.1). In fact, changing β and b, a family of theoretical curves results, and the one that best fits to the experimental points (red points) then corresponds to the optimum value. Then from the definition of the shape factor (equation 7.3) we can obtain the the IT value (Maze and Burnet, 1969; Liggieri and Passerone, 1989; Loglio et al., 2001, 2011).

A typical DST is composed by a cell where a drop or a bubble is formed inside the other fluid, continuously monitored by a camera, which allows drop profile acquisition in an automatic way. The detection of profile points provides a subpixel value of the profile position with a resolution

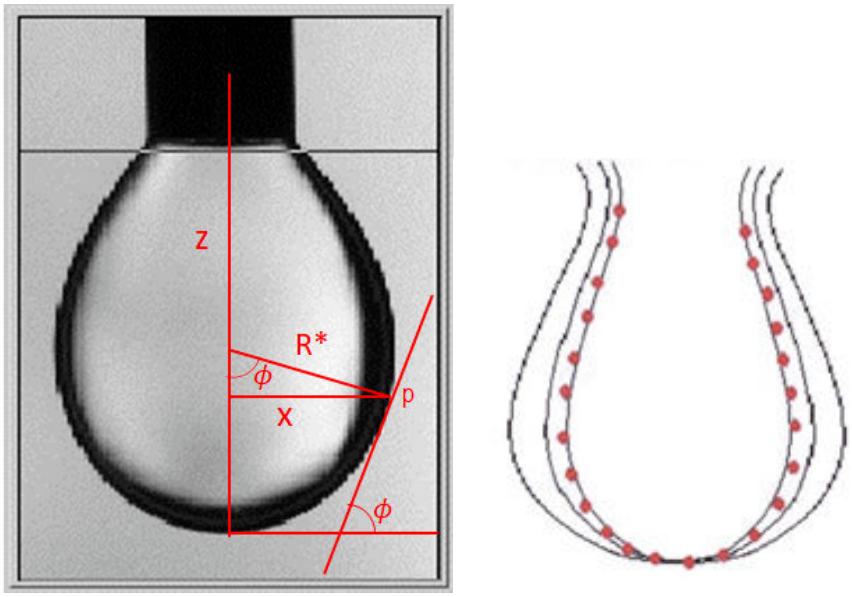

(a) (b)

Figure 7.1: (a) Acquired pendant drop picture with illustration of the symbols utilised in equation 7.2; (b) principle of fitting the Bashforth-Adams equation to the drop profile.

of about 2 μm. Moreover, a LabView program allows one to control the volume and area of the drop formed through a syringe pump (figures 7.2 and 7.3). In our case the cell is filled by SO, the pendant drop is composed by the proteins acqueous solution and measurements has been performed at 35°C, in order to simulate physiological conditions.

DST is applicable to liquids with an appreciable density difference; in fact, if the two liquids were isodense, the drop would take a spherical shape and the IT would result undetermined.

The knowledge of the liquid densities is thus an important issue for the pendant drop technique, in order to obtain the IT from the best fit values of β and b. In fact, as for the definition of β, the relative error on the value of $\Delta\rho$ equals the relative error on the IT. Since in our case the density difference between SO and aqueous solution is extremely small, accurate measurements of the densities are required for the method to be reliable. For SO, density measurements as a function of temperatures have been kindly provided by Rutherford Appleton Laboratory in Oxfordshire, UK (Dr. Mario Campana) and have been performed employing the densimeter Anton Paar DMA4100 M, which has a precision of 0.1 Kg/m^3. The measurement is based on the oscillating U-tube technique where the density is accurately calculated from the frequency of oscillation. The tube is filled via a syringe and a camera ensures the absence of bubbles. The instrument was calibrated with air and water right before the measurement to ensure an adequate response. Through this instrument it was possible to obtain the density value with accuracy up to the fourth decimal place as reported in table 7.1.

At 35°C we found a value of SO density of 961.2 Kg/m^3. For the densities of serum aque-

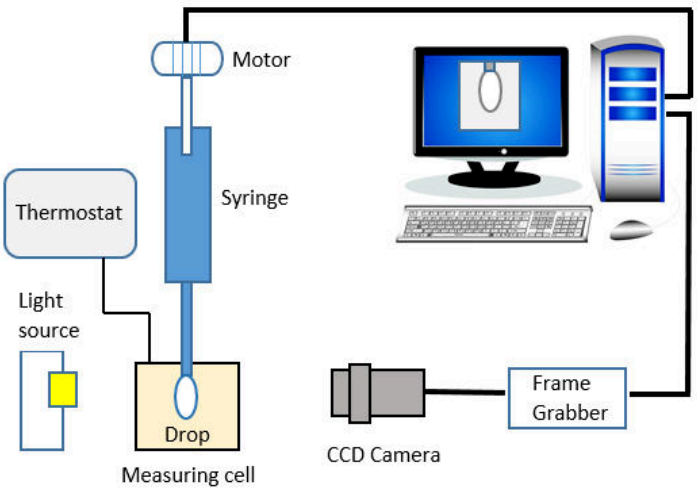

Figure 7.2: Sketch of the experimental setup.

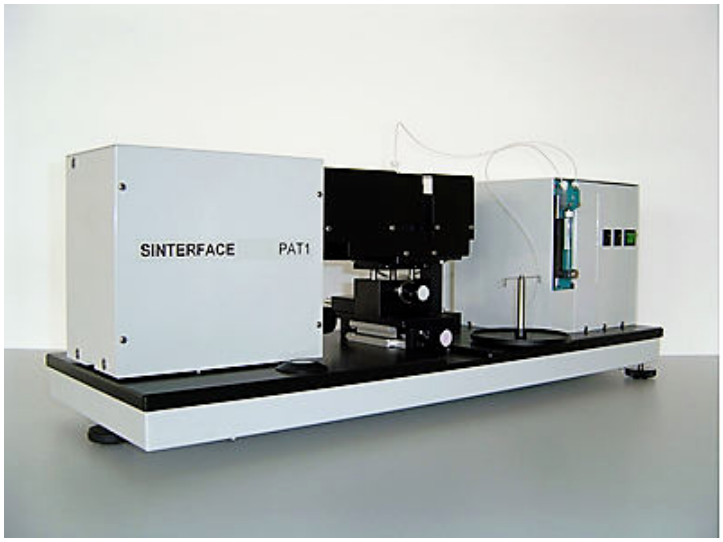

Figure 7.3: Picture of the drop shape tensiometer (PAT1) designed by Sinterface.

Temperature ($°C$)	Density (Kgm^{-3})
5	988.1
10	983.6
15	979.1
20	974.6
25	970.1
30	965.6
35	961.2
40	956.8
45	952.2
50	947.9

Table 7.1: Density values obtained by Anton Paar DMA 4100 M densiometer (kindly performed at Rutherford Appleton Laboratory, Oxfordshire).

ous solutions we used values calculated as weighted averages between the density of the DPBS, namely 1007.5 Kg/m^3, corresponding to the value of a 10 Kg/m^3 solution of NaCl at 35°C (P H and G, 1985) and the density of the serum at 35°C (1025 Kg/m^3) (Sniegoski and Moody, 1979). The densities of single protein aqueous solutions were calculated using a similar approach and assuming that the density of the solution of albumin plus γ-globulins in physiological concentration equals that of serum.

For measurements concerned with the SD, the density value of DPBS at 35°C was assumed for the supernatant, being the latter for the most part of a saline solution.

Exploiting the area control features of the PAT, DV values were measured using the oscillating drop method, based on the measurement of the IT response to harmonic oscillations of the interfacial area (Miller and Liggieri, 2009) as described in section 6.3.

7.3 Description of a typical test

A typical experiment started with the formation of a fresh (nearly free from adsorbed surfactant) interface of aqueous solution in SO. This is obtained by abruptly stopping the quick formation and detachment of a train of drops at the tip of a needle. The experiment then proceeded in two phases. Right after the drop was formed, its surface area was kept constant until the IT reached the equilibrium value. This is a standard test to follow the kinetic of adsorption at liquid interfaces. In the presence of surfactants, during this phase a decrease of IT from an initial value, corresponding to the IT of the newly formed interface, to the final equilibrium value is observed. In the absence of surfactant molecules, as we expect in the in the case of the SO-ultrapure water interface, the IT remains constant and equal to its initial value.

In the second phase of the test, which followed the previous one with no interruption, the DV was measured. The drop area was varied sinusoidally in time, with an oscillation amplitude $\tilde{A}$ =

$0.02 \cdot A^0$ and for a set of different frequencies, in the range 0.001 Hz to 0.1 Hz. Higher frequencies were not tested, since the effect of SO bulk viscosity would have induced unacceptable distortions in the IT response (non harmonic in time). For each frequency, a number of oscillation periods were applied, from 3 at the lowest frequency, to 10 for the largest one. For low frquencies we acquired 1 image per second; 2-3 images per second were captured when higher frequencies were imposed.

Because of its large bulk viscosity, SO opposes a significant resistance to the expansion or contraction of the drop volume at high frequencies of oscillations. This might result in deviations of the drop shape from that at mechanical equilibrium. This effect was limited by reducing as much as possible the amplitude of the perturbation.

The estimate of the phase angle ϕ, typically results in larger errors than that of the amplitude $\tilde{\gamma}$. For this reason, we focused our analysis on the modulus of the DV, defined as

$$|E| = \frac{\tilde{\gamma}}{\tilde{A}/A^0}. \tag{7.4}$$

In figure 7.4, the green curve shows the measured surface area of the drop in a typical experiment. Once the test was completed, for each frequency, the amplitudes and phases of the IT response and of the drop area signals were obtained with a Fourier analysis (Loglio et al., 2011) and DV values were calculated according to equation 6.13.

7.4 Results in absence of proteins

In figure 7.4 we show the results obtained in the absence of proteins, for the interface between SO and both water and DPBS. For the SO-water interface, the measured IT is close to 42 mN/m, which is consistent with existing measurements (Barca et al., 2014). Both systems show a small and relatively quick decrease of the IT right after the formation of the drop. However, when the unsteady phase of the experiment starts, the IT does not show any response to surface area variation, which indicates the absence of adsorption processes at the interface. Within the experimental error, we find that the IT for the interface between SO and DPBS has the same value as for the interface between SO and pure water. We then conclude that SO, DPBS and water do not contain surfactant impurities.

7.5 Results with endogenous proteins

In figure 7.5 we show the corresponding results obtained for solutions of either albumin or γ-globulins in DPBS. For each protein, we report the data corresponding to 1 and $\approx$ 1/10 of its average physiological concentration in blood. Let us consider γ-globulins first (light blue and red curves in the figure). For the smallest value of concentration (light blue) at the beginning of the experiment IT values are significantly different from those observed in the absence of proteins and decrease on a time scale of thousands of seconds, nearly achieving an equilibrium

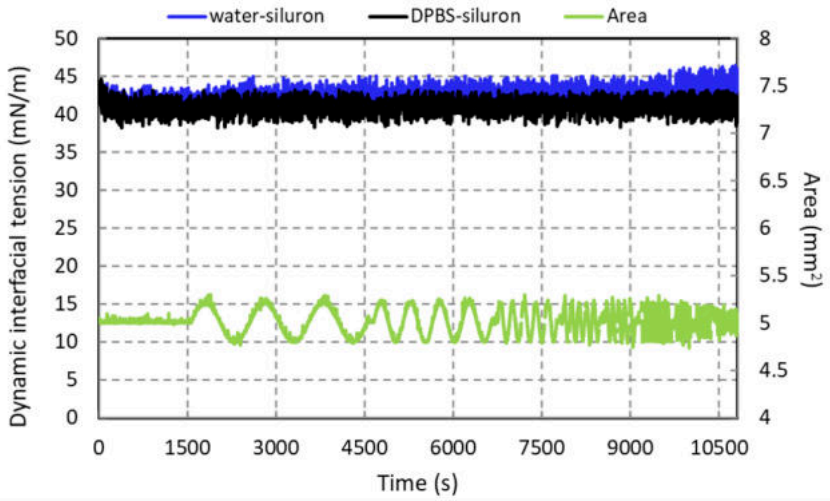

Figure 7.4: Time evolution of the dynamic IT of the SO-DPBS (black) and SO-water (blue) interfaces (left y-axis). For the first 1800 s the interfacial area is kept fixed. From there on oscillations of the interfacial area with an amplitude of 2% are imposed, for a range of different frequencies. The green line represents the interfacial area variation in time (right y-axis)

value of ≈ 23 mN/m, which is almost half of the value observed in the absence of proteins. This confirms the occurrence of an adsorption process of the protein at the interface. The oscillatory phase of the experiment starts at 5000 s. When surface oscillations are imposed the IT also shows large variations, indicating the existence of a significant DV. For the physiological value of γ-globulins concentration (red curve), the results are similar but the IT decreases to an even smaller value, ≈ 21 mN/m.

For albumin (figure 7.5, blue and green curves), the adsorption process is faster and the IT equilibrium values are smaller than for γ-globulins, achieving values of ≈ 17 mN/m, for both concentrations tested. In addition, the amplitude of IT oscillations in response to variations of the surface area is much smaller, and almost vanishes for the largest concentration value. This is because the adsorption time scale is quite fast, so that the IT recovers very rapidly its equilibrium value in response to the applied variations of the surface area.

Figure 7.6 shows the equilibrium IT for solutions containing albumin, γ-globulins and a mixture of the two proteins, in physiological ratio. The concentrations are normalised with their average physiological content in blood. Equilibrium values are extrapolated from the adsorption kinetics experiments, applying a long-time approximation scheme, as proposed by Makievski et al. (1997). In all cases the IT decreases as the concentration of surfactant molecules increases, down to a saturation value. Such a value for both proteins is achieved already at a concentration of about 1/10 of their physiological value, with IT reduction of $\approx 50\%$ with respect to the SO-DPBS interface. The effect of the mixture of the two proteins in physiological ratio does not differ from the effects of the single proteins, which calls for a poor interaction between them,

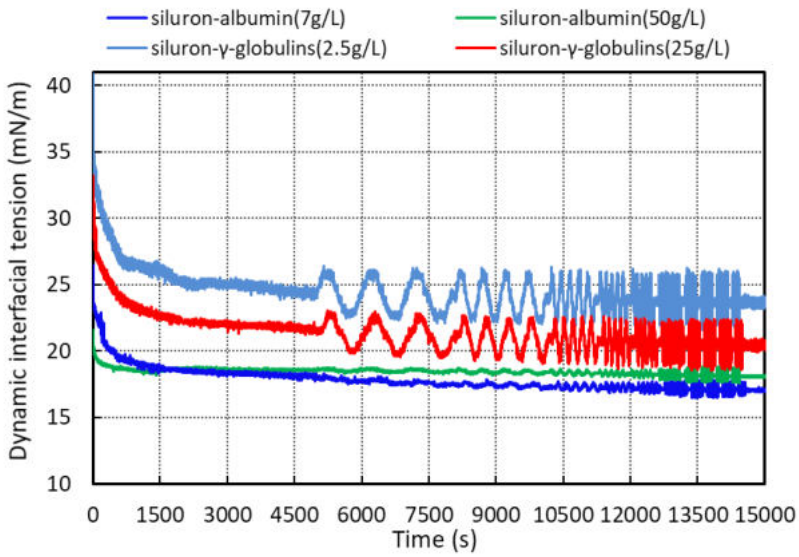

Figure 7.5: Time evolution of the dynamic IT between SO and buffer solutions containing γ-globulins and albumin. Curves refer to different concentrations, which values are normalised with the corresponding value in blood. 0.14 light blue, 1.0 red, 0.1 blue and 1.0 green.

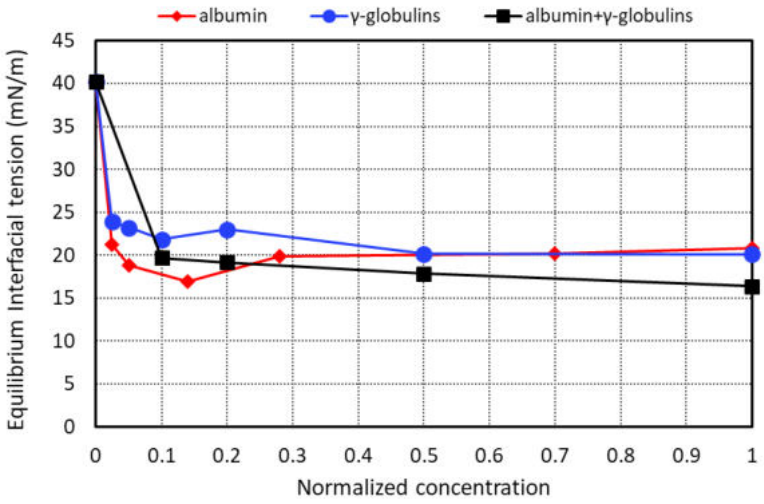

Figure 7.6: Equilibrium IT as a function of protein concentration. Concentration is normalised with the value corresponding to the concentration in blood.

once adsorbed.

The DV modulus is shown in figure 7.7 as a function of the normalised concentration and for two different frequencies, among those measured. In agreement with what we found for the amplitude of IT variations (figure 7.5) the DV modulus is larger for γ-globulins than for albumin solutions. We note that the values measured for γ-globulins are much larger (even by an order of magnitude) than those observed for ordinary surfactants. The values measured for the mixture

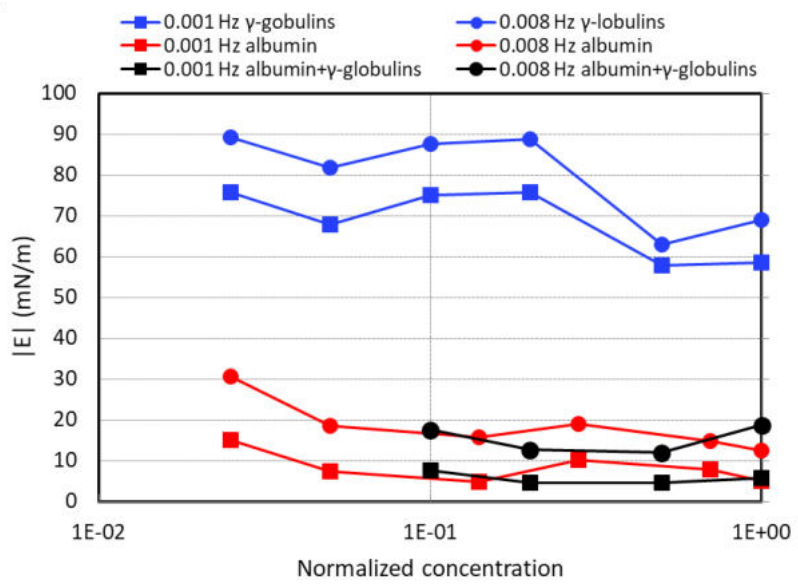

Figure 7.7: DV modulus as a function of protein concentration for different perturbation frequencies.

of proteins are similar to those obtained for albumin, which, therefore, plays a dominant role on the interface rheological behavior.

These findings are also confirmed by the values of DV modulus as a function of frequency for different proteins concentrations in the aqueous solution (see figure 7.8). This plot shows that the modulus increases with the increase of the frequency for all the investigated system. As observed in figure 7.7, the effect of the mixture (black curve), is similar to that of albumin alone (red curve).

Similar experiments have also been conducted on solutions of whole human blood serum (WHBS) in DPBS, adopting values of the volumetric concentration ranging between $5 \cdot 10^{-6}$ to $5 \cdot 10^{-2}$, in order to investigate the overall effects of blood proteins, even at very low concentrations. Examples of the IT measured during these experiments are given in figure 7.9. IT equilibrium values for WHBS solutions are reported in figure 7.10. For the sake of comparison, figure 7.10 also reports the IT values relative to albumin, γ-globulins and their mixtures (the same data as in figure 7.6). The normalised concentrations for the single proteins and the volumetric concentration for blood serum are in fact directly comparable. This is because a value of the normalised concentration equal to 1 for a single protein corresponds to its volumetric concentration equal to 1 in the non-diluted serum.

Figure 7.10 shows that values of IT comparable to those observed for the proteins alone, are achieved in WHBS solutions at concentrations that are two orders of magnitude smaller. This is clear evidence that WHBS contains other surface active fractions in addition to the proteins considered here that have an important role. The WHBS IT values for concentrations above 0.01

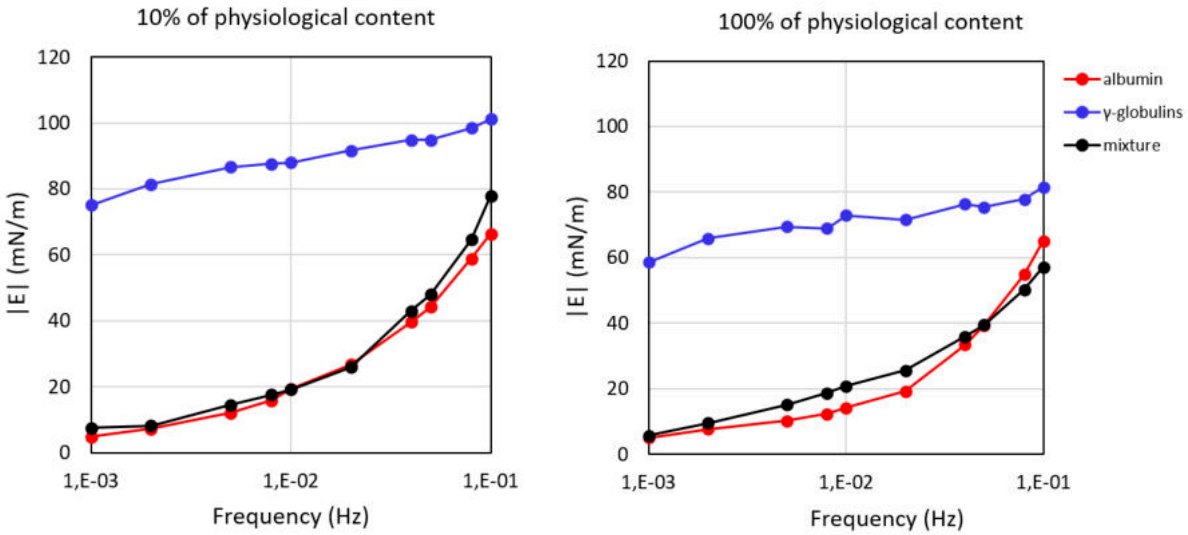

(a) (b)

Figure 7.8: DV modulus as a function of frequency for different protein concentrations: (a) 10%, (b) 100% of physiological content in blood.

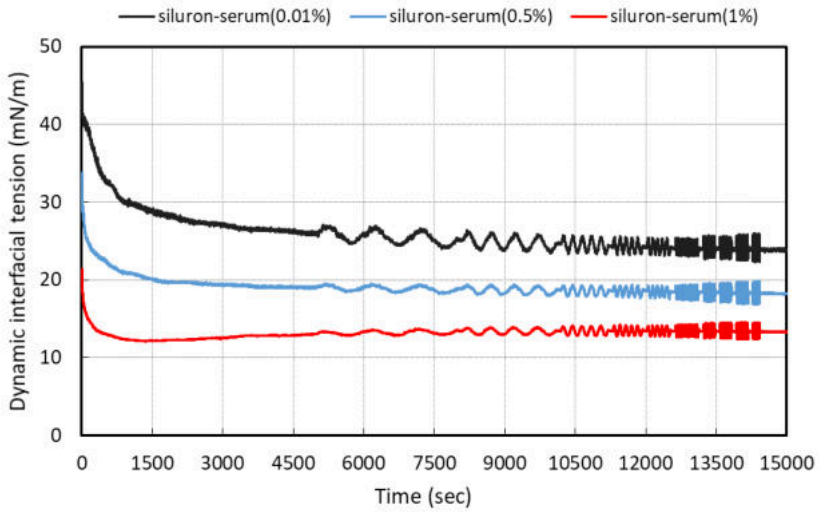

Figure 7.9: Time evolution of the dynamic IT between SO and WHBS solutions in DPBS buffer at different volumetric concentrations.

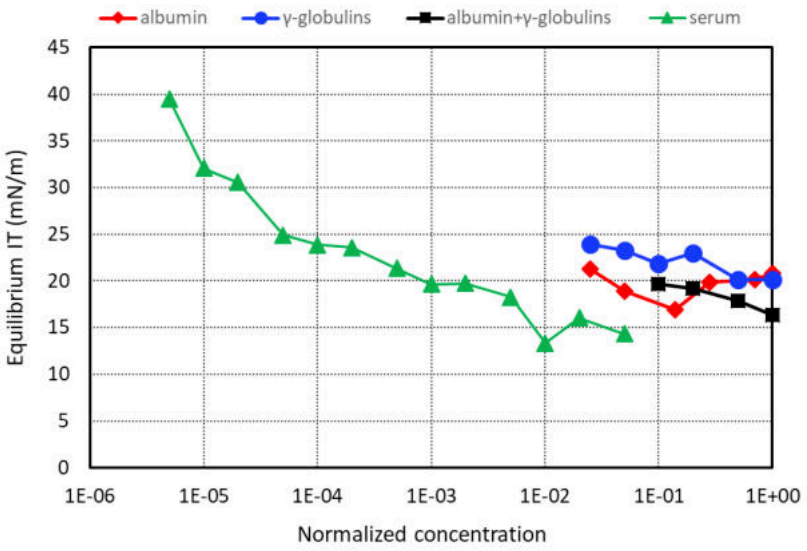

Figure 7.10: Equilibrium IT values as a function of protein concentration. Concentration is normalised with the value corresponding to the concentration in blood.

compare well with those reported in Nakamura et al.Nakamura et al. (1990) for the liquefied vitreous.

In figure 7.11 we show the DV modulus for the WHBS solutions as a function of the concentration for all tested frequencies. The DV modulus varies with both concentration and frequency and attains values as large as (or even larger than) those observed with γ-globulins. The values increase with the frequency, which is coherent with the observation that the observed adsorption timescales are larger than the maximum oscillation period investigated. The values of the DV modulus around the maximum are from 3 to 10 times larger than those typically observed for ordinary surfactants. Moreover, we observe that in all cases the maximum value of DV modulus is achieved for very low concentrations values.

In figure 7.12 we plot the DV modulus as a function of frequency for three different WHBS concentrations. Dilational viscoelasticity values increase with frequency; moreover, they increse with lower concentrations of WHBS, as observed in figure 7.11. This beahaviour could imply good stability of the generated SO droplets.

The comparison between DV modulus results obtained with WHBS solutions and those found with albumin and γ-globulins, is reported in figure 7.13. It is worth to notice that the behavior of the WHBS reflected that of albumin.

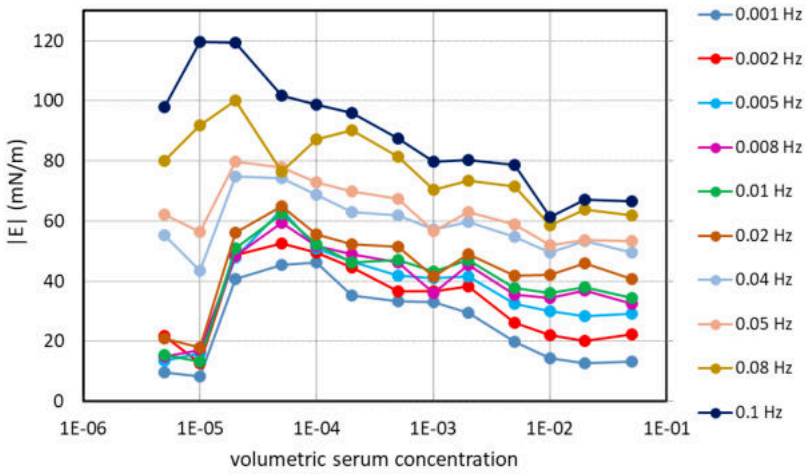

Figure 7.11: DV modulus as a function of WHBS concentration for different perturbation frequencies.

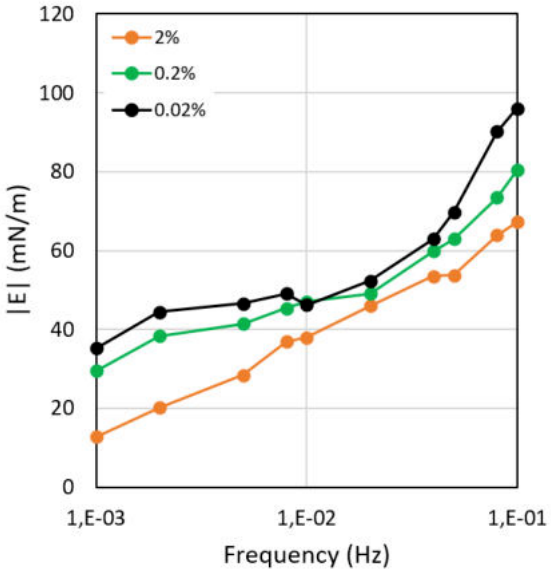

Figure 7.12: DV modulus as a function of frequency for different WHBS concentrations.

7.6 RESULTS WITH THE SD

We also performed similar experiments using the SD. Figure 7.14 shows the equilibrium IT reached in the case of interface between SO and the drug supernatant (red curve) and DPBS (black curve). As can be seen from the graph, the equilibrium value is almost the same for both curves ($\approx$ 40 mN/m).

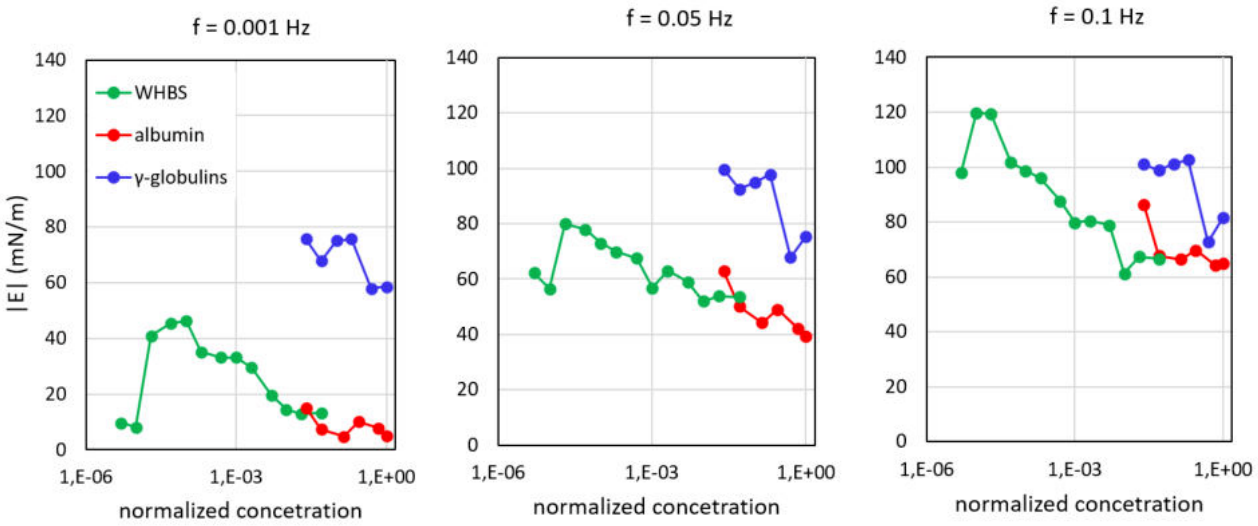

(a) (b) (c)

Figure 7.13: DV modulus as a function of protein concentration for different perturbation frequencies: (a) 0.001 Hz, (b) 0.05 Hz, (c) 0.1 Hz.

In the case of the supernatant, a small decrease of the IT is observed and during the oscillatory stage the IT responds with small amplitude oscillations. Such a behavior is not observed for DPBS and indicate the presence in the supernatant of surface-active impurities, which however does not give rise to relevant values of the DV.

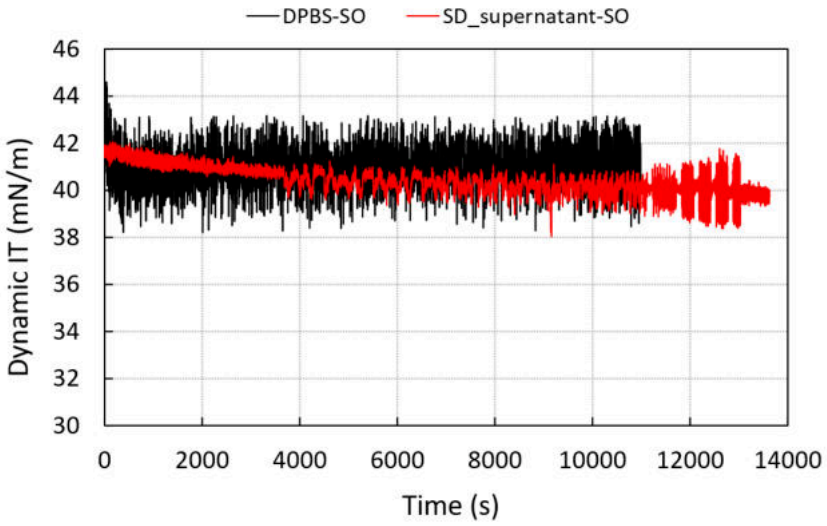

Figure 7.14: Time evolution of IT between SO-DPBS (black) and SO-supernatant (red) during the experiments. For the first 5000 s the interfacial area is kept fixed. From there on oscillations of the interfacial area with an amplitude of 2% are imposed, for a range of different frequencies.

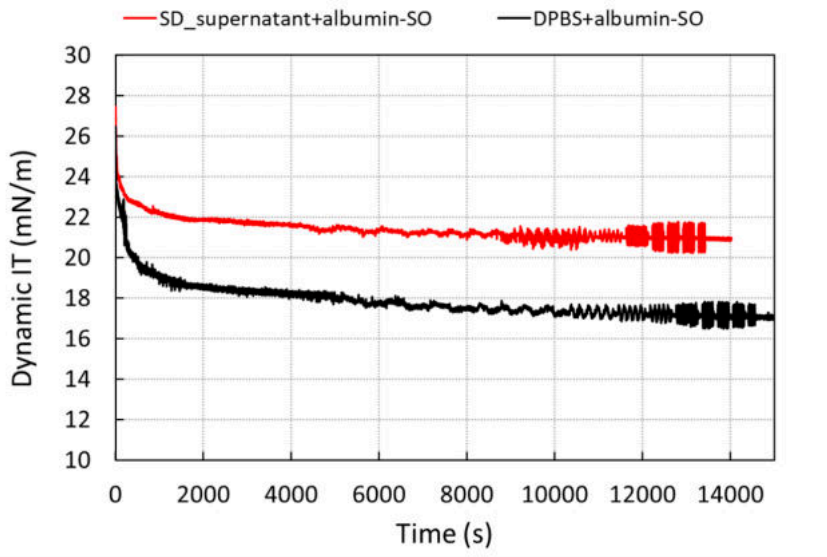

Figure 7.15: Time evolution of IT between SO-supernatant (red) and DPBS-supernatant (red) containing albumin. Curves refer to different albumin concentrations, whose values are normalised with the corresponding value in blood: 0.14 (black), 0.10 (red).

Figure 7.15 shows the temporal evolution of IT between SO and supernatant containing albumin (red curve) and DPBS containing albumin (black curve). Compared to figure 7.14, it can be observed that in the static phase of the experiment (for the time t < 5000 s), the IT decreases progressively and slowly. This indicates the presence of adsorption of molecules at the interface which, acting as a surfactant, effectively decreases the IT up to a value (≈ 21 mN/m) which is about half the supernatant in the absence of albumin. Furthermore, during the oscillatory phase, the IT responds with oscillations of significant amplitude.

In particular, figure 7.16 shows the values of the DV modulus, as a function of the frequency of the perturbation applied to the surface area of the drop, in the case of supernatant containing albumin (red curve) and DPBS containing albumin (black curve). The values shown in this graph indicate that the presence of albumin generates a considerable viscoelasticity of the interface. These data are in agreement with the results obtained for albumin solutions in DPBS, an example of which is represented by the black curves in figure 7.15 and figure 7.16. These results suggest that drug particles suspended in the supernatant do not interact with albumin and do not influence the adsorption of this protein at the interface with SO.

7.7 Discussion

The reported results are concerned with the role of endogenous surfactant molecules on the interfacial properties between SO and aqueous solutions. In particular, we considered endogenous biomolecules (albumin, γ-globulins and whole human blood serum, WHBS) that can be produced

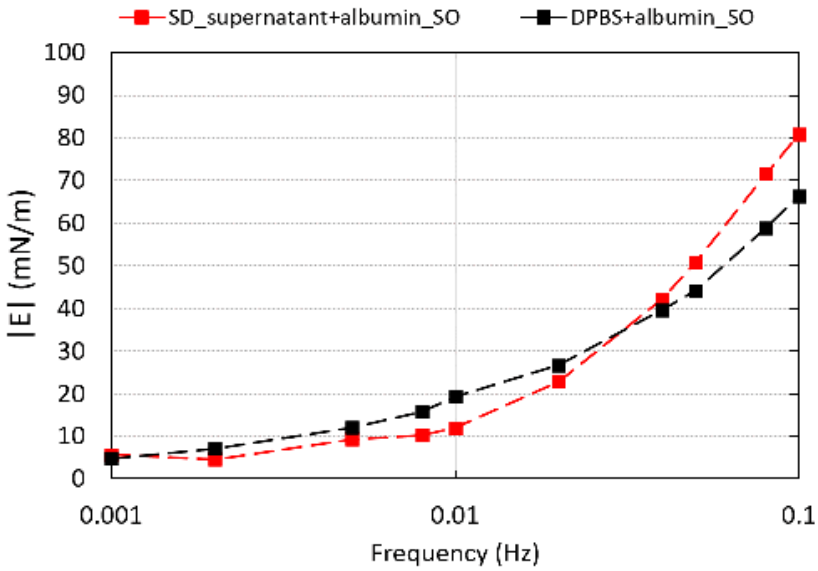

Figure 7.16: DV modulus at adsorption equilibrium measured as a function of the different perturbation frequencies. Curves refer to different albumin concentrations, whose values are normalised with the corresponding value in blood: 0.14 (black), 0.10 (red).

by inflammation of ocular tissues in response to surgery (Savion et al., 1996; Pralits et al., 2017). We studied whether such proteins can modify the interfacial properties enough to make them compatible with the generation of an emulsion. We focused on two properties: the interfacial tension (IT) and the dilational interfacial viscoelasticity (DV). The former quantity is associated with the possible generation of an emulsion: low values of IT promote the generation of emulsions. On the other hand, large values of the DV modulus confer high mechanical stability to the liquid interface, preventing droplets coalescence once the emulsion is formed and determining, therefore, its evolution in time (Santini et al., 2007; Lucassen-Reynders, 1993).

We first performed experiments with a saline buffer solution and measured values of IT similar to those reported in the literature, that almost invariably refer to the interface with pure water (Barca et al., 2014; Foster, 2008).

We then performed experiments with aqueous solutions containing blood proteins (γ-globulins and albumin). These measurements show that, even at small protein concentrations, the interfacial rheological properties change significantly and the equilibrium IT decreases to ≈ 20 mN/m, which is approximately half of its original value (interface between SO and bare buffer). This result is even more evident when human serum proteins are present in the solution. In this case, the IT decreases to values of ≈ 14 mN/m, which are compatible with the formation of an emulsion (Maldonado-Valderrama et al., 2008). We also found that both in the presence of single proteins and WHBS serum, large values of the DV modulus are attained, even 3 to 10 times larger than for ordinary surfactants. This indicates that, once formed, emulsions may be quite

stable in time. It is particularly significant that values of the IT and DV comparable to those of the single proteins are already observed if WHBS is present in trace concentrations. The surface activity of serum seems, therefore, much stronger than that of the two major proteins or of their mixtures. This calls for relevant surface active effects of other biomolecule fractions, in addition to the proteins considered here.

Results obtained from experiments involving the supernatant of the SD do not show a significant lowering of IT over time that can be associated with the formation of an emulsion, nor significant elasticity values. The measurements carried out with supernatant with the addition of albumin are in line with what was previously obtained from previous studies, highlighting that the few particles of SD in suspension do not interact with the protein forming surfactant complexes.

CHAPTER 8

SO EMULSIONS AND THEIR STABILITY

The capability of blood proteins to stabilise SO emulsions were tested with albumin, γ-globulins and albumin+γ-globulins. For this purpose, emulsification experiments are executed following a specific protocol that allows us to obtain repeatable and comparable results.

To this aim, emulsions have been produced according to the Double-Syringe method (Gaillard et al., 2017) We used two 5 ml syringes connected by a 15 mm long Luer-lock connector, with an inner diameter of 1 mm. Each syringe was initially filled with one of the two liquids to be emulsified. The liquids were then alternatively and completely exchanged from one syringe to the other by operating the system manually. Each stroke lasted about two seconds and we applied five cycles. In this way, emulsion forms due to shearing forces. The syringes were then stored in vertical position to monitor the possible separation of the liquid phases and therefore, to assess the time evolution of the emulsion. Although this emulsification method it is far from the mechanism of formation of SO emulsion in the eye, these simple screening tests are significant to compare the capability of the different protein solutions to produce stable SO emulsions.

8.1 EMULSIFICATION TESTS WITH PROTEINS

Using the Double-Syringe method, the following SO-aqueous phase systems have been investigated:

- 50% of SO and 50% of DPBS;
- 50% of SO and 50% of DPBS with albumin;
- 50% of SO and 50% of DPBS with γ-globulins;

- 50% of SO and 50% of DPBS with a mixture of the two proteins.

For each type of protein, four different concentrations have been investigated: 0.01%, 0.5%, 1%, 5%. For the mixture of the two proteins three concentrations have been considered: 0.01%, 0.1% and 1%.

Moreover, an additional experiment was conducted considering SO and buffer solution with a concentration of albumin at 1% of the physiological content in blood. This experiment is carried out in order to assess whether, using the volumes adopted in the surgical practice, the emulsion is generated in syringes. To this end, we used 80% of SO (Siluron 1000 cs, Fluoron GmbH) and 20% of aqueous solution, that corresponds to: 4 ml of SO and 1 ml of aqueous solution with albumin. This last experiment is analysed only in a qualitative way in order to understand whether or not the emulsion is generated.

Two type of analysis have been performed on the obtained emulsions: the first one consist on monitoring the emulsion formation in time through the acquisition of images of the formed meniscus evolution; the second type analys is based on observations at the optical microscope of samples of the formed emulsions.

In the last case, a small amount of the emulsion (about 0.4 ml) is diluted with the continuous phase and placed between two sterile lab slides, spaced by a 0.2 mm thick spacer, and analaysed with an optical microscope (Leica DVM6). Through the Leica Application Suite X proprietary software, micro-photos of the emulsions are taken with magnifications of 700x, 900x and, in a few cases, 1000x. Methods and results of this analysis are presented in detail in chapter 10.

Previous studies demonstrated through fluorescence microscopy, that in the case of a larger presence of SO with respect to aqueous solution with proteins, droplets of W/O are present, thus the emulsion resulted a W/O emulsion. On the contrary, if the amount of the aqueous solution is larger than the oil one, the emulsion generated resulted O/W (Soós et al., 2020).

In order to understand what kind of emulsion is formed a simple test is executed: a droplet of emulsion is posed on a sterile lab slide, then a droplet of buffer is placed near the one of the emulsion. What it is possible to see at the microscope is that, after some time, the droplet of emulsion and the droplet of buffer coalesce (see figure 8.1). This allows one to consider the emulsion as O/W. To verify this result the same test has been performed positioning an oil droplet close to a droplet of emulsion. In this case, these two phases do not coalesce, confirming that the continuous phase of the emulsion is the buffer solution resulting in O/W emulsions.

This result is confirmed by the calculations of the Stoke's terminal velocity. Considering a droplet with diameter of 15 μm and an emulsion volume 1 cm thick (sizes consistent with the observations), the terminal velocity of a SO droplet in water is equal to 3.71×10^{-4}cm/s. Thus, a drop of oil will take 45 minutes to cream. The terminal velocity of a water drop of teh same size in SO is instead 3.41×10^{-7}cm/s and it will take about 1 month to sediment. Thus, a droplet of water needs more time to separate than a SO droplet. This result suggests that the emulsion is composed by droplets of SO dispersed in DPBS.

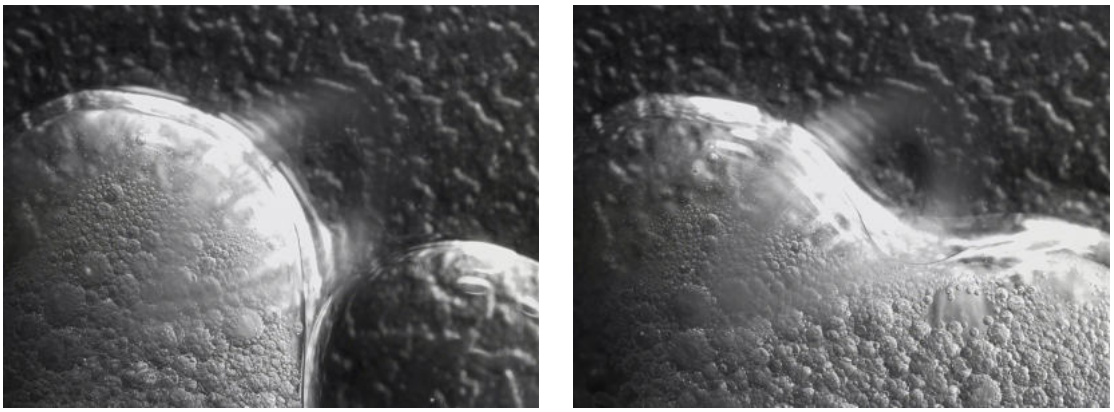

(a) (b)

Figure 8.1: Consecutive acquired frames of the coalescence test. (a) DPBS droplet (right) positioned close to the droplet of emulsion (left); (b) Occurred colescence between the two droplets.

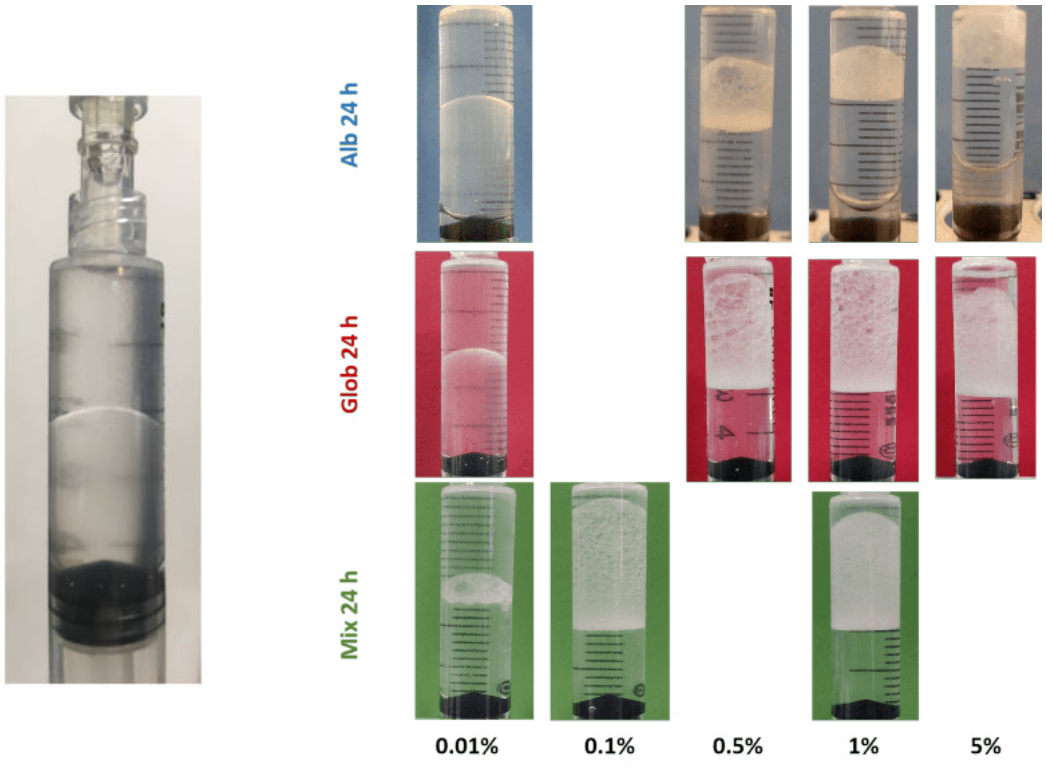

(a) (b)

Figure 8.2: Status of the emulsions obtained with the Double-Syringe method. (a) SO-DPBS 1 hour after the experiment. (b) SO vs albumin (light blue), γ-globulins (red) and mixture (green) solutions 24 hours after emulsification, for all the investigated concentrations in DPBS.

As shown in figure 8.2(a), after one hour from formation, the emulsion produced with the bare buffer is fully separated, while the situation is different for those containing the proteins as shown in panel (b) of the same figure.

In particular, in case of SO and a solution with the mixture of albumin and γ-globulins, we observed stable emulsions for all the investigated concentrations. In case of SO with aqueous solutions containing a single protein insted, a stable emulsion is observed only for concentrations of: 0.5%, 1% and 5%. For a concentration of 0.01% we only observed a modest amount of drops. We observed also that, the curvature of emulsion menisci, as well as the amount of emulsified volume, vary depending on the type and concentration of protein used.

In addition, for the solution made of 80% of SO and 20% of DPBS with albumin at 1%, the emulsion is formed (see figure 8.3), resulting stable over time scale of months. For γ-globulins solutions, these observations are comparable with those of Nakamura et al. (1990), though the authors used a different emulsification method.

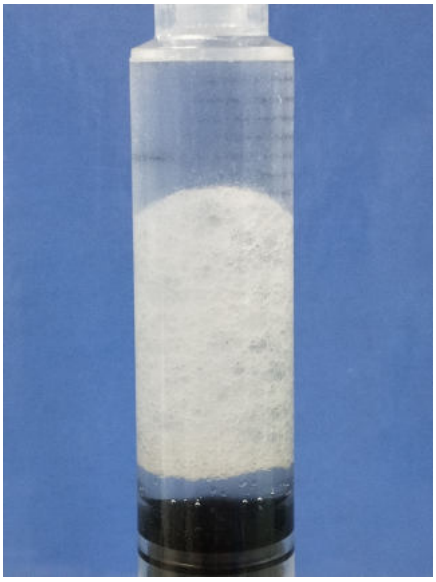

Figure 8.3: Emulsion of 80% of SO and 20% of buffer solution with albumin at 1% in syringe.

8.2 EMULSIFICATION TESTS WITH THE SD

It is known that partially hydrophobic solid particle dispersions can give rise to particularly stable emulsions, known as Pickering Emulsions (Binks, 2002). The stabilisation mechanisms of these emulsions differ from those of the surfactants, as the particles are, for energetical reasons, irreversibly adsorbed at the liquid-liquid interface. In the emulsion, the droplets of the dispersed liquid are therefore covered by an almost continuous layer of solid particles, which, due to the steric effect, prevents coalescence with other droplets. Due to this interface “solidification”

mechanism, Pickering-type emulsions can be extremely stable, in relation to those stabilised by surfactants (Ravera et al., 2021).

Since the SD product is a dispersion of hydrophobic micro-crystals, preliminary measurements were carried out to establish their potential ability to create Pickering-type emulsions even in the absence of surfactant molecules. To this aim, emulsions consisting of SO for 70% of the total volume (5 ml) and for 30% of the following aqueous phases:

- sample 0: pure DPBS;
- sample 1: SD as it is;
- sample 2: SD diluted 1: 3 with DPBS;
- sample 3: SD diluted 1: 8 with DPBS.

Figure 8.4 shows the state of the emulsions obtained with the above samples 24 hours after emulsification. For all samples containing the SD, the presence of an emulsion layer is evident whose thickness decreases with increasing dilution. The sample containing the DPBS was already separated a few minutes after the emulsion formation.

Thus, we can conclude that a dispersion of the investigated SD is able to stabilise Pickering-type emulsions. In perspective, it is therefore important to investigate cooperative effects that may arise from the interaction of drug crystals with blood proteins.

These results confirmed the ability of SO to emulsify in the presence of both biomolecules and SDs. In order to study the phenomenon of SO emulsification after vitreoretinal surgery, it is essential to conduct a study on SO emulsification in the presence of surfactant molecules under realistic conditions, both in terms of the considered domain and conditions of motion induced in the vitreous chamber due to eye movements.

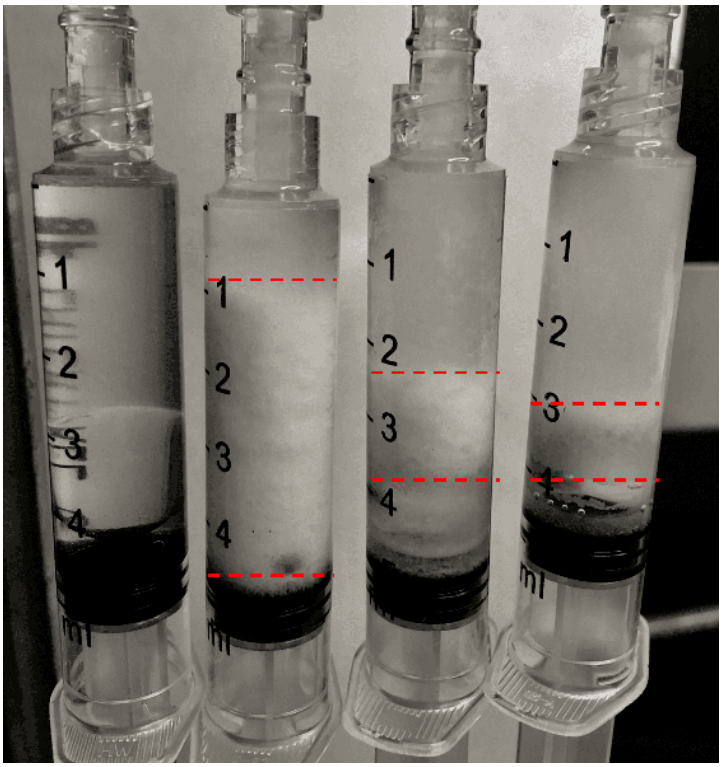

Figure 8.4: Status of the emulsions obtained with the Double-Syringe method 24 hours after emulsification. From left: sample containing pure DPBS, sample containing the SD as it is, sample containing SD diluted 1:3 with DPBS, sample containing SD diluted 1:8 with DPBS. The dashed lines in red indicate the thickness of the emulsion layer formed in each sample containing the SD.

CHAPTER 9

THE ROLE OF EYE MOVEMENTS IN THE PROCESS OF SO EMULSIFICATION

9.1 INTRODUCTION

The human eye is subject to various types of movements. The most important in inducing vitreous motion within the vitreous chamber is the saccadic motion. Saccadic movements are rapid eye rotations performed to redirect sight from a target to another. They are characterised by the following features (Wurtz and Goldberg, 1989): (i) high angular acceleration at the beginning of the rotation (up to $30000°s^{-2}$), (ii) an arrest of the rotation induced by a relatively gradual deceleration, (iii) a peak of angular velocity that increases with the amplitude of the saccade up to a value of saturation ranging between 400–$600°s^{-1}$.

On average, three saccades per second are performed with different frequency during wakefulness and deep sleep (Lisi et al., 2017). Saccade amplitudes range between 0.05° (microsaccade) to a maximum of 80-90°, which is the physical limit of the orbit (Repetto et al., 2005).

Repetto et al. (2005) use a fifth-degree polynomial function and define the angular displacement as a function of time as $\theta(t)$:

$$\theta(t) = c_0 + c_1 t + c_2 t^2 + c_3 t^3 + c_4 t^4 + c_5 t^5. \tag{9.1}$$

The most important metrics of saccadic movements are: the amplitude of the saccade represented by the variable A, the duration of the saccade, D, the peak of angular velocity, Ω_p, and the acceleration time, t_p. It is possible to consider a relationship between the duration and the amplitude of the saccade (Becker, 1989) as:

$$D = D_0 + dA. \tag{9.2}$$

A is included within the range $5° < A < 50°$, d assumes the value of 0.0025 s·deg^{-1} and D_0 is generally between 0.02 and 0.03 s. The average angular velocity during a saccadic movement is defined as $\bar{\Omega} = A/D$. The ratio between peak velocity and average velocity is approximately a constant value, equal to 1.64. For 50° saccades, the t_p/D ratio is about 0.25.

The six coefficients of equation 9.1 have to be calculated imposing the following physical conditions: $\theta(0) = 0$, $\theta(D) = A$, $\dot{\theta}(0) = 0$, $\dot{\theta}(D) = 0$, $\dot{\theta}(t_p) = \Omega_p$, $\ddot{\theta}(t_p) = 0$, where the quantities D, Ω_p and t_p are obtained from experimental evidence and from the mathematical relationships that exist between them. The resulting functions $\theta(t)$ and $\Omega(t) = d\theta(t)/dt$ obtained by Repetto et al. (2005) and shown in figure 9.1, efficiently reproduce the main characteristics of the real saccadic movements reported by Becker (1989).

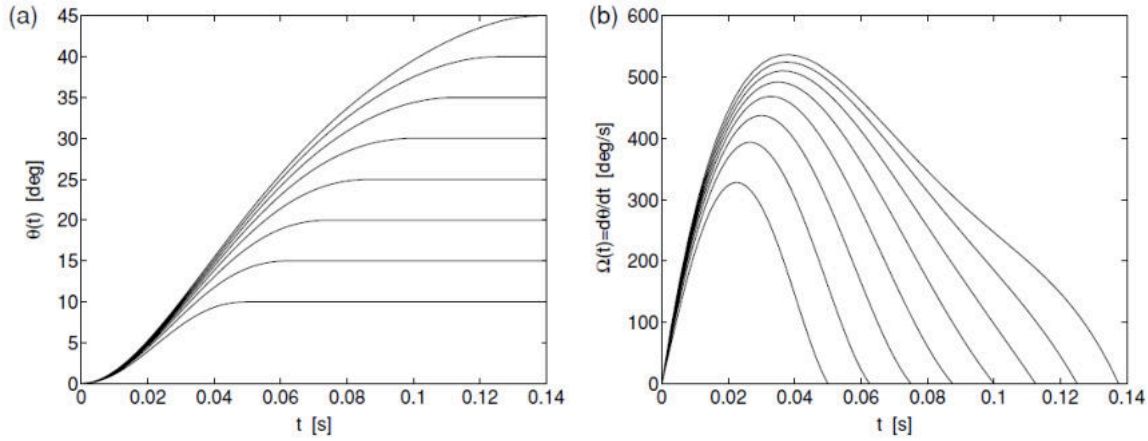

Figure 9.1: Examples of saccadic eye movements predicted by Repetto et al. (2005) using equation 9.1. (a) Angular displacement, (b) angular velocity.

Bonfiglio et al. (2015), David et al. (1998) and Meskauskas et al. (2011) describe saccadic movements as purely sinusoidal rotations:

$$\epsilon(t) = A\sin(\omega t), \tag{9.3}$$

where ϵ represents the angular displacement of the eye globe, while ω the angular frequency, t is the time. On the other hand, Wang et al. (2020) represent saccadic rotations as alternate rectangular pulses of duration D and latency time L between each pulse.

All these time laws provide information that can be used to compute the angular displacement of the vitreous body caused by saccadic rotations. The motion generated inside the vitreous chamber, firstly, can produce a shear stress on the wall of the eyeball and this can cause a retinal detachment (Repetto et al., 2005; Dyson et al., 2004; David et al., 1998). Secondly, it can be one of the reasons for the formation of an emulsion between SO and the fluid present in the vitreous chamber of vitrectomised eyes (Yilmaz and Güler, 2008).

In this chapter we present an experimental study aimed at investigating the effects of mechanical energy provided by periodic eye movements on the emulsion formation in a physical model of the vitreous chamber of the eye in the presence of surfactant biomolecules. Results reported in the following, are aimed at describing the emulsification process in a qualitative way, in order to assess the main features characterising the emulsification mechanism, such as the time scale of the process and the equilibrium shape of the interface. A quantitative analysis is shown in chapter 10.

9.2 Materials and methods

9.2.1 Experimental setup

A model of a vitreous chamber in Plexiglass has been employed. The considered domain has been developed in order to simulate the real physiological conditions in terms of temperature and geometry. The eye model consists of a cylindrical container, with a spherical cavity of 12.5 mm of radius. In order to obtain a more realistic geometry, a lens was glued inside the spherical cavity with the aim to reproduce the indentation produced by the lens. The lens has a volume of 916.3 mm^3 and it is made of black PLA (figure 9.2). The shape of the lens has been designed in order to adhere perfectly to the spherical wall of the cavity and in order to ensure the real physiological distance (15 mm) between the back pole of the lens and the posterior wall of the sphere, which represents the retina (Nogueira et al., 2011; Atchison and Smith, 2000).

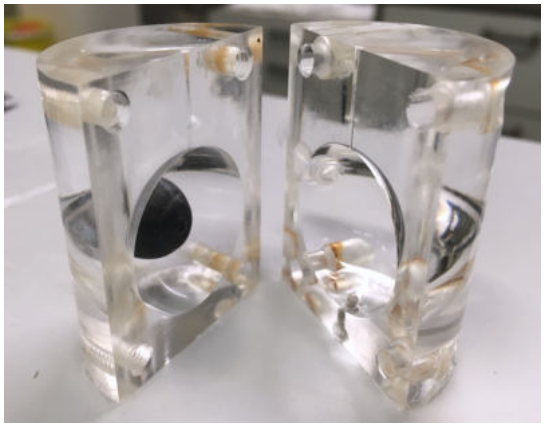

Figure 9.2: Eye model with the lens.

The experimenal setup consists of a mechano-fluid dynamic simulator of the saccadic rotations, made up of a table equipped with a shaft set in motion by a motor, which is controlled by computer (figure 9.3). The motor is controlled through a LabView program developed for previous studies at DICCA. The LabView interface allows one to generate a sinusoidal function with a given amplitude and frequency, repesenting the axial rotation to be applied to the eye model.

In order to verify if the motor performs the movements imposed by LabView, a second software has been considered: MOOG (*WinDrive)*. This software allows the operator to compare the waveform generated by the program and the one executed by the motor, with the aim of evaluating wether the motor moves in the correct way.

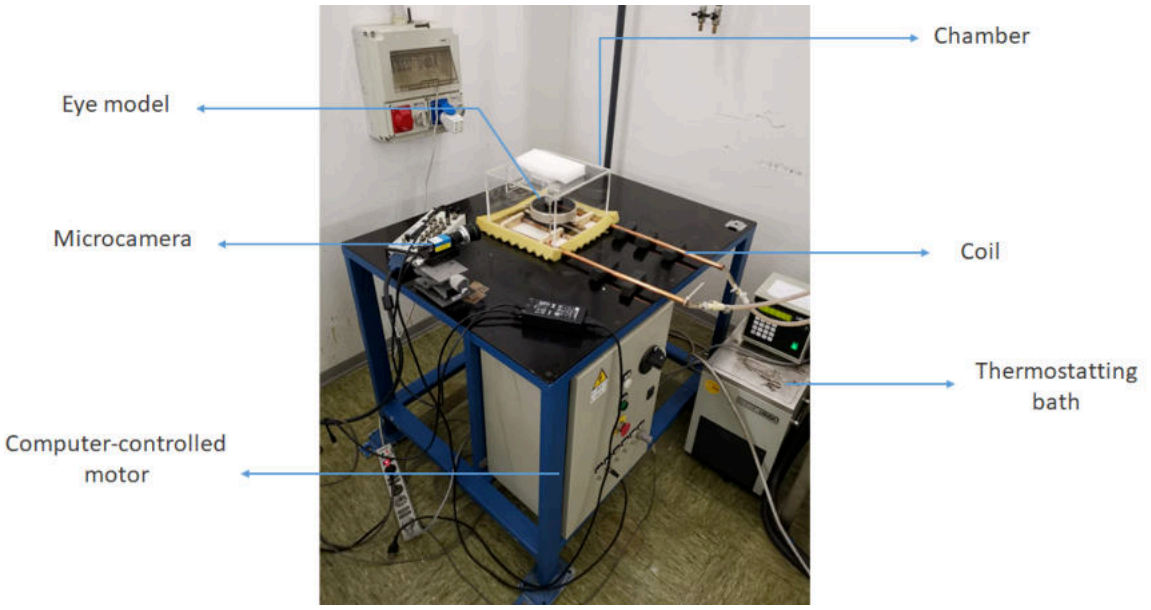

Figure 9.3: Picture of the experimental apparatus.

In order to perform the experiments with a temperature close to that of the physiological condition, the rotating stage to which the eye model is anchored, is covered by a thermostated chamber. The chamber consists of an insulated base (26×26 cm) and a removable plexyglass covering parallelepiped. The temperature inside the chamber was maintained by pumping water of a thermostatic bath (RC 6 CP LAUDA) in a copper serpentine in the chamber, as shown in figure 9.3. The thermostatic bath was calibrated at T=75°C in order to ensure a constant temperature equal to 35°C within the chamber.

The eye model was monitored in real time by a GigE monochrome industrial micro-camera (IMAGING SOURCE,) equipped with a 15 mm lens. The camera resolution is 1600×1200 (1.9 MP), its frame rate is up to 20 fps and the sensor used is the Sony Pregius CMOS Global Shutter. The camera was mounted on a micropositioning stage that allows one to place it at the right distance from the target (figure 9.3). Using this optical systems, we captured movies of the entire duration of each experiment and we also acquired pictures of the eye cavity at the beginning, 10 minutes after the beginning of the test and at the end of the experiment (see figure 9.4). These pictures allowed us to perform a first qualitative analysis of the formation of the emulsion. In particular, it has been possible to evaluate from the macroscopic point of view, the formation of new droplets during the experiment, which were thus not due to the injection phase.

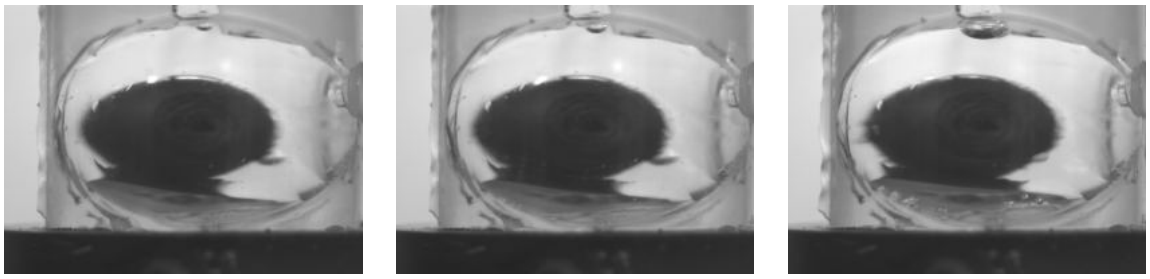

(a) (b) (c)

Figure 9.4: Example of acquired pictures at different times of the experiment: (a) $t = 0$, (b) $t = 10$ minutes, (c) $t = 1$ hour.

9.2.2 FILLING OF THE EYE MODEL

Before of any operations the eye model underwent a cleaning procedure, following the standard surface cleaning protocol, in order to remove all the possible impurities. Then, a layer of inert rubber was placed between the two halves of the cylindrical model and as a seal. The external rims were in addition covered by vaseline as a further sealing barrier. Finally, the two halves of the eye model were assembled and fixed together by four screws covered with teflon. For the filling procedure of the eye model a hole located on the side of the model has been exploited. The air has been put out from a second aperture at the top of the model.

The total volume of the spherical cavity with the presence of the lens is 7.261 ml. Literature considers the percentage of aqueous solution with proteins contained in the eye to be at least 10% of the total volume. In these experiments we decided to introduce 20% of aqueous solution with proteins. The solutions containing endogenous molecules were prepared with the same modalities described in section 7.1, with different concentrations of albumin (0, 1 and 5% of the corresponding concentration in blood). The choice to use albumin is due to the fact that, as shown in chapter 7, albumin has a surface-active behaviour comparable to that of the mixture of albumin and γ-globulins. Once the eye model was filled with the aqueous solution containing proteins, the inner walls of the model was treated in order to ensure a homogeneous wettability and then, the remaining part (80% of the total volume),was filled with SO. The study involved the use of a SO used in ophthalmic surgery, the RS-OIL 1000 cSt (Alchimia srl).

During the filling phase, some air bubbles may remain trapped in the vitreous chamber of the model. Removal of these bubbles can become impractical as applying any stress to the inserted fluids, could compromise the integrity of the experiment. The presence of these bubbles does not affect either the qualitative or the quantitative analysis under the microscope (chapter 10) as they are totally distinguishable from the drops of oil and water.

Albumin conc. (%)	Amplitude (deg)	Amplitude (V)
0	50	10.53
1	50	10.53
1	40	8.42
1	30	6.31
5	50	10.53
5	40	8.42
5	30	6.31
5	20	4.14

Table 9.1: List of the performed experiments.

9.2.3 SIMULATION OF SACCADIC MOVEMENTS

Once filled, the eye model is mounted on a support connected to the computer-controlled motor. In this study, harmonic rotations were considered: this choice is suggested by the fact that a harmonic law is the simplest way to represent a sequence of saccadic eye movements in both directions with prescribed amplitude and duration, according to equation 9.1.

The model has been tested for different values of amplitude (20°–50°) and with an imposed frequency equal to 5 Hz, for the duration of 1 hour, comparable with those reported in the literature. All performed experiments are summarised in table 9.1. In order to assess the reproducibility of the experiments, we conducted two tests with the same set parameters, obtaining the same results both in terms of time scale of the emulsification process and of the observed emulsion.

The motor is controlled by two parameters: the frequency (Hz) and the amplitude (V). In order to define the voltage value that corresponds to the degrees of interest, we carried out a calibration of the instrument, adopting the software MOOG. In particular we compared the signal imposed by LabView to the motor and the one recorded by MOOG. Two frequencies have been considered for the calibration: 1 Hz and 8 Hz. For each value of frequency, ten amplitudes values have been imposed in the range of $1 \div 10$ V. In this way, for each value of frequency, ten waveforms are considered. Each waveform is characterised by several values of amplitude; the maximum and the minimum of these values have been aquired in order to define the average amplitude for each value of the same imposed amplitude. The average value is defined as the half of the sum between the maximum and the minimum amplitude value.

9.3 RESULTS

Figure 9.5 shows that the experiment with the sample containing DPBS alone, did not produce emulsions in the eye model. This result demonstrates that the presence of a small amount of slightly surface-active impurities in the oil (low molecular weight components) cannot favour

the emulsification process. This finding confimed the results related to the interfacial properties obtained both in terms of IT and DV, as shown in section 7.3, and the preliminary emulsification tests performed with the Double-syringe method (figure 8.2).

Another interesting result concerns the equilibrium shape of the interface found both before and at the end of the experiment (see figure 9.5). We observed that the equilibrium configuration of the interface is in agreement with results obtained by Isakova et al. (2017) both in the posterior-anterior and nasal-temporal directions.

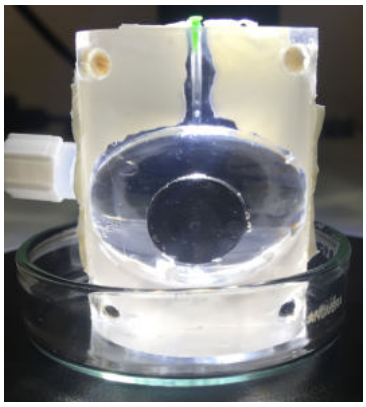

Figure 9.5: SO-DPBS 1 hour after the experiment: no emulsion is present in the vitreous chamber model.

When proteins are dissolved in the aqueous solution what is observed in the vitreous chamber of the model is significantly different. In particular, we found formation and persistence of emulsions even when a low concentration of albumin was present (1% of the physiological concentration in blood) and for $A > 30°$, as shown in figure 9.6. The obtained emulsions for a rotation amplitude of 40° and 50° appear very dense and with a layer of emulsion at the top part of the interface, that increases in thickness with increasing amplitude.

The equilibrium shape of the interface at the end of the experiment is also very different. This does not remain confined at the bottom of the lens, as in the case of DPBS in absence of proteins, but reaches the upper part of the eye cavity, above the lens. This behavior could depend on the wettability of the wall in the presence of biomolecules and on the density of the SO droplets formed.

Emulsion formation was recorded by the digital camera. Already in the first 10 minutes of rotation of the eye model formation of an emulsion was observed; an example is reported in figure 9.7. From the image it is possible to observe an entire opaque area around the lens whose edge (the interface) determines a shape that is not the definitive one (figure 9.6(b)), as it is still subject to motion.

Moreover, keeping the formed emulsions on static conditions at room temperature, the situation did not change significantly after 1 week, showing that the emulsions are stable in time.

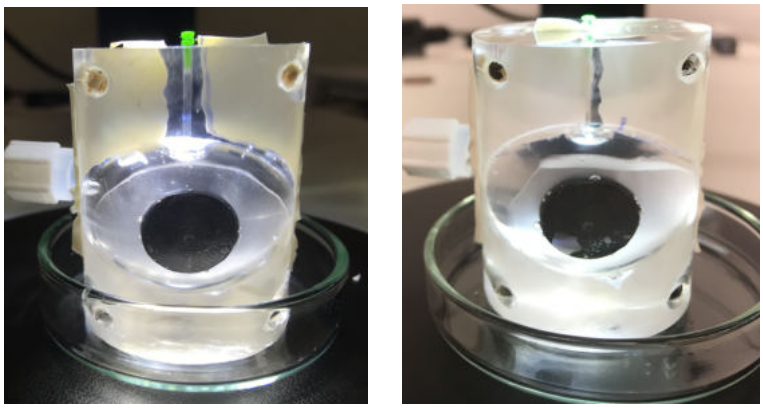

(a) (b)

Figure 9.6: 80:20 volume ratio emulsions between SO and aqueous phases containing an albumin concentration of 1%, 1 hour after formation and with different amplitudes (A); (a) $A = 40°$, (b) $A = 50°$. The formed emulsion is the visible opalescent area around the lens.

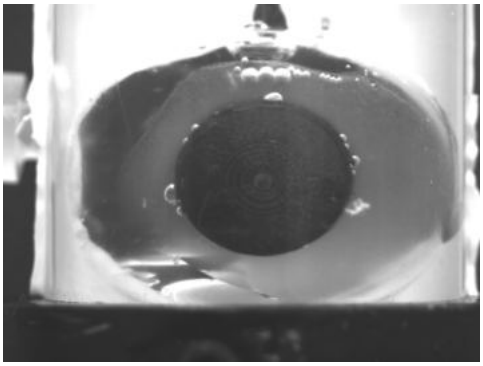

Figure 9.7: Acquired image by the digital camera at $t = 10$ minutes from the beginning of the experiment. Albumin concentration 1%, imposed amplitude $A = 50°$.

Results obtained with a concentration of 5% of albumin in aqueous solutions are shown in figure 9.8. Also in these cases, we observe the presence of emulsions with a more concentrated layer of droplets which increases in thickness with increasing of the imposed rotation amplitude.

With a higher concentration of albumin we observe an appreciable formation of emulsion even for an imposed amplitude of 30° and with an equilibrium interface configuration very similar to those obtained with a lower concentration of albumin (figure 9.8(a)).

Emulsions obtained with higher values of amplitudes (figure 9.8(b,c)) show an interface with a more wavy shape, almost as if to reproduce the shape of the lens.

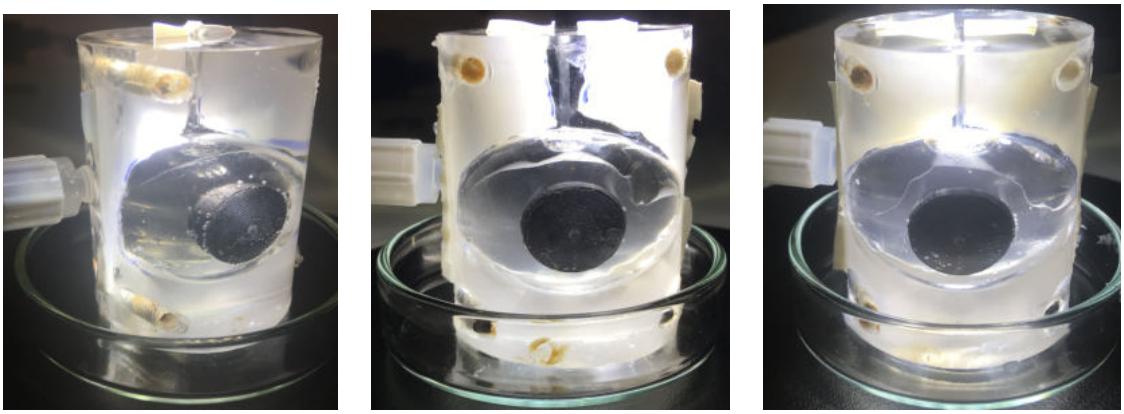

(a) (b) (c)

Figure 9.8: 80:20 volume ratio emulsions between SO and aqueous phases containing an albumin concentration of 5%, 1 hour after formation and with different amplitudes: (a) $A = 30°$, (b) $A = 40°$, (c) $A = 50°$.

9.4 Discussion

Recently Wang et al. (2020) tried to produce emulsions in a spherical model of the vitreous chamber using SO and aqueous solutions with the addition of albumin. The eye model was subject to motion for several minutes and the interface between the two liquids was monitored with a camera and then analysed through a microscope. The authors never observed the formation of an emulsion. The formation and persistence of bulk emulsions observed in our study could be thus correlated to the experimental conditions which are closer to the physiological ones. In fact, the model of the eye adopted in our experiments is equipped with the lens (more realistic geometry) and furthermore, for the entire duration of the measurements, the vitreous chamber is kept at a temperature close to that of the human body.

Results of this qualitative analysis provided information about the mechanisms underlying the emulsion generation and their time scales as a function of the quantities of surface-active molecules, thus, from a macroscopic point of view. In particular, we observed dense emulsions with $A > 20°$ and $A > 30°$ for solutions containing albumin at 5% and 1%, respectively. In chapter 10, a quantitative analysis carried out through microscopy will be illustrated, with the purpose of evaluating the characteristic dimensions of the droplets and the type of emulsions formed after each experiment.

All the values of frequency and amplitudes imposed in the present analysis are comparable with those reported in the literature and, in these conditions, the eye model rotations correspond to eye quick clicks to one and the other direction. Obviously, this cannot be considered a realistic eye movement for a long time but, in the case of a duration of few seconds, this movement becomes realistic. Considering that the emulsion forms starting from the first minutes, it is

reasonable to think that the emulsification can occur when these short movements are repeated for fairly frequent intervals.

These findings demonstrate that eye movements and the presence of surfactants can be considered as co-factors in SO emulsification after vitrectomy.

CHAPTER 10

QUANTITATIVE CHARACTERISATION OF SO-EMULSION DROPLET DISTRIBUTION

The size of the emulsion drops plays an important role among the clinical consequences that can arise after vitrectomy. In particular, the smallest droplets appear to be correlated with most of the serious complications associated with SO emulsification. Therefore, a quantitative analysis aimed at investigating the drop size distribution of SO emulsions could be clinically relevant. In this chapter, we show a microscopy analysis aimed at identifying the characteristic dimensions of the found droplets as results of the emulsification tests conducted in chapters 8 and 9, as a function of the proteins concentration dissolved in the aqueous solution.

10.1 MICROSCOPE IMAGE ACQUISITION

At the end of each experiment described in chapter 9, the eye model has been removed from its support and the emulsion inside has been characterised with a microscope analysis. For this purpose, a DVM6-M optical microscope (Leica, Hamburg, Germany), with a CMOS sensor (3664×2748 pixel) and equipped with PlanAPO FOV 3.60 objective, which guarantees a maximum resolution of 2366 lp/mm, has been used to determine droplet distribution and size.

As a first step, images of the content of the spherical cavity are captured with magnifications of 200x, directly placing the eye model under the microscope. This allowed us to locate the formed emulsions within the vitreous chamber and to observe possible coalescence phenomena.

Once the existence of an emulsion was identified, when the volume of emulsion was sufficient, samples have been taken from the model and analysed on microscope glass slides. Only when the amount of emulsion was not enough to be collected, namely when the drops were al-

ready sufficiently disperse and less than 100 per image, the characteristic sizes of droplets were evaluated directly from the images taken with the fluid still in the vitreous chamber model.

A coalescence test was carried out with a sample to determine the type of emulsion formed and it was possible to establish that we are in presence of an O/W emulsion, as described in chapter 8. Once the continuous phase of the emulsion has been determined, It was then possible to proceed with the analysis of the droplet distribution: a small amount of the emulsion (about 0.4 ml) was diluted with the continuous phase (i.e. the aqueous solution) in order to obtain a good spacing of the droplets, and placed between two sterile microscope slides, kept at a distance of a 0.2 mm by a spacer. It should be noted that the collected quantity is equal to 5.5% of the total volume of the vitreous chamber model and that it is in turn diluted with an amount of aqueous solution that can vary from sample to sample. The reproducibility of this method is therefore affected by an experimental error which we are not able to estimate, due to the variability of the observed samples. It is however important to underline that the dilution with the same solution as the matrix phase, while spacing the droplets in the emulsion, simplifying the analysis of the acquired pictures, does not change their size distribution.

Using the Leica Application Suite X proprietary software, micro-photos of the emulsions have been taken with different magnifications of 700x, 900x and, only in a few cases 1200x. The use of different magnifications affected the resolution of the acquired image, which in our case may vary in the range of 0.2 – 0.7 μm. These resolutions are comparable with the physical limits of the optical microscopy. Moreover, for the present analysis we considerd drops with diameters above 1 μm. For each sample about 10 images were acquired, sufficient to cover the entire sample.

All the acquired images of the emulsions were then analysed through the same software. A specific tool of this software allows the operator to highlight all drops within an image and, for each one, the perimeter is automatically traced from the definition of three points on the boundary of the droplet. In this way, the software is able to define a circle that identifies the droplet of interest. Finally, this application returns all the characteristic dimensions (radius, diameter, area, etc.) of the emulsion droplets detected manually. An example of manual detection performed with Leica Application Suite X is reported in figure 10.1. Since SO droplets reflected the light of the microscope, droplet boundaries could vary of 1-2 μm in thickness. For the present analysis we considered the external diameter for all the droplets. The size of the large drops can therefore be affected by an error of about 1 μm.

This analysis has been performed also for samples of emulsion obtained with the Double Syringe method (chapter 8), since a procedure well recognised for the characterisation of emulsions (Dziza et al., 2020).

In order to define a size distribution of the detected droplets for all investigated systems, the image analysis has been carried out considering different ranges of diameters and counting the total number of droplets for each range. Moreover, for each test, we evaluated the surface

occupied by the emulsion droplets over the total area of the acquired images, S. This quantity was computed as

$$S = \frac{\sum_{k=1}^{N} \sum_{i=1}^{M_k} s_k^{(i)}}{\sum_{k=1}^{N} A_k}, \tag{10.1}$$

where N is the number of considered images, M_k is the number of droplets in the k-th image, A_k is the area of the k-th image and $s_k^{(i)}$ is the area of the i-th droplet in the k-th image. This dimensionless number S allowed us to compare images obtained with different magnifications in terms of area occupied by the droplets.

The statistical analysis we performed is based on the hypothesis that the drops observed on the focal plane of interest were a sufficiently representative sample of those of the emulsion. Moreover, we grouped the drops into size classes that have an amplitude (5 μm) much greater than the error we could make in estimating their diameters (< 1 μm).

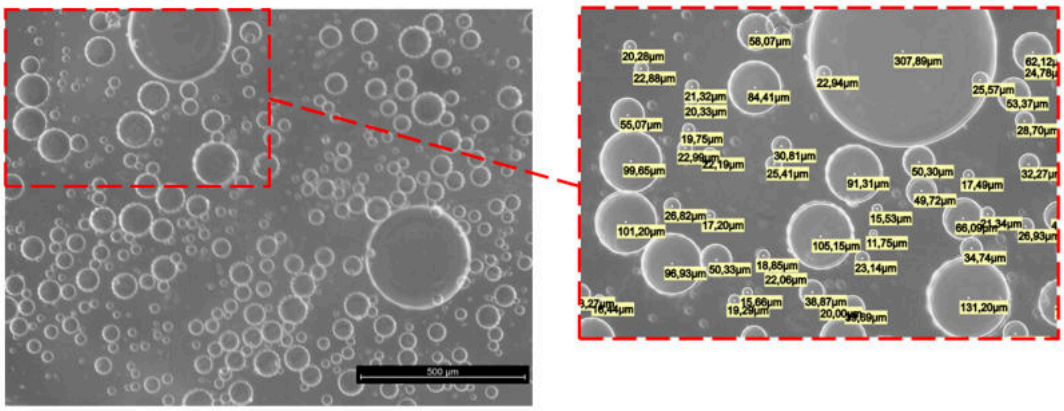

Figure 10.1: Example of drop detection.

10.2 RESULTS RELATIVE TO EMULSIONS IN THE EYE MODEL

An important result obtained from this analysis is that we did not detect emulsions, even after observation with the microscope, in absence of proteins in aqueous solution. This finding is in agreement with the studies performed on interfacial properties conducted in chapter 7.

Another interesting result is provided by the coalescence tests, which confirmed that all the emulsions found in our experiments are of the O/W type, in agreement with the Bancroft rule (Bancroft, 1913).

Through this quantitative analysis we were able to assess that an emulsion has been generated during all the tests containing albumin in the aqueous solution, also for experiments with the lowest rotation amplitudes for each investigated albumin concentration (1% with A =

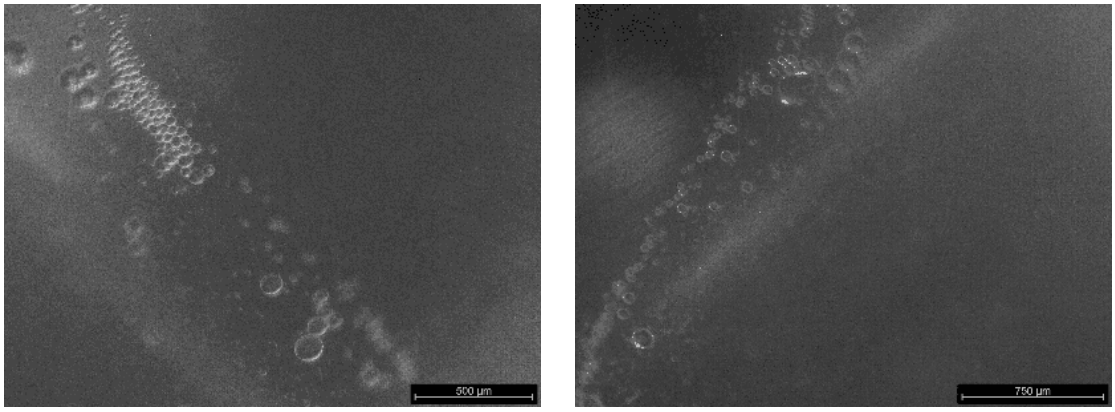

Figure 10.2: Microscope images of the emulsion formed. Albumin at 1%, $A = 30°$.

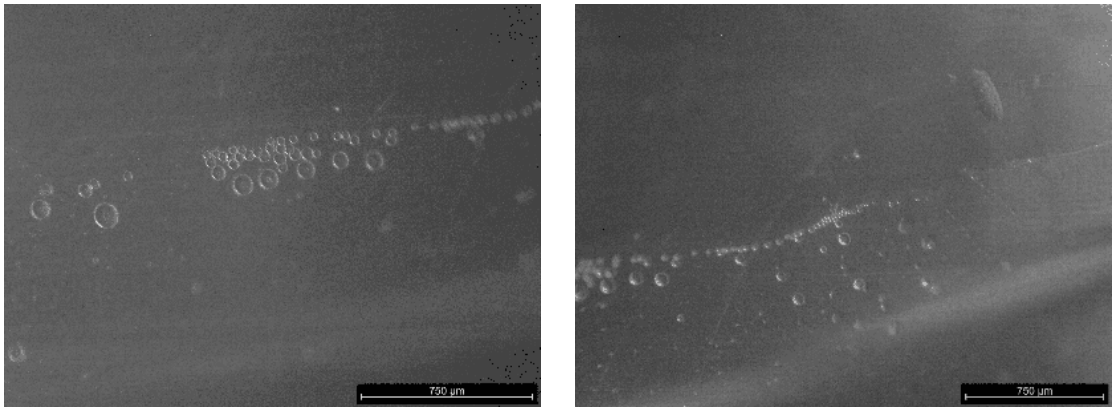

Figure 10.3: Microscope images of the emulsion formed. Albumin at 5%, $A = 20°$.

30° and 5% with $A = 20°$), as shown in figures 10.2 and 10.3. The reported images have been acquired directly by observing the model of the eye with the optical microscope. Inspection of these images shows the presence of oil droplets with different sizes formed at the interface between the two fluids. In fact, after each experiment, the greatest concentration of drops was observed with the microscope at the interface between the two fluids, in the upper part of the model, as presented in chapter 9. An example is reported in figure 10.4.

Figures 10.5 e 10.6 refer to tests conducted with an albumin concentration of 1%, with imposed amplitudes of 40° and 50°, respectively. These images clearly confirmed the presence of different populations of drops, as well as entire areas of submicrometric droplets, too small to be detected by the software. In fact we note that the droplet size distributions presented in the following will not account for diameters smaller than one micron.

Some images related to experiments with a concentration of albumin of 5% are reported in figures 10.7, 10.8 and 10.9 for different values of rotation amplitude. In general, the detected

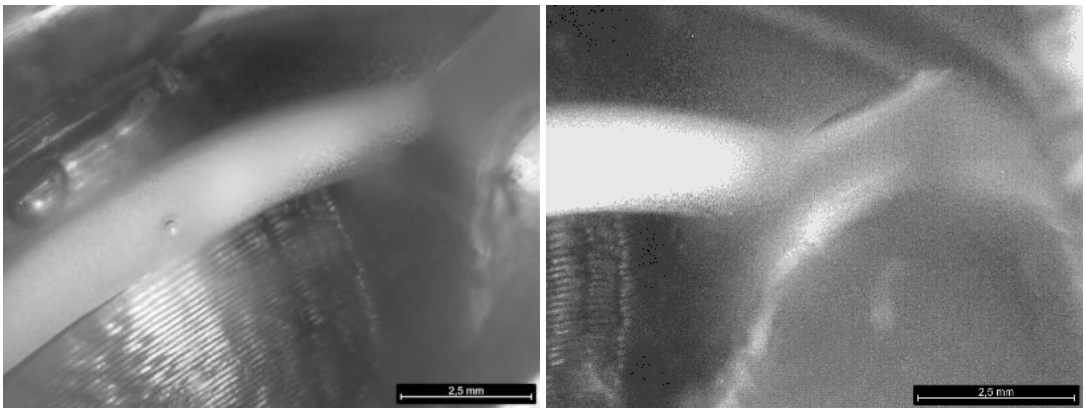

Figure 10.4: Example of microscope images acquired to localise the formed emulsion in the vitreous chamber of the eye model. It is possible to observe the emulsion, a portion of the interface between the two fluids and the lens below.

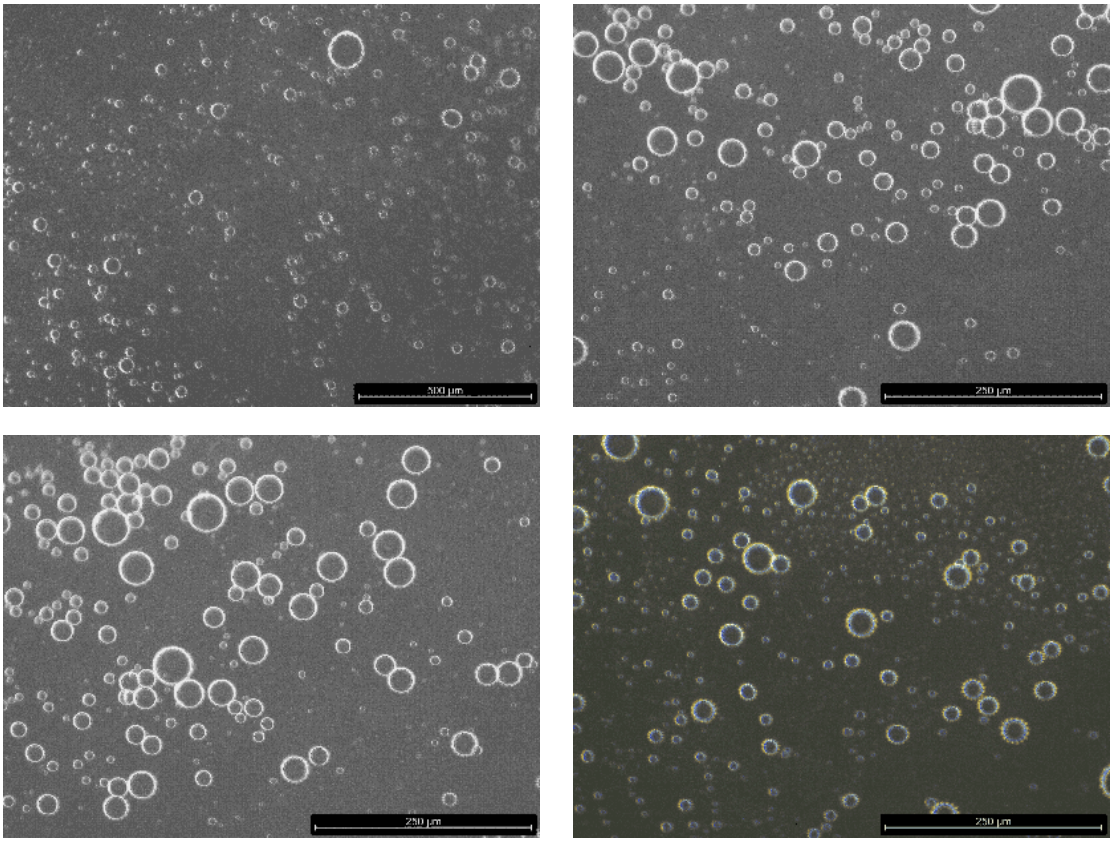

Figure 10.5: Microscope images of the emulsion formed. Albumin at 1%, $A = 40°$.

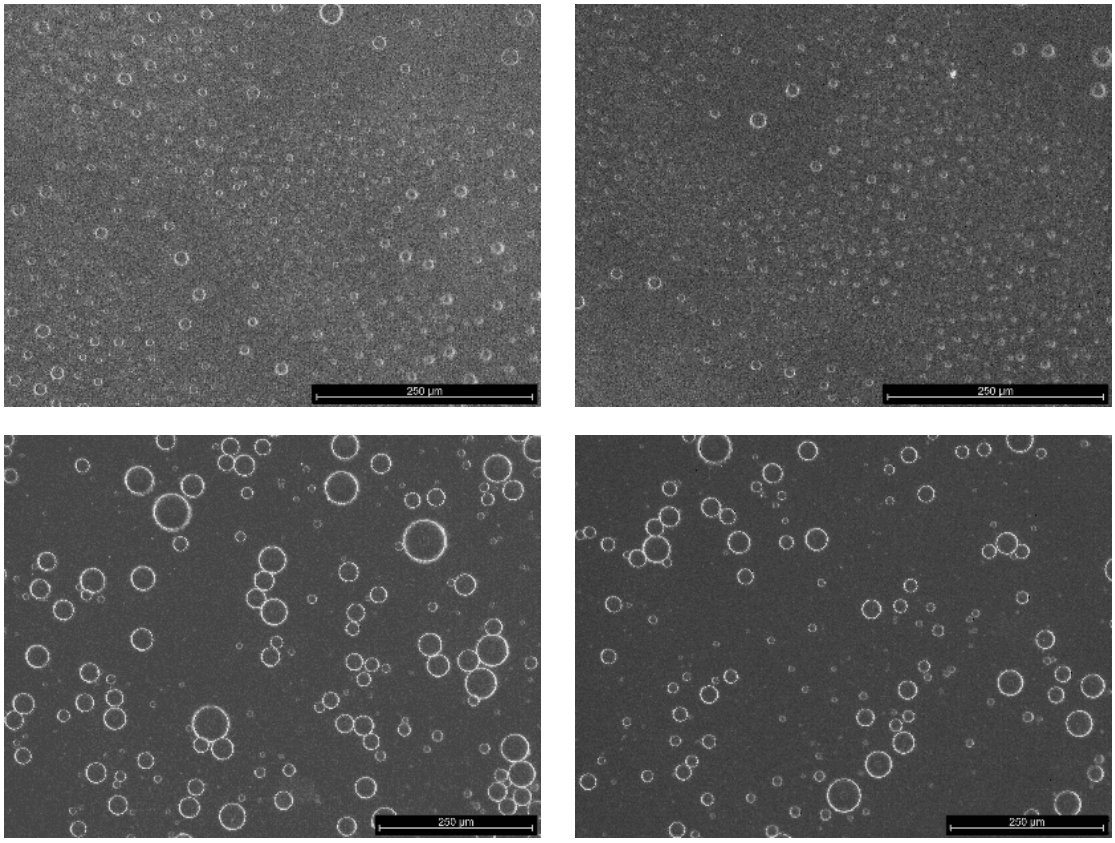

Figure 10.6: Microscope images of the emulsion formed. Albumin at 1%, $A = 50°$.

drops were similar to those observed in the case of 1% of albumin concentration. However, for an amplitude of 50° a significantly larger area occupied by droplets for each image can be observed, as shown in figure 10.9.

This finding has been confirmed by result reported in figure 10.10, where we plot the parametes S, defined earlier, as a function of the imposed amplitude. In this plot the red curve corresponds to the concentration of albumin at 1%, the black curve to that at 5%. It is interesting to note that the curves seem to have the same behavior and, as mentioned before, for albumin concentration of 5% and with $A = 50°$, S resulted higher with respect all the other tests. We did not perform tests with values of $A > 50°$ since unrealistic conditions for ocular physics. However, these results must be interpreted with care, since each emulsion sample could be subject to experimental error of different origin, such as the amount of solution used in order to guarantee the dilution of the sample.

Through images analysis acquired by the microscope, we have been able to obtain information about the drop size distribution, for each investigated system. The droplet distribution according to the range of the considered diameters is shown in figure 10.11. The two plots refer to the two investigated concentrations of albumin. Moreover, different colors correspond to

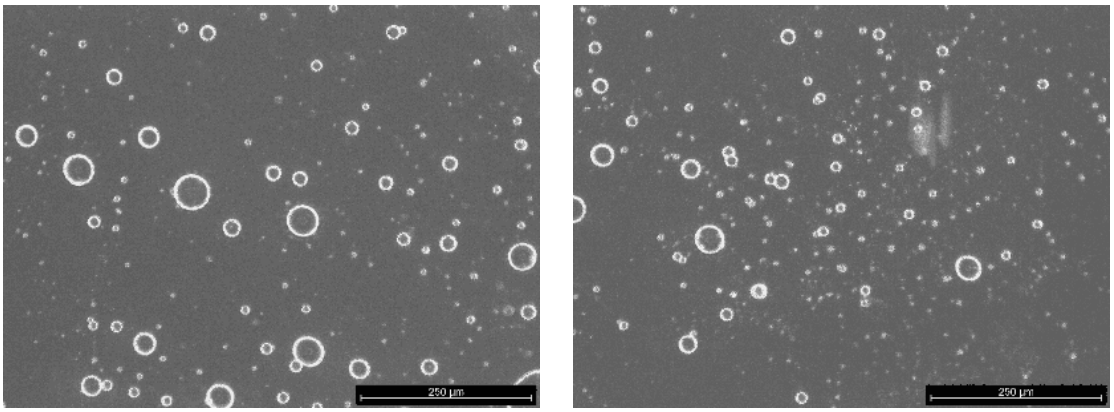

Figure 10.7: Microscope images of the emulsion formed. Albumin at 5%, $A = 30°$.

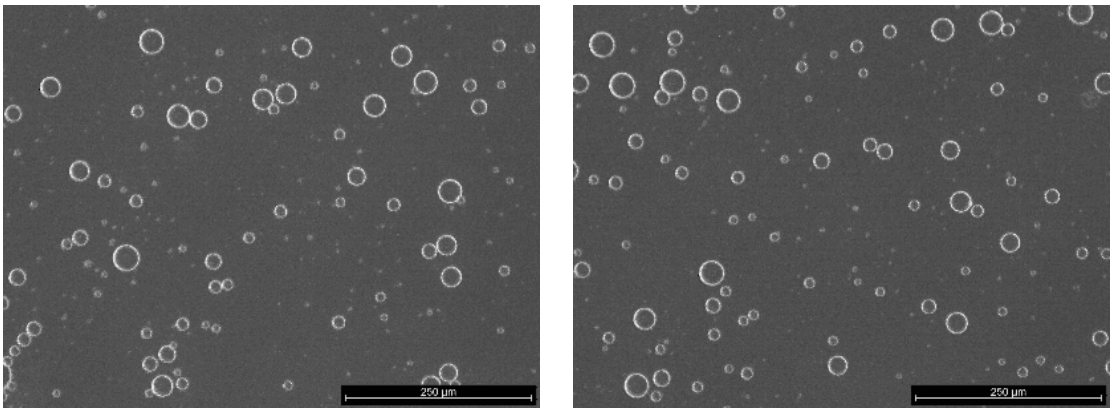

Figure 10.8: Microscope images of the emulsion formed. Albumin at 5%, $A = 40°$.

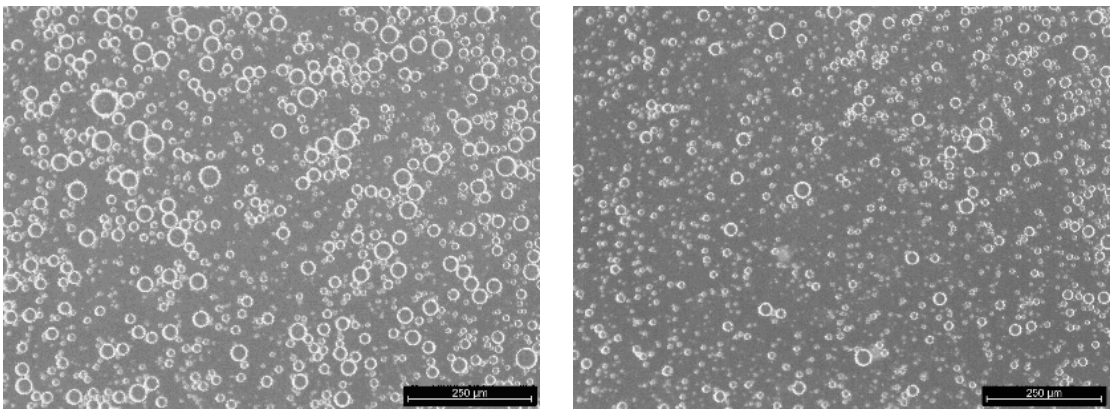

Figure 10.9: Microscope images of the emulsion formed. Albumin at 5%, $A = 50°$.

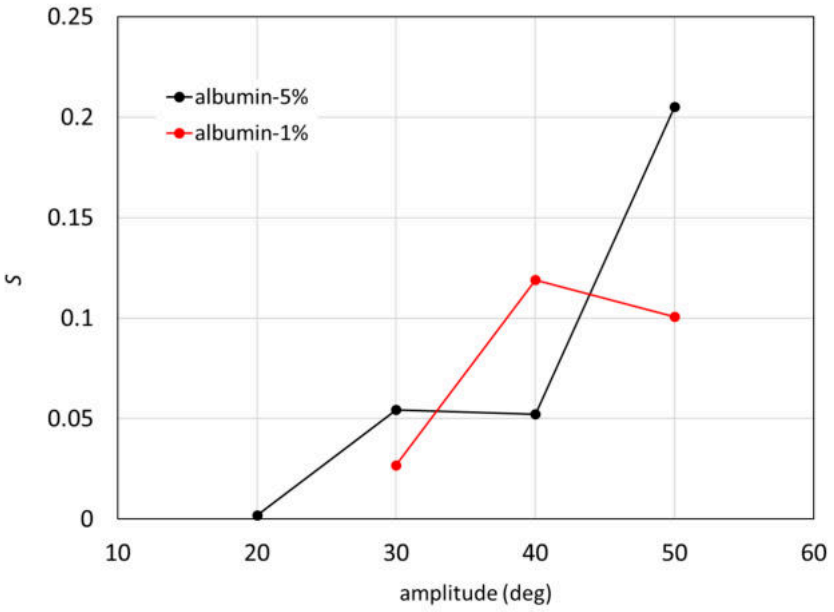

Figure 10.10: Surface area occupied by droplets with respect to the area of the acquired images (S), as a function of the imposed amplitude. Different colours correspond to different albumin concentration.

different imposed amplitudes and each considered range of diamaters has an interval of 5 μm.

In general, as shown in the normalised droplets distributions, the majority of the drops had a very small diameter: in the range of $0-5$ μm. The two curves corresponding to the $A = 20°$ and $A = 30°$ for albumin concentrations of 5% and 1% respectively, showed instead droplets of larger diameters. This result suggests a dependency of the droplet size on the imposed amplitude. In fact, for both investigated albumin concentrations, we observed that by increasing the A, the droplet diameters generally decreased.

10.3 Results of emulsification in syringe

In this section we report the distributions of the diameters obtained from the quantitative analysis carried out on the emulsions generated in syringe.

Droplet size distributions for different albumin and γ-globulins concentrations are shown in figures 10.12(a) and 10.12(b). In both cases, investigated proteins had most of the droplets diameters between $10-30$ μm and their distributions are comparable with Poisson distributions. Moreover, no particular differences are observed between the various concentrations.

In figure 10.12(c) we show the comparison between distributions of the droplets obtained with a concentration of 1% of albumin, γ-globulins and mixture in the aqueous solutions. Also in this case, the three curves are comparable.

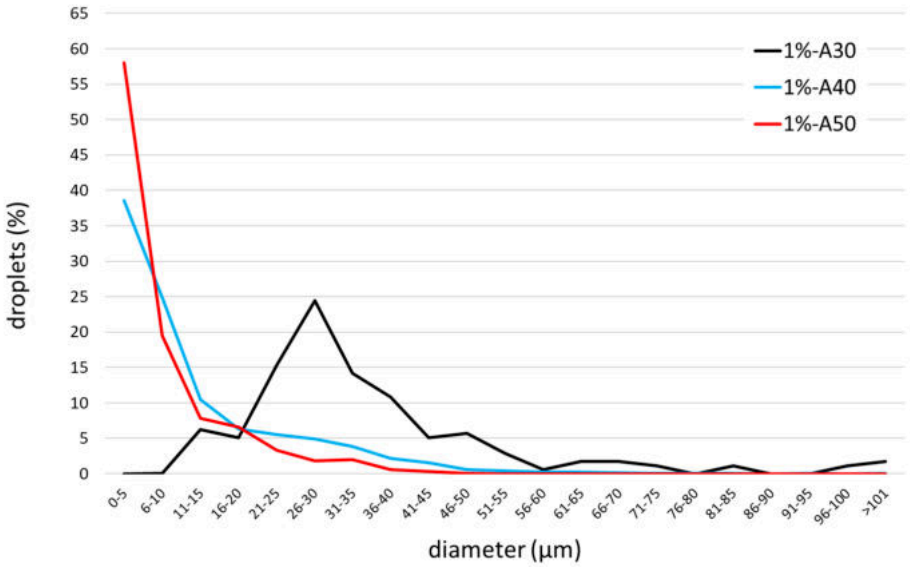

(a)

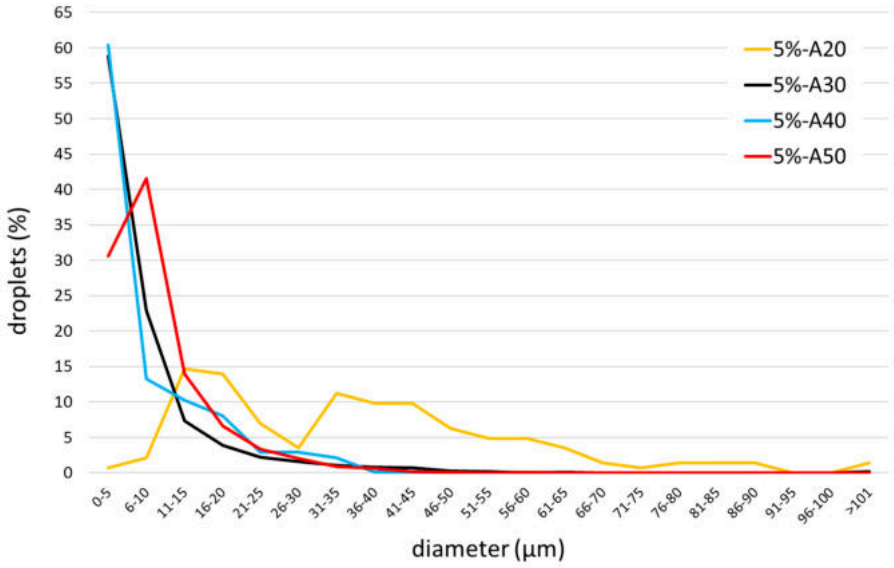

(b)

Figure 10.11: Droplets distributions for all the investigated amplitudes. (a) Solutions containing albumin with concentration of 1%; (b) solutions containing albumin with concentration of 5%. Different color bars correspond to different imposed amplitudes.

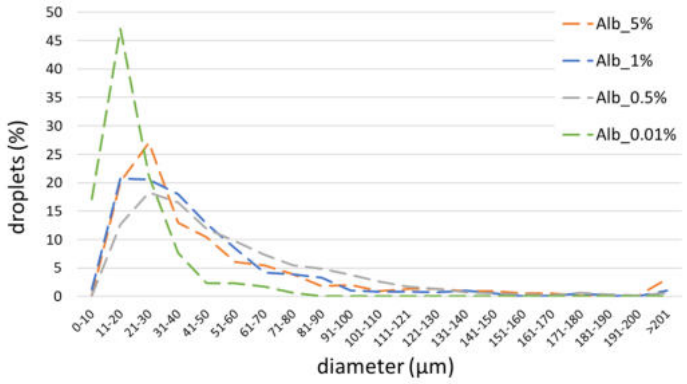

(a)

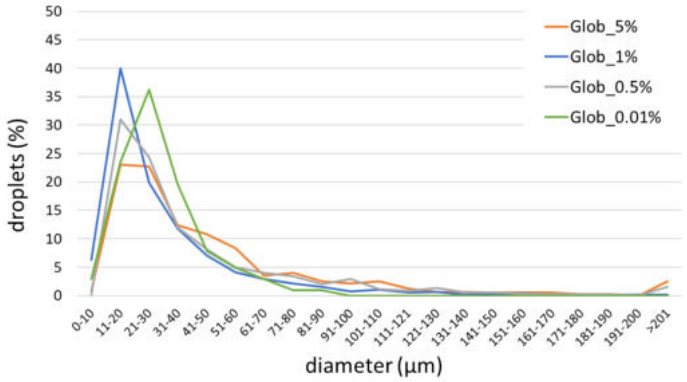

(b)

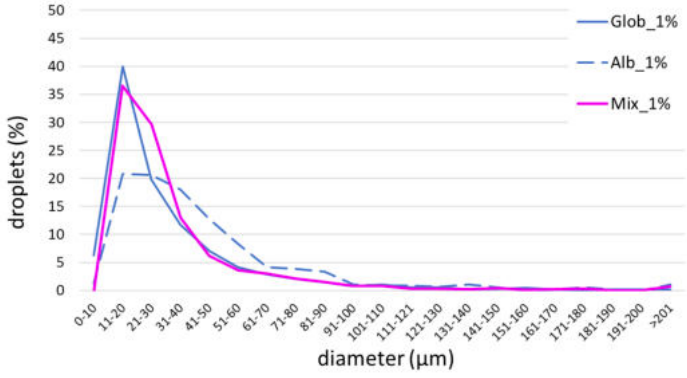

(c)

Figure 10.12: Comparison of droplets distribution of emulsions obtained through the Double Syringe method. (a) Tests with all the investigated albumin concentrations; (b) tests with all the investigated γ-globlulins concentrations. (c) Comparison of distributions obtained for a concentration of 1% of albumin, γ-globlulins and mixture of the two proteins.

10.4 Discussion

In this chapter we presented a quantitative analysis of the characteristics of emulsions generated in the experiments described in chapters 8 and 9.

Emulsions produced in syringes allowed us to evaluate the efficacy of proteins, and their interaction, in generating and stabilising SO emulsions. In chapter 8 we observed that emulsion menisci vary depending on the type of protein used as well as on their concentration. From the analysis carried out with the microscope, however, no particular differences emerged between the investigated systems in terms of droplet diameters. In fact, all distributions of the diameters were found to assume maximum values in the range 10 – 30 μm and, in general, they showed the same trend. The fact that we have found emulsion droplets with the same characteristics regardless of the parameters involved, is a common result in systems where emulsification occurs in domains with particular geometric constraints, as in the case of the Double Syringe method. (Xu and Nakajima, 2004; Utada et al., 2005). This result confirms the importance to generate emulsions in more realistic conditions, as we did in the experiments performed using the eye model.

The microscope analysis showed that in all the tests conducted in the eye model with proteins dissolved in the aqueous phase, an emulsion was generated. To our knowledge, this is the first study that systematically demonstrated the generation of bulk emulsions following SO injection into the vitreous chamber and with in-vitro conditions similar to physiological ones.

Both with a 50:50 and 80:20 ratio between SO and aqueous solution containing proteins, we obtained O/W type emulsions. Recently, an experimental study conducted by Soós et al. (2020), demonstrated that in the case of a larger presence of SO (80% of the total volume) with respect to aqueous solution with proteins, the observed emulsion resulted a W/O emulsion. This result could be due to the different content of species in the aqueous solution used for the experiments. In fact, we used albumin dissolved in BSS whereas Soós et al. (2020) used samples of porcine vitreous which contain several natural biomolecules such as collagen and hyaluronic acid.

The most significant result of this analysis is the fact that most of the droplets detected after the experiments, had very small sizes, with diameters less than 10 μm. Furthermore, areas composed of submicrometric droplets were observed. These findings have a strong clinical relevance, since small drops favor the onset of serious ocular complications. It is interesting to note that such small droplet sizes were not observed in emulsification tests in syringe, although the kinetic energy provided to generate an emulsion manually is much greater compared to that induced by eye movements.

The size of the detected droplets was also found to be correlated to the amplitude of the harmonic oscillations imposed. In fact, as the amplitude increased, we found drops of smaller size and in general, a larger amount of emulsion. This result is consistent with the fact that higher amplitudes imply a larger kinetic energy content on the interface between the two fluids, favoring the emulsification process.

Conclusions and future directions

Pars plana vitrectomy, is a surgery which involves removing the vitreous humor from the eye. The vitreous humor has the consistency of a gel and, in order to aspirate it out of the eye, vitreous cutters are employed. A vitreous cutter consists of two needles, one inside the other. The outer needle has a lateral port and the inner one moves back and forth, effectively acting as a guillotine and cutting the vitreous gel engaged in the port. The motion of the fluid generated by the aspiration mechanism has been studied by various research groups, as it is crucial for both the efficacy and safety of the surgical technique.

During vitrectomy, when aspiration starts, the pressure inside the vitreous cavity experiences a sudden drop, which can have adverse consequences on the surgical outcomes. Both ocular hypertension and hypotony can lead to serious complications. An important aspect of the surgical procedure is therefore, the prevention of excessive intraocular pressure (IOP) changes. Furthermore, high frequency pressure fluctuations associated with the movement of the cutter blade are thought to be associated with the generation of retinal tractions, with the possible occurrence of retinal breaks and inadvertent tissue removal. Vitrectomy devices are equipped with compensating systems aimed at balancing IOP fluctuations in the eye during surgery. However, direct IOP measurements during surgery are not performed, which makes it difficult to achieve effective pressure compensation.

In cases in which the retina is teared, in order to avoid the progression of a retinal detachment, tamponade fluids are inserted in the eye. Their role is to improve the contact between the detached retina and the retinal pigment epithelium, thus facilitating retinal reattachment. At present, the most widely used tamponade fluids are Silicone Oils (SOs). They have many desirable properties, such as stability, biocompatibility and their density can be tuned to tamponade superior (light oils) or inferior (heavy oils) retinal breaks. However, SOs cannot be left for very long times in place as they tend to emulsify with the aqueous humor produced by the eye. Emulsion is a highly undesirable event since it decreases the transparency of the fluid and triggers tissue inflammation. Moreover, when oil droplets get small enough they tend to move to the anterior segment of the eye and can block the drainage of the aqueous humor, by accumulating into the trabecular meshwork. This my lead to increase of IOP, which is a significant risk factor for the development of glaucoma.

In this thesis we make a humble contribution to understanding fluid dynamic mechanisms involved during vitrectomy procedure and after SO injection as tamponade fluid. Although some

of the answers have been obtained, there are still plenty of open questions in the field. In what follows we briefly describe the main conclusions of the work and suggest some possibilities for future developments.

The vitreous humour has a complex rheological behavior. In spite of the significant quantitative differences in the mechanical properties estimated with different methods, all authors characterise the vitreous as a viscoelastic material. However, measurement of the complex modulus using a rheometer is extremely challenging, owing to the tendency of the vitreous to create a thin lubricating aqueous layer. Moreover, the gel structure rapidly degrades after dissection. In the present work we proposed artificial vitreous (AV) solutions prepared in such a way as to span a wide but realistic range of rheological parameters of the fluid so as to mimic all possible conditions that might be encountered during surgery, from a completely liquefied vitreous to a relative firm vitreous, typical of young subjects. We characterised the mechanical behavior of each fluid through rheological tests in order to have a good control on the fluid properties. The resulting AV solutions were found to reproduce satisfactorily the properties of the human vitreous and this allowed us to conduct experimental tests in conditions close to physiological ones.

Although the fluidics of mechanical vitreous cutters has been quite extensively investigated, the performance of the new technology probes based on ultrasound vibrating tip is much less studied. In the present thesis we assessed the performance of different ultrsound probes in terms of fluidics and heat production. Results were compared with those obtained with traditional guillotine cutters. The flow generated by uillotine cutters is quite different between balance salt solution and AVs. In the latter cases, the axial-symmetry is broken and the flow structure is strongly three dimensional. In particular, we found that large velocities keep confined within a region in front of the guillotine cutter port and this is relevant from the surgical point of view since the orientation of the cutter tip used in the vicinity of the retina can affect the stress generated on it. In the case of ultrasound probes the flow is highly unsteady and irregular in time and space. Rossi et al. (2014b) proposed to assess safety and efficiency of vitrectomy cutters using a diagram where the values of the flow rate Q and the corresponding acceleration $|\mathbf{a}|$ are reported for a given set of controlling parameters. From the surgical point of view, the larger the flow rate the shorter the duration of surgery. Moreover, the generation of small accelerations on the retina is associated with a safer vitrectomy procedure. Following this approach, we compared the performance of ultrasound and guillotine cutters in a $(Q - |\mathbf{a}|)$ plane, finding that, for a given flow rate, accelerations were smaller for the ultrasound probes. Finally, with ultrasound temperature increased only at high stroke values, yet remaining in a physiological range.

All these measurements so far have been taken in a cubical, open and relatively large chamber. The same types of measurements could be carried out in a closed domain with a more realistic shape. This would imply the need of adding an infusion line to compensate for fluid aspiration. We expect that, since some of the flow structures observed in the present work have

the spatial scale of the domain, different flow fields will be observed in a realistic model of the vitreous chamber. Moreover, our experimental results, together with knowledge of the rheological parameters obtained from this work, could be useful for the implementation of numerical studies on the motion generated within the eye by vitreous cutters.

Prevention of IOP changes within the eye is another important issue for the optimisation of the surgical procedure. In this respect, we reproduced the vitrectomy procedure in vitro, using a phaco-vitrectomy system in a real scale model of the vitreous chamber. When aspiration starts, the pressure in the eye model drops. This pressure drop is typically reduced (sometimes very efficiently) when the vitrectomy device compensation mode is activated. However, results showed that in some cases compensation may lead to a significant pressure increase in the eye model, which is an undesirable effect. The present work represents an attempt to directly measure pressure fluctuations in an eye model during vitrectomy and provides useful information about what happens during the real surgery. Based on our measurements we can suggest general guidelines for optimising pressure compensation and avoid significant IOP changes. Our results showed that high frequency pressure oscillations due to the cutter blade motion are much smaller than the average pressure changes. The obtained pressure signals, showed however that the amplitude of pressure fluctuations is larger at the posterior pole than in the anterior region of the vitreous chamber model. The fact that the jet generated by the infusion line can generate higher pressures on the retina, already observed by Dal Vecchio et al. (2017), is a physical phenomenon that requires further investigations.

The second part of this thesis focuses on the study of the possible formation of an emulsion of SO due to the presence of surfactants and to the kinetic energy provided by saccadic rotations of the eye. In particular, we studied the effect of blood proteins on the interfacial properties between SOs and aqueous solutions. So far, much effort has been devoted to analyse the reasons for which emulsions form and to develop SOs more resistant to emulsification. The present work originates from the hypothesis that release of proteins from ocular tissues (typically as an inflammatory response to surgery) may have a significant role in decreasing the interfacial tension (IT) between the SO and aqueous solution, thus facilitating the formation of an emulsion. Surprisingly enough, this problem has not yet been addressed systematically from the chemico-physical point of view.

In this thesis we characterised the rheological properties of the interface between SOs and aqueous solutions containing albumin and γ-globulins (and combinations of these two proteins). These endogenous molecules were chosen as they are present in high concentrations in blood. In this work we measured the static value of the IT and also performed oscillatory rheological tests that allowed us to measure the so call dilational viscoelastic modulus of the interface. This is an important physical parameter since it provides information about the adsorption processes of the surfactant molecules at the interface. Moreover, the existence of a significant elasticity of the surface is typically associated with stability of emulsions. Experiments were carried out at

CNR-ICMATE in Genoa, making use of facilities already present in the laboratory. However, the experimental device and procedures had to be suitably adapted for the present measurements. This is because the conditions we has to deal with were not ideal due to the very small difference in density between the SO and water, which make it very challenging to use the pendant drop technique to measure the IT. Another difficulty inherent with the present experiments is related to the fact the SOs used in ophthalmic surgery have a very high viscosity. Thus, when oscillatory tests on pendant drops were performed at high frequencies, they could be affected by the bulk viscosity of the fluid.

We first performed experiments with a saline buffer solution and measured values of the IT with SO similar to those reported in the literature. We then performed experiments with aqueous solutions containing blood proteins. These experiments showed that when proteins are dissolved in the aqueous solution the rheological properties of the interface significantly change. In particular both with γ-globulins and albumin the equilibrium IT decreases to less than half of its original values (interface between SO and buffer solution with no proteins). Moreover, experiments performed on whole human serum samples revealed IT values compatible with the generation of an emulsion, even for concentrations of two order of magnitude lower than those of the mixture of the two considered proteins. The dependency of the equilibrium IT on the concentration resulted highly non-linear, with an initial significant drop at low values of the concentration and a slower decrease as the concentration is further increased. It is also important to remark that all obtained values are compatible with the generation of an emulsion.

Oscillatory experiments performed by imposing harmonic variations of the area of the drop and measuring the time evolution of the IT, showed that protein concentration, in dependence of protein type, and the time scale of the perturbation, had a significant role on the dilational viscoelasticity modulus of the interface, which achieved very large values. The existence of large values of the dilational viscoelasticity modulus make an emulsion very stable. The capability of such molecules to generate stable emulsions has been verified by emulsification tests. Preliminiary emulsification experiments in syringe demonstrated that the emulsion is an oil-in-water type. Moreover, these measurements allowed us to observe that in case of buffer solution without proteins the emulsion does not occur. This result suggested that the coalescence phenomenon has an important role at the SO-acqueous interface. Experiments with SO and buffer solution with proteins demonstrated that, when a system with SO and buffer solution with only one type of protein (either albumin or γ-globulins) is considered, the emulsion is formed for concentrations higher than 0.5%. A different situation was observed when the buffer solution contains a mixture of both proteins. In this case, the emulsion occured also for concentrations as small as 0.01%. Moreover, all the formed emulsions resulted stable for months.

The same experiments were conducted using a steroid drug to evaluate if it played a role on the emulsification phenomenon. Although this product neither showed a significant decrease of IT that can be associated with the formation of an emulsion, nor led to significant DV values,

preliminary emulsification tests confirmed that the steroid drug is able to stabilise Pickering-type emulsions.

We also investigated the effects of surfactant biomolecules and mechanical energy induced by eye rotations on the emulsion formation in a physical model of the vitreous chamber. The considered domain has been developed in order to simulate the real physiological conditions in terms of temperature and geometry. The motion imposed to the eye model by the motor, follows a sinusoidal time law and the imposed values of frequency (5Hz) and amplitudes (20°–50°) are comparable with those reported in the literature. The main result obtained from these experiments consists in the formation of emulsions even when a low concentration of albumin has been dissolved in the aqueous solution (1% of the physiological concentration in blood). The presence of an emulsion did not occur, in absence of proteins, for the same experimental conditions. Moreover, our results confirmed the capability of albumin to form stable SO in water emulsions once formed. Through images analysis acquired by an optical microscope, we have been able to obtain information about the number of droplets formed by the emulsification process and their size distribution, for each investigated system. As a result, we found oil-in-water emulsions, mostly characterised by oil drops with diameter less than 10 μm. This finding has clinical relevance, since droplets of small size can cause occlusion of the trabecular meshwork if they migrate in the anterior segment of the eye and can be swallowed by macrophages that, releasing chemioactive substances, induce inflammatory stimuli.

The present results showed the importance of accounting for proteins in the aqueous solution in the eye in order to understand why emulsion invariably occurs. Blood proteins are likely to be present in the aqueous in contact with the SO, especially owing to inflammatory processes that take place after surgery. In the literature it is often reported that formation of an emulsion triggers an inflammatory response. The story could however be different: inflammation itself could be responsible for the release of proteins in the aqueous that, by decreasing the surface tension and modifying rheological interfacial properties, could in turn cause the emulsion. Obviously, the emulsion can further inflame the retinal tissue.

This last set of experiments is a preliminary step towards the understanding the role of endogenous proteins in emulsification in a realistic domain. In fact, it is foundamental to integrate our results with experiments with other protein species. Moreover, for the present study we considered harmonic rotations. It would be useful to adopt more realistic time laws to describe a saccade.

Droplet detection analysis that we performed through Leica tool is limited by the timing of acquisition of the results. In fact, in the case of an image full of droplets, the time required for the analysis can be of the order of hours. In order to improve this aspect, we are developing a software of image analysis using the Matlab computing environment in order to obtain information about the number and size of the droplets formed in an automatic way. However, several steps are required to define the accuracy and reliability of the software.

Our findinings can pave the way to alternative approaches to inhibit or limit the formation of emulsions of SOs in the eye. In particular, a feasible strategy could be that of minimising the inflammatory response of the tissue, thus limiting the release of proteins in the eye. This could be done by inserting anti inflammatory drugs in the SO that, ideally, should be slowly released in time. Another strategy could be that of adding to the SO species capable of counteracting the surfactant role of endogenous proteins released by the inflamed tissue.

To summarise, in the present thesis we have tried to provide answers from mechanical perspective to certain questions related to fluids in the eye during and after vitrectomy. Despite many contributions from different research groups, the field remains open for further questions. We sincerely hope that the research will keep moving in that direction and wish luck to those who will try to unravel the ideal conditions for a safe and efficient surgery.

ACKNOWLEDGEMENTS

I would like to express the deepest gratitude to all my supervisors for the constant support during these three years and for transmitting me research competence, knowledge and values.
I should like to express my special thanks to the research group of the CNR-ICMATE for the hospitality at their laboratories and for promoting any scientific initiative despite the difficulties caused by the COVID-19 emergency situation.
I thank D.O.R.C and Bausch+Lomb ophthalmic companies for providing the surgical systems for the experimental measurements. I gratefully acknowledge the help of Dr. Mario Campana (Rutherford Appleton Laboratory, Oxfordshire, UK) for the measurements of Silicone oil density versus temperature. I would like also thank Fluoron GmbH and Alchimia srl for supplying Silicone Oil samples.

La mia più profonda riconoscenza è rivolta ai miei genitori, che hanno saputo costantemente alimentare il mio entusiasmo, sostenermi nei momenti di difficoltà e soprattutto per aver sempre dimostrato partecipazione e curiosità verso i miei studi.
Ringrazio con amore Giorgio, per essere stato un perfetto complice in ogni tappa di questo percorso, come in tutte le nostre avventure di vita.
Un sincero ringraziamento va a Ludovica, Valeria, Masha e Krystyna, i migliori esempi di integrità, determinazione e passione che potessi avere.
Un importante riconoscimento va a Luigi, non solo per avermi iniziata alla scienza nei laboratori del CERN undici anni fa, ma per aver sempre creduto in me.

BIBLIOGRAPHY

O. Abouali, A. Modareszadeh, A. Ghaffariyeh, and J. Tu. Numerical simulation of the fluid dynamics in vitreous cavity due to saccadic eye movement. *Medical engineering & physics*, 34 (6):681–692, 2012.

D. J. K. Abulon. Vitreous flow rates through dual pneumatic cutters: effects of duty cycle and cut rate. *Clinical ophthalmology (Auckland, NZ)*, 9:253, 2015.

D. J. K. Abulon and D. C. Buboltz. Performance comparison of high-speed dual-pneumatic vitrectomy cutters during simulated vitrectomy with balanced salt solution. *Translational vision science & technology*, 4(1):6–6, 2015.

D. J. K. Abulon and D. C. Buboltz. Porcine Vitreous Flow Behavior During High-Speed Vitrectomy up to 7500 Cuts per Minute. *Translational Vision Science & Technology*, 5(1):7–7, 02 2016. ISSN 2164-2591. doi: 10.1167/tvst.5.1.7. URL `https://doi.org/10.1167/tvst.5.1.7`.

A. M. Al-Jazzaf, P. A. Netland, and S. Charles. Incidence and management of elevated intraocular pressure after silicone oil injection. *Journal of glaucoma*, 14(1):40–46, 2005.

D. Alberghina, C. Giannetto, I. Vazzana, V. Ferrantelli, and G. Piccione. Reference intervals for total protein concentration, serum protein fractions, and albumin/globulin ratios in clinically healthy dairy cows. *Journal of Veterinary Diagnostic Investigation*, 23(1):111–114, 2011.

G. Anand, S. Sharma, A. K. Dutta, S. K. Kumar, and G. Belfort. Conformational transitions of adsorbed proteins on surfaces of varying polarity. *Langmuir*, 26(13):10803–10811, 2010.

D. Atchison and G. Smith. *Optics of the human eye*. Butterworth Heinemann, 2000.

D. A. Atchison, C. E. Jones, K. L. Schmid, N. Pritchard, J. M. Pope, W. E. Strugnell, and R. A. Riley. Eye shape in emmetropia and myopia. *Investigative Ophthalmology & Visual Science*, 45(10):3380–3386, 2004.

D. A. Atchison, N. Pritchard, K. L. Schmid, D. H. Scott, C. E. Jones, and J. M. Pope. Shape of the retinal surface in emmetropia and myopia. *Investigative ophthalmology & visual science*, 46(8):2698–2707, 2005.

S. P. Azen, D. C. Boone, W. Barlow, B. W. McCuen, A. F. Walonker, M. M. Anderson, J. S. Lean, R. L. Mowery, S. J. Ryan, W. Stern, et al. Methods, statistical features, and baseline results of a standardized, multicentered ophthalmologic surgical trial: the silicone study. *Controlled clinical trials*, 12(3):438–455, 1991.

W. D. Bancroft. The theory of emulsification, v. *The Journal of Physical Chemistry*, 17(6):501–519, 1913. doi: 10.1021/j150141a002.

F. Barca, T. Caporossi, and S. Rizzo. Silicone oil: different physical proprieties and clinical applications. *BioMed research international*, 2014, 2014.

E. Bartov, F. Pennarola, N. Savion, N. Naveh, and G. Treister. A quantitative in vitro model for silicone oil emulsification. role of blood constituents. *Retina (Philadelphia, Pa.)*, 12(3 Suppl): S23–7, 1992.

F. Bashforth and J. C. Adams. *An attempt to test the theories of capillary action*. University Press, 1883.

J. Bayat, H. Emdad, and O. Abouali. Numerical simulation of the fluid dynamics in a 3d spherical model of partially liquefied vitreous due to eye movements under planar interface conditions. *Journal of Computational Applied Mechanics*, 50(2):387–394, 2019.

J. Bayat, H. Emdad, and O. Abouali. Numerical investigation of partially liquefied vitreous dynamics as two-phase viscoelastic-newtonian fluid flow in a planar cavity due to oscillatory motion. *International Journal of Multiphase Flow*, page 103259, 2020.

W. Becker. The neurobiology of saccadic eye movements ed rh wurtz and me goldberg, 1989.

J. Benjamins, A. Cagna, and E. Lucassen-Reynders. Viscoelastic properties of triacylglycerol/water interfaces covered by proteins. *Colloids and Surfaces A: Physicochemical and Engineering Aspects*, 114:245–254, 1996.

F. A. Bettelheim and T. J. Wang. Dynamic viscoelastic properties of bovine vitreous. *Experimental eye research*, 23(4):435–441, 1976.

B. P. Binks. Particles as surfactants - similarities and differences. *Current Opinion in Colloid & Interface Science*, 7(1):21 – 41, 2002. ISSN 1359-0294. doi: https://doi.org/10.1016/S1359-0294(02)00008-0. URL `http://www.sciencedirect.com/science/article/pii/S1359029402000080`.

R. B. Bird and C. F. Curtiss. Fascinating polymeric liquids. *Physics Today*, 37(1):36–43, 1984.

R. B. Bird, R. C. Armstrong, and O. Hassager. Dynamics of polymeric liquids. vol. 1: Fluid mechanics. 1987.

D. Boger, M. Crochet, and R. Keiller. On viscoelastic flows through abrupt contractions. *Journal of non-newtonian fluid mechanics*, 44:267–279, 1992.

G. Böhme. On steady streaming in viscoelastic liquids. *Journal of non-newtonian fluid mechanics*, 44:149–170, 1992.

S. Boluriaan and P. J. Morris. Acoustic streaming: from rayleigh to today. *International Journal of aeroacoustics*, 2(3):255–292, 2003.

A. Bonfiglio, R. Repetto, J. H. Siggers, and A. Stocchino. Investigation of the motion of a viscous fluid in the vitreous cavity induced by eye rotations and implications for drug delivery. *Physics in Medicine & Biology*, 58(6):1969, 2013.

A. Bonfiglio, A. Lagazzo, R. Repetto, and A. Stocchino. An experimental model of vitreous motion

induced by eye rotations. *Eye and Vision*, 2(1):1–10, 2015.

R. F. Brubaker. Intraocular surgery and choroidal hemorrhage. *Archives of Ophthalmology*, 102 (12):1753–1754, 1984.

E. Caló and V. V. Khutoryanskiy. Biomedical applications of hydrogels: A review of patents and commercial products. *European Polymer Journal*, 65:252–267, 2015.

A. Caramoy, S. Schröder, S. Fauser, and B. Kirchhof. In vitro emulsification assessment of new silicone oils. *British journal of ophthalmology*, 94(4):509–512, 2010.

S. Chakarova and A. E. Carlsson. Model study of protein unfolding by interfaces. *Physical Review E*, 69(2):021907, 2004.

Y. K. Chan, C. O. Ng, P. C. Knox, M. J. Garvey, R. L. Williams, and D. Wong. Emulsification of silicone oil and eye movements. *Investigative ophthalmology & visual science*, 52(13):9721–9727, 2011.

Y. K. Chan, N. Cheung, and D. Wong. Factors influencing the shear rate acting on silicone oil to cause silicone oil emulsificationphysical factors of silicone oil emulsification. *Investigative ophthalmology & visual science*, 55(11):7451–7456, 2014a.

Y. K. Chan, R. L. Williams, and D. Wong. Flow behavior of heavy silicone oil during eye movements. *Investigative ophthalmology & visual science*, 55(12):8453–8457, 2014b.

Y. K. Chan, K. H. S. Sy, C. Y. Wong, P. K. Man, D. Wong, and H. C. Shum. In vitro modeling of emulsification of silicone oil as intraocular tamponade using microengineered eye-on-a-chip. *Investigative ophthalmology & visual science*, 56(5):3314–3319, 2015.

S. Charles. An engineering approach to vitreoretinal surgery. *Retina*, 24(3):435–444, 2004.

S. Charles. Fluidics and cutter dynamics. In *Microincision Vitrectomy Surgery*, volume 54, pages 31–37. Karger Publishers, 2014.

J. C. Chen. *Convective Flow Boiling*. Taylor & Francis, 1995.

J. Chung and R. Spaide. Intraretinal silicone oil vacuoles after macular hole surgery with internal limiting membrane peeling. *American journal of ophthalmology*, 136(4):766–767, 2003.

U. N. R. Commission. *Biological Effects and Exposure Limits for" hot Particles"*. Number 130. Ncrp, 1999.

A. Crisp, E. de Juan, and J. Tiedeman. Effect of silicone oil viscosity on emulsification. *Archives of ophthalmology*, 105(4):546–550, 1987.

S. Curry, H. Mandelkow, P. Brick, and N. Franks. Crystal structure of human serum albumin complexed with fatty acid reveals an asymmetric distribution of binding sites. *Nature structural biology*, 5(9), 1998.

A. F. da Silva, M. A. M. Alves, and M. Oliveira. Rheological behaviour of vitreous humour. *Rheologica Acta*, 56:377–386, 2017.

M. Dal Vecchio, A. M. Fea, R. Spinetta, S. L. Marasso, M. Cocuzza, L. Scaltrito, and G. Canavese. Behaviour of the intraocular pressure during manual and vented gas forced infusion in a simulated pars plana vitrectomy. *International Journal of Applied Engineering Research*, 12

(17):6751–6757, 2017.

E. Daniel and H. Felix. Protein, 2017.

T. David, S. Smye, T. Dabbs, and T. James. A model for the fluid motion of vitreous humour of the human eye during saccadic movement. *Physics in Medicine & Biology*, 43(6):1385, 1998.

L. R. de Corral, S. B. Cohen, and G. A. Peyman. Effect of intravitreal silicone oil on intraocular pressure. *Ophthalmic Surgery, Lasers and Imaging Retina*, 18(6):446–449, 1987.

E. de Juan Jr, B. McCuen, and J. Tiedeman. Intraocular tamponade and surface tension. *Survey of ophthalmology*, 30(1):47–51, 1985.

P. R. C. De Oliveira, A. R. Berger, and D. R. Chow. Vitreoretinal instruments: vitrectomy cutters, endoillumination and wide-angle viewing systems. *International journal of retina and vitreous*, 2(1):1–15, 2016.

J. de Queiroz Jr, J. C. Blanks, S. A. Ozler, D. V. Alfaro, and P. E. Liggett. Subretinal perfluorocarbon liquids. an experimental study. *Retina (Philadelphia, Pa.)*, 12(3 Suppl):S33–9, 1992.

D. De Silva, K. Lim, and W. Schulenburg. An experimental study on the effect of encircling band procedure on silicone oil emulsification. *British journal of ophthalmology*, 89(10):1348–1350, 2005.

R. Defay, A. Bellemans, and I. Prigogine. Surface tension and adsorption. 1966.

F. Di Michele, A. Tatone, M. R. Romano, and R. Repetto. A mechanical model of posterior vitreous detachment and generation of vitreoretinal tractions. *Biomechanics and Modeling in Mechanobiology*, 19(6):2627–2641, 2020.

E. Dickinson. Adsorbed protein layers at fluid interfaces: interactions, structure and surface rheology. *Colloids and surfaces B: Biointerfaces*, 15(2):161–176, 1999.

B. Diniz, R. B. Fernandes, R. M. Ribeiro, J.-C. Lue, A. G. Teixeira, O. Magalhães, M. Maia, and M. S. Humayun. Analysis of a 23-gauge ultra high-speed cutter with duty cycle control. *Retina (Philadelphia, Pa.)*, 33(5):933, 2013.

J. H. Dresp and D.-H. Menz. Preparation and processing of vitreoretinal instrumentation and equipment as a risk factor for silicone oil emulsification. *Retina*, 24(1):110–115, 2004.

R. Dyson, A. Fitt, O. Jensen, N. Mottram, D. Miroshnychenko, S. Naire, R. Ocone, J. Siggers, and A. Smithbecker. Post re-attachment retinal re-detachment. *Proceedings of the 4th Medical Study Group*, 2004.

K. Dziza, E. Santini, L. Liggieri, E. Jarek, M. Krzan, T. Fischer, and F. Ravera. Interfacial properties and emulsification of biocompatible liquid-liquid systems. *Coatings*, 10(4):397, 2020.

I. Eames, R. I. Angunawela, G. W. Aylward, and A. Azarbadegan. A theoretical model for predicting interfacial relationships of retinal tamponades. *Investigative Ophthalmology & Visual Science*, 51(4):2243–2247, 2010.

M.-H. Errera, S. E. Liyanage, M. Elgohary, A. C. Day, L. Wickham, P. J. Patel, J.-A. Sahel, M. Paques, E. Ezra, and P. M. Sullivan. Using spectral-domain optical coherence tomography imaging to identify the presence of retinal silicone oil emulsification after silicone oil

tamponade. *Retina*, 33(8):1567–1573, 2013.

P. Falabella, F. R. Stefanini, J.-C. L. Lue, M. Pfister, J. Reyes-Mckinley, M. J. Koss, A. Teixeira, P. Schor, and M. S. Humayun. Intraocular pressure changes during vitrectomy using constellation vision system's intraocular pressure control feature. *Retina*, 36(7):1275–1280, 2016.

F. Fang and I. Szleifer. Competitive adsorption in model charged protein mixtures: equilibrium isotherms and kinetics behavior. *The Journal of chemical physics*, 119(2):1053–1065, 2003.

I. Fawcett, R. Williams, and D. Wong. Contact angles of substances used for internal tamponade in retinal detachment surgery. *Graefe's archive for clinical and experimental ophthalmology*, 232(7):438–444, 1994.

J. D. Ferry. *Viscoelastic properties of polymers*. John Wiley & Sons, 1980.

B. A. Filas, Q. Zhang, R. J. Okamoto, Y.-B. Shui, and D. C. Beebe. Enzymatic degradation identifies components responsible for the structural properties of the vitreous body. *Investigative ophthalmology & visual science*, 55(1):55–63, 2014.

O. Findl, K. Strenn, M. Wolzt, R. Menapace, C. Vass, H.-G. Eichler, and L. Schmetterer. Effects of changes in intraocular pressure on human ocular haemodynamics. *Current eye research*, 16 (10):1024–1029, 1997.

W. J. Foster. Vitreous substitutes. *Expert review of ophthalmology*, 3(2):211–218, 2008.

G. N. Foulks, D. L. Hatchell, A. D. Proia, and G. K. Klintworth. Histopathology of silicone oil keratopathy in humans. *Cornea*, 10(1):29–37, 1991.

J. H. Francis, P. A. Latkany, and J. L. Rosenthal. Mechanical energy from intraocular instruments cause emulsification of silicone oil. *British journal of ophthalmology*, 91(6):818–821, 2007.

S. Friberg, P. O. Jansson, and E. Cederberg. Surfactant association structure and emulsion stability. *Journal of Colloid and Interface Science*, 55(3):614–623, 1976.

T. Gaillard, M. Roché, C. Honorez, M. Jumeau, A. Balan, C. Jedrzejczyk, and W. Drenckhan. Controlled foam generation using cyclic diphasic flows through a constriction. *International Journal of Multiphase Flow*, 96:173–187, 2017.

J. D. M. Gass and R. Parrish. Outer retinal ischemic infarctiona newly recognized complication of cataract extraction and closed vitrectomy: Part 1. a case report. *Ophthalmology*, 89(12): 1467–1471, 1982.

J. W. Gibbs. Scientific papers of josiah willard gibbs, vol. 1, 1906.

A. Groisman and V. Steinberg. Elastic turbulence in a polymer solution flow. *Nature*, 405(6782): 53–55, 2000.

S. Hartland. *Surface and Interfacial Tension: Measurement, Theory, and Applications*. Surfactant Science. Taylor & Francis, 2004.

H. Heidenkummer, A. Kampik, and S. Thierfelder. Emulsification of silicone oils with specific physicochemical characteristics. *Graefe's Archive for Clinical and Experimental Ophthalmology*, 229(1):88–94, Jan. 1991. ISSN 0721-832X, 1435-702X. doi: 10.1007/BF00172269.

H. P. Heidenkummer, A. Kampik, and S. Thierfelder. Experimental evaluation of in vitro stability of purified polydimethylsiloxanes (silicone oil) in viscosity ranges from 1000 to 5000 centistokes. *Retina (Philadelphia, Pa.)*, 12(3 Suppl):S28–32, 1992. ISSN 0275-004X. PMID: 1455079.

H. Heimann, T. Stappler, and D. Wong. Heavy tamponade 1: a review of indications, use, and complications. *Eye*, 22(10):1342–1359, 2008.

A. Hirata, N. Yonemura, T. Hasumura, Y. Murata, and A. Negi. Effect of infusion air pressure on visual field defects after macular hole surgery. *American journal of ophthalmology*, 130(5): 611–616, 2000.

S. G. Honavar, M. Goyal, A. B. Majji, P. K. Sen, T. Naduvilath, and L. Dandona. Glaucoma after pars plana vitrectomy and silicone oil injection for complicated retinal detachments. *Ophthalmology*, 106(1):169–177, 1999.

J. P. Hubschman, A. Gupta, D. H. Bourla, M. Culjat, F. Yu, and S. D. Schwartz. 20-, 23-, and 25-gauge vitreous cutters: performance and characteristics evaluation. *Retina*, 28(2):249–257, 2008.

P. Ichhpujani, A. Jindal, and L. J. Katz. Silicone oil induced glaucoma: a review. *Graefe's Archive for Clinical and Experimental Ophthalmology*, 247(12):1585–1593, 2009.

K. Isakova, J. O. Pralits, R. Repetto, and M. R. Romano. A model for the linear stability of the interface between aqueous humor and vitreous substitutes after vitreoretinal surgery. *Physics of Fluids*, 26(12):124101, 2014.

K. Isakova, J. O. Pralits, M. R. Romano, J.-W. M. Beenakker, D. P. Shamonin, and R. Repetto. Equilibrium shape of the aqueous humor-vitreous substitute interface in vitrectomized eyes. *Journal for Modeling in Ophthalmology*, 1(3):31–46, 2017.

I. B. Ivanov. Effect of surface mobility on the dynamic behavior of thin liquid films. *Pure and Applied Chemistry*, 52(5):1241–1262, 1980.

I. B. Ivanov and P. A. Kralchevsky. Stability of emulsions under equilibrium and dynamic conditions. *Colloids and Surfaces A: Physicochemical and engineering aspects*, 128(1-3):155–175, 1997.

K. Januschowski, C. Irigoyen, J. C. Pastor, G. K. Srivastava, M. R. Romano, H. Heimann, P. Stalmans, K. Van Keer, K. Boden, P. Szurman, et al. Retinal toxicity of medical devices used during vitreoretinal surgery: a critical overview. *Ophthalmologica*, 240(4):236–243, 2018.

V. N. Kazakov, O. V. Sinyachenko, V. B. Fainerman, U. Piso, and R. Miller. Chapter 1 theory of protein adsorption and model experiments. In *Dynamic Surface Tensiometry in Medicine*, volume 8 of *Studies in Interface Science*, pages 1 – 40. Elsevier, 2000.

R. Keiller, J. Rallison, and J. Evans. Sink flows of a suspension of rigid rods: the failure of a similarity solution. *Journal of non-newtonian fluid mechanics*, 42(3):249–266, 1992.

S. Kenney, K. Poper, G. Chapagain, and G. F. Christopher. Large deborah number flows around confined microfluidic cylinders. *Rheologica Acta*, 52(5):485–497, 2013.

M. A. Khan, A. Shahlaee, B. Toussaint, J. Hsu, A. Sivalingam, P. U. Dugel, R. R. Lakhanpal, C. D. Riemann, M. H. Berrocal, C. D. Regillo, and A. C. Ho. Outcomes of 27 gauge microincision vitrectomy surgery for posterior segment disease. *American Journal of Ophthalmology*, 161: 36 – 43.e2, 2016. ISSN 0002-9394. doi: https://doi.org/10.1016/j.ajo.2015.09.024. URL `http://www.sciencedirect.com/science/article/pii/S0002939415005942`.

J. Kim and G. A. Somorjai. Molecular packing of lysozyme, fibrinogen, and bovine serum albumin on hydrophilic and hydrophobic surfaces studied by infrared- visible sum frequency generation and fluorescence microscopy. *Journal of the American Chemical Society*, 125(10): 3150–3158, 2003.

S. H. Kim and K. S. Choi. Changes of intraocular pressure during experimental vitrectomy. *Current eye research*, 37(8):698–703, 2012.

Y. J. Kim, S. H. Park, and K. S. Choi. Fluctuation of infusion pressure during microincision vitrectomy using the constellation vision system. *Retina*, 35(12):2529–2536, 2015.

N. Kociok, C. Gavranic, B. Kirchhof, and A. M. Joussen. Influence on membrane-mediated cell activation by vesicles of silicone oil or perfluorohexyloctane. *Graefe's Archive for Clinical and Experimental Ophthalmology*, 243(4):345–358, 2005.

K. Kubiak-Ossowska and P. A. Mulheran. Multiprotein interactions during surface adsorption: a molecular dynamics study of lysozyme aggregation at a charged solid surface. *The Journal of Physical Chemistry B*, 115(28):8891–8900, 2011.

M. P. Kummer, J. J. Abbott, S. Dinser, and B. J. Nelson. Artificial vitreous humor for in vitro experiments. In *2007 29th Annual International Conference of the IEEE Engineering in Medicine and Biology Society*, pages 6406–6409. IEEE, 2007.

D. Langevin. Influence of interfacial rheology on foam and emulsion properties. *Advances in Colloid and Interface Science*, 88(1):209–222, 2000.

R. G. Larson. Instabilities in viscoelastic flows. *Rheologica Acta*, 31(3):213–263, 1992.

J. S. Lean, W. H. Stern, A. R. Irvine, S. P. Azen, S. Azen, W. Barlow, D. Boone, B. Quillen-Thomas, M. Cox, M. Blumenkranz, et al. Classification of proliferative vitreoretinopathy used in the silicone study. *Ophthalmology*, 96(6):765–771, 1989.

B. Lee, M. Litt, and G. Buchsbaum. Rheology of the vitreous body. Part I: viscoelasticity of human vitreous. *Biorheology*, 29:521–533, 1992.

B. Lee, M. Litt, and G. Buchsbaum. Rheology of the vitreous body: Part 2. viscoelasticity of bovine and porcine vitreous. *Biorheology*, 31(4):327–338, Aug. 1994. ISSN 0006-355X. PMID: 7981433.

I. M. Lifshitz and V. V. Slyozov. The kinetics of precipitation from supersaturated solid solutions. *Journal of physics and chemistry of solids*, 19(1-2):35–50, 1961.

L. Liggieri and R. Miller. Relaxation of surfactants adsorption layers at liquid interfaces. *Current Opinion in Colloid & Interface Science*, 15(4):256–263, 2010.

L. Liggieri and A. Passerone. An automatic technique for measuring the surface tension of liquid

metals. *High Temperature Technology*, 7(2):82–86, 1989.

M. Lisi, P. Bisiacchi, and A. Vallesi. L'analisi dei movimenti oculari come strumento di indagine dei processi cognitivi. *Il cervello al lavoro. Nuove prospettive in neuropsicologia, Il Mulino*, 2017.

G. Loglio, P. Pandolfini, R. Miller, A. Makievski, F. Ravera, M. Ferrari, and L. Liggieri. Drop and bubble shape analysis as tool for dilational rheology studies of interfacial layers. In *Novel methods to study interfacial layers*, pages 439–484. Elsevier Science, 2001.

G. Loglio, P. Pandolfini, L. Liggieri, A. V. Makievski, and F. Ravera. Determination of interfacial properties by the pendant drop tensiometry: Optimisation of experimental and calculation procedures. *Bubble and drop interfaces*, 2:7, 2011.

L. I. Los, R. J. van der Worp, M. J. van Luyn, and J. M. Hooymans. Age-related liquefaction of the human vitreous body: Lm and tem evaluation of the role of proteoglycans and collagen. *Investigative ophthalmology & visual science*, 44(7):2828–2833, 2003.

B. Lou, Z. Yuan, L. He, L. Lin, Q. Gao, and X. Lin. The changes of retinal saturation after long-term tamponade with silicone oil. *BioMed research international*, 2015, 2015.

L. Lourenço and A. Krothapalli. True resolution piv: a mesh-free second order accurate algorithm, 10th int. In *Symp. on Applications of Laser Techniques in Fluid Mechanics (Lisbon)*, 2000.

E. Lucassen-Reynders. Interfacial viscoelasticity in emulsions and foams. *Food Structure*, 12(1): 1, 1993.

J. Ma, Q. Wang, and H. Niu. Comparison of 27-gauge and 25-gauge microincision vitrectomy surgery for the treatment of vitreoretinal disease: A systematic review and meta-analysis. *Journal of Ophthalmology*, 2020, 2020.

C. W. Macosko. Rheology principles. *Measurements and Applications*, 1994.

O. Magalhaes Jr, L. Chong, C. DeBoer, P. Bhadri, R. Kerns, A. Barnes, S. Fang, and M. Humayun. Vitreous dynamics: vitreous flow analysis in 20-, 23-, and 25-gauge cutters. *Retina*, 28(2):236–241, 2008.

A. Makievski, V. Fainerman, R. Miller, M. Bree, L. Liggieri, and F. Ravera. Determination of equilibrium surface tension values by extrapolation via long time approximations. *Colloids and Surfaces A: Physicochemical and Engineering Aspects*, 122(1-3):269–273, 1997.

A. V. Makievski, V. B. Fainerman, M. Bree, R. Wüstneck, J. Krägel, and R. Miller. Adsorption of proteins at the liquid/air interface. *The Journal of Physical Chemistry B*, 102(2):417–425, 1998.

J. Maldonado-Valderrama, A. Martín-Rodriguez, M. J. Gálvez-Ruiz, R. Miller, D. Langevin, and M. A. Cabrerizo-Vílchez. Foams and emulsions of β-casein examined by interfacial rheology. *Colloids and Surfaces A: Physicochemical and Engineering Aspects*, 323(1):116–122, 2008.

W. Manschot. Glaucoma; vascular necrosis; expulsive haemorrhage. *Ophthalmologica. Journal international d'ophtalmologie. International journal of ophthalmology. Zeitschrift fur Augen-*

heilkunde, 112(3):171, 1946.

B. Mao, T. Divoux, and P. Snabre. Normal force controlled rheology applied to agar gelation. *Journal of Rheology*, 60(3):473–489, 2016.

S. Matsumoto, Y. Kita, and D. Yonezawa. An attempt at preparing water-in-oil-in-water multiple-phase emulsions. *Journal of Colloid and Interface Science*, 57(2):353–361, 1976.

C. Maze and G. Burnet. A non-linear regression method for calculating surface tension and contact angle from the shape of a sessile drop. *Surface Science*, 13(2):451–470, 1969.

G. H. McKinley, R. C. Armstrong, and R. Brown. The wake instability in viscoelastic flow past confined circular cylinders. *Philosophical Transactions of the Royal Society of London. Series A: Physical and Engineering Sciences*, 344(1671):265–304, 1993.

G. H. McKinley, L. E. Rodd, M. S. Oliverira, and J. Cooper-White. Extensional flows of polymer solutions in microfluidic converging/diverging geometries. *Journal of Central South University of Technology*, 14(1):6–9, 2007.

J. Meskauskas, R. Repetto, and J. H. Siggers. Oscillatory motion of a viscoelastic fluid within a spherical cavity. *Journal of Fluid Mechanics*, 685:1, 2011.

A. Metzner and J. Reed. Flow of non-newtonian fluidscorrelation of the laminar, transition, and turbulent-flow regions. *Aiche journal*, 1(4):434–440, 1955.

G. Michelson, M. Groh, and M. Langhans. Perfusion of the juxtapapillary retina and optic nerve head in acute ocular hypertension. *German journal of ophthalmology*, 5(6):315–321, 1996.

J. B. Miller, T. D. Papakostas, and D. G. Vavvas. Complications of emulsified silicone oil after retinal detachment repair. In *Seminars in ophthalmology*, volume 29, pages 312–318. Taylor & Francis, 2014.

R. Miller and L. Liggieri. *Progress in Colloid and Interface Science*. CRC Press, 2009.

R. Miller, V. Fainerman, A. Makievski, J. Krägel, D. Grigoriev, V. Kazakov, and O. Sinyachenko. Dynamics of protein and mixed protein/surfactant adsorption layers at the water/fluid interface. *Advances in colloid and interface science*, 86(1):39–82, 2000.

M. Minami, H. Oku, T. Okuno, M. Fukuhara, and T. Ikeda. High infusion pressure in conjunction with vitreous surgery alters the morphology and function of the retina of rabbits. *Acta Ophthalmologica Scandinavica*, 85(6):633–639, 2007.

K. Mitsui, J. Kogo, H. Takeda, A. Shiono, H. Sasaki, Y. Munemasa, Y. Kitaoka, and H. Takagi. Comparative study of 27-gauge vs 25-gauge vitrectomy for epiretinal membrane. *Eye*, 30(4): 538–544, 2016.

D. Möbius and R. Miller. *Proteins at liquid interfaces*, volume 7. Elsevier, 1998.

A. Modarreszadeh and O. Abouali. Numerical simulation for unsteady motions of the human vitreous humor as a viscoelastic substance in linear and non-linear regimes. *Journal of Non-Newtonian Fluid Mechanics*, 204:22–31, 2014.

L. C. Moorhead and C. D. Armeniades. Variations in Intraocular Pressure During Closed-System Surgical Procedures. *Archives of Ophthalmology*, 104(2):269–272, 02 1986. ISSN

0003-9950. doi: 10.1001/archopht.1986.01050140127034. URL https://doi.org/10.1001/archopht.1986.01050140127034.

L. C. Moorhead, T. W. Gardner, H. M. Lambert, R. E. OMalley, A. W. Willis, L. S. Meharg, and W. D. Moorhead. Dynamic intraocular pressure measurements during vitrectomy. *Archives of Ophthalmology*, 123(11):1514–1523, 2005.

F. Morescalchi, C. Costagliola, S. Duse, E. Gambicorti, B. Parolini, B. Arcidiacono, M. R. Romano, and F. Semeraro. Heavy silicone oil and intraocular inflammation. *BioMed research international*, 2014, 2014.

S. Mrejen, T. Sato, Y. Fisher, and R. F. Spaide. Intraretinal and intra-optic nerve head silicone oil vacuoles using adaptive optics. *Ophthalmic Surgery, Lasers and Imaging Retina*, 45(1):71–73, 2014.

K. Nakamura, M. F. Refojo, and D. Crabtree. Factors contributing to the emulsification of intraocular silicone and fluorosilicone oils. *Investigative ophthalmology & visual science*, 31(4): 647–656, 1990.

L. M. Nayef, M. F. Khan, and M. A. Brook. Low molecular weight silicones particularly facilitate human serum albumin denaturation. *Colloids and Surfaces B: Biointerfaces*, 128:586–593, 2015.

I. Nepita, A. Stocchino, A. Dodero, S. Vicini, M. Ferrara, M. Romano, and R. Repetto. Dynamic pressure measurements in a model of the eye. In preparation.

I. Nepita, R. Repetto, J. O. Pralits, M. R. Romano, F. Ravera, E. Santini, and L. Liggieri. The role of endogenous proteins on the emulsification of silicone oils used in vitreoretinal surgery. *BioMed Research International*, 2020, 2020.

I. Nepita, R. Repetto, A. Dodero, S. Vicini, M. Ferrara, M. R. Romano, and A. Stocchino. Experimental assessment of the performance of vitreous cutters with fluids with different rheological properties. *Graefe's Archive for Clinical and Experimental Ophthalmology*, pages 1–9, 2021.

S. Nesrinne and A. Djamel. Synthesis, characterization and rheological behavior of ph sensitive poly (acrylamide-co-acrylic acid) hydrogels. *Arabian Journal of Chemistry*, 10(4):539–547, 2017.

R. S. Newsom, R. Johnston, P. M. Sullivan, G. B. Aylward, G. E. Holder, and Z. J. Gregor. Sudden visual loss after removal of silicone oil. *Retina*, 24(6):871–877, 2004.

C. S. Nickerson, J. Park, J. A. Kornfield, and H. Karageozian. Rheological properties of the vitreous and the role of hyaluronic acid. *Journal of biomechanics*, 41(9):1840–1846, 2008.

P. Nogueira, M. Zankl, H. Schlattl, and P. Vaz. Dose conversion coefficients for monoenergetic electrons incident on a realistic human eye model with different lens cell populations. *Physics in Medicine & Biology*, 56(21):6919, 2011.

D. Odrobina and I. Laudańska-Olszewska. Analysis of the time and location of the silicone oil emulsification by spectral-domain optical coherence tomography after silicone oil tamponade. *BioMed research international*, 2014, 2014.

H. Oh and Y. Oshima. Microincision vitrectomy surgery: Emerging techniques and technology. 2014.

F. Okamoto, Y. Sugiura, Y. Okamoto, Y. Hasegawa, T. Hiraoka, and T. Oshika. Measurement of ophthalmodynamometric pressure with the vented-gas forced-infusion system during pars plana vitrectomy. *Investigative ophthalmology & visual science*, 51(8):4195–4199, 2010.

A. Okubo. Horizontal dispersion of floatable particles in the vicinity of velocity singularities such as convergences. *Deep Sea Research and Oceanographic Abstracts*, 17(3):445–454, 1970. ISSN 0011-7471. doi: https://doi.org/10.1016/0011-7471(70)90059-8. URL `https://www.sciencedirect.com/science/article/pii/0011747170900598`.

D. Oliver. The prediction of angle of convergence for the flow of viscoelastic liquids into orifices. *The Chemical Engineering Journal*, 6(3):265–271, 1973.

S. Osawa and Y. Oshima. Innovations in 27-gauge vitrectomy for sutureless microincision vitrectomy surgery. *Retina Today*, 9:42–45, 2014.

Y. Oshima, T. Wakabayashi, T. Sato, M. Ohji, and Y. Tano. A 27–gauge instrument system for transconjunctival sutureless microincision vitrectomy surgery. *Ophthalmology*, 117(1):93–102, 2010.

M. Ovchinnikov, J. Zhou, and S. Yalamanchili. Acoustic streaming of a sharp edge. *The Journal of the Acoustical Society of America*, 136(1):22–29, 2014.

R. P H and D. G. *Perry's Chemical Engineers' Handbook*. McGraw-Hill (Sixth Edition), 1985.

P. Pakdel and G. H. McKinley. Elastic instability and curved streamlines. *Physical Review Letters*, 77(12):2459, 1996.

R. Parrish, J. D. M. Gass, and D. R. Anderson. Outer retina ischemic infarctiona newly recognized complication of cataract extraction and closed vitrectomy: Part 2. an animal model. *Ophthalmology*, 89(12):1472–1477, 1982.

S. Pastor-Idoate, R. Bonshek, L. Irion, I. Zambrano, P. Carlin, A. Mironov, P. Bishop, D. McLeod, and P. E. Stanga. Ultrastructural and histopathologic findings after pars plana vitrectomy with a new hypersonic vitrector system. qualitative preliminary assessment. *PLoS One*, 12(4): e0173883, 2017.

K. T. Patton and G. A. Thibodeau. *Anthony's Textbook of Anatomy & Physiology-E-Book*. Elsevier Health Sciences, 2018.

M. Piccirelli, O. Bergamin, K. Landau, P. Boesiger, and R. Luechinger. Vitreous deformation during eye movement. *NMR in Biomedicine*, 25(1):59–66, 2012.

V. J. Pinfield, E. Dickinson, and M. J. Povey. Modeling of concentration profiles and ultrasound velocity profiles in a creaming emulsion: importance of scattering effects. *Journal of colloid and interface science*, 166(2):363–374, 1994.

J. Pokki, O. Ergeneman, S. Sevim, V. Enzmann, H. Torun, and B. J. Nelson. Measuring localized viscoelasticity of the vitreous body using intraocular microprobes. *Biomedical microdevices*, 17(5):85, 2015.

J. O. Pralits, R. Repetto, I. Nepita, M. R. Romano, F. Ravera, E. Santini, and L. Liggieri. The effect of albumin on the interfacial tension of silicone oil in vitrectomized eyes. *Investigative Ophthalmology & Visual Science*, 58(8):5006–5006, 2017.

W. H. Press, S. A. Teukolsky, B. P. Flannery, and W. T. Vetterling. Numerical recipes in fortran 77: volume 1, volume 1 of fortran numerical recipes: the art of scientific computing. 1992.

F. Ravera, L. Liggieri, and R. Miller. Molecular orientation as a controlling process in adsorption dynamics. *Colloids and Surfaces A: Physicochemical and Engineering Aspects*, 175(1):51–60, 2000.

F. Ravera, L. Liggieri, and G. Loglio. Dilational rheology of adsorbed layers by oscillating drops and bubbles. *Progr. Colloid Interface Sci., Interfacial Rheology: Eds. R. Miller and L. Liggieri. Leiden: Brill*, 1:137, 2009.

F. Ravera, K. Dziza, E. Santini, L. Cristofolini, and L. Liggieri. Emulsification and emulsion stability: The role of the interfacial properties. *Advances in Colloid and Interface Science*, 288: 102344, 2021. ISSN 0001-8686. doi: https://doi.org/10.1016/j.cis.2020.102344. URL `https://www.sciencedirect.com/science/article/pii/S0001868620306138`.

R. Repetto. An analytical model of the dynamics of the liquefied vitreous induced by saccadic eye movements. *Meccanica*, 41(1):101–117, 2006.

R. Repetto and M. Dvoriashyna. Mathematical models of vitreous humour dynamics and retinal detachment. In *Ocular Fluid Dynamics*, pages 303–325. Springer, 2019.

R. Repetto, A. Stocchino, and C. Cafferata. Experimental investigation of vitreous humour motion within a human eye model. *Physics in Medicine & Biology*, 50(19):4729, 2005.

R. Repetto, J. H. Siggers, and A. Stocchino. Steady streaming within a periodically rotating sphere. *Journal of Fluid Mechanics*, 608:71, 2008.

R. Repetto, J. Siggers, and A. Stocchino. Mathematical model of flow in the vitreous humor induced by saccadic eye rotations: effect of geometry. *Biomechanics and modeling in mechanobiology*, 9(1):65–76, 2010.

R. Repetto, J. H. Siggers, and J. Meskauskas. Steady streaming of a viscoelastic fluid within a periodically rotating sphere. *Journal of fluid mechanics*, 761:329–347, 2014.

R. M. Ribeiro, A. G. Teixeira, B. Diniz, R. B. Fernandes, Y. Zhong, R. Kerns, and M. S. Humayun. Performance analysis of ultrahigh-speed vitreous cutter system. *Retina*, 33(5):928–932, 2013.

N. Riley. Steady streaming. *Annual review of fluid mechanics*, 33(1):43–65, 2001.

S. Rizzo, F. Barca, T. Caporossi, and C. Mariotti. Twenty-seven–gauge vitrectomy for various vitreoretinal diseases. *Retina*, 35(6):1273–1278, 2015.

S. Rizzo, G. Fantoni, D. P. Mucciolo, A. Giorni, L. Volpi, M. Pierallini, A. Mazzoni, and F. Faraldi. Ultrasound in vitrectomy: An alternative approach to traditional vitrectomy techniques. *Retina*, 40(1):24–32, 2020.

M. Romano, M. Ferrara, I. Nepita, J. DAmato Tothova, A. Giacometti Schieroni, D. Reami, R. Mendichi, L. Liggieri, and R. Repetto. Biocompatibility of intraocular liquid tamponade

agents: an update. Accepted for publication.

M. R. Romano, M. Angi, V. Romano, F. Parmeggiani, C. Campa, X. Valldeperas, and C. Costagliola. Intraocular pressure changes following the use of silicone oil or densiron® 68 as endotamponade in pars plana vitrectomy. *Clinical Ophthalmology (Auckland, NZ)*, 4:1391, 2010.

M. R. Romano, G. Cennamo, M. Ferrara, M. Cennamo, and G. Cennamo. Twenty-seven-gauge versus 25-gauge vitrectomy for primary rhegmatogenous retinal detachment. *Retina*, 37(4): 637–642, 2017.

M. R. Romano, A. Stocchino, M. Ferrara, A. Lagazzo, and R. Repetto. Fluidics of single and double blade guillotine vitrectomy probes in balanced salt solution and artificial vitreous. *Translational vision science & technology*, 7(6):19–19, 2018.

T. Rossi, G. Querzoli, G. Pasqualitto, M. Iossa, L. Placentino, R. Repetto, A. Stocchino, and G. Ripandelli. Ultrasound imaging velocimetry of the human vitreous. *Experimental eye research*, 99:98–104, 2012.

T. Rossi, G. Querzoli, G. Angelini, C. Malvasi, M. Iossa, L. Placentino, and G. Ripandelli. Fluid dynamics of vitrectomy probes. *Retina*, 34(3):558–567, 2014a.

T. Rossi, G. Querzoli, G. Angelini, C. Malvasi, M. Iossa, L. Placentino, and G. Ripandelli. Introducing new vitreous cutter blade shapes: a fluid dynamics study. *Retina*, 34(9):1896–1904, 2014b.

T. Rossi, G. Querzoli, G. Angelini, A. Rossi, C. Malvasi, M. Iossa, and G. Ripandelli. Instantaneous flow rate of vitreous cutter probes. *Investigative ophthalmology & visual science*, 55(12): 8289–8294, 2014c.

T. Rossi, G. Querzoli, G. Angelini, A. Rossi, C. Malvasi, M. Iossa, and G. Ripandelli. Ocular perfusion pressure during pars plana vitrectomy: a pilot study. *Investigative ophthalmology & visual science*, 55(12):8497–8505, 2014d.

T. Rossi, G. Querzoli, C. Malvasi, M. Iossa, G. Angelini, and G. Ripandelli. A new vitreous cutter blade engineered for constant flow vitrectomy. *Retina*, 34(7):1487–1491, 2014e.

T. Rossi, G. Querzoli, G. Angelini, C. Malvasi, A. Rossi, M. Morini, G. Esposito, A. Micera, N. M. di Luca, and G. Ripandelli. Hydraulic resistance of vitreous cutters: the impact of blade design and cut rate. *Translational Vision Science & Technology*, 5(4):1–1, 2016.

T. Rossi, G. Querzoli, A. Gelso, G. Angelini, A. Rossi, P. Corazza, L. Landi, S. Telani, and G. Ripandelli. Ocular perfusion pressure control during pars plana vitrectomy: testing a novel device. *Graefe's Archive for Clinical and Experimental Ophthalmology*, 255(12):2325–2330, 2017.

T. Rossi, G. Querzoli, G. Angelini, A. Rossi, C. Malvasi, L. Landi, S. Telani, and G. Ripandelli. Predicting infusion pressure during pars plana vitrectomy: a physically based model. *Journal for Modeling in Ophthalmology*, 2(3):88–103, 2019.

M. Saito, L.-J. Yin, I. Kobayashi, and M. Nakajima. Comparison of stability of bovine serum albumin-stabilized emulsions prepared by microchannel emulsification and homogenization.

Food Hydrocolloids, 20(7):1020–1028, 2006.

E. Santini, L. Liggieri, L. Sacca, D. Clausse, and F. Ravera. Interfacial rheology of span 80 adsorbed layers at paraffin oilwater interface and correlation with the corresponding emulsion properties. *Colloids and Surfaces A: Physicochemical and Engineering Aspects*, 309:270–279, 11 2007.

A. Sarkar, K. K. Goh, R. P. Singh, and H. Singh. Behaviour of an oil-in-water emulsion stabilized by β-lactoglobulin in an in vitro gastric model. *Food Hydrocolloids*, 23(6):1563–1569, 2009.

N. Savion, A. Alhalel, G. Treister, and E. Bartov. Role of blood components in ocular silicone oil emulsification. studies on an in vitro model. *Investigative ophthalmology & visual science*, 37 (13):2694–2699, Dec. 1996. ISSN 0146-0404. PMID: 8977484.

A. Schulz, S. Wahl, A. Rickmann, J. Ludwig, B. V. Stanzel, H. von Briesen, and P. Szurman. Age-related loss of human vitreal viscoelasticity. *Translational vision science & technology*, 8(3): 56–56, 2019.

J. Sebag. Age-related changes in human vitreous structure. *Graefe's archive for clinical and experimental ophthalmology*, 225(2):89–93, 1987.

J. Sebag. *The vitreous: Structure, Function and Pathobiology*. Springer and Verlag, 1989.

J. Sebag. *Vitreous: In Health and Disease*. Springer, 2014.

F. Semeraro, A. Russo, F. Morescalchi, E. Gambicorti, S. Vezzoli, F. Parmeggiani, M. R. Romano, and C. Costagliola. Comparative assessment of intraocular inflammation following standard or heavy silicone oil tamponade: a prospective study. *Acta ophthalmologica*, 97(1):e97–e102, 2019.

S. Shafaie, V. Hutter, M. B. Brown, M. T. Cook, and D. Y. Chau. Diffusion through the ex vivo vitreal body–bovine, porcine, and ovine models are poor surrogates for the human vitreous. *International journal of pharmaceutics*, 550(1-2):207–215, 2018.

P. Sharif-Kashani, J. Hubschman, D. Sassoon, and H. P. Kavehpourlee. Rheology of the vitreous gel: effects of macromolecule organization on the viscoelastic properties. *Journal of Biomechanics*, 44(3):419–423, Feb. 2011. ISSN 1873-2380. doi: 10.1016/j.jbiomech.2010.10.002. PMID: 21040921.

P. Sharif-Kashani, K. Nishida, H. P. Kavehpour, S. D. Schwartz, and J. P. Hubschman. Effect of cut rates on fluidic behavior of chopped vitreous. *Retina*, 33(1):166–169, 2013.

A. Shiang, A. Özkekin, J.-C. Lin, and D. Rockwell. Hydroelastic instabilities in viscoelastic flow past a cylinder confined in a channel. *Experiments in fluids*, 28(2):128–142, 2000.

A. F. Silva, F. Pimenta, M. A. Alves, and M. S. Oliveira. Flow dynamics of vitreous humour during saccadic eye movements. *Journal of the Mechanical Behavior of Biomedical Materials*, 110:103860, 2020.

K. C. Sippel and R. Pineda. Phacoemulsification and thermal wound injury. In *Seminars in ophthalmology*, volume 17, pages 102–109. Taylor & Francis, 2002.

L. T. Sniegoski and J. R. Moody. Determination of serum and blood densities. *Analytical chem-*

istry, 51(9):1577–1578, 1979.

N. Soman and R. Banerjee. Artificial vitreous replacements. *Bio-medical materials and engineering*, 13(1):59–74, 2003.

P. Somasundaran and L. Zhang. Adsorption of surfactants on minerals for wettability control in improved oil recovery processes. *Journal of Petroleum Science and Engineering*, 52(1):198–212, 2006.

J. Soós, M. D. Resch, S. Berkó, A. Kovács, G. Katona, A. Facskó, E. Csányi, and M. Budai-Szűcs. Comparison of hydrophilic ophthalmic media on silicone oil emulsification. *PloS one*, 15(6): e0235067, 2020.

M. G. Speaker, P. N. Guerriero, J. A. Met, C. T. Coad, A. Berger, and M. Marmor. A case-control study of risk factors for intraoperative suprachoroidal expulseve hemorrhage. *Ophthalmology*, 98(2):202–210, 1991.

P. E. Stanga, S. Pastor-Idoate, I. Zambrano, P. Carlin, and D. McLeod. Performance analysis of a new hypersonic vitrector system. *PloS one*, 12(6):e0178462, 2017.

P. E. Stanga, J. I. Williams, S. A. Shaarawy, A. Agarwal, A. Venkataraman, D. A. Kumar, T. T. You, and R. S. Hope. First-in-human clinical study to investigate the effectiveness and safety of pars plana vitrectomy surgery using a new hypersonic technology. *Retina (Philadelphia, Pa.)*, 40(1):16, 2020.

D. H. Steel and S. Charles. Vitrectomy fluidics. *Ophthalmologica*, 226(Suppl. 1):27–35, 2011.

P. Sternberg, D. L. Hatchell, G. N. Foulks, and M. B. Landers. The effect of silicone oil on the cornea. *Archives of Ophthalmology*, 103(1):90–94, 1985.

A. Stocchino, R. Repetto, and C. Cafferata. Eye rotation induced dynamics of a newtonian fluid within the vitreous cavity: the effect of the chamber shape. *Physics in Medicine & Biology*, 52 (7):2021, 2007.

A. Stocchino, I. Nepita, R. Repetto, A. Dodero, M. Castellano, M. Ferrara, and M. R. Romano. Fluid dynamic assessment of hypersonic and guillotine vitrectomy probes in viscoelastic vitreous substitutes. *Translational Vision Science & Technology*, 9(6):9–9, 2020.

Y. Sugiura, F. Okamoto, Y. Okamoto, T. Hiraoka, and T. Oshika. Intraocular pressure fluctuation during microincision vitrectomy with constellation vision system. *American journal of ophthalmology*, 156(5):941–947, 2013.

K. Swindle, P. Hamilton, and N. Ravi. In situ formation of hydrogels as vitreous substitutes: Viscoelastic comparison to porcine vitreous. *Journal of Biomedical Materials Research - Part A*, 87A(3):656–665, Dec. 2008. ISSN 1549-3296.

P. Szabo, J. Rallison, and E. Hinch. Start-up of flow of a fene-fluid through a 4: 1: 4 constriction in a tube. *Journal of non-newtonian fluid mechanics*, 72(1):73–86, 1997.

H. Tabandeh, P. M. Sullivan, P. Smahliuk, H. W. Flynn Jr, and J. Schiffman. Suprachoroidal hemorrhage during pars plana vitrectomy: Risk factors and outcomes. *Ophthalmology*, 106(2): 236–242, 1999.

R. I. Tanner. Engineering rheology. 52, 2000.

J. T. Thompson. Advantages and limitations of small gauge vitrectomy. *Survey of ophthalmology*, 56(2):162–172, 2011.

W. Thomson. 4. on the equilibrium of vapour at a curved surface of liquid. *Proceedings of the Royal Society of Edinburgh*, 7:63–68, 1872.

M. Tokita, Y. Fujiya, and K. Hikichi. Dynamic viscoelasticity of bovine vitreous body. *Biorheology*, 21(6):751–756, 1983.

K. Tozer, M. W. Jhonson, and J. Sebag. Vitreous aging and posterior vitreous detachment. In S. J., editor, *Vitreous in Health and Disease*, pages 131–150. Springer-Verlag, 2014.

N. K. Tram and K. E. Swindle-Reilly. Rheological properties and age-related changes of the human vitreous humor. *Frontiers in bioengineering and biotechnology*, 6:199, 2018.

B. C. Tripp, J. J. Magda, and J. D. Andrade. Adsorption of globular proteins at the air/water interface as measured via dynamic surface tension: concentration dependence, mass-transfer considerations, and adsorption kinetics. *Journal of colloid and interface science*, 173(1):16–27, 1995.

N. J. Turro, X.-G. Lei, K. Ananthapadmanabhan, and M. Aronson. Spectroscopic probe analysis of protein-surfactant interactions: the bsa/sds system. *Langmuir*, 11(7):2525–2533, 1995.

J. M. Urueña, A. A. Pitenis, R. M. Nixon, K. D. Schulze, T. E. Angelini, and W. G. Sawyer. Mesh size control of polymer fluctuation lubrication in gemini hydrogels. *Biotribology*, 1:24–29, 2015.

A. S. Utada, E. Lorenceau, D. R. Link, P. D. Kaplan, H. A. Stone, and D. Weitz. Monodisperse double emulsions generated from a microcapillary device. *Science*, 308(5721):537–541, 2005.

L. Wagenfeld, O. Zeitz, C. Skevas, and G. Richard. Long-lasting endotamponades in vitreoretinal surgery. *Ophthalmologica*, 224(5):291–300, 2010.

K. A. Walton, C. H. Meyer, C. J. Harkrider, T. A. Cox, and C. A. Toth. Age-related changes in vitreous mobility as measured by video b scan ultrasound. *Experimental Eye Research*, 74(2): 173–80, Feb. 2002. ISSN 0014-4835. doi: 10.1006/exer.2001.1136. PMID: 11950227.

R. Wang, M. Snead, P. Alexander, and D. Ian Wilson. Assessing bulk emulsification at the silicone oil–saline solution interface in a 3d model of the eye. *Acta ophthalmologica*, 2020.

A. Watanabe, A. Tsuzuki, K. Arai, T. Gekka, and H. Tsuneoka. Treatment of dropped nucleus with a 27-gauge twin duty cycle vitreous cutter. *Case Reports in Ophthalmology*, 7(1):44–48, 2016.

J. Weiss. The dynamics of enstrophy transfer in two-dimensional hydrodynamics. *Physica D: Nonlinear Phenomena*, 48(2):273–294, 1991. ISSN 0167-2789. doi: https://doi.org/10.1016/0167-2789(91)90088-Q. URL `https://www.sciencedirect.com/science/article/pii/016727899190088Q`.

L. Wickham, R. H. Asaria, R. Alexander, P. Luthert, and D. G. Charteris. Immunopathology of intraocular silicone oil: enucleated eyes. *British journal of ophthalmology*, 91(2):253–257,

2007.

P. A. Wierenga, M. R. Egmond, A. G. Voragen, and H. H. de Jongh. The adsorption and unfolding kinetics determines the folding state of proteins at the air–water interface and thereby the equation of state. *Journal of colloid and interface science*, 299(2):850–857, 2006.

R. Williams, M. Day, M. Garvey, G. Morphis, C. Irigoyen, D. Wong, and T. Stappler. Injectability of silicone oil-based tamponade agents. *British journal of ophthalmology*, 95(2):273–276, 2011.

D. Wong, I. Kumar, S. Quah, H. Ali, X. Valdeperas, and M. R. Romano. Comparison of postoperative intraocular pressure in patients with densiron-68 vs conventional silicone oil: a case–control study. *Eye*, 23(1):190–194, 2009.

R. H. Wurtz and M. E. Goldberg. *The neurobiology of saccadic eye movements*, volume 3. Elsevier Science Limited, 1989.

Q. Xu and M. Nakajima. The generation of highly monodisperse droplets through the breakup of hydrodynamically focused microthread in a microfluidic device. *Applied Physics Letters*, 85 (17):3726–3728, 2004.

P. Yadav, H. Yadav, V. G. Shah, G. Shah, and G. Dhaka. Biomedical biopolymers, their origin and evolution in biomedical sciences: A systematic review. *Journal of clinical and diagnostic research: JCDR*, 9(9):ZE21, 2015.

T. Yilmaz and M. Güler. The role of nystagmus in silicone oil emulsification after pars plana vitrectomy and silicone oil injection for complex retinal detachment, 2008.

C. Zehetner, M. Moelgg, E. Bechrakis, C. Linhart, and N. E. Bechrakis. In vitro flow analysis of novel double-cutting, open-port, ultrahigh-speed vitrectomy systems. *Retina*, 38(12):2309–2316, 2018.

C. Zhang, X. Guo, P. Brunet, M. Costalonga, and L. Royon. Acoustic streaming near a sharp structure and its mixing performance characterization. *Microfluidics and Nanofluidics*, 23(9): 1–15, 2019.

R. L. Zimmerman. In vivo measurements of the viscoelasticity of the human vitreous humor. *Biophys. J.*, 29:539–544, 1980.